Reaction dynamics of small molecules in solution

Denis Leshchev

To cite this version:

Denis Leshchev. Reaction dynamics of small molecules in solution. Atomic and Molecular Clusters [physics.atm-clus]. Université Grenoble Alpes, 2016. English. NNT : 2016GREAY023 . tel-01489776

HAL Id: tel-01489776
https://theses.hal.science/tel-01489776

Submitted on 14 Mar 2017

Communauté
UNIVERSITÉ Grenoble Alpes

THÈSE

Pour obtenir le grade de

DOCTEUR DE L'UNIVERSITÉ DE GRENOBLE

Spécialité : **Physique**

Arrêté ministérial : août 2006

Présentée par

Leshchev Denis

Thèse dirigée par **Michael Wulff**

préparée au sein **d'Installation Européene de Rayonnement Synchrotron**
et de **d'École Doctorale de Physique Grenoble, France**

La dynamique de réaction de petites molécules en solution

Thèse soutenue publiquement le **12 Juillet 2016**,
devant le jury composé de :

M Hans Peter Trommsdorff
Professeur à Laboratoire Interdisciplinaire de Physique, Saint Martin d'Hères, Président du Jury et Examinateur

M Maciej Lorenc
Chercheur à l'Institut de Physique de Rennes, Examinateur

M Anton Plech
Professeur à Institut de technologie de Karlsruhe, Rapporteur

M Martin Meedom Nielsen
Professeur de l'Université technique du Danemark, Rapporteur

M Michael Wulff
Chercheur à d'Installation Européene de Rayonnement Synchrotron, Directeur de thèse

Reaction dynamics of small molecules in solution

Denis Leshchev

Abstract

This thesis investigates photoinduced transient dynamics of small molecules in solution with the use of time-resolved wide angle x-ray scattering (TR-WAXS). The core of the thesis is the precise determination of transient structures with the use of various structural optimization schemes. Some of the TR-WAXS results are supplemented with transient absorption optical spectroscopy (TOAS) and time-resolved x-ray emission spectroscopy (TR-XES) measurements allowing for a more complete description of the systems.

The work includes four different projects which can be grouped into two classes according to the type of reaction appearing upon photoexcitation: dissociation and electron transfer. The first class includes the simple triatomic molecules mercury halides and triiodide where we study the recombination dynamics of the free photofragments. This part of the thesis demonstrates the possibility to gain new knowledge about the dynamics of these model systems such as new recombination channels and reaction intermediates appearing in less than 100 ps, the x-ray pulse length from the synchrotron, by the use of time-slicing technique. The second class of systems includes transition metal complexes that are highly relevant for light harvesting applications, $[Fe(NHC)_2]^{2+}$ and Ru=Co, where the spin and structural dynamics are investigated. These projects extend previous work to a family of more complex systems constituted of relatively low-Z atoms (first row transition metals) and bring new insights into the photochemistry of the compounds.

Résumé

Ce rapport de thèse présente une étude de la dynamique transitoire de molécules de taille réduite en solution induite par photoexcitation. Celle-ci est réalisée au travers d'une expérience de mesure de diffusion de rayons X aux grands angles (TR-WAXS). La partie principale de ce rapport s'articule autour de la dertermination des structures transitoires avec l'utilisation de plusieurs schémas structurelles d'optimisation. Certains résultats obtenus par TR-WAXS sont complétés avec ceux obtenus par spectroscopie optique résolue dans le temps (TOAS) ainsi que par spectroscopie d'émission de rayons X de ces molécules (TR-XES) permettant une plus complète description de ces systèmes.

Ce travail est composé de 4 differents projets lesquelles peuvent être regroupé en 2 groupes selon le type de réaction declenchées par photoexcitation : dissociation et transfert d'électron. Le premier groupe comprends la molécule triatomique de mercure, halogénure métallique et le triiodide où nous étudions la dynamique de recombinaison des photofragments libres. Cette partie démontre la possibilité de développer de nouvelles connaissances concernant la dynamique de ces modèles, comme par exemple, la découverte de la recombinaison par canaux ou bien par l'apparition de réactions intermédiaires en moins de 100 ps, correspondant à la longueur de l'impulsion de rayons X générée par le synchrotron, mise en évidence en utilisant la technique de découpage temporelle. Le deuxième groupe de systèmes est composé de complexes de métaux de transition, très pertinents pour les applications liées à la récolte de lumière, $[\mathrm{Fe(NHC)_2}]^{2+}$ et Ru=Co, où le spin et les structures dynamiques sont étudiées. Ces projets prolongent de précedents travaux à une famille de systèmes plus complexes avec un numéro atomique bas (première colonne de transition metallique) et fait la lumière sur de nouveaux composés en photochimie.

Acknowledgements

First of all I would like to thank Michael Wulff for supervising this thesis. Thanks to your guidance and support in science and administration I managed to make my way through the PhD. I appreciate the freedom I was given for development of my own ideas and the feedback you have given on every stage of the project. Thanks to your help in establishing the collaborations, which gave birth to very interesting projects. I am looking forward to working together on future exciting science.

A special thanks goes to Dmitry Khakhulin. Dmitry, through the past three years you have been the key person in the progress of my thesis. I highly appreciate your style of mentoring which was the right approach for stimulating my work. I thank you for your feedback on almost everything I have done and all the scientific discussions we had. Your help in almost all experiments performed in this work is invaluable. Working with you in the team is always exciting and I hope that we will work together in the future.

I would like to thank Gemma Newby. Thank you for all your help and support in everything. Thanks to your attitude we had a lot of fun in the past three years. I also want to thank you for proofreading this manuscript. Thanks to your efforts I feel that my English level has grown enormously.

Thanks to Pierre Ribault for being a good friend in these PhD times. We had a lot of fun together during and outside the working hours, which I will warmly remember. I highly appreciate all your help in solving the French administration issues. I must say that without your help I would be completely lost!

Thanks to Norman Kretzschmar and Martin Pedersen. I thank you for your kindness and all the scientific discussions we had.

Thanks to Wolfgang Reichenbach for helping solve the engineering issues at the beamline. Thank you for helping me and Gemma in creating the new capillary nozzle.

Thanks to Franc Sever and Laurent Claustre for providing excellent software support

during the measurements. Thanks to your efforts, the experiments ran smoothly and we managed to collect lots of interesting data.

I would like to thank Tobias Harlang, Mads Laursen, Lisa Fredin and Elisa Biasin for very fruitful collaboration on the carbene molecule.

Thanks to Sophie Canton for a very good collaboration on the ruthenium-cobalt complex. I would also like to thank you for giving me a crush course on transition metal chemistry and sharing your knowledge about spin crossover and light harvesting.

Thanks to all my friends which made life outside the synchrotron very enjoyable.

A very big thanks to my mother and sister for supporting me from Moscow. Without your support this thesis would be simply impossible. I really appreciate your help and that I can always rely on you.

Finally, I would like to thank my wife, Nataliya. Thank you for the unconditional love and all the support you have given to me through these years. We had fantastic times together and I am really happy to have you by my side. Thank you for patience and understanding during the stressful times. I love you.

Contents

List of Figures

List of Tables

Acronyms

ID	insertion device
ESRF	European Synchrotron Radiation Facility
TR	time-resolved
RF	radio-frequency
FWHM	full-width-half-maximum
WAXS	wide angle x-ray scattering
SAXS	small angle x-ray scattering
XES	x-ray emission spectroscopy
TOAS	transient optical absorption spectroscopy
IRF	instrument response function
ML	multilayer
DFT	density functional theory
MD	molecular dynamics
FT	Fourier transform
RDF	radial distribution function
IAD	integrated absolute differential
PGR	primary geminate recombination
SGR	secondary geminate recombination
NGR	non-geminate recombination
CIP	contact ion pair
GTA	glycerol triacetate
ET	electron tranfer
GS	ground state
MLCT	metal-to-ligand-charge-transfer
MC	metal centered
NHC	N-heterocyclic carbene

Chapter 1

Introduction

A deep understanding of a chemical reaction requires a full description of all the pathways between reactants and products via intermediates, if they exist, and the time scales of the corresponding molecular transformations. Solution phase chemical reactions are of a particular interest, since the liquid medium is hosting many of biological and chemical processes in nature. The first steps in the investigation of the reaction dynamics in real time were done shortly after the advent of pulsed laser sources. Initially it was only possible to study some of the simplest reactions, for example, the diffusive recombination of radicals produced after flash photolysis. Later, ultra-short pulse sources reached femtosecond resolution allowing the observation of elementary chemical processes such as bond breakage and formation.

Optical pump-probe techniques supported by theory provided great insight into the dynamical understanding of chemical reactions. However, while spectroscopic observables can be easily interpreted for small molecular systems, with the increase in system size and complexity it becomes difficult to unambiguously interpret the experimental data and obtain a comprehensive understanding of the dynamics [1–3]. On the other hand, with the emergence of structurally sensitive tools such as x-ray scattering and spectroscopy, direct studies of static structure with atomic precision became possible. The combination of these new x-ray tools with the pump-probe method led to the development of time-resolved x-ray techniques providing a complete four-dimensional (space-time) picture of chemical dynamics[1]. The latter became possible due to the appearance of bright x-ray

---

[1] Note, that together with the advent of the x-ray tools, time-resolved electron diffraction was also broadly applied for investigation of transient dynamics (see, for example [4]). However, in the field of physical chemistry electron diffraction is mainly used for studies of gas phase reactions, which are out of

sources like third generation synchrotrons and more recently free electron lasers. Some of the most successful techniques for studying solution phase chemistry include time-resolved x-ray scattering, absorption and emission spectroscopy which address different aspects of transient dynamics [5–8].

This thesis aims at bringing new insights into the dynamics of transient species in solution with an emphasis on determination of their precise molecular structure. This is achieved by using time-resolved wide angle x-ray scattering (TR-WAXS) as the main tool for structural analysis. Other techniques such as transient optical absorption spectroscopy (TOAS) and time-resolved x-ray emission spectroscopy (TR-XES) are used as complementary tools for aiding in the assignment of transient species nature. The experimental setup for these techniques and the data analysis procedures are described in the following two chapters 2, 3 (Experimental apparatus and Data analysis). The systems studied in this work are divided into two groups according to the type of photoinduced reaction. First, we investigate the dissociation reactions of model triatomic molecules, mercury halides (HgX_2, X = I, Br) and triiodide (I_3^-) (Chapter 4, Dissociation reactions). The goal of the study of HgX_2 is to obtain a more complete picture of the recombination dynamics of the free radicals produced by photodissociation; the work is extended by a study of the geminate recombination dynamics of triiodide, where the interactions between the photofragements and the surrounding liquid medium leads to the formation of a so-called contact ion pair. It is demonstrated that for triatomic molecules it is possible to precisely determine the structures of both the ground and excited state, which are then compared to theoretical and experimental results from the literature. Additionally, for all the studied systems in this section, transient optical absorption spectroscopy measurements were performed for benchmarking the x-ray kinetic results. The second group of systems includes two transition metal complexes: an iron-based complex belonging to a promising family of dye sensitizers and a bimetallic ruthenium-cobalt complex serving as a prototype system for the study of electron transfer over large distances (Chapter 5, Electron transfer reactions). Investigation of the first system has a goal of structural, thermodynamic and kinetic characterization of the complex in the excited state and their relations with the photochemical properties of the compound. Determination of the precise structure of the complex required the development of a new structural optimization protocol, appearing to be promising in dealing with increasingly complex molecular structures. The bimetallic complex extends

---

the scope of present work.

the work on photoactive systems by providing new insights into multi-scale changes in the structure of the complex. Here, the analysis is supported by direct observation of the Co spin and charge dynamics via x-ray emission spectroscopy. Through out the thesis we discuss the strengths and limitations of the x-ray scattering for determining of the excited state structures. The importance of using multilayer optics providing a well defined x-ray spectrum of the probe pulse without a large penalty on the incident flux is particularly emphasized. Finally, the thesis is concluded with an overview of the results and an outlook for future work (Chapter 6, Conclusions).

Introduction

1.1 Introduction (version française)

Une compréhension profonde d'une réaction chimique nécessite une description complète de toutes les voies entre les réactifs et les produits via des intermédiaires, si elles existent, et les échelles de temps des transformations moléculaires correspondantes. Les réactions chimiques dans solution ont d'un intérêt particulier, puisque le milieu liquide est l'hôte d'un grand nombre de processus biologiques et chimiques dans la nature. Les premières étapes de l'enquête sur la dynamique de réaction en temps réel ont été effectuées peu après l'avènement de sources lasers pulsés. Initialement, il n'était possible qu'étudier certaines des réactions les plus simples, par exemple, la recombinaison diffusive des radicaux produits après photolyse éclair. Ensuite les sources d'impulsions ultra-courtes atteint une résolution femtoseconde qui permet l'observation des processus chimiques élémentaires, tels que la rupture et la formation des liaisons.

Les techniques pompe-sonde optique completées par la théorie offrent un excellent aperçu de la compréhension dynamique des réactions chimiques. Cependant, alors que les valeurs observables spectroscopiques peuvent être facilement interprétées pour les petits systèmes moléculaires, avec l'augmentation de la taille et de la complexité du système, il devient difficile d'interpréter les données expérimentales sans ambiguïté et d'obtenir une compréhension globale de la dynamique [1–3].. D'un autre côté, des études directes de structure statique avec une précision atomique est devenues possible avec l'émergence d'outils structurellement sensibles tels que la diffusion et la spectroscopie de rayons X. La combinaison de ces nouveaux outils de rayon X avec la méthode pompe-sonde a conduit au développement des techniques de rayons X résolue en temps fournissant une image complète à quatre dimensions (espace-temps) de la dynamique chimique [2]. Il est devenu possible

---

[2] Il faut noter qu'avec l'avènement des outils de rayons X, la diffraction d'électrons résolue dans le

grâce à l'apparition de sources lumineuses de rayons X comme la troisième génération de synchrotrons et de lasers à électrons libres plus récemment. Certaines des techniques les plus efficaces pour étudier la chimie en phase de solution comprennent la diffusion des rayons X, la spectroscopie de l'absorption et l'émission résolues dans le temps qui abordent différents aspects de la dynamique transitoire [5–8].

Le but de cette thèse est d'apporter de nouvelles connaissances sur la dynamique des espèces transitoires en solution en mettant l'accent sur la détermination de leur structure moléculaire précise. Cela est réalisé à l'aide de diffusion de rayons X d'un grand angle résolue dans le temps (TR-WAXS) comme outil principal pour l'analyse structurelle. D'autres techniques telles que la spectroscopie d'absorption optique transitoire (TOAS) et spectroscopie émission des rayon X résolue dans le temps (TR-XES) sont utilisés comme des outils complémentaires pour aider à l'attribution des transitoires nature des espèces. Le dispositif expérimental pour ces techniques et les procédures d'analyse des données sont décrites dans les deux chapitres suivants (chapitres 2, 3). Les systèmes étudiés dans ce travail sont divisés en deux groupes selon le type de réaction photoinduite. En premiere, nous étudions les réactions de dissociation de molécules modèles triatomiques, des halogénures de mercure (HgX_2, X = I, Br) et triiodide (I_3^-) (chapitre 4). Le but de l'étude de HgX_2 est d'obtenir une image plus complète de la dynamique de recombinaison des radicaux libres produits par photodissociation ; le travail est étendu par une étude de la dynamique géminée de recombinaison de triiodure, où les interactions entre les photofragements et le milieu liquide environnant conduit à la formation d'une paire de contacts d'ions. Il est montré qu'il est possible pour des molécules triatomiques de déterminer précisément les structures à la fois à l'état fondamental et excité, qui sont ensuite comparés aux résultats théoriques et expérimentaux de la littérature. En outre, pour tous les systèmes étudiés dans cette section, les mesures transitoires de spectroscopie d'absorption optique ont été effectuées pour l'étalonnage des résultats cinétiques des rayons X. Le deuxième groupe de systèmes comprend deux complexes de métaux de transition : un complexe à base de fer appartenant à une famille prometteuse de sensibilisateurs de colorant et d'un complexe de ruthénium-cobalt bimétallique servant de prototype pour l'étude du transfert d'électrons sur de grandes distances (chapitre 5). Enquête sur le premier système a pour l'objectif

---

temps a été aussi largement appliquée pour l'étude de la dynamique transitoire (voir, par exemple [4]). Cependant, dans le domaine de la chimie physique la diffraction d'électrons est principalement utilisée pour les études de réactions en phase gazeuse, qui sont hors de la portée du présent ouvrage.

de caractérisation structurale, thermodynamique et cinétique du complexe à l'état excité et leurs relations avec les propriétés photochimiques du composé. Détermination de la structure précise du complexe a nécessité le développement d'un nouveau protocole d'optimisation structurelle, ce qui semble être prometteur dans le traitement des structures moléculaires plus complexes. Le complexe bimétallique étend le travail sur les systèmes photoactifs en fournissant de nouvelles connaissances sur les changements multi-échelles dans la structure du complexe. Ici, l'analyse est soutenue par l'observation directe du spin et de charge dynamique de Co par la spectroscopie d'émission de rayons X. A travers de cette thèse, nous discutons les avantages et les défauts de la diffusion des rayons X pour déterminer des structures à l'état excité. L'importance de l'utilisation de l'optique multicouches fournissant un spectre de rayons X bien défini est particulièrement souligné. Enfin, la thèse se termine par un aperçu des résultats et des perspectives pour les travaux futurs (chapitre 6).

Chapter 2

Experimental apparatus

This chapter gives a brief overview of the measurement philosophy and the experimental setup on the ID09 beamline at the European Synchrotron Radiation Facility (ESRF, Figure 2.1, a), where all the experiments were performed. The beamline has a variety of tools for investigating many different dynamic phenomena; however, we will focus on the elements which were employed in the present thesis. Here we also discuss the transient optical absorption spectroscopy setup based on the ID09 laser system which was used for the optical spectroscopy measurements.

2.1 ESRF storage ring

The relevant information about the ESRF synchrotron can be summarized as follows. It is a third generation synchrotron, i.e. specially designed for delivery of high brilliance x-rays (small source size, low divergence, high intensity). The machine consists of three main components: the linear accelerator which increases the energy of the electrons produced by the electron gun up to 200 MeV; the booster which accelerates the electrons further up to 6 GeV; the storage ring which keeps the electrons on a stationary circular orbit (circumference ∼850 m). The storage ring consists of 64 bending magnets (each steering the beam by 5.6°) and 32 straight sections, where special magnetic structures for efficient production of x-rays (insertion devices, ID) are installed. In order to recover the energy of the electrons lost on radiation during the orbit revolution (∼5 MeV/turn) six radio-frequency (RF) cavities are installed in the ring. These cavities accelerate the electrons according to their time of arrival, which makes only bunch structures possible. The RF frequency of ESRF is 352.2 MHz and the orbit frequency of the electrons is its 992$^{\mathrm{th}}$ sub-

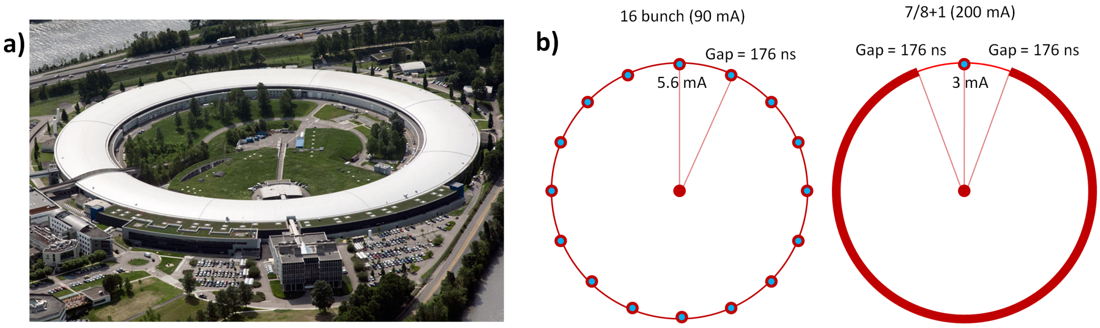

Figure 2.1. ESRF storage ring (a) and its filling modes used in the thesis (b).

harmonic, i.e. 355 kHz. As we will see below, the RF frequency provides a natural clock for synchronization of the whole experimental setup, which is important for reliable data collection.

Two filling modes of the synchrotron were used throughout the thesis, 16-bunch and 7/8+1. The first one corresponds to 16 electron bunches evenly spaced throughout the ring with a time gap of 176 ns between each of the bunches (Figure 2.1, b). The second mode corresponds to the filling where 7/8 of the ring is quasi-uniformly filled with electron microbunches and one single bunch placed in the middle of the empty 1/8 space of the ring. This bunch is separated from the uniform tails by 176 ns time gaps (Figure 2.1, b). In both cases, the single bunch current is in the range of 2-8 mA allowing the production of 80-120 ps x-ray flashes. The electron beam has a size of $\sim$100$\times$10 μm(h)$\times$$\mu$m(v) (FWHM) in the ID09 insertion devices.

2.2 Pump-probe technique

The pump-probe technique is a well known method for measuring transient dynamics and it originates from optical spectroscopy. The idea is to coherently prepare an ensemble of species in an excited state with a short (pump) pulse and then probe the changes of some experimental observable with a second delayed pulse. For example, in the case of TOAS, the observable is the optical density of the sample measured by the second (probe) pulse. By using suitable fast detectors, the temporal resolution of these experiments is limited to the duration of the optical pulses [9].

For experiments where an x-ray pulse serves as a probe one can use a similar approach. This works sufficiently for x-ray absorption and emission spectroscopy experiments where

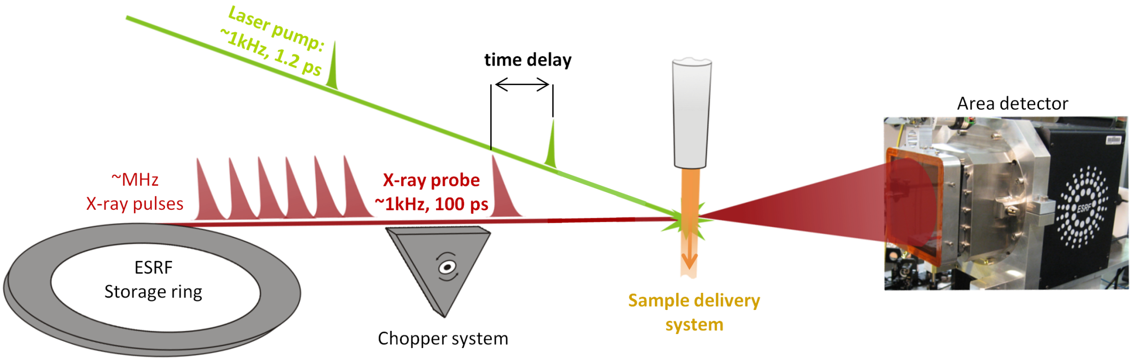

Figure 2.2. Schematic of the experimental setup implemented on ID09. The chopper system is used to match the rep-rates of the laser and x-ray pulse trains. Since each pair of pulses pumps and probes a new portion of sample, the detector "sees" a frozen picture of the dynamics appearing at the given time delay.

a fast photodiode collects the isotropically emitted x-rays [10, 11]. However, for measuring x-ray scattering patterns, which by nature are anisotropic [1], using a point detector is extremely inefficient, since one would need to perform measurements at many scattering angles. The best way to efficiently collect scattered x-rays in a wide range of scattering angles is the use of 2D area detector. Another problem arises here concerning the readout time of the detector. If one desires to have a temporal resolution limited by the (optical and/or x-ray) pulse duration, it is necessary to readout every single pulse x-ray scattering pattern (image). Since synchrotrons produce pulses with a frequency of ∼MHz, it is technically challenging to readout large 2D images with a corresponding frequency, although recent technical developments are aiming at this goal [12, 13].

On ID09 a different approach is realized which is based on a stroboscopic effect which does not require a time-resolved detector [14, 15]. Here, a mechanical chopper system (described below) is employed for the selection of single pulses coming from the synchrotron with a repetition rate (rep-rate) matching that of the laser (∼1 kHz). Simultaneously, the sample solution under investigation is circulated through a jet put in place where two beams overlap. The speed of circulation is set such that the sample is refreshed for each pair of pump and probe pulses (Figure 2.2). Since every single x-ray pulse probes the light-induced structural changes after a fixed time delay on a new portion of sample, the 2D detector "sees" a frozen picture of chemical reaction at this time delay. By setting different time delays between the pulses, one can "film" reactions in real time. At ID09 the

---

[1] Scattering intensity from the liquid is a function of the scattering angle 2θ, see chapter 3

temporal resolution of the setup is mainly defined by the duration of the x-ray pulses (100 ps) since they are much longer than the pump laser pulse (1 ps). In the following section we describe the hardware realization of the discussed principles.

2.3 ID09 beamline

The ID09 beamline was designed for time-resolved x-ray scattering experiments and later adopted an x-ray emission spectroscopy setup. Since the experiments are performed in the kHz rep-rate regime, the total x-ray flux available for experiments is $\sim$1000 times less than in a typical beamline dedicated to static studies. For this reason, the beamline was designed to operate with white beams, i.e. without a classical monochromator that selects a well defined x-ray energy. This approach gives an x-ray flux on the sample comparable with steady-state setups employing monochromatic beams at a relatively small cost of spatial resolution available in experiments. The latter is due to a (weak) smearing of the observed scattering features as discussed in detail in the following chapters.

The experimental station includes several components: the x-ray source, a pair of undulators (IDs); the optics hutch, where the x-ray beam is "prepared" for the experiment; the experimental hutch where the actual experiment is performed. The experimental hutch contains a few x-ray optical and synchronization components, the laser and the sample delivery system. Different components of the beamline are introduced below.

Undulators

Historically the beamline was equipped with two undulators, U17 and U20 (magnetic field period is correspondingly 17 and 20 mm), which were used for different purposes in this thesis[2]. The x-ray spectrum produced by these devices depends on the size of the gap between the magnetic "jaws". The main workhorse of the thesis was the U17 undulator with the vertical gap of 8.62 mm, which produces 5×10^8 photons per pulse at the fundamental energy of 18 keV and the FWHM of the spectrum is 3 %. Thanks to the high flux in this configuration one can quickly investigate a wide range of time delays and obtain an idea about the light induced structural changes and the kinetics of the sample. Additionally, the soft x-ray tail of the spectrum stimulates the x-ray emission of some elements (for example, transition metals) allowing simultaneous measurements of

---

[2] At the time of writing this thesis U20 was removed.

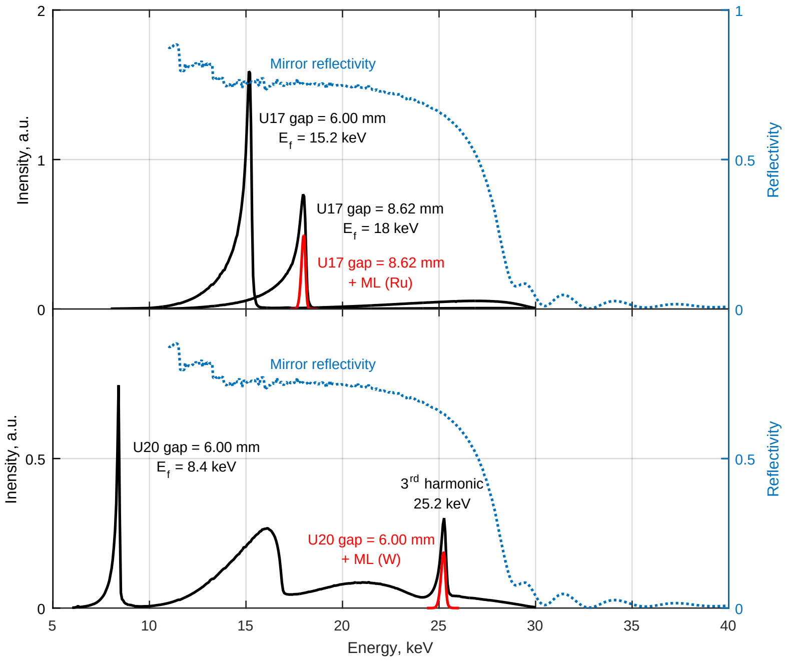

Figure 2.3. X-ray spectra produced by U17 (top panel) and U20 (bottom panel) undulators at different gap settings. Higher harmonics of the undulators are suppressed by the mirror (blue dashed line represents its reflectivity). The red lines represent the spectra which can be obtained with the use of multilayer monochromators installed in the experimental hutch.

scattering and emission. At closed gap, the U17 undulator produces softer x-rays (E_f = 15.2 keV) which increase the count rate of the emission spectroscopy measurements allowing a more effective exploration of the XES signals. Another undulator, the U20 at 6 mm was sometimes used simultaneously with the U17 (6 mm) facilitating the XES measurements, since its fundamental (E_f = 8.4 keV) allows a more efficient measurement of XES signals from first row transition metals. However, the main purpose of the U20 was the measurement of high energy scattering data by selecting the undulator's third harmonic (25.2 keV) with a multilayer monochromator (see below). That configuration allows the study of transient structures with high precision. The x-ray spectra employed in this work are shown in Figure 2.3.

Optics hutch

The radiation produced by the undulators enters the optics hutch through the front end shutter 20 m downstream the source. The principle components of the hutch are sketched in Figure 2.4. The main optical component is a toroidal mirror used for focusing the beam

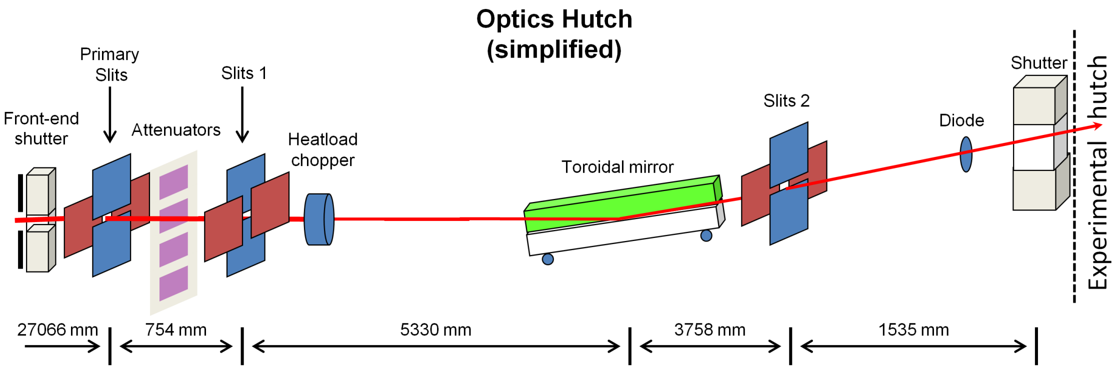

Figure 2.4. Schematic showing principle components of the optics hutch.

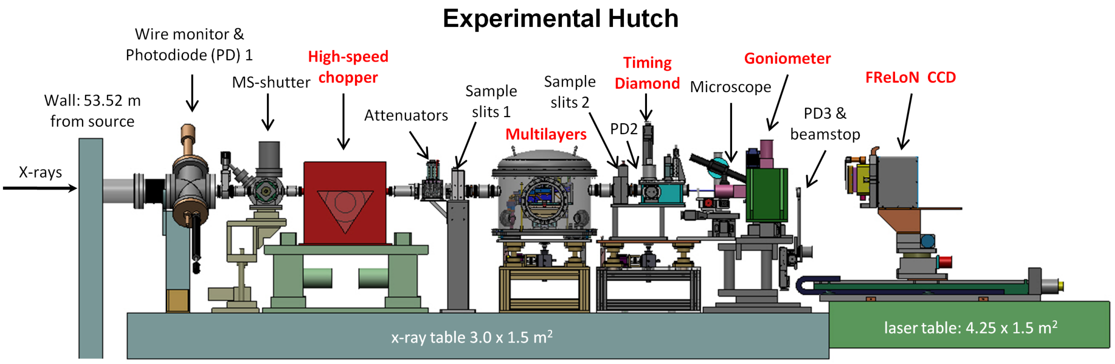

Figure 2.5. Schematic showing the principle components of the experimental hutch. The most important components are shown in red.

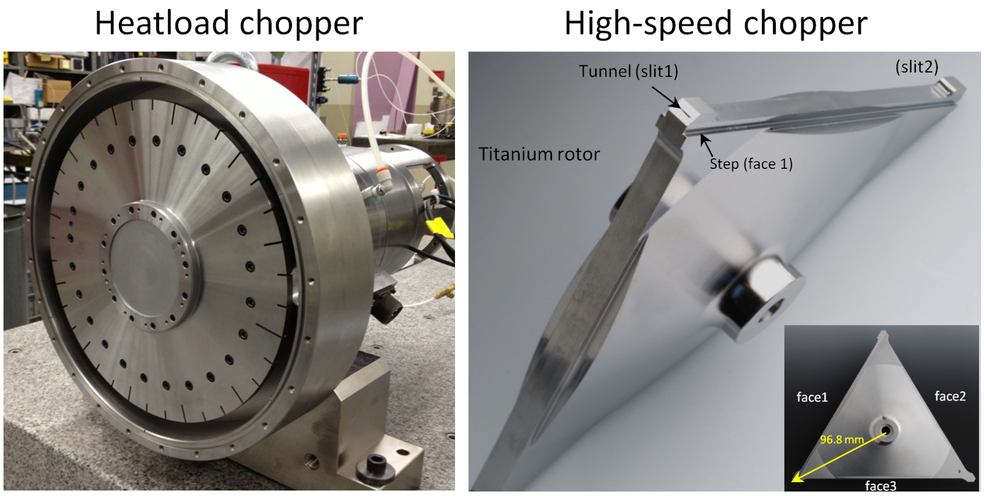

Figure 2.6. Heatload (left) and high-speed (right) choppers serving for single pulse selection.

on the sample 56.5 m from the source (center of undulator straight section). The mirror is made of Si and coated with platinum for better reflectivity at higher energies [16]. The mirror receives the 7.0×0.7 mm(h)×mm(v) beam from the primary slits at an angle of 2.608 mrad and focuses it to 90×60 μm(h)×μm(v) on the sample. The mirror is designed such that only the fundamental radiation of the undulators is efficiently reflected, so the measured scattering patters are freed of the high energy x-ray contamination (reflectivity curve is shown in Figure 2.3). Another component of this hutch is the heatload chopper[3], which has 12 slots and rotates at the frequency 82.19 Hz (4320th harmonic of electron orbit frequency) providing an opening time of 36 μs for each of the slots (Figure 2.6). The purpose of this chopper is to reduce the heat load on downstream devices from unused x-ray pulses coming from the storage ring (it takes 97.6 % of all the incoming power). Other components include shutters, several slits for shaping the beam and a photodiode.

Experimental hutch

From the optics hutch the x-ray beam enters the experimental hutch through the safety shutter (Figure 2.5). One of the main components of the hutch is the high-speed chopper, which allows the selection of single x-ray pulses. The chopper is a triangular rotor made of titanium (tip radius is 96.8 mm and its speed is 600 m/s), which has a tunnel on one of the three sides with dimensions of 3.04×0.126 mm(h)×mm(v) (Figure 2.6) [17]. The chopper is held in a vacuum chamber by magnetic bearings and spins at a frequency of 986.3 Hz (360th harmonic of electron orbit frequency). Taking into account the size of the tunnel and the rotation speed, the opening time of the tunnel is 242 ns. This opening time is short enough to select a single pulse out of the x-ray pulse train produced by the synchrotron (16 bunch mode has 176 ns pulse separation). The principle of single pulse selection with two choppers is shown in Figure 2.7. Another important component in the hutch is the chamber with multilayer optics, Ru- and W-based monochromators, which can select quasi-monochromatic 18 (Ru) and 25.2 keV (W) beams with 1.9 and 1.55 % bandwidths respectively. As will be shown in the following chapters, scattering data collected with such quasi-monochromatic x-rays can resolve the structure with better precision. Some additional detectors are also installed in the hutch for alignment (photodiodes)

---

[3] The heatload chopper described here was installed during this project. The old one was also used for the experiments; its operational principles are similar so we do not describe it here. Details can be found in [15].

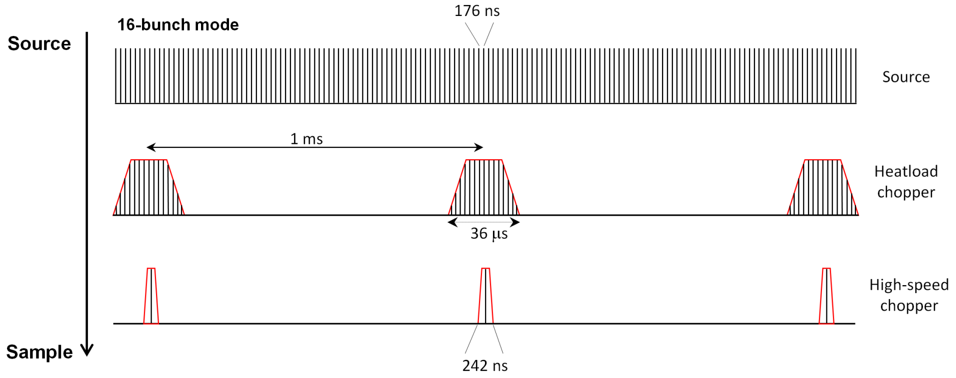

Figure 2.7. Principle of the single x-ray pulse selection from the pulse train produced by ESRF with the chopper system implemented at ID09 beamline. The heatload chopper takes most of the pulses produced by the ring and produces pulse trains of 36 μs duration with a frequency of 986.3 Hz. The downstream high-speed chopper has an opening time (242 ns) which is shorter than two time gaps between pulses ($176{\times}2 = 352$ ns) allowing to select single pulses at the frequency of 986.3 Hz.

and calibration of timing between x-ray and laser pulses (fast GaAs detector).

Laser system

The laser system is installed in the experimental hutch and consists of several units. A mode-locked femtosecond Ti:sapphire oscillator synchronized with the forth harmonic of the RF (88.05 MHz) produces 100-fs pulses with the central wavelength of 800 nm. Then these pulses are passed to the multipass Ti:sapphire chirped pulse amplifier operating at 986.3 Hz, which increases the pulse energy to 3-4 mJ. Before entering the amplification stage, the fs pulses are stretched to 100 ps in order to avoid damage to the amplifier's optical elements. After amplification, the pulses are compressed back down to 1 ps. Depending on the experiment's requirements, the output laser beam from the amplifier can be sent to doubling or tripling units for obtaining 400 or 266 nm wavelengths. Another option is the optical parametric amplifier with additional mixing crystals that allow tuning the laser wavelength between 290 and 1500 nm. At the final stage, the laser beam is focused on the sample to 150-250 μm and the energy is usually set to 30-100 μJ per pulse. In these conditions the number of photons in the laser pulse roughly matches the number of molecules ($\sim 10^{14}$ for 10 mM solution) in the pumped sample volume which ensures efficient excitation. The time delay between the laser and x-ray pulses can be electronically set in the range 0-1 ms with a resolution of 5 ps. The jitter between pulses was measured to be less than <2 ps.

Sample delivery system

The sample delivery system consists of the sample reservoir, pump and sample cell. The pump takes the sample solution from the reservoir and brings it to a nozzle installed at the top of the cell. The nozzle is made of sapphire and produces a 300 μm thick liquid sheet, which has a laminar region used for the experiments (see Figure 2.8). The pump pressure is set such that the speed of the liquid in the jet is $\sim$3 m/s, which ensures that every pump-probe pair of pulses (arriving at 986.3 Hz frequency) will hit a new portion of the sample. This speed limits the laser-x-ray time delays which are possible to investigate with this setup. If the laser beam is $\sim$200 μm, after about 30 μs the excited portion of the sample will move by half of the laser spot size, so the x-rays will "see" only weakly excited sample for a 30 μs time delay. This problem can be solved by moving the laser beam upwards to compensate for this effect. After the pump-probe event takes place, the sample is sent back to the reservoir through the catcher (funnel) at the bottom of the cell. The whole cell is held by the goniometer allowing fine tuning the position of the jet exposed to the x-rays. Concerning the sample in this thesis we used 1-30 mM solutions of molecules.

Detector for x-ray scattering

The scattered x-rays are collected by the integrating FReLoN camera[4]. Its operation principle can be described as follows. The x-rays are first absorbed in the phosphor screen (GdO_2S, 75 μm) which then converts them to the optical photons that in turn are transmitted by the fiber optic taper to the 2048×2048 CCD chip. The chip is kept at -15 C° for reducing the dark current, which is 0.1 ADU/pixel/s. The readout noise of the camera is about 2.5 ADU/pixel (rms). The conversion factor for ADU is $\sim$1 for 18 keV photons. The detection area of the camera and the pixel size are 105×105 mm^2 and 52 μm respectively. The detector is typically placed 40-45 mm from the sample, which allows covering angles up to $\sim$60° (therefore wide-angle x-ray scattering, WAXS). In 16-bunch mode with a 18 keV pink beam, the typical exposure time for an image is 3-5 seconds.

---

[4] At the time of writing the thesis, a new detector from Rayonix HS170 was installed on ID09.

Figure 2.8. Photographs of the ID09 sample cell (left) and the microscope view on the laminar part of the liquid jet (right). The exit slit of the nozzle is 8×0.3 mm rectangle which determines the size of the liquid jet. In a typical experiment the x-ray and laser beams are overlapped on the sample and with an angle between them of ~10°. For the purpose of stability only the laminar part of the jet is used for measurements.

XES spectrometer

The Johann x-ray emission spectrometer was installed at ID09 in 2014 as a complementary tool to x-ray scattering. It will be described in more detail since it has not yet been thoroughly presented in the literature. The basics of the XES technique and the information which can be derived from the measurements are given in the next chapter.

The x-ray emission spectrometer is based on the Johann type spherical bend crystal analyzer placed in a horizontal Rowland circle geometry coupled to a solid state detector (Figure 2.9). The emitted hard x-rays are collected at takeoff angle of ~140° by the crystal (10 cm diameter) and quasi-focused on the detector. The emission spectra are collected by scanning the crystal analyzer angle and coupling the translation of the detector on the Rowland circle. For the measurements of Co Kα emission lines in section 5.2, we used a Si (531) crystal bound to a curved glass substrate with a bending radius of ~1 m. Typical Bragg angles were in a range of 75-80°. The crystal quasi-focuses the emitted radiation to a spot 4×10 mm(h)×mm(v) on the detector. Another component of the spectrometer is a helium chamber which was designed in order to reduce significant x-ray absorption in air (x-ray travel path in the spectrometer is about 2 m!). The resolution of the spectrometer was calculated to be $\delta E/E \sim 10^{-4}$ roughly corresponding to the experimentally determined value (see Appendix A).

In this thesis two detectors were employed: the Ketek Silicon Drift Diode (SDD) [18] and the Maxipix detector [19]. The SDD is a photon counting detector with an active area of 90 mm^2 and energy resolution of ~100 eV. The latter is important on ID09 where the

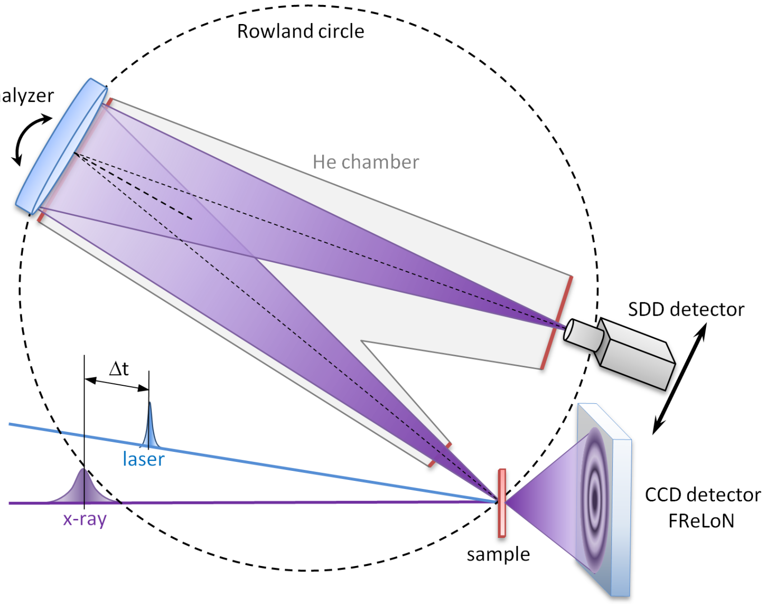

Figure 2.9. Setup for simultaneous x-ray scattering and emission spectroscopy implemented on ID09 (top view).

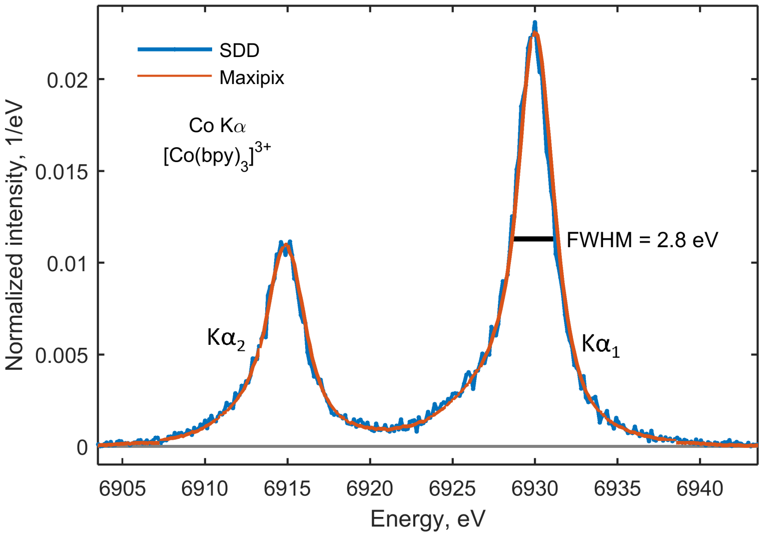

Figure 2.10. Comparison of Maxipix and SDD detectors. The Co Kα emission lines were measured on the reference sample $[\mathrm{Co(bpy)_3}]^{3+}$ (bpy = bipirydine). Based on the width of the measured Kα_1 line (2.8 eV) and the known natural width of the line (2.33 eV, from [20]), one can estimate the resolution of the spectrometer to $\delta E/E \sim 1$ eV (1.5×10^{-4} at 6930 eV).

pink beam has a long soft x-ray tail. The emission signal from a dilute solution is very weak and it is imposed on a large background coming from the elastic scattering of soft x-rays. Therefore at least a course energy resolution of the detector is necessary for making successful measurements of weakly emitting samples.

Another specificity of ID09 is that the x-ray emission comes in short bursts with a duration of 100 ps which makes the pile-up probability in the detector quite high. Generally, this is not a problem for solution samples due to the small amplitude of the emission signals. However, as we will see in the following chapter, in order to quantify the TR-XES signals one needs to perform measurements on reference samples which are usually available in the solid state. The x-ray emission from solid state samples is much stronger than from dilute solutions, which causes very high pile-up probability in the SDD detector. In order to overcome this problem, the beam is attenuated, which means that detection with this type of detector is not optimal. In order to reduce the experimental time spent on reference measurements, we used the Maxipix. The detector has 516×516 pixels with a pixel size of 55 μm. Due to the small pixel size, the emission signal is spread over many pixels preventing pile-up and allowing for fast and efficient data collection. This detector does not have energy resolution, which turns out to work well for solid state samples where the XES signal is much stronger than the background. By contrast, the signals from liquid samples are noisy due to the large background, thus preventing the use of this detector. Both detectors were checked to give the same signals on Co Kα lines (Figure 2.10), ensuring the robustness of the XES analysis.

Time slicing technique

In addition to the described experimental setup it is important to mention the time slicing technique which was used for several projects in this thesis. Time slicing is used in order to increase the temporal resolution of the experiment performed at a synchrotron. In the literature two different methods are called with this (same) name. In the first one, a fs laser source is installed inside of the ring such that one can use fs optical pulses for spatial separation of a small part of the electron bunch (defined by duration of the fs pulse) and use the radiation produced by this fs bunch for experiments [21, 22]. This allows the measurement of transient dynamics with fs time resolution, but it comes at the cost of flux. This method found applications for studying coherent collective motions in crystals (for example [23, 24]). This method was not used at ID09, so we will not discuss it further.

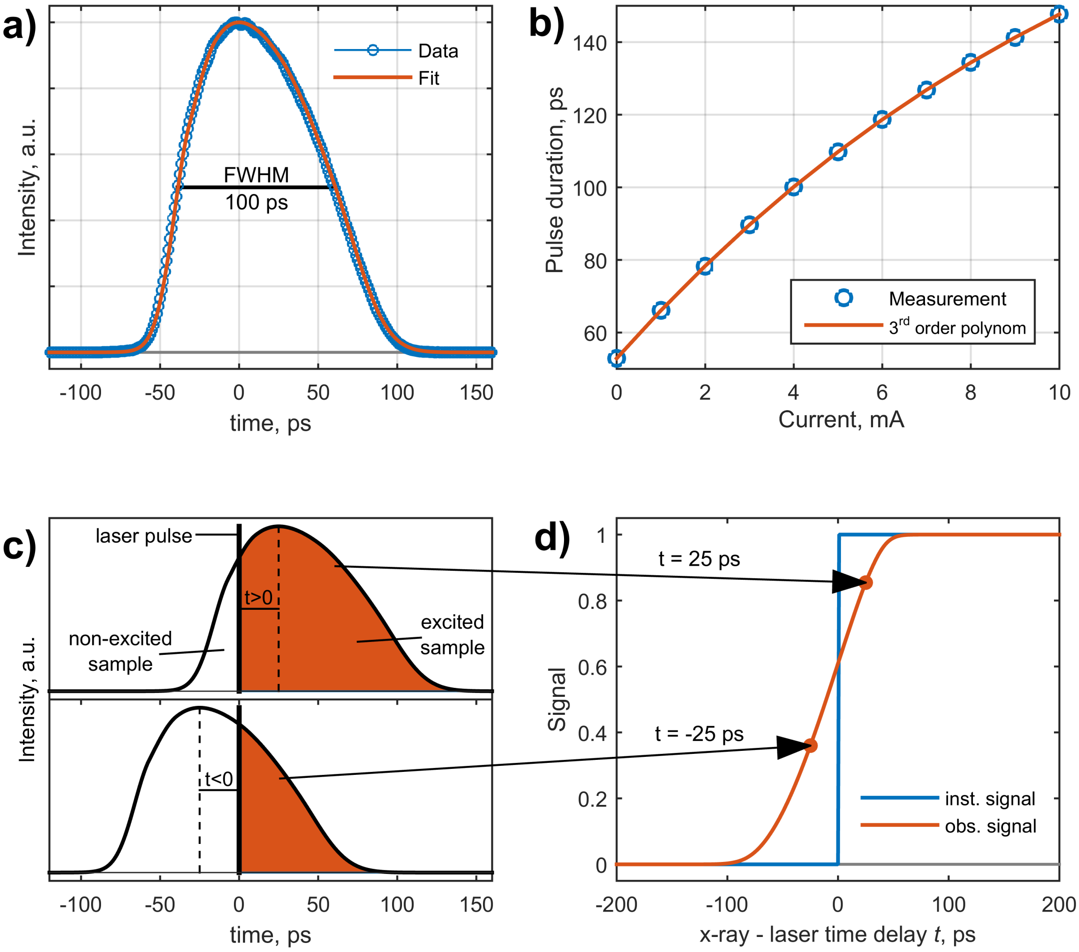

Figure 2.11. Time slicing method. a) Temporal profile of the x-ray pulse produced by a single bunch with a current of 4 mA. The profile measured with a streak camera is fitted with a combination of four asymmetric Gaussians giving a FWHM value of 100 ps. b) Dependence of the x-ray pulse duration from the single bunch current. The resolution of the setup can be improved by performing experiments in filling modes with smaller single bunch currents, for example the 7/8+1 mode. c) Time slicing is based on fine scanning of the transient signals around time zero. In this case, the laser pulse is “placed” inside of the x-ray pulse so only part of the x-ray pulse goes through the excited sample. The time delay between pulses is defined as the time between the maximums of the two pulses. d) Scanning around time zero leads to the broadening of the observed signals due to effects of convolution of the instantaneous signals with the instrument response function. Note that due to the asymmetry of the x-ray pulse, time zero appears to be shifted towards positive delays in comparison to the middle of the rising edge of the signal.

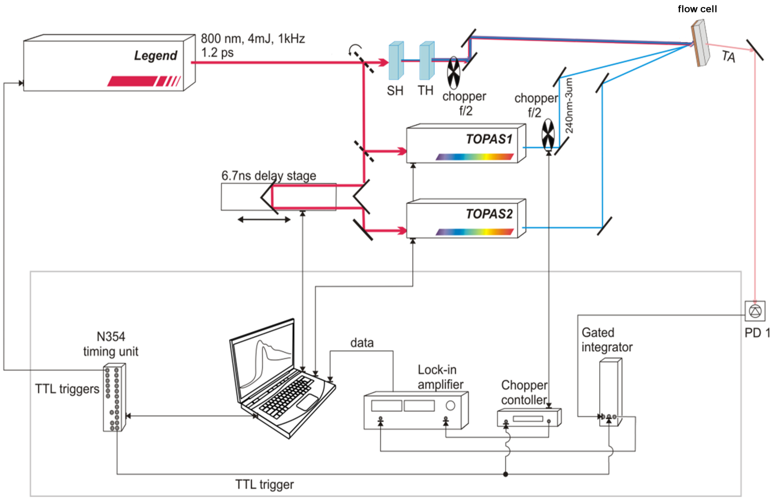

Figure 2.12. Layout for the optical pump-probe transient absorption spectroscopy.

The second method discussed in the literature and implemented on ID09 consists of scanning of the laser/x-ray delay in very small steps (10 ps) from -100 ps (negative time delay, i.e. laser comes *after* the x-ray pulse) up to 100-500 ps (positive time delay, i.e. laser comes *before* the x-ray pulse). The method takes advantage of the laser pulse being much shorter than the x-ray pulse (1 ps and 100 ps) and that the synchronization is very accurate and stable. At intermediate time delays, for example at 0 ps, the optical pulse is “placed” in the middle of the x-ray pulse (in time), so only half of the x-ray pulse goes through the excited sample. Overall, the measured time-dependent signal is a convolution of three functions: the instantaneous system response function, x-ray temporal pulse profile and laser pulse profile (Figure 2.11, c, d). The latter can be neglected due to the laser pulse being much shorter (∼1 ps) compared to the x-ray pulse. This method allows the investigation of faster dynamics on time scales down to a few tens of ps. The lower limit for the time scale that one can exploit with this method can be reduced further by using electron bunches with smaller charge. In the 7/8 mode at ESRF, the single bunch current is ∼2-3 mA which has a pulse duration of 80-90 ps (Figure 2.11, b). As an example of a successful experiment using time slicing we can mention the recent work on the vibrational cooling of iodine I_2 in carbon tetrachloride CCl_4 [25]. In this thesis we extensively employ the method and investigate its limitations in chapter 4.

2.4 Transient optical absorption spectroscopy setup

Optical pump-probe measurements were conducted in order to support the x-ray assignments made in chapter 4. A typical single-color-pump single-color-probe spectrometer layout is shown in Figure 2.12. The output of the Legend amplifier is split into two beams, for the pump and for the probe respectively. A number of options is available for tuning the energy of the photons: generation of the second or third harmonics and parametric amplifiers. After the preparation of the beams they are focused on the sample such that the probe beam is smaller than the pump and overlapped. Sometimes an additional microscope on the sample was installed to facilitate the overlap procedure. The detection of the transient signal is done in a classical way with the use of a lock-in amplifier. The pump pulse train comes at half of the probe frequency, so the transmittance of the sample for the probe pulse alternates according to the excited/non-excited state of the sample. The signal measured with a fast photodiode (rise time ~1 ns) is averaged with a boxcar integrator and then processed with the phase sensitive lock-in amplifier (SR830 from Stanford Research Systems). Since the experiment is usually performed with weak pump and probe pulse intensities and with the use of very dilute samples, the changes in sample transmission induced by the pump are very small and the signal is easily lost in electronic noise. Therefore lock-in detection appears to be efficient in capturing it. The pump-induced signal is then measured at each time delay which is controlled by a mechanical stage. Since the analysis of these measurements involves only fits of simple kinetic models (typically first or second order reactions), which are performed in a straightforward way, we will not discuss it in detail. The details of the kinetic models are discussed together with the data when it is presented.

Chapter 3

Data analysis

In this chapter we present the ingredients for understanding TR-WAXS and TR-XES measurements. First we will give a brief review of the x-ray scattering theory. Then the data reduction and the analysis will be presented. The following section introduces reader to basics of x-ray emission spectroscopy and the treatment of the data.

3.1 Time-resolved wide angle x-ray scattering

Time-resolved x-ray scattering is one the primary methods for the study of structure of transient species in solution. It relies on the analysis of the interference patterns produced by elastically scattered x-ray photons from the sample. These patterns are directly related to the pair distribution function of the sample via the Fourier transform and it therefore provides information about short (chemical bonding) and intermediate (intermolecular ordering) range order in the sample. Depending on the goal of the experiment, revealing the structure of large proteins or small molecules, one distinguishes between small or wide angle x-ray scattering (SAXS or WAXS) respectively. In this thesis we are studying small molecules ranging from triatomic molecules to transition metal complexes containing $\sim$100 atoms exhibiting relatively small-scale changes in structure upon photoexcitation. We therefore use TR-WAXS which allows to cover the necessary angular range for solving the structural problems. Note that this method has different names in the literature such as time-resolved x-ray diffuse scattering, time-resolved x-ray liquidography and, slightly misleading, time-resolved x-ray diffraction. The following subsections will introduce reader to the basic theory of elastic scattering from liquids, the concept of the differential measurements, the data reduction and analysis.

3.1.1 X-ray scattering: background

The interference between elastically scattered x-ray photons from electrons in the sample contains spatial information about the global average atomic structure in the probed volume. The orientation-averaged[1]signal arising from this process is described by the Debye formula [26,27]:

$$S(q) = \sum_{i,j} f_i(q) f_j(q) \frac{\sin qr_{ij}}{qr_{ij}}, \tag{3.1}$$

where q is momentum transfer defined as $q = \frac{4\pi}{\lambda}\sin\theta$ with λ and 2θ being the wavelength of the incident x-rays and the scattering angle respectively; r_{ij} is the distance between the i^{th} and j^{th} atoms; f_i and f_j are the form-factors of i^{th} and j^{th} atoms; finally, the sum in this expression extends over all the pairs of atoms in the sample. The form-factor is defined as the Fourier transform of the electron density $\rho(r)$ of an atom: $f(q) = \int \rho(r) \exp{(-i\mathbf{q}\cdot\mathbf{r})} d\mathbf{r}$. The values of f as a function of q can be numerically approximated according to Cromer-Mann parametrization:

$$f(q) = \sum_{i=1}^{4} a_i \exp\left(- b_i \left(\frac{q}{4\pi} \right)^2 \right) + c, \tag{3.2}$$

where the a_i, b_i and c coefficients have tabulated values for each element in the periodic table [28].

In liquids due to disordered nature the distances between atoms are broadly distributed around certain average values. Therefore, it is convenient to describe liquid structure with pair distribution functions rather then a set of discrete distances used in Debye formula. Based on that, the scattered intensity can be rewritten as

$$S(q) = \sum_{\alpha,\beta} f_\alpha(q) f_\beta(q) \left[N_\alpha \delta_{\alpha\beta} + \frac{N_\alpha N_\beta}{V} \int\limits_0^\infty g_{\alpha\beta}(r) \frac{\sin qr}{qr} 4\pi r^2 dr \right], \tag{3.3}$$

where the indexes α and β go through all atom types; N_α is the number of atoms of α type in the volume V of the sample; $\delta_{\alpha\beta}$ is the Kronecker delta; $g_{\alpha\beta}$ is the pair distribution function for atom types α and β.

---

[1] In this work we study liquid samples where the probed volume represents an ensemble of randomly oriented molecules.

Expressions 3.1 and 3.3 describe the elastic scattering of x-rays; however, the total scattering signal observed in the experiment also contains inelastic x-ray (Compton) scattering. This component does not contain any structural information since the phase of the photons is lost in this process [27]. Compton scattering is nevertheless important for data scaling purposes as shown below. Its calculation is done using analytical expressions from the literature [29].

3.1.2 Time-resolved signals

The samples used in this work are dilute solution (1-30 mM), where the "liquid" unit cell consists of one solute among a few thousand solvent molecules. At these concentrations the solute contributes less than 1 % to the total scattering signal, which makes solute structure characterization (static or time-resolved) based on total scattering data very difficult. Attempts in this direction have been made with a certain success with systems containing high-Z atoms such as Pt and I [30,31]; however, sometimes even high-Z molecules are impossible to characterize due to difficulties with the solvent contribution subtraction [32].

Time-resolved experiments employ a differential measurement strategy, which eliminates the issue with the large background from the solvent. Here, the scattering patterns of the excited and non-excited sample are subtracted from each other after suitable scaling and corrections (see below), to give the differential signal. In this scheme, the static contribution from the solvent is significantly reduced, leading to detection of only transient changes in the sample. Importantly, the measurements do not give access to the ground nor excited state structure, but only the difference between them. Due to that, the analysis of the experimental data typically requires substantial theoretical support for producing structural models of the molecules in the different states.

The time-resolved signal obtained in this way contains the following contributions:

$$\Delta S_{exp}(q,t) = \Delta S_{solute}(q,t) + \Delta S_{cage}(q,t) + \Delta S_{solvent}(q,t), \tag{3.4}$$

where the first term describes changes of the solute structure, the second term corresponds to a reorganization of the solvation shell (cage) and the third one reflects the structural changes in the bulk solvent (hydrodynamics). The obtained experimental signal is then analyzed by composing a theoretical signal from these three components which are either calculated or measured separately as described below.

The first two terms of eq. 3.4 can be rewritten as a solute-related contribution:

$$\Delta S_{solute}(q,t) + \Delta S_{cage}(q,t) = \frac{1}{R}\left[\sum_k c_k(t)S_k(q) - c_g(t)S_g(q)\right], \tag{3.5}$$

where $S_k(q)$ and $S_g(q)$ are the combined (solute + cage) contribution for the transient species of the k^{th} type and that for the molecule in its ground state respectively; $c_k(t)$ are the concentrations of the k^{th} transient species; $c_g(t)$ is the concentration of the ground state molecules and R is the number of solvent molecules per solute molecule. The expression assumes that the time dependent signal can be factorized as products $c_k(t)S_k(q)$ where the latter is time independent. The transition between states is thus assumed to be ultrafast. The solute signals are usually estimated by theoretical calculations (density functional theory, DFT) for the excited and ground state, whereas the cage signals are estimated by molecular dynamics (MD) simulations. It is important to note that for most of the projects in this thesis the cage contribution was omitted. For high-Z molecules in low-Z liquids it has been demonstrated that the cage contribution appears to be insignificant in comparison to the solute [31, 33], a fact exploited in the analysis of data on mercury halides and triiodide in chapter 4. For the analysis of the measurements on transition metal complexes (chapter 5), the cage contribution was simulated for one of the projects; the corresponding signal was found to be insignificant in the high-q part of the scattering data. Given broad q-range of experimental data sets, it was possible to analyze the data without cage contribution (see chapter 5 for details).

The $\Delta S_{solvent}(q,t)$ contribution comes from a redistribution of the photon energy absorbed by the solute to the solvent hereby changing its hydrodynamic state (temperature, density and pressure). Since only two of the three hydrodynamic variables are independent, the solvent change can be written as a combination of two components (in this work we chose temperature and density):

$$\Delta S_{solvent}(q,t) = \left(\frac{\delta S}{\delta T}\right)_\rho \Delta T(t) + \left(\frac{\delta S}{\delta \rho}\right)_T \Delta\rho(t), \tag{3.6}$$

where the temperature $\Delta T(t)$ and density $\Delta\rho(t)$ define the hydrodynamic state of the liquid as a function of time. The time-dependent behavior of $\Delta T(t)$ and $\Delta\rho(t)$ can easily be calculated from the known values of the relative energy levels of the transient species with respect to the ground state, the hydrodynamic properties of the solvent and the laser beam parameters [34]. The scattering differentials $(\delta S/\delta T)_\rho$ and $(\delta S/\delta\rho)_T$ can be determined from separate measurements, either by using infrared laser pulses [35] or by visible laser pulses with a dye containing solution [36]. The latter approach was employed throughout the thesis.

For the interpretation of the time-resolved scattering data it is useful to look at the differential radial distribution function (RDF). Based on the equation 3.3 one can introduce the corresponding function:

$$\Delta S(r,t) = \frac{1}{2\pi^2 r}\int\limits_0^{q_{max}} q\Delta S_{exp}(q,t)\left[\sum_{i\neq j} f_i(q)f_j(q)\right]^{-1} e^{-(\alpha q)^2}\sin(qr)dq, \tag{3.7}$$

where the factor in square brackets is the so-called sharpening function; the exponential term is introduced in order to reduce termination ripples due to the finite q-range; the corresponding parameter α is the Warren factor (typically between 0.15 and 0.25 Å). Note, that due to the use of a beam stop in real experiments, the low-q part (0-0.5 Å^{-1}) of the signal is usually missing. For reconstructing this part of the signal one typically extrapolates the data with the use of a theoretical curve obtained from the fitting (see below). This approach does not bias the RDF as shown in previous studies [34]. This function contains information about the motions of atoms in r-space. For small molecules, $\Delta S(r,t)$ is often easily interpreted. Negative dips in this function correspond to the removal of interatomic correlations at a certain distance whereas positive peaks correspond to the appearance of new correlations. This quantity is widely used for the discussion of the experimental results in this thesis.

3.1.3 Data reduction

Now we will briefly describe the procedure for data reduction from raw 2D images from the detector to 1D differential scattering patterns. A thorough discussion of the procedure can be found in the literature [34, 37, 38]. Initially, the raw 2D images are corrected for a number of distortions appearing due to imperfections of the detector and the experimental setup itself. The former includes the subtraction of the dark current and a correction for the non-uniform detector response (flat field correction). The dark current measurements are typically done prior to the actual measurements whereas the non-uniformity of the detector can be taken into account by a division of the measured image by a specifically produced flat field correction file. Other factors include correction for polarization of the incident x-ray beam, a geometry correction mapping the flat detector onto a spherical one and a correction for the x-ray absorption in the sample (liquid jet) and phosphor screen in the detector. Additionally, some areas of the detector are manually masked because they are contaminated by the shadows from the laser and x-ray beam stop. After that the corrected 2D image is azimuthally averaged to produce a 1D scattering pattern. A typical scattering pattern of liquid water at ambient conditions obtained by this procedure is shown in Figure 3.1. The measured data shows good agreement with the reference data [39], proving the correctness of the procedure.

The next step in the construction of the differential curves requires subtraction of the total scattering patterns obtained from the excited and non-excited sample: $\Delta S(q,t) = S_{\mathrm{ON}}(q,t) - S_{\mathrm{OFF}}(q)$. Since the time-resolved signal contributes to a very small fraction of the total signal ($\lesssim$1 %), the total scattering curves ("ON" and "OFF") have to be properly scaled prior to subtraction. It has been proposed to use isosbestic points in the differential pattern for scaling, since at these points, the total scattering intensity is constant independent of the sample excitation [34]. In case if no isosbestic points can be found or they are not known *apriori*, one can use a broad range of scattering vectors q (for example, 5-8 Å^{-1}), containing one or more oscillations in the differential signal [37]. In this thesis, the latter approach was used and it was found to work sufficiently well for all the reported experiments. Typical scattering patterns from excited and non-excited sample and the corresponding differential curve are shown in Figure 3.1, a.

For obtaining good statistics one has to collect about a hundred identical curves in case of high-Z systems (for example, HgX_2 and I_3^- in chapter 4) and a few hundred curves for low-Z systems (for example, transition metal complexes in chapter 5). Based on multiple repetitions, it is also possible to estimate the experimental uncertainties at each point using standard formulas. The averaged difference curve with corresponding error bars for HgI_2 (chapter 4) is shown in Figure 3.2, b.

Finally, the obtained scattering patterns have to be scaled from arbitrary units to the electronic units (e.u.). This is done by requiring that the total scattering curves match the theoretical scattering (from solvent) in the high-q limit comprising Debye and Compton contributions. The assumption being that the solution scattering, in the high-q limit, approaches the atomic scattering of a gas of atoms from the "liquid" cell stoichiometry of

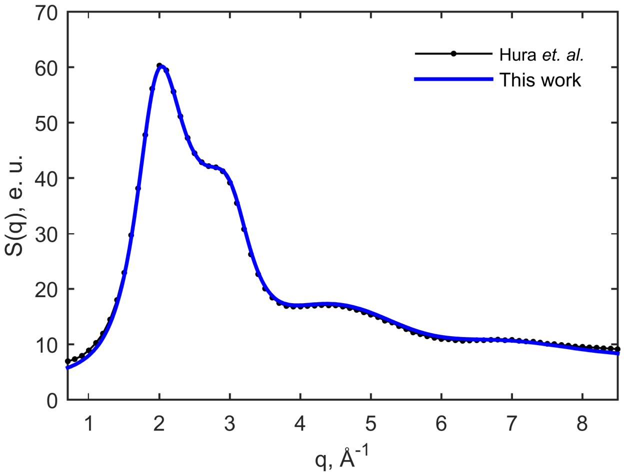

Figure 3.1. X-ray scattering pattern of pure water at ambient conditions. The data was taken with the 18 keV monochromatic x-ray beam. Then it was reduced according to the procedure described in text. Additionally, the background scattering from the setup was subtracted from the final curve. The measured curve is compared to the reference data from [39]. Good agreement between curves indicates correctness of the data reduction procedure.

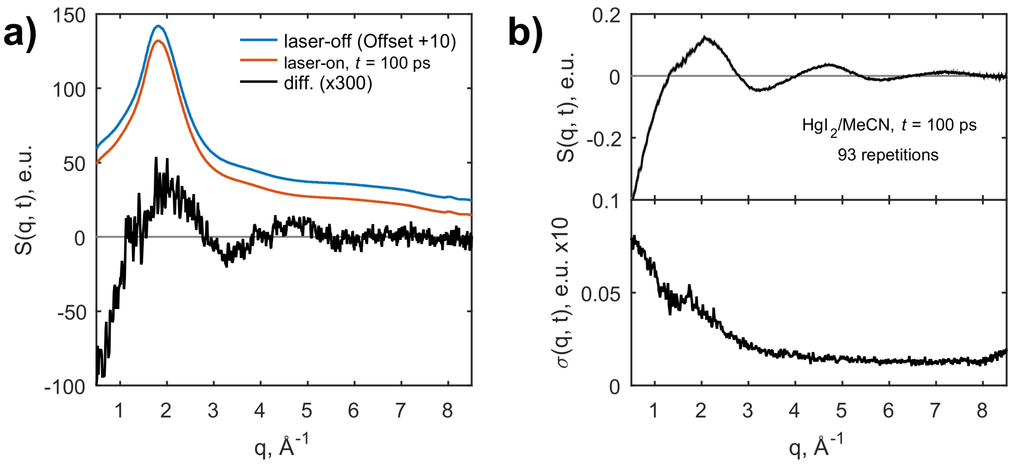

Figure 3.2. Construction of differential curves. a) Difference of total scattering curves with and without laser excitation results in the differential data. b) Repeting the deferential measurements many times improves the statistics of the curve. The top panel shows the average of 93 curves collected for HgI_2/MeCN sample (Chapter 4). The bottom panel represents the standard error of the differential data. The q-dependence of the data reflects the interplay between Poisson noise of the total scattering curve and number of pixels used for calculation of certain q-point.

the solution. The scaling factor obtained in this way is used to scale the differential data.

3.1.4 Data analysis

The analysis of the measured data involves several steps that can be summarized as follows.

1. Determination of the main reaction pathway.

In a typical study there are several candidate species that can potentially describe the data. Therefore, one has to understand the nature of the transient species by a comparison of the signals from those candidates with the measured data a at certain time delay t. The model for the data is usually the sum of a solute contribution, calculated based on theoretical prediction (DFT and/or MD), and the solvent heating, measured separately as mentioned above. This model contains up to 3 parameters: the excited state fraction, temperature rise and density change [2]. The fitting is performed by minimizing χ^2 defined as:

$$\chi^2 = \sum_q \left(\frac{\Delta S_{exp}(q,t) - \Delta S_{th}(q,t)}{\sigma(q,t)} \right)^2, \tag{3.8}$$

where $\Delta S_{exp}(q,t)$ and $\Delta S_{th}(q,t)$ are the measured and theoretically predicted curves respectively ; $\sigma(q)$ is the standard error of the measured curve. For determining the best model it is convenient to compare the reduced χ^2 defined as $\chi^2_{red} = \chi^2/(N-p-1)$, where N is the number of measured points and p is the number of fitting parameters (2 or 3 in the present case). The model with the smallest χ^2_{red} value is then the best candidate. Throughout the rest of the thesis we use the reduced χ^2_{red}. Hereafter we will refer to it as χ^2.

2. Structural optimization.

When the main reaction pathway is determined it is then possible to optimize the structure of the transient species based on the experimental data. In order to do that we have implemented an approach widely used in the x-ray absorption community for the treatment of extended x-ray absorption fine structure (EXAFS) [40–43]. Below we describe a slightly modified version applicable for TR-WAXS and demonstrate it on one of the data sets discussed in this thesis (HgI_2, chapter 4).

In this framework the structural optimization is treated as a signal processing problem

---

[2] The density change is negligible at early time delays $\lesssim$5 ns [35].

where the analysis is performed on the Fourier transform (FT) of the experimental curve $\Delta S_{exp}(q)$[3]. The FT of the data contains both real and imaginary parts due to finite q-range in the experiment. It can be calculated as:

$$\begin{aligned}\Delta S^{\mathrm{Re}}_{exp}(r) &= \mathrm{Re}\big[\mathrm{FT}\{\Delta S(q)\}\big] = \int\limits_{q_{min}}^{q_{max}} \Delta S_{exp}(q)\cos{(qr)}dq,\\ \Delta S^{\mathrm{Im}}_{exp}(r) &= \mathrm{Im}\big[\mathrm{FT}\{\Delta S(q)\}\big] = \int\limits_{q_{min}}^{q_{max}} \Delta S_{exp}(q)\sin{(qr)}dq.\end{aligned} \tag{3.9}$$

The grid of r values used for calculating the FTs, can in principle be arbitrary; however, only a finite number of the FT points will be independent. Based on Nyquist theorem, it is easy to show that the independent r points are spaced by $\delta_r = \pi/\Delta_q$, where $\Delta_q = q_{max} - q_{min}$ is the range of q-values used for the FT. The maximum r value which can be achieved with a given data corresponds to $r_{Ny} = \pi/2\delta_q$, where δ_q is the distance between two neighboring points in q-space. Therefore, the FT is calculated on points in r-space ranging from 0 to r_{Ny} with the a step of δ_r.

For the fitting procedure using the χ^2-metrics one also needs to calculate the uncertainties of the FTs. This can be done, for example, by calculating the FTs of the individual scattering curves (collected independently), rather then for the average one, and then estimating the uncertainties from the distribution of the individual FTs [34]. This approach however, does not allow to calculate the correlations between the neighboring points of the FT, which can bias the fitting results. Due to this, a more generic approach is used. If we assume that there are no correlations between the experimental data points, the covariance matrix $\mathbf{C}$ for the $\Delta S(q)$ curve has only diagonal elements, $\mathrm{C}_{ii} = (\sigma(q_i))^2$. If $\mathbf{F}^{\mathrm{Re}}$ and $\mathbf{F}^{\mathrm{Im}}$ are the matrix representations of the real and imaginary parts of the FT operator, the covariance matrices of the FT transform can be calculated as:

$$\begin{aligned}\mathbf{C}_{\mathrm{Re}} &= \mathbf{F}^{\mathrm{Re}}\mathbf{C}\big[\mathbf{F}^{\mathrm{Re}}\big]^{\mathrm{T}},\\ \mathbf{C}_{\mathrm{Im}} &= \mathbf{F}^{\mathrm{Im}}\mathbf{C}\big[\mathbf{F}^{\mathrm{Im}}\big]^{\mathrm{T}}.\end{aligned} \tag{3.10}$$

For performing the fit one has to introduce a model based on a structural parametrization of the system. Usually, the ground state properties of the molecules are relatively

---

[3] In this discussion we will omit the time dependence of the ΔS_{exp} curves, assuming that the data was measured at a certain meaningful time delay.

well known, so the parametrization concerns only the excited state structure. However, for certain simple systems one can simultaneously determine the structure of both the ground and excited state [32, 33] as shown for the triatomic molecules in chapter 4. After parametrization of the excited state alone or for both excited and ground state structure, one has to calculate the signal in q-space with the use of Debye formula and pass it through the FT in as shown in eq. 3.9. Then, taking into account the experimental data and the corresponding covariance matrices, the fit is performed via minimization of the following χ^2-estimator in r-space:

$$\begin{aligned}\chi_r^2 = &\left[\mathbf{\Delta S}_{exp}^{\mathrm{Re}} - \mathbf{\Delta S}_{th}^{\mathrm{Re}}\right]^{\mathrm{T}} \mathbf{C}_{\mathrm{Re}}^{-1} \left[\mathbf{\Delta S}_{exp}^{\mathrm{Re}} - \mathbf{\Delta S}_{th}^{\mathrm{Re}}\right] + \\ &\left[\mathbf{\Delta S}_{exp}^{\mathrm{Im}} - \mathbf{\Delta S}_{th}^{\mathrm{Im}}\right]^{\mathrm{T}} \mathbf{C}_{\mathrm{Im}}^{-1} \left[\mathbf{\Delta S}_{exp}^{\mathrm{Im}} - \mathbf{\Delta S}_{th}^{\mathrm{Im}}\right],\end{aligned} \tag{3.11}$$

where the bold font represents the vector representation of the data. The fit is performed in a certain range in r-space Δ_r, which is chosen to correspond to the size of the molecule. After the fitting it is useful to compare the minimized χ_r^2 with the number of degrees of freedom $\nu = N_{ind} - p - 1$, where N_{ind} is the number of independent points and p is the number of parameters in the fit. The N_{ind} can easily be determined from Nyquist theorem and results in the famous Stern's rule [44]: $N_{ind} \approx \frac{2}{\pi}\Delta_q\Delta_r$. If the experimental noise is described by normal distribution, for a statistically limited fit $\chi_r^2/\nu \sim 1$. The parameter uncertainties are then obtained from the parameter covariance matrix calculated from the Hessian of χ_r^2.

Now we will illustrate this methodology on the photodissociation reaction of mercury diiodide HgI_2 which is horoughly discussed in chapter 4. The data was collected at 100 ps after photoexcitation with 18 keV pink beam. The experimental signal and the corresponding diagonal covariance matrix are shown in Figure 3.4, a and b; the calculated FT of the signal and the corresponding covariance matrices are shown in Figure 3.4, c-f. Note, that the FT points are correlated as seen by the non-zero off-diagonal elements of the covariance matrices for both the real and imaginary part. The structural model has four parameters: two Hg · ·I distances, the

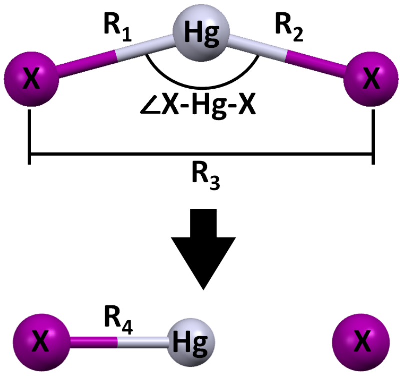

Figure 3.3. Structural model for HgX_2 and HgX (X = I).

$\angle \mathrm{I} - \mathrm{Hg} - \mathrm{I}$ angle of the ground state $\mathrm{HgI_2}$ molecule and the $\mathrm{Hg} \cdot \cdot \mathrm{I}$ bond length of the HgI photofragment[4] (Figure 3.3). Additional fitting parameters include the excited state fraction and the temperature rise. Here, as in the rest of the thesis, the fitting procedure was done with home written routines in MATLAB® using the Levenberg–Marquardt optimization algorithm. The fit is performed in the q-range 1-8.5 Å^{-1} and r-range 1-6.5 Å ($N_{ind} \approx 26$). The fitting results are shown in Figure 3.4.

In the current discussion we are not interested in the actual values of the parameters (discussed in the corresponding chapter), but rather in the relations between the fit and the data. The qualitative agreement between the fit and data is excellent both in q-space and its FT. However, the corresponding value of $\chi_r^2/\nu = 50$, which statistically indicates poor quality of the fit and contradicts the qualitative observation. The large values of χ_r^2 might come from systematic errors which are not taken into account. The source of these errors include the inhomogeneity of the detector (imperfect flat field correction) and pixel crosstalk. The former can lead to the appearance of small frequency modulations of the signal, which can be significant at the frequencies used for the fitting and therefore cause an increase in χ_r^2. The pixel crosstalk can lead to a statistical dependence of the detected intensities in adjacent pixels of the detector which can increase the resulting χ_r^2 if it is not taken into account correctly. Some works find this contribution to be significant for CCD detectors [45,46]; however it is difficult to characterize the pixel crosstalk quantitatively due to its complex nature. Interestingly, in EXAFS spectroscopy researchers often encounter similar problems of the dominance of systematic errors over experimental noise [41]. The common approach (for good fits) is to scale the experimental error bars by $\sqrt{\chi_r^2/\nu}$, which forces χ_r^2/ν to be unity and results in additional increase in the parameter uncertainties (by the same factor) [42].

The described approach was employed in structural optimization because it allows taking systematic errors into account and it provides reasonable uncertainty values. All uncertainties in the thesis are reported as 2σ errors, i.e. 95 % confidence interval.

3. Kinetic analysis. When the nature and precise structure of the transient species are established, the analysis of the population dynamics can be done in order to determine the rates of the reactions. Initially, each of the TR-WAXS curves at different time delays

---

[4] In chapter 4 we prove that this channel is dominating the dissociation reaction; the structural model is also discussed in more details.

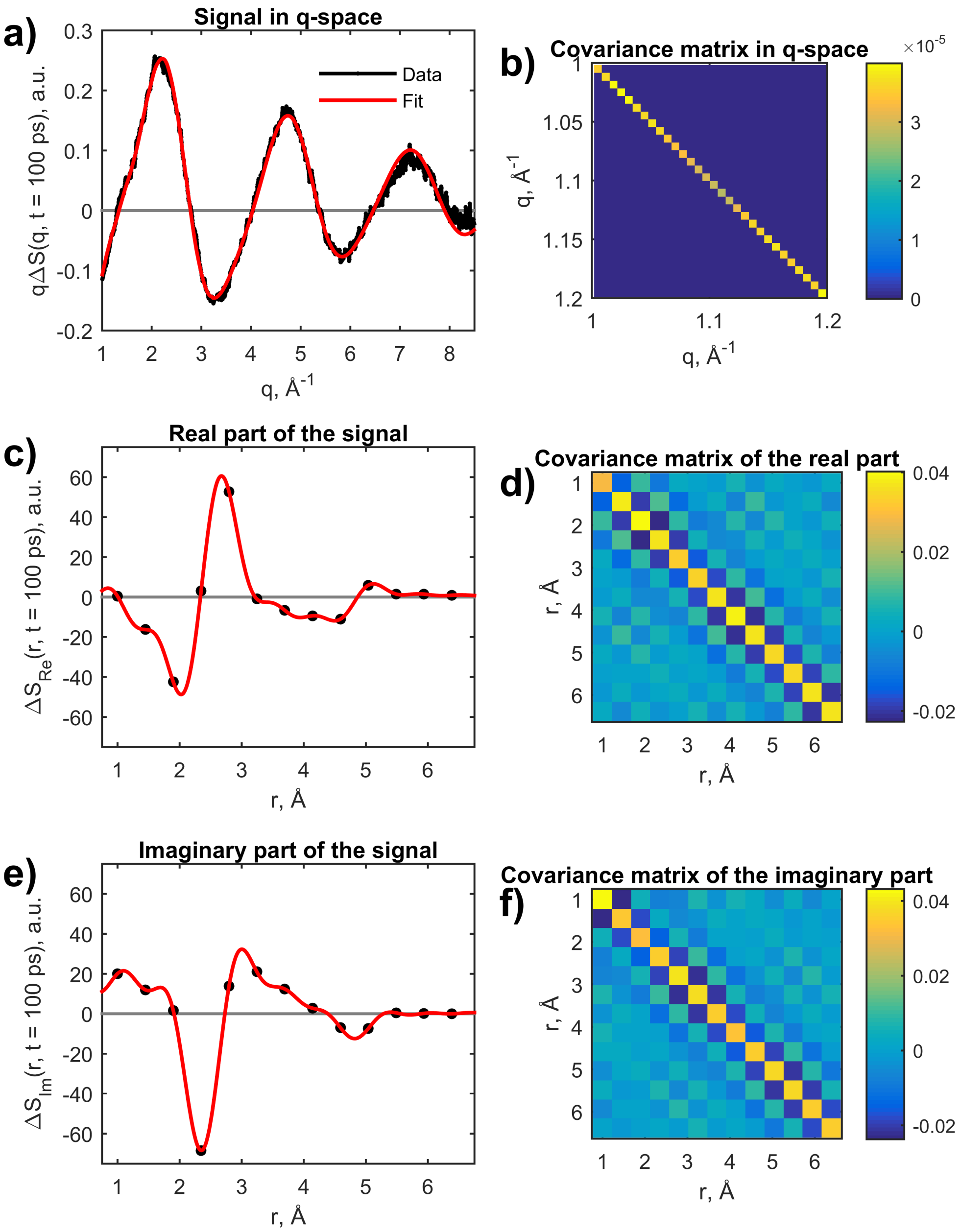

Figure 3.4. Structural fitting of TR-WAXS data. a) Signal in q-space and the corresponding fit obtained with the procedure described in the main text. The signal was collected for HgI_2/MeCN at 100 ps with pink beam ($E_f = 18$ keV) b) Covariance matrix of the signal in q-space. The matrix is shown only for a limited q-range for clarity. c) The real part of the signal FT with the fit; the fitted curve was calculated on a fine r-grid ($\delta r = 0.01$ Å) for clarity. d) Covariance matrix for the FT real part. Note that it is substantially non-diagonal indicating the correlations between the points. e), f) The same as c), d), but for the imaginary part. Obtained value of $\chi_r^2/\nu = 50$.

are fitted individually to monitor trends in the formation and decay of the reaction intermediates. Then, for the determination of the kinetic parameters one can use the global fitting procedure, which is thoroughly described in the literature [34]. Here, the fitting parameters include the excited state fraction, reaction rates (or lifetimes) and possibly the branching ratios, if two type of reactions appear after the photoabsorption event. To obtain optimized values, the following χ^2_{tot} is minimized:

$$\chi^2_{tot} = \sum_{q,t} \left(\frac{\Delta S_{exp}(q,t) - \Delta S_{th}(q,t)}{\sigma(q,t)} \right)^2, \tag{3.12}$$

where $\Delta S_{exp}(q,t)$ and $\Delta S_{th}(q,t)$ are the measured and theoretical signals at the scattering vector q and time delay t; $\sigma(q,t)$ is the experimental uncertainty. The theoretical signal is calculated according to equations 3.4-3.6 as a function of parameters describing the population dynamics (excited state fraction, branching ratios, lifetimes). In order to obtain this signal, one has to calculate the concentration dependencies of the transient species, which are typically described by simple differential equations (first or second order reactions). Then, knowing the relative energies of the excited states with respect to the ground state (from theory or other studies), it is necessary to calculate the amount of heat dissipated to the solvent and the corresponding changes in temperature and density as functions of time (see ref. [34] for mathematical description). Finally, with known structural signals from solute and solvent it is possible to construct the full theoretical signal $\Delta S_{th}(q,t)$. The obtained temporal signals have to be corrected for the finite temporal resolution of the setup by convolution of the signal with the instrument resolution function (100 ps x-ray pulse, Figure 2.11). The global fit approach allows to couple the kinetics and hydrodynamics of the ongoing chemical reaction and greatly reduce the number of free parameters in the fitting procedure.

3.2 Time resolved x-ray emission spectroscopy

X-ray emission spectroscopy (XES) is a relatively novel tool in the arsenal of time-resolved x-ray methods. It allows to probe the electronic state of the absorbing atom by observing the emission from it. Typically XES measurements can precisely determine the spin and oxidation state of the absorbing atom, which is particularly useful in studies of transition metal complexes exhibiting charge transfer and/or spin crossover.

3.2.1 X-ray emission: background

X-ray emission is a two-step process involving absorption of an x-ray photon by an atom which promotes an electron from an occupied (core) level either to one of unoccupied states or to the continuum (i.e. creates photoelectron), and following emission due to repopulation of the core hole (Figure 3.5, a) [27]. In this thesis we have employed x-ray emission spectroscopy (XES) for studying spin and charge dynamics in the bimetallic transition metal complex as discussed in section 5.2. There we analyzed the most intense $K\alpha$ emission ($2p \rightarrow 1s$ transition) of Co atoms, which was shown to be sensitive to the charge and spin state of the metal [47–51].

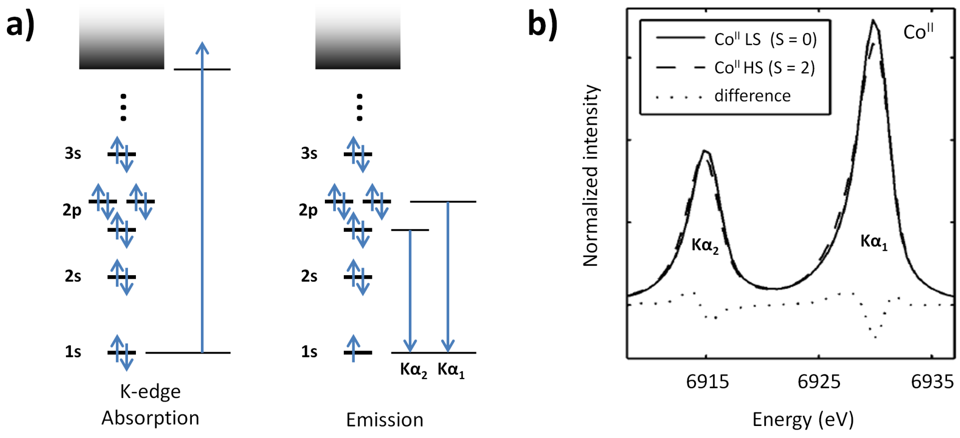

Figure 3.5. X-ray emission spectroscopy principles. a) Sketch of x-ray emission process. First, the incident x-ray photon is absorbed by a core electron, which is promoted to the valence shell or continuum. Second, the photon is emitted due to recombination of the core hole with one of the electrons in $2p$ orbitals (for $K\alpha$ lines). b) $K\alpha_{1,2}$ emission lines of Co$^{\mathrm{II}}$ ion in low (S=0) and high spin (S=2) states (adapted from [49]). The difference between spectra confirms the sensitivity of the technique to the details of electronic structure of the emitting atom.

The Kα emission has two peaks coming from the $2p_{\frac{1}{2}}$ and $2p_{\frac{3}{2}}$ levels split by the spin-orbit coupling. The two lines are called Kα_2 and Kα_1 respectively and their intensity ratio is 1:2, which comes directly from the degeneracy of the $2p_{\frac{1}{2}}$ and $2p_{\frac{3}{2}}$ levels. The widths and positions of the Kα_1 and Kα_2 lines differ between different spin states due to change in exchange interactions between the $3d$ electrons and the $2p$ core holes (Figure 3.5, b). That explains the sensitivity of the technique to the details of the electronic structure of the emitting atom.

3.2.2 Time-resolved signals

In order to quantify the spin changes of a metal center upon photoexcitation, the measurements typically include two steps. First, one has to measure the line shape of the differential transient signal. For this, the laser-ON and laser-OFF spectra are taken at a certain time delay (typically, 100-200 ps) and then, after normalization of the spectra area to unity [49], they are subtracted from each other: $\Delta I(E,t) = I_{\mathrm{ON}}(E,t) - I_{\mathrm{OFF}}(E)$. Since the theoretical description of Kα emission is quite complex and have not yet reached the quantitative level, the best way to analyze time resolved spectra is to compare them with reference line shapes produced from emission measured on known compounds [49]. For this reason one typically measures many different references in order to compare them with the time-resolved signal and make a conclusion about the final spin state. When the electronic configuration of the atom in its excited state is known, the excited state fraction can be found within integrated absolute differential (IAD) framework. The excitation fraction $\gamma(t)$ is given by the ratio:

$$\gamma(t) = \frac{\int |\Delta I(E,t)|\, dE}{\int |\Delta I_{ref}(E)|\, dE}, \tag{3.13}$$

where $\Delta I(E,t)$ and $\Delta I_{ref}(E)$ are the time-resolved and reference spectra respectively.

The second step of the measurements involves the time scan of a certain differential feature in order to retrieve the lifetime of the excited state. The spectrometer is tuned to an energy corresponding to some (usually, the strongest) feature in the differential spectrum and then the XES intensity is monitored as a function of time. This step is usually coupled to the simultaneous TR-WAXS measurements. After calculation of the differential signals as before, the fit of the data with a kinetic model allows to determine the excited state lifetime.

Chapter 4

Dissociation reactions

Dissociation reactions triggered with light are of primary interest from a fundamental and application point of view both in gas and liquid phases. Although it is one of the simplest fundamental processes even for small systems, photodissociation is quite a complex phenomenon. If one considers a generic molecule in solution, the process of the photodissociation and the following recombination can be described as follows. An incoming photon promotes an electron from a bound state to a repulsive state. After this quasi-instantaneous electronic transition ($\sim$1 fs), the constituents of the system are separated by the repulsive potential of the excited state. The complete separation appears on the time scales of 50-200 fs [52], after which one can consider the parts of the former molecule as free photofragments. If the reaction takes place in a liquid medium, the photofragments will collide with the surrounding molecules of the liquid, the so-called cage, and will lose the kinetic energy obtained in the dissociation process. This is followed by a cascade of different recombination events, which can generally be organized into three categories [53, 54]. Most of the newly formed photofragments (or radicals) will stay inside the parent molecule's cage and directly recombine to form the initial molecules in highly energetic or "hot" state. Such process is called Primary Geminate Recombination (PGR). After that, these species undergo the process of vibrational cooling which typically takes from a few hundred femtoseconds to few hundred picoseconds depending on the solute and the solvent [55]. Contrary to that some part of the radicals will leave the parent molecule's cage and will undergo diffusive motion driven by random collisions with the molecules of the liquid. This motion can eventually lead the initial photofragments to recombine geminately; this channel is termed Secondary Geminate Recombination (SGR) and takes place on the time scale of few tens to hundreds of picoseconds [56]. Finally, the radicals can diffuse away from each other, followed by the slow recombination with the radicals produced from other dissociated species. This phenomenon is known as Non-Geminate Recombination (NGR) and happens on much longer time scales: from nanoseconds to milliseconds, depending on the concentration and mobility of the radicals.

The above considered case appears for some of the simplest systems. Complex electronic structure and interactions with the surrounding solvent can affect the time scale of the reaction and result in multiple reaction products or completely change the character of the reaction. Such cases appear even for some simple systems such as molecular I_2, which upon photodissociation has the possibility of recombining to the bound excited state A/A'. The latter relaxes to the ground state non-radiatively on the nanosecond time scale [55]. Another example is the dissociation reaction of large metaloorganic molecules, where the fluidity of the solvent determines the rates and yields of the PGR channel [57]. Similarly, for large organic molecules, orientation restrictions increase the characteristic time required for two radicals to recombine via SGR [58, 59]. Finally, in the context of present work, it is necessary to mention another channel where excited ionic species can form so-called contact ion pairs, where photofragments remain inside the parent cage in the excited state. The relaxation then require an additional step of the electron transfer from one radical to another [60–64].

In this chapter we will focus on geminate recombination of small molecules in solution. First, we will consider the simplest case, dissociation, and follow the recombination dynamics of the mercury halides HgX_2 (X = I, Br). The SGR and NGR processes are characterized both by TOAS spectroscopy and TR-WAXS. Additional structural analysis performed on both systems allow us to compare the theoretical predictions for the ground state and reaction product structures with the experimental results. Possible extensions for the future structural characterization of the SGR process are outlined. Another system which we will consider is the trihalide anion, triiodide I_3^-. The excitation of the ion leads to the formation of the contact ion pairs, which structure is in the focus of the work. The structural dynamics of the system is characterized with the TOAS and the TR-WAXS. The analysis of both the excited and ground state structures is performed; possible models for the contact ion pair formed upon laser excitation are discussed.

4.1 Recombination dynamics of mercury halides

Mercury halides attracted attention as good model systems for studying different aspects of gas and liquid phase reactions. Optical spectroscopic investigations revealed absorption bands and corresponding electronic transitions for both HgX_2 (X = I, Br) systems and dissociation reaction products [65,66]. Technological interest in these compounds has been stimulated by fluorescence emission properties of HgX_2 radicals [67,68]. Later, with the development of femtosecond laser sources, details of the wavepacket motions in the gas phase have been resolved [69]. The femtosecond mass spectroscopy studies addressed the details of the dissociation process for HgI_2 [70,71]. Simple structure and photoreactivity allowed a comprehensive investigation of the coherence transfer and vibrational and rotational relaxation in the solution phase [72–74]. Some of the first successful time-resolved x-ray scattering studies were also performed on HgI_2 [75]; with increased signal to noise ratio, this technique revealed the reaction mechanism for both systems on 100 ps to 1 μs time scale [76,77].

Historically, the motivation for this work was driven by a successful study of the vibrational cooling process of the I_2 in CCl_4 [25]. There, the evolution of the average bond length I··I was measured and coupled to the process of the energy redistribution between the solvent and solute species. Another important result of that work was the observation of cage shrinkage around the solute molecules following the shortening of the average bond length between the I atoms. Study of heavy triatomic halides seemed to be a natural step further in complexity in comparison to the model I_2/CCl_4 system. Further details of the solute-solvent interactions could be addressed directly from the structural point of view. Interestingly, the present x-ray experiments found rapidly decaying components in the structural signal which could not be attributed to the previously studied non-geminate recombination. Initially, we attempted to interpret the data in a similar fashion to I_2/CCl_4. However, detailed investigation of the time-resolved x-ray data and new optical measurements cast doubt on such interpretation of the signals. Careful analysis and literature studies pushed for a new explanation. Here, the experimental results are interpreted in terms of secondary geminate recombination of separated radicals via diffusive motion through the solvent. More generally, in this chapter we describe the recombination dynamics of mercury halides in solution and show how the present work adds new insight to the previous experiments.

Before reporting the results we will summarize the relevant knowledge about the electronic structure, photodissociation process and initial steps of the product relaxation for both systems. Figure 4.1 represents the UV-vis absorption spectra of HgI_2 and $HgBr_2$ solvated in methanol with the corresponding electronic transitions [77]. Note that in this work we use acetonitrile (MeCN) as a solvent; however, since the dielectric constants for methanol and acetonitrile are close, the absorption spectra for the HgX_2 and the photodissociation reaction products are also similar [78]. For both molecules, the excitation at 267 nm from the bound ground state Σ_{g}^{+} to the repulsive excited state of Π_{u} symmetry [65,79]. The molecules dissociate after promotion to the repulsive state, giving, in principle, two photoframents HgX and X. Depending on the distribution of the initial photon energy between the fragments and the strength of the bond, the HgX radical can further dissociate into Hg and X [73]. For solvated HgI_2 the excitation leads to the formation of HgI and I, whereas for $HgBr_2$ both two- and three-body dissociation appears to be possible [76,77].

After photodissociation, vibrationally hot HgX radicals are formed in the ground state X and they cool down on the time scale of a few ps [80,81]. The free halide radicals (I or Br) are formed in two different spin-orbit states, $^2P_{3/2}$ and $^2P_{1/2}$ [82]. The $^2P_{1/2}$ state is relaxing to $^2P_{3/2}$ on the subpicosecond time scale [83,84]. The relaxed halogen radicals form contact charge transfer complexes with polar solvent molecules [85].

The newly formed radical pairs recombine to form the final products of the reaction. As discussed in the introduction, most of the photofragments form the parent HgX_2 molecule after a few collisions with the surrounding cage. Other photofragments leave the initial cage and recombine via diffusive motion geminately or non-geminately. Importantly, the recombination leads to the HgX_2 species being formed in highly excited vibrational states, which relax afterwards via collisions with the surrounding liquid. The time scale of this process for the hot HgX_2 species is similar to that for the small molecules in the light organic solvents lasting less than 10 ps [86]. Note that it is opposed to the rather special case of I_2/CCl_4, where the process takes about 100 ps due to lower collision-energy-transfer of the heavy CCl_4 molecules [55].

The discussion will be organized as following. First, we will present the results from TOAS for both systems. At the same time the theoretical description of the SGR will be introduced and different models will be discussed. In the following section the observation of SGR will be discussed from the x-ray experiment point of view. Finally, the precise structural analysis will be presented and possible developments outlined.

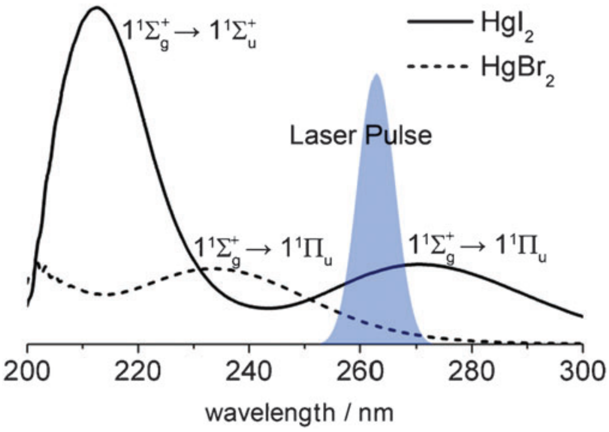

Figure 4.1. Absorption spectra of HgI_2 and $HgBr_2$ in methanol at room temperature (adopted from ref. [77]).

4.1.1 TOAS results

TOAS has been applied to both systems, HgI_2 and $HgBr_2$, in order to investigate the early recombination dynamics up to $\sim$ 3 ns. The radical population dynamics after photodissociation of the HgX_2 molecules can, in principle, be accessed by probing the HgX absorption band arising from the $X \rightarrow B$ transition (380 – 520 nm) [73,80]. The general experimental setup allowing this has been described previously (see Chapter 1); the specific experimental details will be given below.

The pump beam with the wavelength $\lambda_{pump} = 266$ nm was focused on the sample by a lense with a 500 mm focal length to produce a round spot of about 0.7 mm (FWHM) on the sample. The probe beam ($\lambda_{probe} = 400$ nm) was focused with a 400 mm focal length lens to a 130 um round spot. The pump and probe energies were of 10 uJ/pulse and 0.2 uJ/pulse respectively. Changes in the transmitted probe pulse intensity induced by the pump correspond to an increase in the optical density at all investigated time delays. The samples were prepared by dissolving HgI_2 and $HgBr_2$ in MeCN up to concentrations of 0.5 and 2 mM respectively. The concentration of the $HgBr_2$ was chosen to be higher due to lower extinction coefficient of $HgBr_2$ at 266 nm by roughly a factor of three. The HgX_2 powders and MeCN were purchased from Sigma Aldrich and used without any further purification. In order to keep the sample degradation effects as small as possible, the solution was flowed though the sapphire jet nozzle described previously. The transient traces have been measured from -40 ps to 3.1 ns. For reducing the data collection time, the time steps in the different ranges of the time delays were varied. In total the collection of 8-

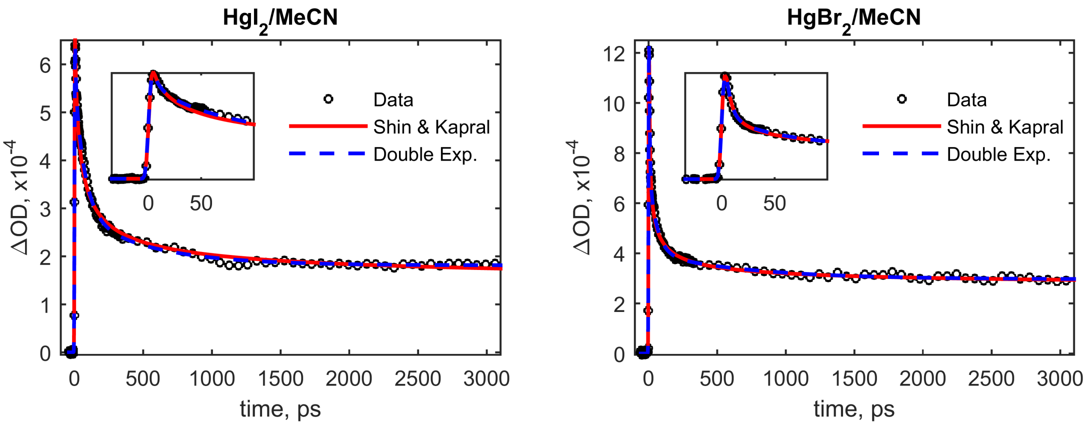

Figure 4.2. Transient absorption spectroscopy results and corresponding fits ($\lambda_{pump} = 267$ nm, $\lambda_{probe} = 400$ nm) for the solvated HgI_2 and $HgBr_2$ in MeCN.

10 traces for each sample was sufficient for obtaining satisfactory statistics. Corresponding TOAS traces were the same within the experimental noise indicating no significant sample degradation during the measurements.

Figure 4.2 shows TOAS traces for both HgI_2 and $HgBr_2$ solvated in MeCN. This data undoubtedly shows the presence of ultrafast dynamics appearing on a short time scale up to 1 ns for both systems. Indeed, at early times the signal quickly decays to about 200 ps, after which the decay takes a slower rate tending towards the plateau at ∼1-2 ns. Additionally, at early time delays up to 10 ps, in both data sets, one can observe an additional rapidly vanishing peak in the induced absorption. According to above discussion, these features are assigned to vibrational and rotational relaxation of the reaction products. Since this work is focused on slower dynamics, the results will not be affected by this ultrafast component given that the model will correctly take it into account.

The induced absorption appears due to the formation of free HgX and X radicals, both of which can potentially contribute to the signal. First, as mentioned above, HgX can absorb a probe photon via the electronic transition $X \to B$, which has been used in the previous spectroscopic solution and gas phase studies [69,80,81]. Second, the complexation of the halogen radical X gives rise to a broad absorption band in the UV region [85]. It has been shown that for the I radical in ethanol this effect can be neglected at 400 nm where the I:Solvent complex contributes only a few percent of the total absorption of the HgI and I mixture [81]. Since the absorption spectrum of the X:Solvent complex is strongly dependent on the solvent [85], the true contribution to the total transient signal for I and Br in MeCN require a separate study. In principle, for the case of HgI_2 this is not a problem for the following reason. Since only two-body dissociation is observed [76], the I and HgI radical concentrations are equal at early time delays, where NGR recombination process is not yet significant. In this case, the detected change in absorption is simply proportional to the concentration of the radical pairs, no matter what the absolute contributions to the signal are. Opposed to that, $HgBr_2$ represents a more complex case, since three-body dissociation also appears upon photodissociation. Here, the geminate recombination of Br and Hg radicals formed in the three-body dissociation process can lead to a more complicated population dynamics of the HgBr radicals. If the contribution from the Br:Solvent complex to the absorption signal is comparable to HgBr, the interpretation of the results can be more difficult. At the moment we will assume that the Br:Solvent absorption, as for I:Ethanol, is insignificant. Moreover, since the radicals produced by three-body dissociation (Hg and 2Br) are highly mobile, we will consider that they rapidly undergo SGR process and do not contribute to the signal. Based on this assumptions the simple models described below will allow us to quantify the processes of HgX and X geminate recombination due to diffusive motion. These assumptions will be reexamined at later stages of the analysis.

Although the application of the theory describing the secondary geminate recombination was not successful in the present study, it is useful to shortly introduce it and mention the associated difficulties. In this description, the model considers the radicals to be non-interacting spherical rigid particles initially separated by a certain distance r_0 after the photolysis event. The radicals are then subject to random Brownian motion in the structureless and uniform liquid until they recombine or separate completely. Interaction between the particles and liquid enters the description only via the particle's random motion; the forces between particles only act at the moment when the distance between them becomes smaller than reaction radius σ_R. Finally, the probability of the pair survival as a function of time is given by the expression calculated by Shin and Kapral [87]:

$$\begin{aligned} p(\tau) = 1 - \frac{\lambda}{\kappa(\lambda+1)} \Bigg\{ \operatorname{erfc}\left[\frac{\kappa-1}{2\sqrt{\tau}}\right] - \exp\Big[(1+\lambda)(\kappa-1)\Big] \exp\Big[(1+\lambda)^2\tau\Big] \\ \times \operatorname{erfc}\left[(1+\lambda)\sqrt{\tau} + \frac{\kappa-1}{2\sqrt{\tau}}\right]\Bigg\}, \end{aligned} \tag{4.1}$$

where λ is given by $\lambda = k_f/k_d$, with k_d being the rate constant for diffusion and k_f that for the recombination rate. These two parameters come from the so-called radiation boundary condition and their ratio is related to the probability of the radical recombination event

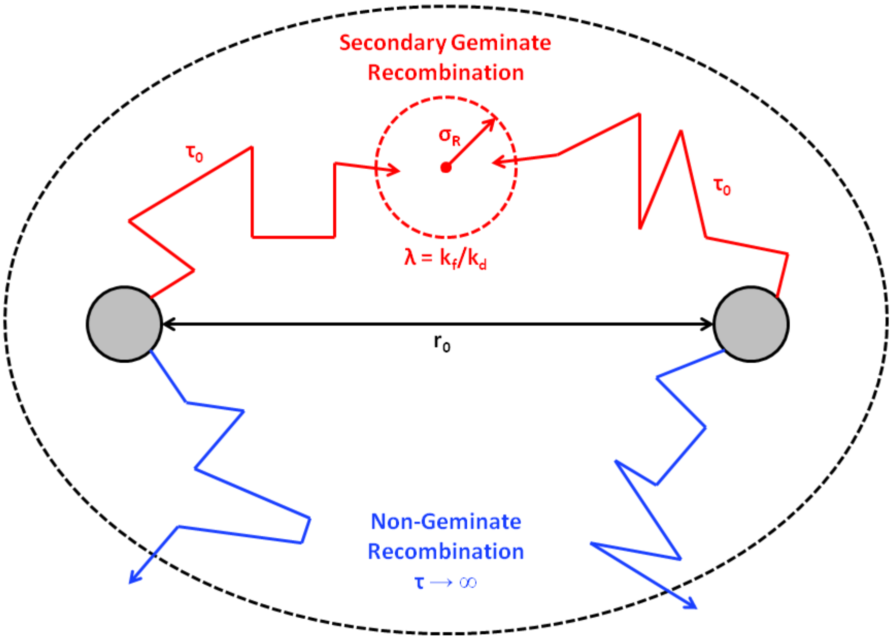

Figure 4.3. Illustration of the secondary geminate according to Shin and Kapral's theory. Initially separated photofragements randomly move in the structureless liquid until the distance between them becomes less than the reaction radius (red trajectory). After that they recombine or diffuse away with the rates k_f and k_d respectively (radiation boundary condition). The time scale of the overall SGR process is defined by the characteristic time τ_0. In case if two fragments do not recombine they separate completely and later undergo the non-geminate recombination (blue trajectory).

upon approaching the reaction radius σ_R. The reduced separation is given by $\kappa = r_0/\sigma_R$ which essentially represents the initial condition for the ensemble of the radical pairs. These two parameters λ and κ mainly define the ratio between number of radical pairs which recombine geminately and those which completely separate. The reduced time is given by $\tau = t/\tau_0$ with $\tau_0 = \sigma^2/D$ and D is diffusion coefficient. The rate of the process therefore depends on the initial separation of the radicals and properties of the radicals and liquid medium. The principles of this approach are illustrated in Figure 4.3.

At long times the survival probability $p(\tau)$ follows the reciprocal square root of time law:

$$p(\tau) = p(\infty)\left(1 + \frac{\lambda}{1+\lambda}\sqrt{\frac{1}{\pi\tau}}\right), \quad \tau \to \infty, \tag{4.2}$$

where $p(\infty) = 1 - \lambda/[\kappa(1+\lambda)]$ is the pair survival probability in the infinite time limit. Such behavior leads to a very slow decrease of the radical population. Depending on parameters

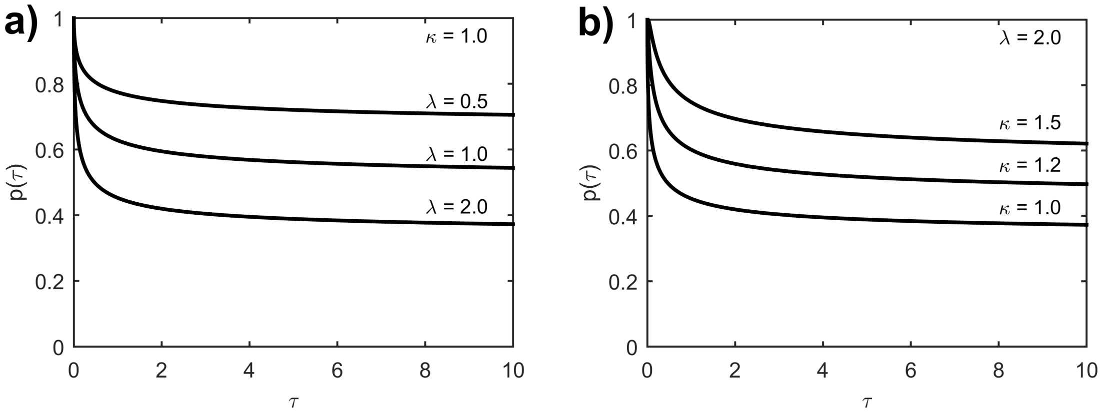

Figure 4.4. Simulated curves based on equation 4.1 for different λ (a) and κ (b).

λ and κ, approaching the limit value of $p(\infty)$, typically requires tens of τ_0 [87].

Curves calculated according to equation 4.1 with different values of λ and κ are shown on Figure 4.4. Clearly, with increase in λ, which corresponds to domination of recombination over diffusion process upon approaching the inter-fragment distance σ_R, the number of particles undergoing the SGR also increases. This is pronounced in lowering of the long time tail of the simulated curves (Figure 4.4, a). On the other hand, by increasing the initial separation of the photofragments (or κ) more particles undergo the non-geminate recombination process due to smaller probability of meeting the geminate partner. Moreover, the particles require longer time to recombine via SGR, since larger separation require longer times for diffusion (Figure 4.4, b).

The measured change in the optical density is proportional to the concentration of the HgX radicals and is therefore also proportional to the pair survival probability $p(\tau)$. The model for the data consists of the scaled pair survival probability derived from eq. 4.1 with an additional exponential decay term, which represents the ultrafast decay below 10 ps. Finally, the obtained expression is convoluted with the instrument response function. The fit of such a model gives good agreement between theory and data (Figure 4.2). The key parameters can be summarized as following. For HgI_2/MeCN: $\lambda = 9$, $\kappa = 1.15$ and $\tau_0 = 900$ ps; for $HgBr_2$/MeCN: $\lambda = 22$, $\kappa = 1.27$ and $\tau_0 = 200$ ps. Although the obtained values fall into a reasonable region (see [87–89]), the parameter uncertainties have the same (or larger) magnitude than the obtained values themselves. Due to the strong correlations between λ, κ and τ the unique set of parameters cannot be obtained leading to large parameter errors (correlation coefficients between the corresponding values derived from covariance matrix of the fit are ≥ 0.95). The problem of non-uniqueness of the parameters has been discussed previously [88]. In order to obtain a unique set of parameters one has to measure the SGR yields for many solvents with varying viscosities and make a fit with the global solvent dependent parameters. In this study we chose a slightly different approach following previous works [89]. It was found that the SGR process can also be described by a semi-empirical model which consists of a sum of several exponential decays. This model allows for simple comparison of the different channel yields (non-geminate and geminate) and the recombination rates of radical pairs produced in different conditions.

With this approach the final model can be developed. It includes three exponential decays corresponding to an ultrafast decay up to 10 ps, and a fast and a slow components of the population dynamics in the time window between 10 ps and 1.5 ns. Finally, it also contains a constant contribution independent of time, which represents the probability of the complete separation (escape) of the radicals for the pairs undergoing non-geminate recombination. Mathematically the expression can be written as

$$f(t) = A^{\mathrm{VC}} exp(-t/\tau_{VC}) + A^{\mathrm{SGR}}_{fast} exp(-t/\tau_{fast}) + A^{\mathrm{SGR}}_{slow} exp(-t/\tau_{slow}) + A^{\mathrm{NGR}}. \qquad (4.3)$$

We coin this model as a double-exponential decay, since only two exponentials describe the SGR process. After convolution with the instrument resolution function and correction for the time-zero, the model gives essentially the same quality of the fits as the Shin & Kapral's theory (Figure 4.2). However, the parameters of the semi-empirical model are well defined and can be summarized as following. For $\mathrm{HgI_2}$ we get $\tau_{fast} = 73 \pm 5$ ps and $\tau_{slow} = 530 \pm 60$ ps; relative amplitudes of the components are $\phi_{fast} = 0.72 \pm 0.03$ ps and $\phi_{slow} = 0.28 \pm 0.03$ ps ($\phi_{fast} = A^{\mathrm{SGR}}_{fast}/(A^{\mathrm{SGR}}_{fast} + A^{\mathrm{SGR}}_{slow})$, $\phi_{slow} = A^{\mathrm{SGR}}_{slow}/(A^{\mathrm{SGR}}_{fast} + A^{\mathrm{SGR}}_{slow})$); the total SGR yield is 0.68 ± 0.03 ($\Phi^{\mathrm{SGR}} = (A^{\mathrm{SGR}}_{fast} + A^{\mathrm{SGR}}_{slow})/(A^{\mathrm{SGR}}_{fast} + A^{\mathrm{SGR}}_{slow} + A^{\mathrm{NGR}})$). For $\mathrm{HgBr_2}$ we get $\tau_{fast} = 56 \pm 4$ ps and $\tau_{slow} = 730 \pm 100$ ps; relative amplitudes of the components are $\phi_{fast} = 0.77 \pm 0.04$ ps and $\phi_{slow} = 0.23 \pm 0.04$ ps; the total SGR yield is $\Phi^{\mathrm{SGR}} = 0.60 \pm 0.04$. The corresponding parameters are also listed in the Table 4.1 in order to facilitate the comparisons with the x-ray results discussed below.

4.1.2 TR-WAXS results

In order to retrieve direct information about the nature and structure of the transient species, the TR-WAXS measurements were carried out on both systems in two separate experimental sessions. The experimental parameters for the HgI_2/MeCN sample were as follows. The 7 mM solution, flowing through the sapphire nozzle, was excited by the pump beam with the wavelength $\lambda = 266$ nm. The laser beam was focused to a diameter of 210 μm with an energy of 150 μJ per pulse of (fluence of 0.32 J/cm^2). The pink x-ray pulses ($E_f = 18$ keV, BW = 3 %) were used to determine the structural changes in the sample from the laser excitation. Differential scattering patterns were measured at about 30 time points covering a time range from -100 ps to 1 μs. For the $HgBr_2$/MeCN solution the experiment was performed in similar conditions. The laser beam was focused to 160 μm with a pulse energy 80 μJ (fluence of 0.33 J/cm^2). The concentration of the sample was chosen to be 25 mM in order to have similar optical density as for HgI_2/MeCN. Similar time points in same time range was collected in this experiment.

A brief inspection of the results for both systems shows the presence of fast dynamics at early time delays which is similar to the TOAS measurements (Figure 4.5, a). The sum of the total signal in the low-Q region shows fast decaying signals in the 25-150 ps range (Figure 4.5, b). This effect is tentatively assigned to the SGR channel. However, the raw $\Delta S(q,t)$ signals contain several components (solute, cage and solvent contributions) and for a clear assignment one needs to decompose the contributions. Before doing that we will briefly review the discussion of the main reaction pathways in order to check the consistency of the new data with the literature.

Main reaction pathway

Four different candidate reaction channels were proposed for the photodissociation reaction of mercury halides [76,77]: (1) two-body dissociation $HgX_2 + h\nu \rightarrow HgX + X$; (2) three-body dissociation $HgX_2 + h\nu \rightarrow Hg + X + X$; (3) direct formation of the diatomic halogen molecule $HgX_2 + h\nu \rightarrow Hg + X_2$; (4) isomerisation of the ground state molecule (4) $HgX_2 + h\nu \rightarrow HgX{-}X$. In the previous work authors have found that HgI_2 dissociates only via the first channel and none of the other products are formed. For $HgBr_2$, the first and the second channel appeared after photodissociation. In addition to that, the formation of molecular iodine and bromine was found at longer time delays with relatively low yield due to non-geminate recombination.

Figures 4.6 and 4.7 represent the fit results of the different models to the TR-WAXS data collected at 100 ps after laser flash photolysis for both systems. The models have been calculated from the structures published in the literature and include solvent and solute

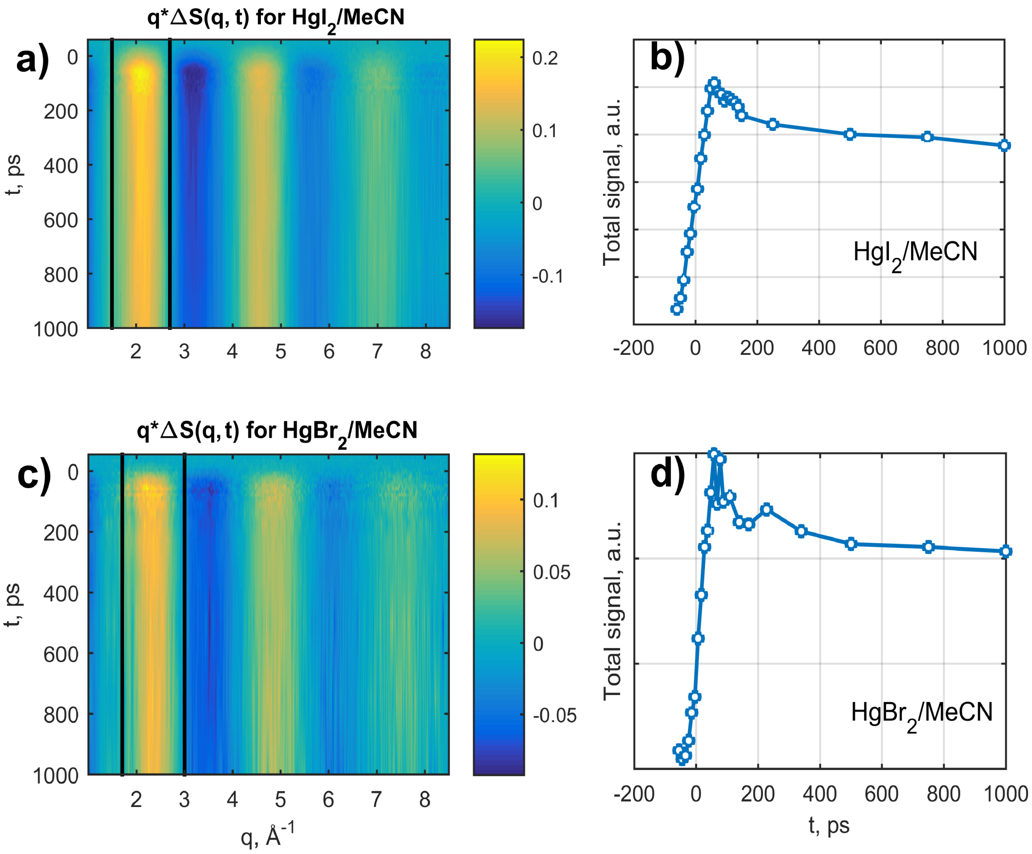

Figure 4.5. Raw TR-WAXS data for HgX_2/MeCN collected with 18 keV pink beam. a) Contour plot of the raw TR-WAXS data collected for HgI_2/MeCN; b) sum of the signal in the region inside the black lines in (a); c) Contour plot of the raw TR-WAXS data collected for $HgBr_2$/MeCN; d) sum of the signal in the region inside the black lines in (c).

contributions. Based on χ^2 analysis , the photochemical behavior of both HgI_2 and $HgBr_2$ in MeCN is found to be similar to that in MeOH. For HgI_2 the two-body dissociation model gives the best fit to the data. The addition of the three-body dissociation has been also tested; however, no significant decrease in the corresponding χ^2 value was observed (not shown). For $HgBr_2$ the combination of the two dissociation channels (1) and (2) gives significant improvement of the fit compared to the situation when only one of the channels (1) or (2) is involved. The same fitting procedure was conducted for other time delays, giving similar results. The only exception was found at later time delays ($\geq$ 100 ns), where additional terms with X_2 were included to describe the data.

The decomposition of the models into components is shown in Figures 4.8 and 4.9. In both cases, the experimental signal is dominated by the solute contribution thanks to the high-Z nature of the products together with the dissociative character of the reaction. The

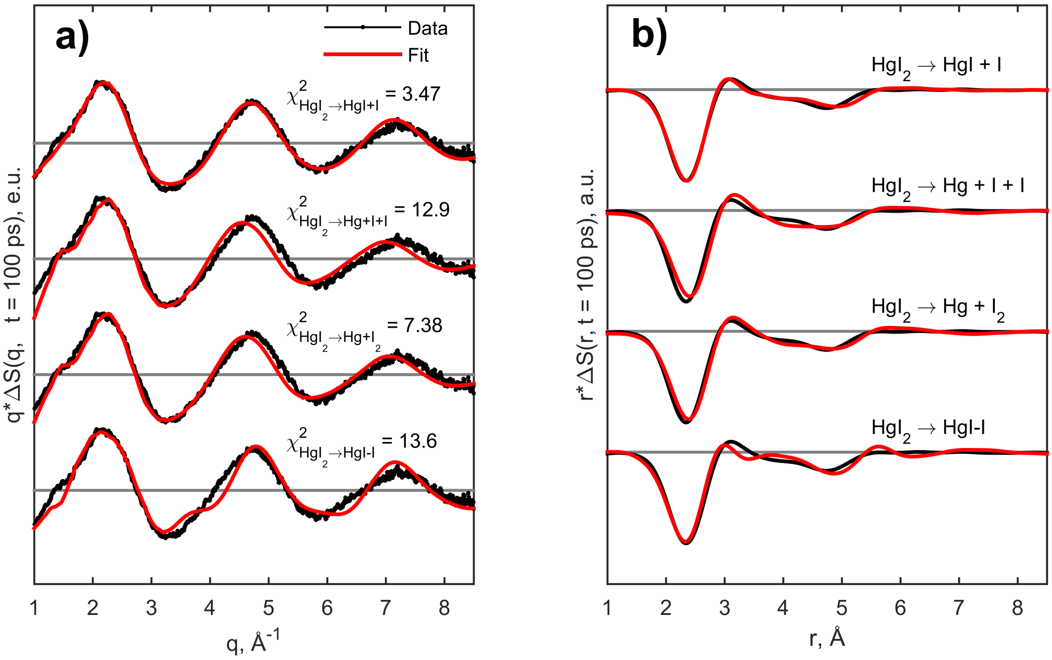

Figure 4.6. Comparison of different reaction channels with the data for HgI_2/MeCN in q- (a) and r-space (b). The data was collected with 18 keV pink beam at 100 ps time delay.

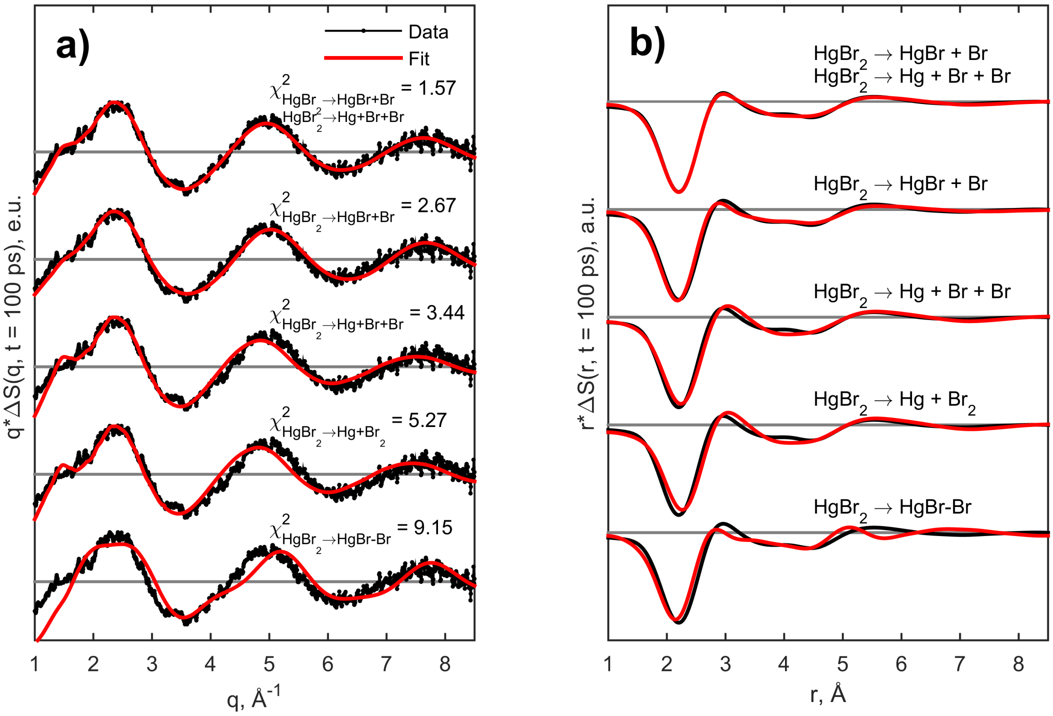

Figure 4.7. Comparison of different reaction channels with the data for $HgBr_2$/MeCN in q- (a) and r-space (b). The data was collected with 18 keV pink beam at 100 ps time delay.

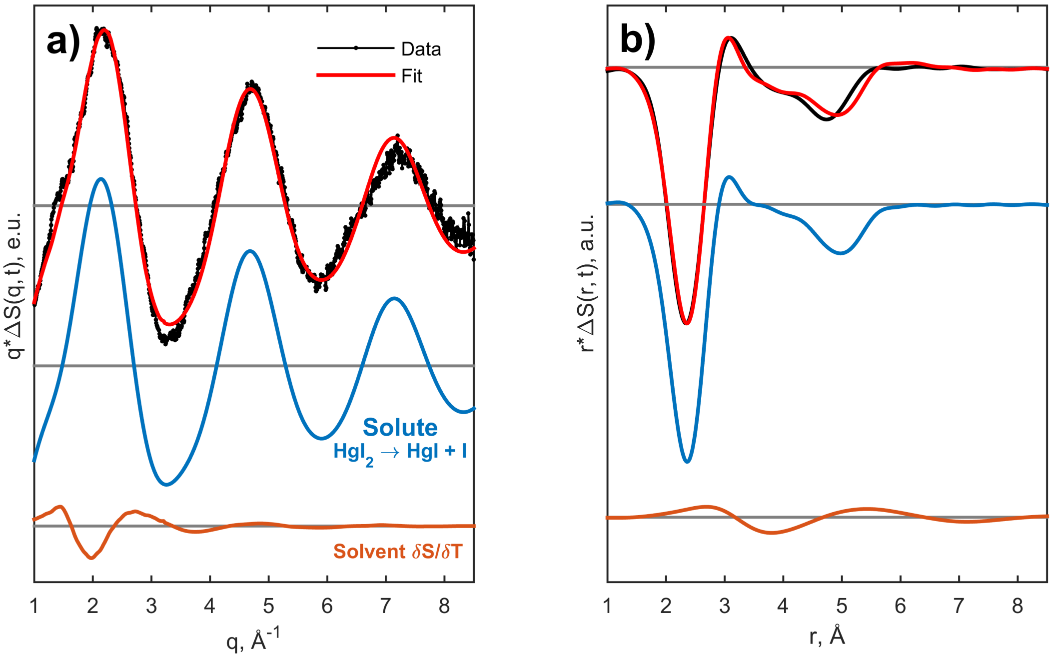

Figure 4.8. Decomposition of the fitted model for HgI_2/MeCN in q- (a) and r-space (b). The data was collected with 18 keV pink beam at 100 ps time delay.

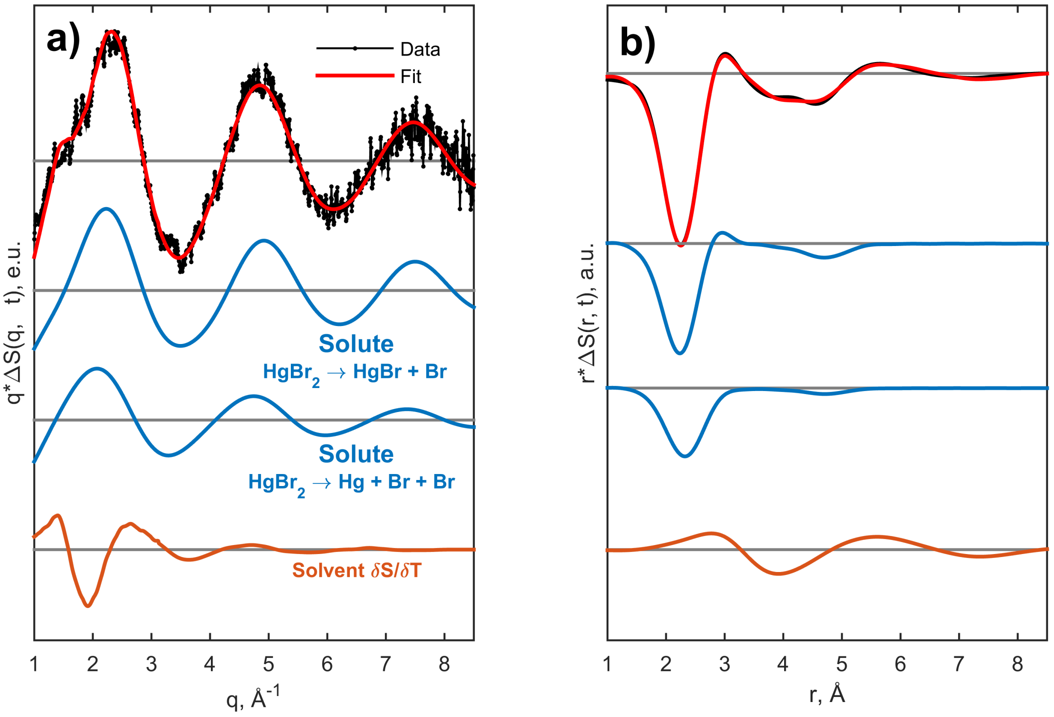

Figure 4.9. Decomposition of the fitted model for $HgBr_2$/MeCN in q- (a) and r-space (b). The data was collected with 18 keV pink beam at 100 ps time delay.

differential radial distribution function $\Delta S(r,t)$ gives additional and more intuitive insight into the structural dynamics. The two dips appearing in the solute contribution of HgI_2 in $\Delta S(r,t)$ located at ~2.5 (Hg-I correlation) and ~5 Å (I-I correlation) correspond to the removal of one of the I atoms from the initial triatomic molecule due to dissociation. Similar dips are found at the corresponding curves for $HgBr_2$; the dips are shifted towards smaller r values, since the size of $HgBr_2$ is slightly smaller than HgI_2. Making similar assignments of the oscillating features for the solute contribution is more complex; however it can be done with the use of molecular dynamics (see the previous works).

Population dynamics

In order to retrieve a qualitative picture of the population dynamics of the radicals formed after photolysis, each of the curves was fitted independently from the others. The only constraint in this procedure is the conservation of mass, so the number of transient species is equal to the corresponding number of the initially excited HgX_2 molecules. In both cases, for the HgI_2 and $HgBr_2$, one finds a rapid decay in the population of the free HgX and X radicals at early times (Figures 4.10 and 4.11). For HgI_2, the HgI and I concentrations rapidly decay before ~3 ns which confirms the simple picture of the SGR recombination derived from the TOAS results. Similarly, for $HgBr_2$, the fast decays can be found for HgBr and Br radicals. Interestingly, for the Hg radical, the fast dynamics can not be easily assigned due to large scatter of the individual points. This is consistent with the previous assumption about the absence of the Hg and Br recombination via SGR channel at early time delays at least within the signal to noise ratio and temporal resolution of the setup.

After qualitative inspection of the results we perform the global fitting procedure described in Chapter 2. The populations of different products now are coupled by a set of differential equations which represent the second order kinetics due to the non-geminate recombination. Additionally, two first order kinetic terms are included in the model, accounting for the corresponding fast and slow decays of the HgX and X populations due to SGR at early time delays. The energy redistribution between solute and solvent is taken into account by calculation of the heat deposited to the solvent and the temperature and density changes by using the values of the energy levels from previous studies. The final global fit was preformed with the use of optimized structures of the transient species, which will be discussed in the following section. All the parameters obtained from the fits for

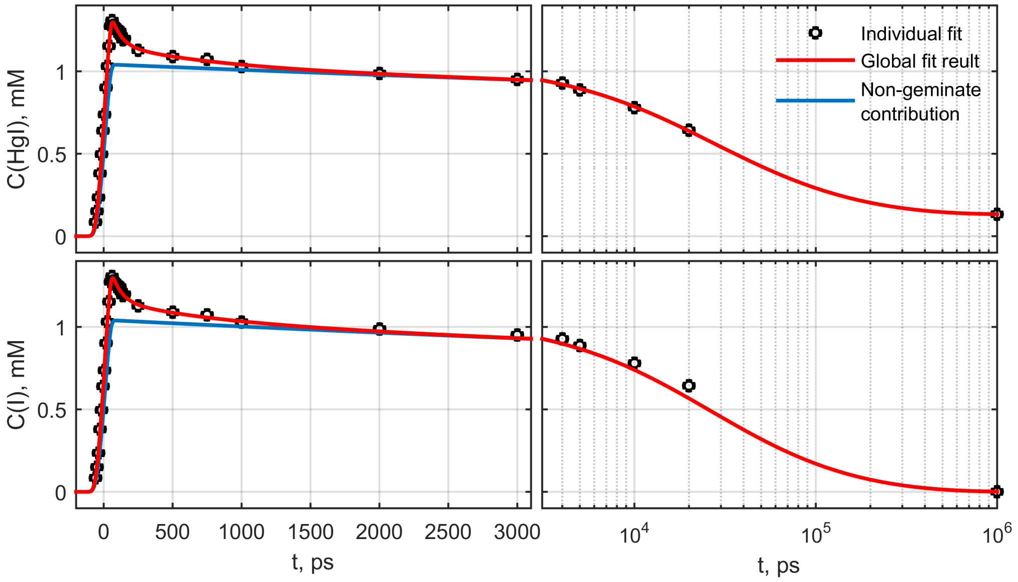

Figure 4.10. Comparison of individual and global fit results for the HgI and I radical concentrations.

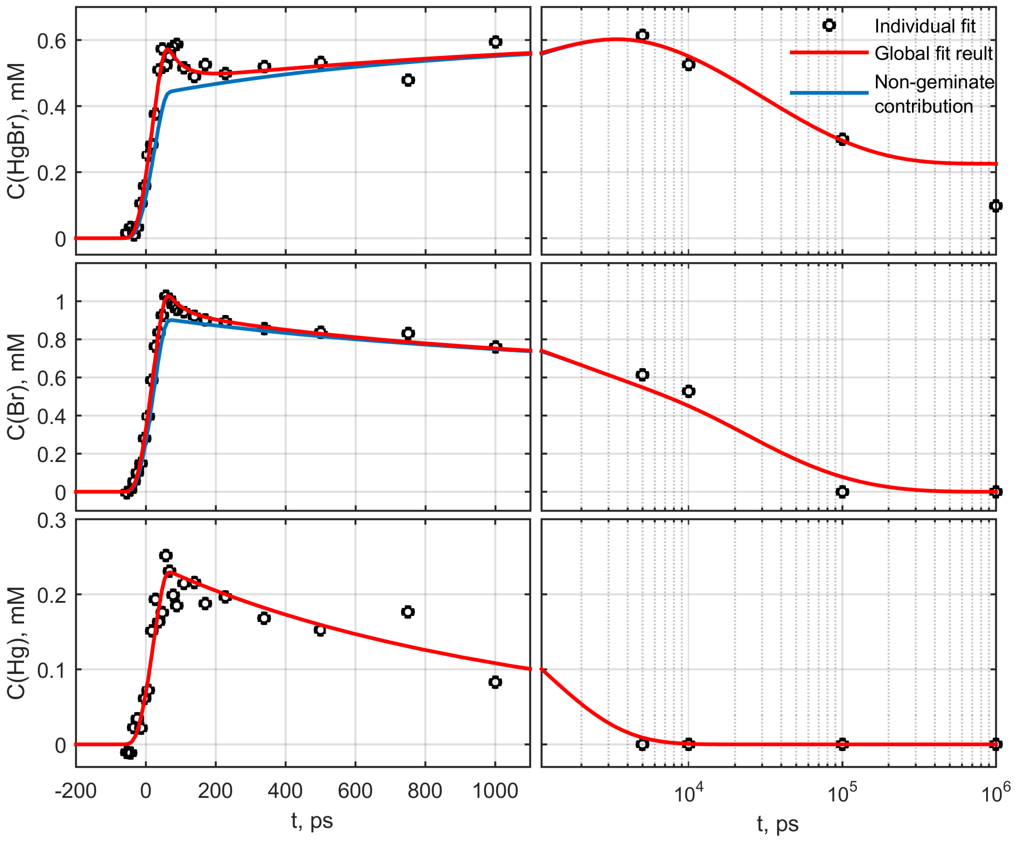

Figure 4.11. Comparison of individual and global fit results for the HgBr, Br and Hg radical concentrations.

Table 4.1. Photodissociation and recombination of HgX_2/MeCN: rates and yields.

	HgI_2		$HgBr_2$	
Parameter	TR-WAXS	TOAS	TR-WAXS	TOAS
Excitation Efficiency, Primary Geminate Recombination and Dissociation Yields				
γ[1]	0.40 ± 0.02	–	0.08 ± 0.01	–
Φ^{PGR} [2]	0.49 ± 0.03	–	0.53 ± 0.05	–
$F_{\mathrm{HgX_2 \to HgX+X}}$[3]	1	–	0.65 ± 0.01	–
$F_{\mathrm{HgX_2 \to Hg+X+X}}$[3]	0	–	0.35 ± 0.01	–
Secondary Geminate Recombination				
$\Phi^{SGR}_{\mathrm{HgX+X \to HgX_2}}$[4]	0.32 ± 0.02	0.68 ± 0.03	0.25 ± 0.03	0.60 ± 0.04
ϕ_{fast}	0.73 ± 0.03	0.72 ± 0.03	0.85 ± 0.15	0.77 ± 0.04
τ_{fast} (ps)	70 ± 10	73 ± 5	50 ± 20	56 ± 4
ϕ_{slow}	0.27 ± 0.03	0.28 ± 0.03	~ 0.15	0.23 ± 0.04
τ_{slow} (ps)	700 ± 200	530 ± 60	~ 230	730 ± 100
Non-geminate Recombination				
$\Phi^{NG}_{\mathrm{HgX+X \to HgX_2}}$[5]	0.61 ± 0.02	–	0.37 ± 0.03	–
$\Phi^{NG}_{\mathrm{Hg+X \to HgX}}$[5]	0	–	0.20 ± 0.03	–
$\Phi^{NG}_{\mathrm{X+X \to X_2}}$[5]	0.07 ± 0.02	–	0.18 ± 0.03	–
$D_{\mathrm{HgX+X \to HgX_2}}$ ($M^{-1} \cdot s^{-1}$)	$(3.2 \pm 0.1) \times 10^{10}$	–	$(3.7 \pm 0.2) \times 10^{10}$	–
$D_{\mathrm{Hg+X \to HgX}}$ ($M^{-1} \cdot s^{-1}$)	–	–	$(10.0 \pm 0.6) \times 10^{11}$	–
$D_{\mathrm{X+X \to X_2}}$ ($M^{-1} \cdot s^{-1}$)	$(3.0 \pm 0.2) \times 10^{9}$	–	$(1.5 \pm 0.3) \times 10^{10}$	–

[1] Excited state fraction, calculated relatively to the total concentraion of HgX_2 in the sample: $\gamma = [\mathrm{HgX_2^*}]/[\mathrm{HgX_2}]_0$;

[2] Fraction of the excited molecules undergone primary geminate recombination (PGR) $[\mathrm{HgX_2}]_{\mathrm{PGR}}$, which is estimated from the difference between observed temperature rise at 1 μs and calculated temperature rise due to observed formation of the reaction products; the value of $\Phi^{PGR} = [\mathrm{HgX_2}]_{\mathrm{PGR}}/[\mathrm{HgX_2^*}]$;

[3] Fraction of the excited molecules which undergone two- or three-body dissociation and left the parent cage. The values are calculated relatively to the total concentration of the radicals which have left the parent cage after photolysis of HgX_2: $F_{\mathrm{HgX_2 \to HgX+X}} = [\mathrm{HgX}]/([\mathrm{HgX_2^*}] - [\mathrm{HgX_2}]_{\mathrm{PGR}})$, $F_{\mathrm{HgX_2 \to Hg+X+X}} = [\mathrm{Hg}]/([\mathrm{HgX_2^*}] - [\mathrm{HgX_2}]_{\mathrm{PGR}})$;

[4] Fraction of excited molecules which have left the initial cage and undergone secondary geminate recombination (SGR). Values are calculated relatively to the total concentration of the X radicals: $\Phi^{SGR}_{\mathrm{HgX+X \to HgX_2}} = [\mathrm{X}]^{\mathrm{SGR}}_{\mathrm{HgX+X \to HgX_2}}/[\mathrm{X}]_0$;

[5] Fractions of the X radicals formed different reaction products via non-geminate recombination. The values are calculated relatively to the total concentration of the X radicals which have left the parent cage after photolysis of HgX_2: $\Phi^{NG}_{\mathrm{HgX+X \to HgX_2}} = [\mathrm{X}]^{\mathrm{NG}}_{\mathrm{HgX+X \to HgX_2}}/[\mathrm{X}]_0$, $\Phi^{NG}_{\mathrm{Hg+X \to HgX}} = [\mathrm{X}]^{\mathrm{NG}}_{\mathrm{Hg+X \to HgX}}/[\mathrm{X}]_0$, $\Phi^{NG}_{\mathrm{X+X \to X_2}} = [\mathrm{X}]^{\mathrm{NG}}_{\mathrm{X+X \to X_2}}/[\mathrm{X}]_0$.

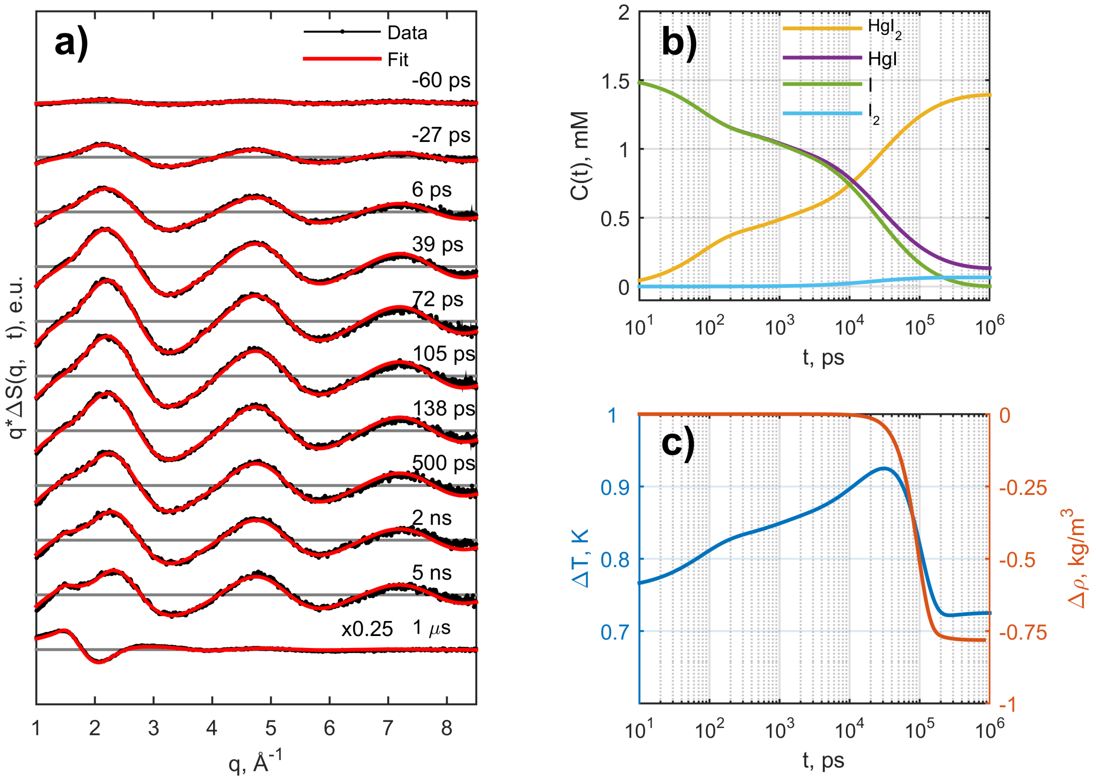

Figure 4.12. Global fitting results for HgI_2/MeCN. a) comparison of the curves obtained with the global fit with the experimental data for HgI_2/MeCN; b) instantaneous concentrations of the transient species c) temperature and density as a function of time.

both systems are summarized in Table 4.1.

Reasonable agreement between the global and individual fits for both systems shows the success of the fitting procedure (Figures 4.10 and 4.11). The obtained parameters for both systems can be summarized in the following way. For HgI_2/MeCN the total excited state fraction in respect to the number of the ground state molecules is $\gamma = 0.40 \pm 0.02$ (2.80 ± 0.14 mM). Similarly to the previous works we predict that the fraction $\Phi^{PGR} = 0.49 \pm 0.03$ of excited molecules recombine to the ground state within first 10 ps via primary geminate recombination. This value is derived from the comparison of the observed experimental temperature rise at 1 μs (0.73 K) and expected temperature rise due to recombination of HgI and I fragments undergoing SGR or PGR (0.36 K). The rest of the yields are represented as fractions calculated relative to the total amount of the I radicals, which have left the initial cage and undergo recombination via diffusive motion (geminately or non-geminately). Fraction $\Phi^{SGR}_{\mathrm{HgI+I \rightarrow HgI_2}} = 0.32 \pm 0.02$ of radicals recombine

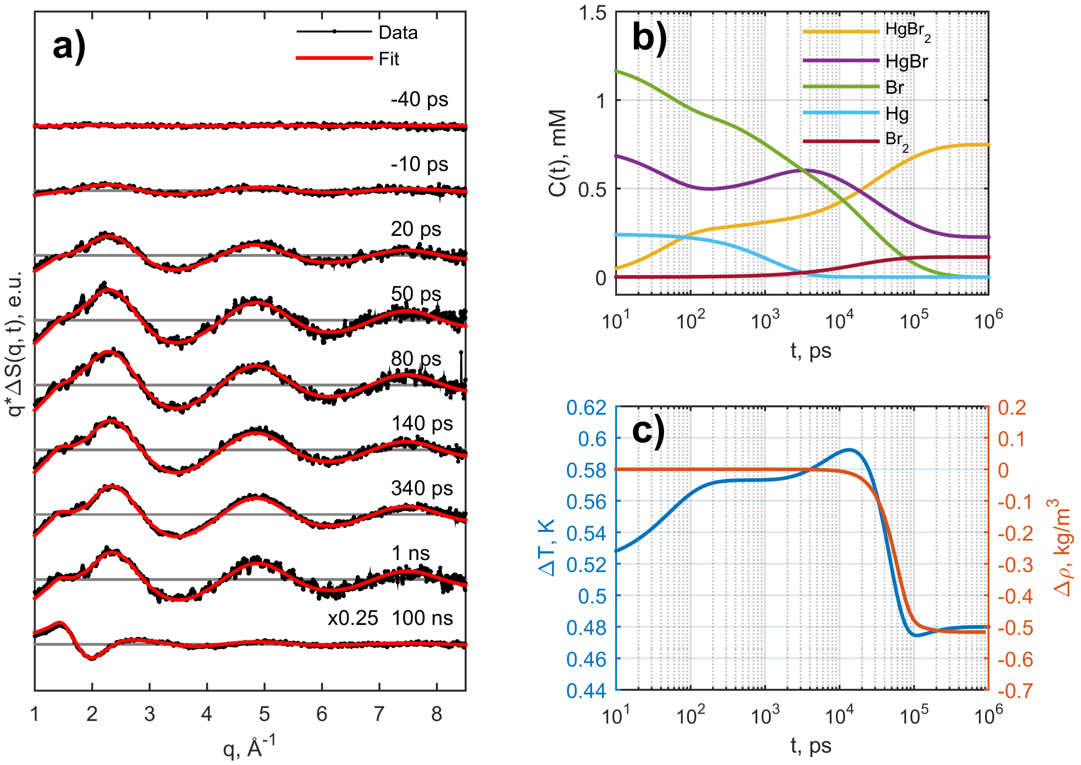

Figure 4.13. Global fitting results for $HgBr_2$/MeCN. a) comparison of the curves obtained with the global fit with the experimental data for $HgBr_2$/MeCN; b) instantaneous concentrations of the transient species c) temperature and density as a function of time.

via SGR with corresponding time constants of $\tau_{fast} = 70 \pm 30$ ps and $\tau_{slow} = 700 \pm 200$ ps and relative amplitudes $\phi_{fast} = 0.73 \pm 0.03$ and $\phi_{slow} = 0.27 \pm 0.03$. Another fraction, $\Phi^{NG}_{\mathrm{HgI+I \to HgI_2}} = 0.61 \pm 0.02$, of the I radicals recombine together with HgI non-geminately to form HgI_2 molecules with the bimolecular rate $D_{\mathrm{HgI+I \to HgI_2}} = (3.2 \pm 0.1) \times 10^{10}$ M^{-1}·s^{-1}. The rest of the I atoms ($\Phi^{NG}_{\mathrm{I+I \to I_2}} = 0.07 \pm 0.02$) form molecular iodine I_2 with the rate $D_{\mathrm{I+I \to I_2}} = (3.0 \pm 0.2) \times 10^9$ M^{-1}·s^{-1}. The corresponding fits and calculated instantaneous time dependent changes in concentrations, temperature and density are shown in Figure 4.12.

For the $HgBr_2$/MeCN the excitation fraction is only $\gamma = 0.08 \pm 0.01$. As forHgI$_2$, the amount $\Phi^{PGR} = 0.53 \pm 0.05$ of radicals was found to recombine via PGR within the first 10 ps. Based on the analysis of the concentrations of radicals which have left the initial cage, we conclude that the fraction $F_{\mathrm{HgBr_2 \to HgBr+Br}} = 0.65 \pm 0.01$ of molecules have dissociated via two-body dissociation. About a quarter of the Br radicals ($\Phi^{SGR}_{\mathrm{HgBr+Br \to HgBr_2}} = 0.25 \pm$

0.03) recombine via SGR with the corresponding number of HgBr radicals with the time constants of $\tau_{fast} = 50 \pm 20$ ps, $\tau_{slow} \sim 230$ ps and relative amplitudes $\phi_{fast} = 0.85 \pm 0.15$, $\phi_{slow} \sim 0.15$. The values of the slow components appear to be ill defined due to the low signal-to-noise ratio, and the optimal values obtained from χ^2 minimization are presented here without error estimates. The fraction $\Phi^{NG}_{\mathrm{Hg+Br\rightarrow HgBr}} = 0.20 \pm 0.03$ of Br recombine non-geminately with the Hg radicals to form HgBr with the bimolecular rate $D_{\mathrm{Br+Hg\rightarrow HgBr}} = (10.0 \pm 0.6) \times 10^{11}$ $\mathrm{M^{-1} \cdot s^{-1}}$. At later time delays, the fraction $\Phi^{NG}_{\mathrm{HgBr+Br\rightarrow HgBr_2}} = 0.37 \pm 0.03$ of free Br recombine non-geminately with the HgBr radicals to form the initial $\mathrm{HgBr_2}$ species with the rate $D_{\mathrm{HgBr+Br\rightarrow HgBr_2}} = (3.7 \pm 0.2) \times 10^{10}$ $\mathrm{M^{-1} \cdot s^{-1}}$. Finally, $\Phi^{NG}_{\mathrm{Br+Br\rightarrow Br_2}} = 0.18 \pm 0.03$ of Br form molecular $\mathrm{Br_2}$ with the rate $D_{\mathrm{Br+Br\rightarrow Br_2}} = (1.5 \pm 0.3) \times 10^{10}$ $\mathrm{M^{-1} \cdot s^{-1}}$. The fits and time dependent changes in concentrations, temperature and density for $\mathrm{HgBr_2}$ are shown in Figure 4.13.

For $\mathrm{HgI_2}$ the parameters describing the SGR process are in good agreement between the TOAS and TR-WAXS measurements (Table 4.1). The only exception is the total SGR yield $\Phi_{SGR}(\mathrm{HgX + X \rightarrow HgX_2})$ derived from two different techniques. Since the x-ray experiment gives direct information about the concentration of the excited species, the value provided from TR-WAXS analysis appears to be more reliable. The bias of the TA measurement can be due to the following. The single-color probe does not allow the disentanglement of the different contributions to the TOAS signal, which might be perturbed by additional components not included into the interpretation of the result. As discussed above, the populations of HgI and I radicals are equivalent in the investigated time window. Therefore, independent of the absolute contributions to the transient signal, the analysis should lead to the correct values of the yields. For this reason, the bias of the TOAS result has to come from a different source, for example, from induced absorption in the solvent. Speculatively, the UV pump pulse can induce changes in the MeCN solvent leading to induced absorption at the probe wavelength. It is noteworthy to mention, that the MeCN absorption in the UV region might also slightly bias the x-ray results leading to an increase in the observed temperature rise and hence the yield of the radicals undergoing recombination within the parent cage (PGR). During the TR-WAXS measurements it was checked that the signal coming from the excitation of the pure MeCN with the 266 nm pulse leads to a temperature rise of only 1-2 % observed in the conducted experiments on $\mathrm{HgX_2}$ systems (not shown). This ensures the reliability of the global analysis and the reported values.

For $HgBr_2$ the agreement between the SGR parameters from TR-WAXS and TOAS is also reasonable. In this case however, the signal-to-noise ratio of the experiment appears to be lower, which prevents a reliable determination of the parameters for the slow component in SGR. Apart from the signal-to-noise ratio, another factor might also contribute to the poor definition of these values. Computational studies of the SGR and NGR processes, based on Monte Carlo methods, show that at low concentrations ($\leq$10-15 mM) the characteristic time scale for NGR is much larger than for SGR [90]. The two processes therefore appear to be well separated in time and do not interfere with each other. In the case of $HgBr_2$, the TR-WAXS measurements were conducted at 25 mM, meaning that even at early time delays the two processes of NGR and SGR already begin to compete, making the population dynamics more complex. In this case some of the radicals, might recombine with the non-geminate partner with a high probability due to close proximity of the initial molecules. The real situation might be even more complex, if one takes into account three-body dissociation. This process leads to the formation of highly mobile radicals which quickly diffuse through the solvent. For example, the presence of Hg radicals leads to rapid non-geminate recombination with free Br coming from both two- and three-body dissociation events. Further concentration dependent studies could help to disentangle the different processes.

The agreement between the SGR parameters obtained from the two different techniques gives a good benchmark for the time-slicing technique employed in these experiments. This approach is therefore quite powerful in determining the details of processes on timescales comparable with the temporal resolution of the setup (50-100 ps).

Finally, the obtained data clearly demonstrates the effect of the radical size on the diffusion rates and, consequently, the recombination rates. Due to the size effects, the diffusion of HgI and I radicals is slower than that for HgBr and Br. This is manifested in longer SGR recombination time scales τ_{fast} and smaller bimolecular rates for the non-geminate recombination $D_{\mathrm{HgX+X\rightarrow HgX_2}}$. Clearly, the most rapidly recombining pair is Hg and Br, which are the smallest and most mobile radicals. The only values which call for a separate examination are the time constants for the slow SGR recombination component. This decay essentially represents the geminate recombination of the part of the free radicals which drift quite significantly apart from each other at early time delays. In this case, the time constant for the HgI and I pair to recombine geminately is slightly smaller than such for the HgBr and Br (based on the TA values). This might happen due to the high mobility of the Br and HgBr radicals which brings this fraction of the radicals ϕ_{slow} further away from each other in comparison to I and HgI. Consequently it might require slightly longer times to come back to recombine geminately. This is a rather qualitative picture derived from our semi-empirical model; such effects are taken properly into account by the Shin & Kapral theory but require extended studies as discussed above.

In the next section we will discuss the structure of the transient species produced after photolysis of HgX_2. Recently, it has been shown that for small di- and triatomic molecules TR-WAXS allows refinement of both ground and excited state structures with good precision [32, 91]. From the structural point of view mercury halides represent a similar case, where both ground and excited state can be described with few geometric parameters. Now we will show how to define all these parameters from a single TR-WAXS measurement.

Structural analysis

In order to retrieve the structural parameters of the reaction products one needs to develop a model. For the HgX_2 photodissociation reaction one needs only four parameters to describe the structures of the ground and excited states: two Hg··X distances (R_1, R_2) and one distance between the two X atoms X··X (R_3) for description of the ground state structure; additionally, it is necessary to optimize the Hg · ·X bond length in the HgX product (R_4) (Figure 4.14). In this particular case, instead of optimizing the distance between the two X atoms R_3 in the ground state, the bending angle of the molecule $\angle$(X−Hg−X) was chosen for the optimization. It allows to automatically keep the geometrical structure of the ground state physically meaningful without imposing constraints on the parameters (such as $R_3 \leq R_1 + R_2$). The model also includes a scaling factor accounting for the excitation fraction (γ) as well as the solvent contribution scaled by the corresponding temperature rise (ΔT). Finally, the model for $HgBr_2$ also includes the branching ratio between the two- and three-body dissociation. The models for both systems are fitted to the data collected at 100 ps and the parameter errors are estimated according to the procedure described in Chapter 2.

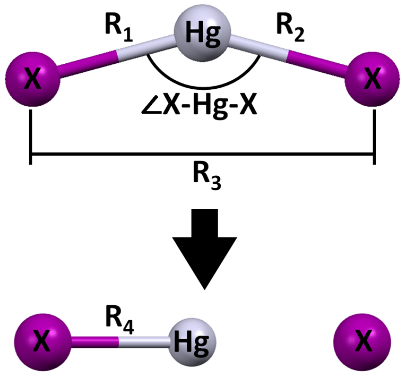

Figure 4.14. Structural model for HgX_2 and HgX.

For HgI_2 the obtained distances $R_1 = 2.59 \pm 0.01$ Å, $R_2 = 2.59 \pm 0.01$ Å, and $R_4 = 2.81 \pm 0.03$ Å are in good agreement with previous works (Table 4.2). The fit converges towards equal R_1 and R_2 bond lengths confirming the symmetry of the molecule. The striking difference appears in the bending angle of the molecule, which converges to the value of 146 ± 3°, leading to an I · ·I distance $R_3 = 4.95 \pm 0.06$ Å. In order to check the significance of such bending, the linearity constraint have been imposed into the fitting procedure (Figure 4.15, a). In this case the χ^2_{red} value increases by factor of roughly 2, which indicates the statistical significance of the bending. The corresponding radial distribution functions also show that the longer I · ·I distance obtained in the linear geometry describes the negative peak at ∼5 Å slightly worse than the bent geometry, being shifted towards higher r compared to the data (Figure 4.15, b).

The same analysis was made for $HgBr_2$. It shows identical behavior, with good agreement between the theoretical and experimental bond lengths: for the ground state the obtained Hg · ·Br distances are $R_1 = 2.40 \pm 0.03$ Å, $R_2 = 2.40 \pm 0.03$ Å; the HgBr photofragment's bond length $R_4 = 2.61 \pm 0.05$ Å (Figure 4.16). The same results are found with respect to the bending in the ground state: without linearity constraint, the $\angle(\mathrm{Br-Hg-Br})$ converges to ∼156°. In this case however, the difference between the corresponding χ^2_{red} values appear to be much less significant (Figure 4.16, a). This might be due to the signal-to-noise ratio of this experiment being lower than for HgI_2, therefore decreasing the sensitivity of the optimization of the Br · ·Br distance. After Fourier-transforming the data it is also evident that bending of the molecule does not make any significant difference in the fit quality (Figure 4.16, b). The final optimization parameters for both systems are summarized in the Table 4.2.

This simple optimization shows the strength of the TR-WAXS technique in the determination of the precise structure of the transient species in solution, at least for the closest interatomic distances. One question about the experimental determination of the structure remains open: why does the structural analysis for HgI_2 lead to the bent geometry? In principle, $HgBr_2$ is also susceptible to this effect, although the statistical evaluation does not allow to differentiate between the bent and linear structures. According to the previous calculations [76, 77] and optical spectroscopic studies [78], both HgI_2 and $HgBr_2$ are linear in the ground state in organic solvents such as MeCN or MeOH. Only in some special cases, such as highly concentrated HgX_2 solutions in DMSO, bending of the molecules is reported with typical values of 150-160° for the $\angle(\mathrm{X-Hg-X})$ angle [92]. One reason for

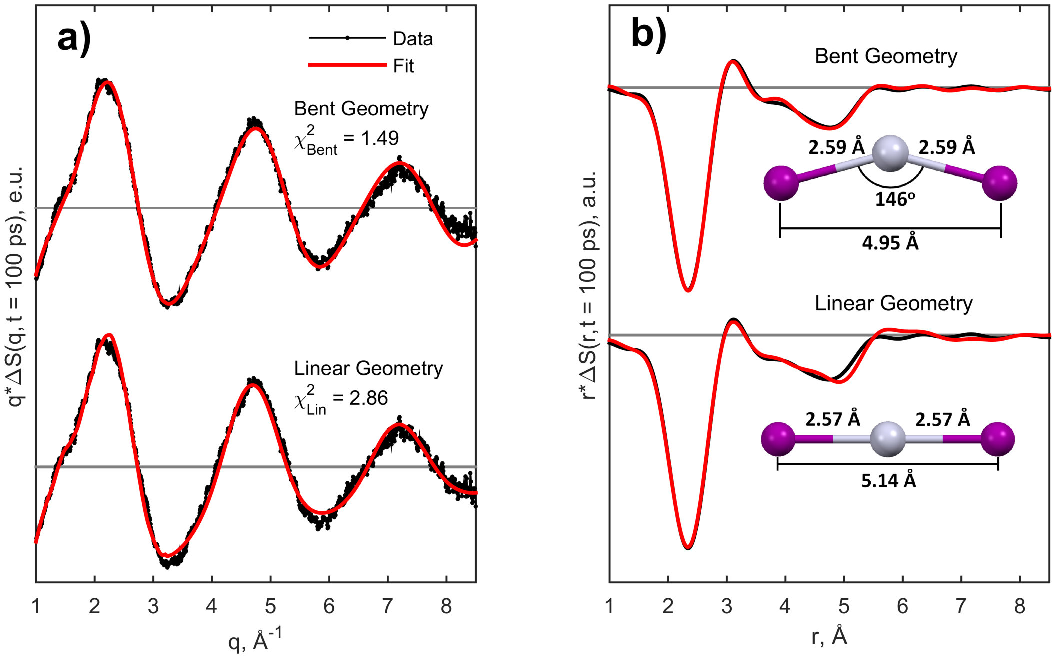

Figure 4.15. Comparison of the fit quality for the bent and linear ground state geometries for HgI_2 in Q- (a) and R-spaces (b).

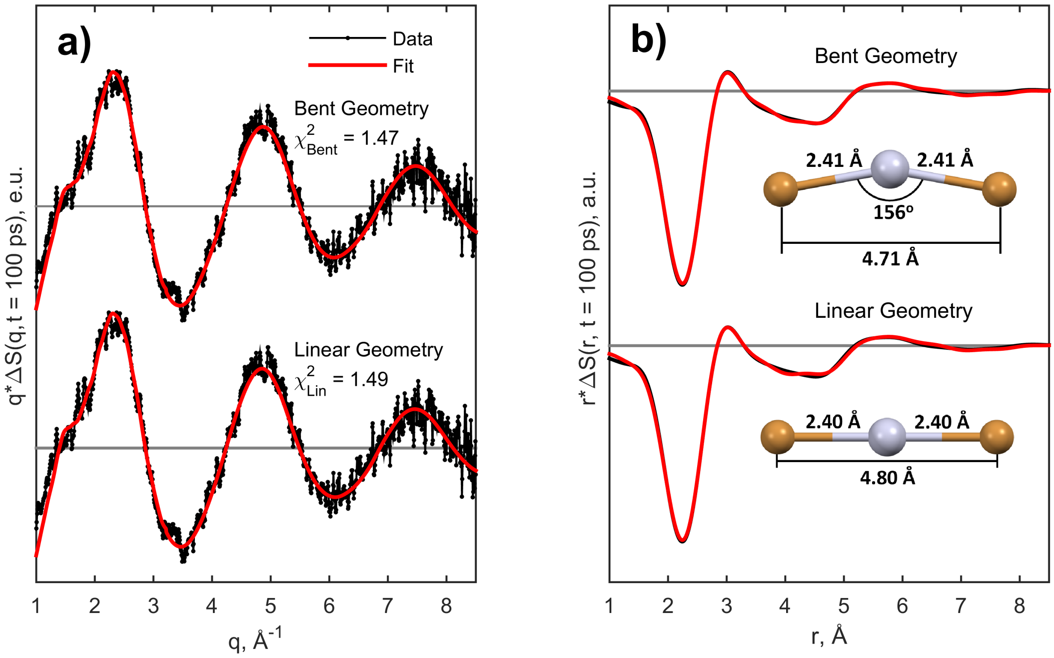

Figure 4.16. Comparison of the fit quality for the bent and linear ground state geometries for $HgBr_2$ in Q- (a) and R-spaces (b).

Table 4.2. Structural parameters of HgX_2 obtained from the optimization procedure.

System		R_1 (Å)	R_2 (Å)	R_3 (Å)	$\angle X\text{-}Hg\text{-}X$ (°)	R_4 (Å)
HgI_2	Theory[1]	2.587	2.587	5.174	180	2.814
	Experiment	2.59 ± 0.01	2.59 ± 0.01	4.95 ± 0.06	146 ± 3	2.81 ± 0.03
$HgBr_2$	Theory[1]	2.405	2.405	4.81	180	2.625
	Experiment	2.40 ± 0.03	2.40 ± 0.03	4.80 ± 0.04	180	2.61 ± 0.05

[1] Values from [77].

this effect could be vibrations of the HgX_2 molecule in the ground state. For example, the bending mode vibrational frequency for a solvated HgI_2 molecule is $\nu_{bend} = 33$ cm^{-1} [72], which is much smaller than room temperature ($k_B T = 206.4$ cm^{-1}). Therefore, thermalized molecules in solution can populate high vibrational levels, leading to an efficient shortening of the mean I· ·I bond length, which is observed in the x-ray experiment. This phenomenon is known as the Bastiansen-Morino shrinkage effect [93, 94], which was first observed in early electron diffraction experiments on linear CO_2 molecules [95, 96]. However, this effect lead to a typical shortening of the I· ·I distance of ∼0.03-0.04 Å at room temperature [97,98], which is clearly smaller than that observed in our experiment (∼0.2 Å for HgI_2). Therefore, this explanation is not satisfactory. Another reason for the bending might be rather trivial. The accuracy of the structural analysis with the use of the pink beam might be biased since the spectrum “seen” by the 2D x-ray detector (FReLoN) is slightly different from the one measured with the photodiode. Since the employment of the pink spectrum leads to slight shifts and damping of the oscillations towards higher Q, the precision of the measured spectrum defines the accuracy of the analysis. In the present fits we can see that the agreement between the theory and data is getting worse in the high-Q region (see, for example, Figure 4.8). This discrepancy can come from the poor definition of the spectrum, which affects the present analysis. This explanation seems to be the most satisfying; this discussion will be extended below during the structural analysis of $I_3{}^-$.

Before concluding the section, it is noteworthy to discuss possible extensions of the work related to a more elaborate description of the secondary geminate recombination process from the structural point of view. In order to do this, it is necessary to revisit the early evolution of the studied systems after the photolysis of the parent molecules. Prior to dissociation the HgX_2 molecules are uniformly distributed in the liquid volume. After photolysis event most of the dissociated radicals recombine to the ground state molecule on

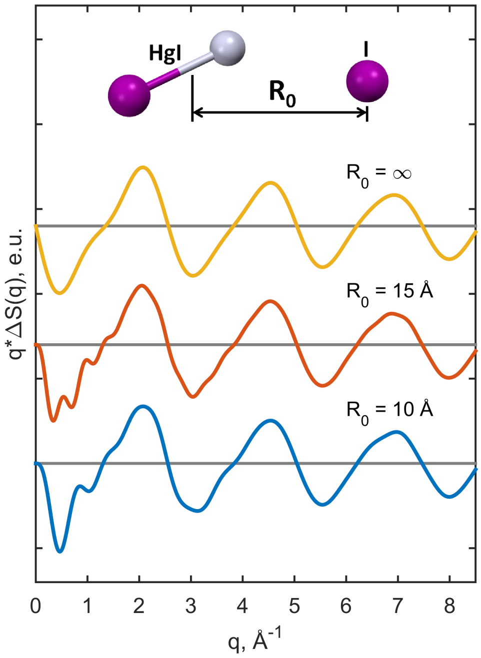

Figure 4.17. Simulation of the TR-WAXS signal produced by the HgI and I fragments located at different distances. The orientation of the HgI radical is averaged relatively to the axis going through the centers of mass of I atom and HgI photofragment.

very short time scales, in less than 10 ps. On the other hand, the radicals, which have left the initial cage are still located in proximity to each other. This closeness of the radicals, in principle, can contribute to the TR-WAXS signal and therefore can also be detected. A simple simulation for HgI_2 shows that if two photofragments HgI and I appear to be close to each other, within 10 or 15 Å, the signal in the low-Q part is changing significantly in comparison to the infinite separation considered in the present analysis (Figure 4.17). These characteristic signals might be used to measure the average distances between the photofragements at early time points during the process of diffusion motion of the radicals. It would require a slightly different experimental approach, optimized on smaller angles, since the signal is hidden in this region. Additionally, the real experiment will be complicated since in the real solution, after photolysis, one obtains not a single distance between the radicals, but rather a distribution, which also has to be taken into account. This is probably the limiting factor for such experiments performed at the synchrotrons, since within 100 ps, the resolution of the setup, the inter-radical distance distribution will change dramatically, excluding any possibility of the quantitative analysis. Another complication is of course the necessity to include the cage term obtained from theoretical simulations, since in these q-values, the solvation dynamics significantly contributes to the signal. Finally, in the present analysis no evidence for such correlations were found, i. e. and the very good agreement between theory and experiment was obtained without including these inter-radical correlations into the analysis. This indicates the insensitivity of the present measurements to the discussed structural correlations between photofragments, which leaves such work for the future development.

4.1.3 Summary

In this section the recombination dynamics of mercury halides after flash photolysis was investigated. It was found that the photochemical behavior of HgI_2 and $HgBr_2$ in MeCN is similar to that in MeOH. A fast decay in the population of the free radicals HgX and X have been observed by transient optical spectroscopy and TR-WAXS which is attributed to secondary geminate recombination. A semi-empirical model was employed for the description of the process and good agreement between the measurements was obtained. These results show good agreement between the two techniques and allow us to benchmark the time-slicing experimental scheme described in Chapter 2 as a robust method for the study of short lived species. Non-geminate recombination of the free radicals has also been addressed and the corresponding product yields and bimolecular rates were obtained. Overall, the results allowed to correlate the reaction rates with the size of the photofragments. Finally, the structure of both the ground state and transient species were determined by structural optimization. The experimental structures show good agreement with the theoretical predictions; however, the HgI_2 experimental ground state geometry was found to be bent. This effect is attributed to the experimental error from using the pink beam. Possible developments for a more complete description of the early stages of free radical diffusion and the potential complications of the analysis were also outlined.

4.2 Recombination dynamics of triiodide

Similarly to the mercury halides, simple structure and rich photochemistry of the triiodide lead to employment of this system for studies of different aspects of the liquid phase chemistry. Together with HgI_2, triiodide was one of the first systems where the fundamental processes of coherence transfer, vibrational and rotational relaxation in solution, were addressed [99–103]. The process of geminate recombination of radicals produced by the photodissociation of I_3^- have been studied systematically in many different molecular and ionic solvents [104, 105]. From the application point of view, the solvated mixture of triiodide (I_3^-) and iodide (I^-) was found to be an efficient electrolyte for dye-sensitized solar cells [106] with anomalously fast charge transport properties if one employs the ionic liquid as a solvent [107–109]. Many other chemical and biological applications of this compound can be found in the literature (see the recent overview [110] dedicated to the celebration of the 200 year anniversary of discovery of the iodine).

One of the interesting phenomena observed in respect to this system is the formation of a long living charge transfer complex, which was suspected to appear in early spectroscopic experiments [100, 104, 111]. The spectroscopic work employing transient hyperspectral probing performed by Ruhman and Baratz clearly revealed this additional reaction product, which was tentatively assigned as a contact ion pair (CIP) $[I_2^- + I]$ [112]. The ion pairing has been known for a long time. It can lead to aggregates of different types, such as free ions, solvent-separated ion pairs and CIP [113, 114]. All the types appear in many fields of chemistry and have a wide range of applications including batteries [115–117] and photovoltaics [118]. Most of the previous studies have addressed the properties of these entities by spectroscopic tools [119, 120]; recently, x-ray investigations of CIP formed in crystalline form deepened the understanding of the phenomenon [121]. In this work we have attempted to address the structure of CIP in solution at room temperature with TR-WAXS and transient optical absorption spectroscopy (TOAS). Although no structural model is available at the moment, the measurements allowed us to clearly distinguish the signal appearing due to the formation of the free ions ($[I_2^-]+[I]$) and CIP ($[I_2^- + I]$).

We will shortly summarize the knowledge about the system from the literature. Triiodide has certain similarities with the mercury halides discussed in the previous section. The absorption spectra show the presence of the two peaks in the UV region (Figure 4.18, a). Although the assignment of the absorption bands is a bit controversial, it is known that

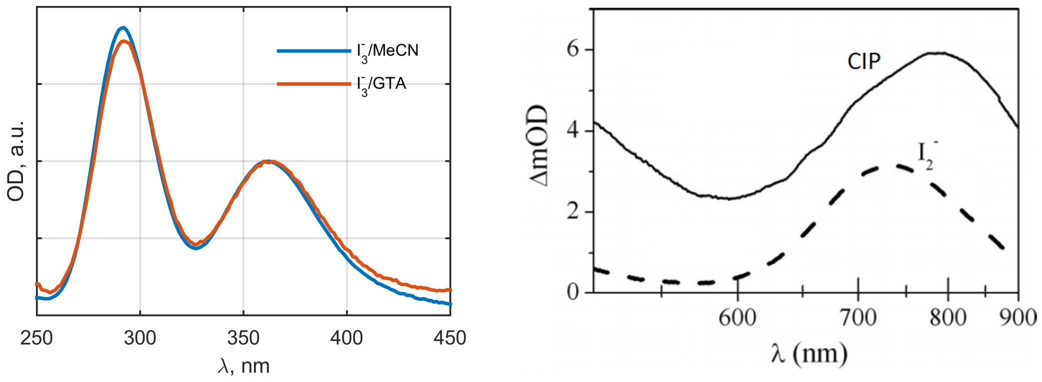

Figure 4.18. Absorption spectra of I_3^- in MeCN and GTA solvents at room temperature (left panel); absorption of the I_2^- and CIP in ethanol from [112] (right panel).

the excitation of I_3^- from the ground state $^1\Sigma_g^+$ at 400 nm leads to the formation of I_2^- in its ground state $^2\Sigma_u^+$ and an iodine atom in the ground spinorbit state $^2P_{3/2}$ [122–124]. Previous considerations (see HgX_2 discussion) about the time scales of vibrational cooling of the products still hold: after ~10ps we expect to have completely cooled down photofragments. This time scale might be even shorter, since the vibrational energy relaxation time constant for I_2^- in molecular solvents is only a few ps [103]. The recombination channels of the radicals (primary and secondary geminate, non-geminate channels), in principle, remain similar to HgX_2; however, for the study of the ionic contact pair, acetonitrile (MeCN) and glycerol triacetate (GTA) were chosen as solvents and some dramatic differences in comparison to HgX_2 appear. Spectroscopic studies revealed no significant contribution of the secondary geminate recombination to the ground state recovery in I_3^-/MeCN due to the low viscosity of the solvent and high mobility of the radicals. In contrast, GTA is a very thick liquid, which does not allow the photofragments to leave the parent molecule's cage, so only two recombination channels are possible: direct in-cage recombination (or primary geminate recombination) and CIP formation [105]. The absorption spectrum of the CIP is quite similar to the one of free I_2^- ions; the only difference appears in broadening and shifting of the band towards the red side of the spectrum (Figure 4.18, b) [112].

The symmetry and structure of the ground state were studied with x-ray absorption spectroscopy [125], transient anisotropy measurements [122] and Raman spectroscopy [126]. The ultimate solution to the problem was given by recent TR-WAXS experiments where the structure was found to be dependent on the nature of the solvent [32] which was supported by theoretical DFT calculations and Molecular Dynamics simulations [127]. The breakage of the molecular symmetry appears upon solvation of $I_3{}^-$ in protic solvents. The amplitude of the bending and asymmetric stretch (inequality of the bond lengths between closest I atoms) of the molecule is strongest in water, weaker in alcohols and not present in aprotic solvents such as MeCN. Interestingly, the lifetime of the CIP also depends on the proticity properties of the solvent, being shortest for water and longest for aprotic solvents [105].

The results will be reported in the following way. First, we will introduce the preliminary results from transient absorption (TA) spectroscopy. Then we will briefly check the consistency of our TR-WAXS measurements with the literature. In the following section we will extract the CIP signals and compare them to the free photofragments model. The population dynamics of the CIP will be discussed as well. Finally, the structural optimization of the ground state $I_3{}^-$ ion and the free photofragment $I_2{}^-$ will be performed. The section will be concluded by a discussion of the effects of using different x-ray probes on the structural analysis precision.

4.2.1 TOAS results

Transient absorption spectroscopy was applied to $I_3{}^-$ solutions in order to study the early recombination dynamics of the photofragments. In this work the formation of the CIP has been observed by probing the induced absorption at 800 nm and the ground state bleach at 290 nm. The details of the experiment are described below.

Samples were prepared by dissolving 0.1 mM potassium iodide (KI) and iodine (I_2) in MeCN and GTA solutions. The GTA solution was heated up to ∼35 C° and steered until the solutes were completely dissolved; afterward it was cooled down to room temperature. All the chemicals were purchased from Sigma Aldrich and used without any further purification. The formation of $I_3{}^-$ was checked by observation of the characteristic absorption features in the UV-vis spectrum of the solution. The pump beam with the wavelength of 400 nm and pulse power of 10 μJ/pulse was losely focused on the sample to form a round spot of 300 μm (FWHM). The probe pulse was spatially overlapped with the pump on the sample and focused to 150 μm (FWHM) with 0.1 μJ pulse energy. These parameters were similar in both measurements with 290 nm and 800 nm. The solutions were kept in the 1 mm optical path cuvette during the measurements. The detection of the signal was performed with the photodiode and a boxcar integration system as described in Chapter 1. It was confirmed that the signals appear due to an induced absorption and bleach for the 800 nm and 290 nm probe wavlengths respectively. The collection of 8-10 traces was

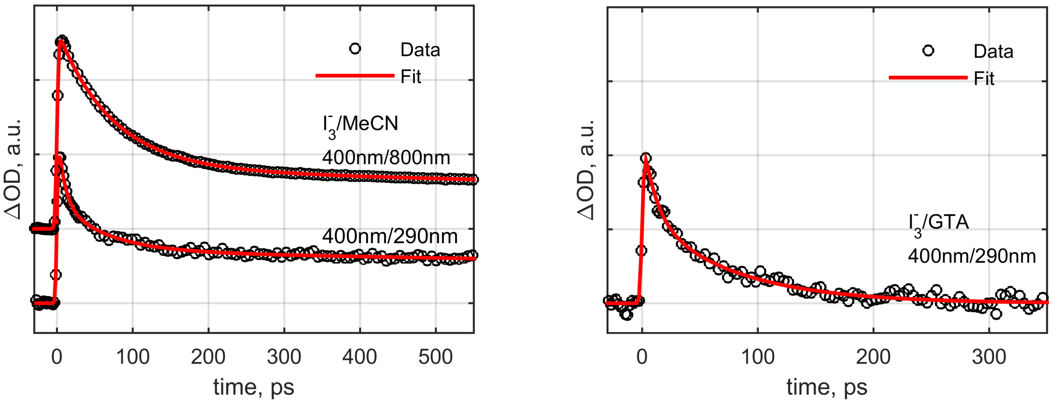

Figure 4.19. Transient absorption spectroscopy results for $I_3{}^-$/MeCN and $I_3{}^-$/GTA. The lifetimes of CIP btained from fits are summarized in Table 4.3.

sufficient for obtaining good statistics. Since triiodide efficiently recombines back to its ground state, no sample degradation was expected, which was confirmed by observation of no significant differences between individual scans. Due to ID09 beamline maintenance, the 800 nm probe measurement was not done for the $I_3{}^-$/GTA sample.

It is important to note that since triiodide is formed via equilibrium between ($I_2 + I^-$) and $I_3{}^-$, the samples used in the experiments contain all of these components. However, since I^- does not absorb at 400 nm (pump wavelength in all experiments) and the extinction coefficient of the I_2 at this wavelength is smaller than for $I_3{}^-$ by factor of 100 [32], the presence of these components will not perturb the analysis of the experiment.

A brief inspection of the results reveals the presence of a fast decaying excited state population for both probe wavelengths in $I_3{}^-$/MeCN (Figure 4.19). This signal is assigned to the induced absorption due to formation of CIP. At later time delays, the transient absorption signals approach a constant value which corresponds to the photofragments undergoing non-geminate recombination. The signal collected at 290 nm also contains a quickly decaying component appearing at early time delays and disappearing within 10-15 ps. By analogy to HgX_2 we attribute this signal to the quickly decaying absorption signal due to vibrational or rotational cooling of the photofragments. A similar dynamics is observed for $I_3{}^-$/GTA. Striking difference appears in comparison to $I_3{}^-$/MeCN at longer time delays around 300 ps, where the transient signal reaches the zero level. This supports the results of the previous spectroscopic works, indicating the absence of photofragments leaving the initial cage due to the high viscosity of the GTA solvent [105].

The kinetic parameters can be easily extracted by fitting the data with a simple mathematical expression:

$$f(t) = A_{\mathrm{VC}} \cdot exp(-t/\tau_{VC}) + A_{\mathrm{CIP}} \cdot exp(-t/\tau_{\mathrm{CIP}}) + A_{\mathrm{NGR}}, \tag{4.4}$$

where the first term represent the fast component from vibrational cooling; the second one corresponds to the decaying population of the CIP reaction product; the constant offset is related to the non-geminate recombination. After convolution with the instrument response function and a correction for time-zero, one obtains good quality fits for all the curves (Figure 4.19). The 800 nm probe data in I_3^-/MeCN is successfully reproduced with the described model without the first term in equation 4.4. The obtained parameters are as following. For I_3^-/MeCN the lifetime of the ionic contact pair are 72 ± 1 ps and 65 ± 10 ps for the 800 nm and 290 nm probe respectively. The yield of the ionic contact pair formation was calculated as $A_{\mathrm{CIP}}/(A_{\mathrm{CIP}} + A_{\mathrm{NGR}})$ and the corresponding values are 0.70 ± 0.05 and 0.5 ± 0.1 for the 800 nm and 290 nm probe respectively. In contrast, the I_3^-/GTA data shows no cage escape therefore giving the CIP yield of 1. The estimated lifetime of the CIP in GTA is 75 ± 10 ps. The obtained lifetimes agree with the previous spectroscopic works [105, 112].

In the case of I_3^-/MeCN, the yields derived from the two measurements appear to be different for the following reasons. As the extinction coefficients of I_2^- as a free photofragment and as a part of ionic contact pair at 800 nm are not equal (Figure 4.18), the yield value derived from the 800 nm probe measurement is expected to be a rather rough estimate of the CIP yield. On the other hand, I_2^- has another broad absorption band in the UV region centered at 375 nm [128], which can potentially contaminate the bleach signal at 290 nm. The exact absorption spectrum of the I_2^- is not known below 350 nm, so a precise estimate of the I_2 and CIP contribution is not possible. The situation might be even more complex since the I atom, which is one of the photoproducts, complexes with the solvent molecules giving a broad absorption band in the UV region, as discussed in respect to the recombination dynamics of HgX_2. Overall, the extracted lifetimes are the most reliable extracted parameters, whereas the yield values have to be considered with caution.

4.2.2 TR-WAXS results

In order to obtain direct information about the structure of the excited species, TR-WAXS measurements were carried out on both systems in two experiments. First, the dynamics of the systems were examined with 18 keV quasi-monochromatic beam [1] (BW = 1.9%, see Chapter 1 for details) by collecting 35 differential scattering patterns in the time range from -100 ps up to 1 ns for both systems. Second, the high energy quasi-monochromatic (BW = 1.55%) beam with the central energy of 25.2 keV was employed to extend the Q-range for a more precise determination of the ground and excited state structures only for I_3^-/MeCN. The latter data was collected at 400 ps time delay after laser excitation. In both experiments the sample to detector distance was 42 mm. The sample was prepared by dissolving potassium iodide (KI) and iodine (I_2) up to 10 mM concentrations. The pump pulses had a wavelength of 400 nm and energy of 70 μJ/pulse with a focus diameter of 150 μm (Fluence of 0.27 J/cm^2). We will begin the analysis by inspecting the 18 keV data and then discuss the photochemistry of I_3^- in both solvents.

The raw TR-WAXS signal collected at 18 keV for I_3^-/MeCN undoubtedly indicates the presence of ultrafast dynamics at early time delays for both systems (Figure 4.20 a, c). For I_3^-/MeCN the integrated signal from the positive feature at $\sim$4 Å^{-1} peaks around 50 ps and decays afterward towards a constant level after 500-600 ps. For the I_3^-/GTA sample, the shape of the signal changes drastically between time zero and 200 ps, which follows the expected dynamics from the optical spectroscopy. If one assumes that at later time delays the signal is dominated by solvent heating, this qualitative observation confirms the formation of the CIP in GTA.

Before discussing the formation of the CIP, we will briefly check the consistency of our results with the literature. We will consider the later time delays ($\Delta t = 400$ ps) and reveal the main reaction pathway for I_3^-/MeCN.

Reaction pathway at longer time delays

Gas phase dissociation experiments suggest that upon excitation I_3^- can form different reaction products depending on the photon energy: (1) $I_3^- + h\nu \rightarrow I_2^- + I$; (2) $I_3^- + h\nu \rightarrow I_2 + I^-$; (3) $I_3^- + h\nu \rightarrow I + I + I^-$ [129,130]. Recent liquid phase TR-WAXS study of the photodissociation reaction of I_3^- in MeOH have shown that upon 400 nm excitation I_3^-

---

[1] Obtained with the use of multilayer (ML) monochromator discussed in chapter 2.

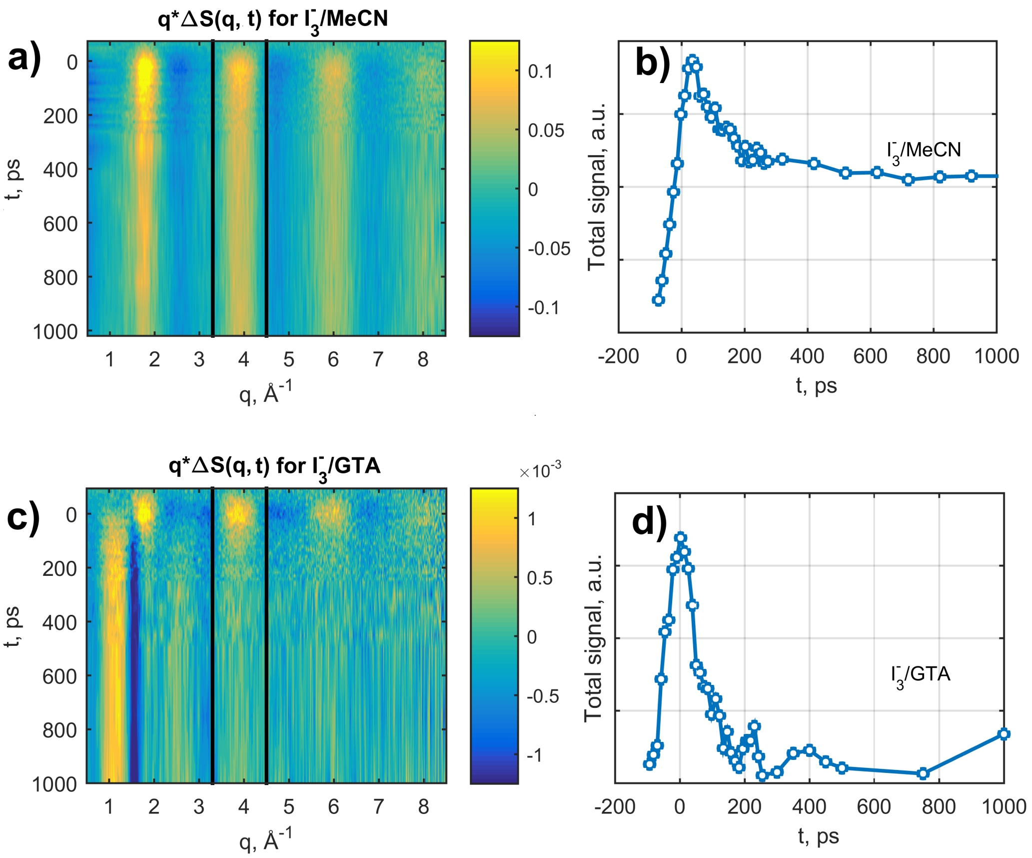

Figure 4.20. Raw TR-WAXS data for I_3^- collected with 18 kev ML beam (BW = 1.9 %). a) Raw TR-WAXS signal for I_3^-/MeCN; b) Sum of the signal in the selected region; c),d) the same for I_3^-/GTA.

undergoes only the first channel [123]. Figure 4.21 shows the comparison of the different models to the data collected at 18 keV at 400 ps for I_3^-/MeCN. The theoretical signals were calculated according to the published structures; the model includes solvent and solute contributions.

It is evident from Figure 4.21 that two body dissociation, described by the first channel, describes the data the best. The possibility of simultaneous dissociation by two- and three-body channels have also been checked; no significant improvement in the corresponding χ^2 values was observed (not shown). Therefore, the photochemistry of the triiodide ion in MeCN is similar to that in MeOH. The corresponding experimental signal is also easily interpreted in R-space. The first dip at ~3 Å corresponds to a depletion of the I-I bond between closest atoms in the parent I_3^- molecule, whereas the second dip at ~6 Å represents the disappearance of the correlation between side I atoms in the parent molecule. Figure 4.22 shows the decomposition of the fitted channel $I_3^- + h\nu \rightarrow [I_2^-]+[I]$ to the

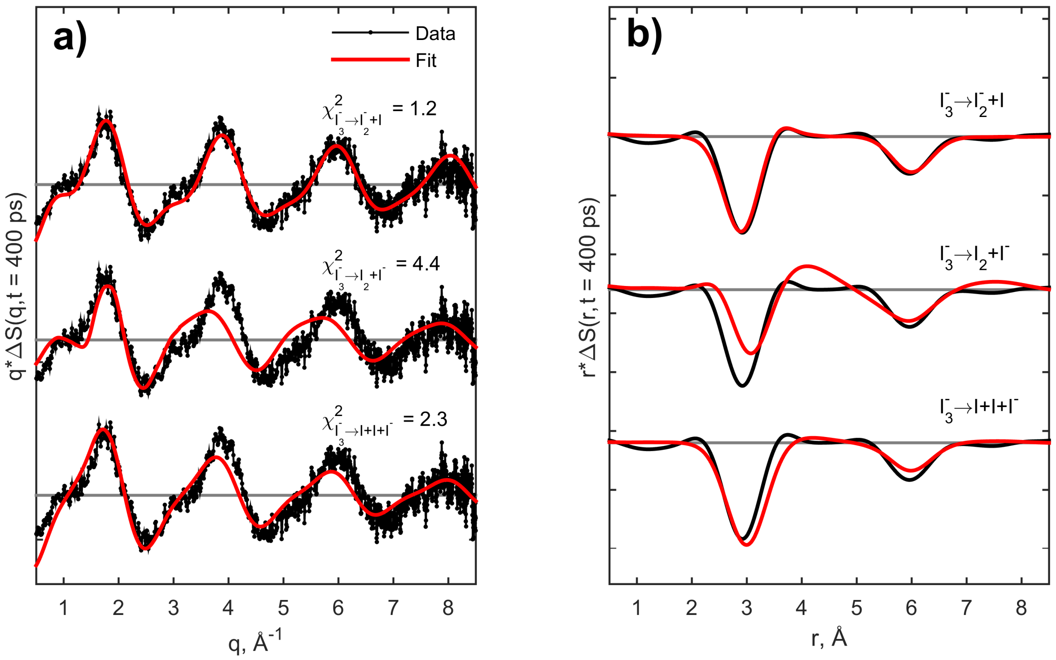

Figure 4.21. Comparisons of the different models with the experimental signal for I_3^-/MeCN collected at 400 ps after laser excitation. a) and b) panels show comparisons in Q- and R-space respectively. The data was collected with 18 keV ML beam (BW = 1.9 %).

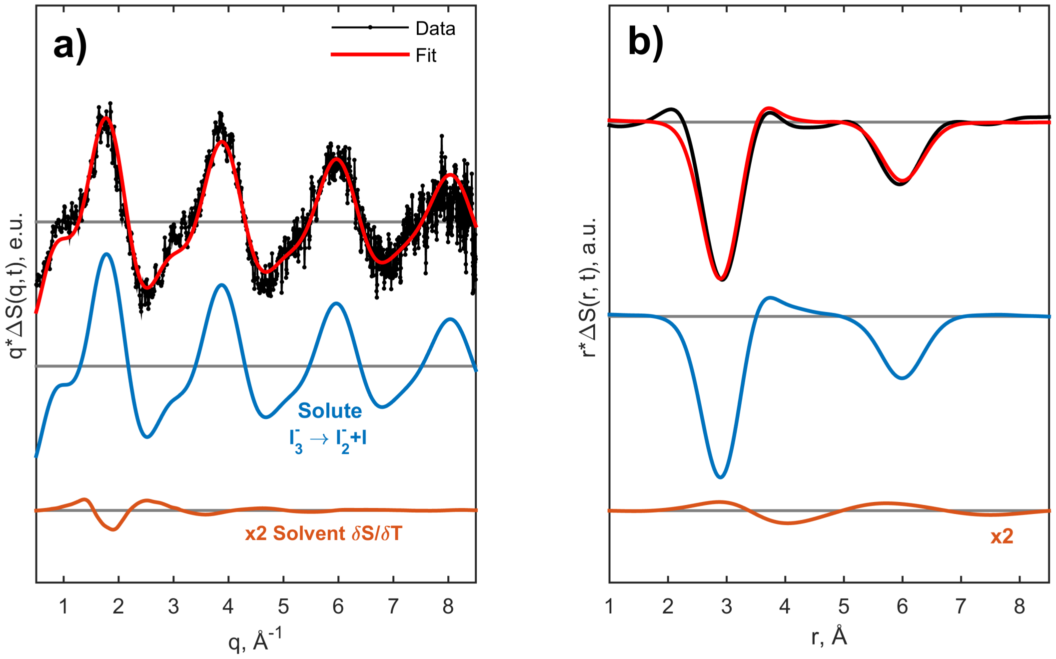

Figure 4.22. Decomposition of the fitted model for I_3^-/MeCN at 400 ps to the components in Q- (a) and R-space (b).

components. Similarly to HgX_2, the signal is dominated by the solute contribution due to high atomic numbers of I atoms (Z = 53).

After confirmation of the data consistancy with the literature we will move to the analysis of the CIP formation. Since the structural model of the CIP is not available, we will now extract the corresponding CIP signal in MeCN and compare it to the structural model for the free photofragments. As discussed above for I_3^-/GTA the extraction is not necessary; this system will be considered in parallel.

Structural signal and population dynamics of the contact ion pair

In order to extract the CIP signal from the I_3^-/MeCN data, we will follow the similar approach used for the extraction of the vibrational cooling signal for I_2/CCl_4 in the recent work [25]. In that paper, the authors extracted the signal from the instantaneous data in R-space corrected for the instrument resolution function with a deconvolution approach. Here, for simplicity of the analysis, the procedure will be performed on the raw data in Q-space without temporal deconvolution. In order to achieve the goal we have to estimate time zero and exact parameters of the instrument resolution function (IRF). After that we can simply take the average signal between 400 ps and 1 ns and, assuming it has constant level, subtract it from the whole data set. The following explains each step in detail.

For the determination of time zero we take the sum of the absolute values of the signal around ~4 Å^{-1} (± 0.5 Å^{-1}) and fit it with the a sum of an exponential decay and a constant convoluted with the IRF and corrected for time zero. The first term qualitatively corresponds to CIP formation, whereas the second reflects the fraction of the photofragments undergoing non-geminate recombination. The width of the IRF and time zero enter into the fit as parameters. The fit and the data points are in good agreement (Figure 4.23). The obtained values for the duration of the x-ray pulse (width of IRF) and time zero are 90 ± 10 ps and 8 ± 4 ps respectively. The first value is in good agreement with the expected IRF for the 16-bunch mode, in which the experiment was performed, whereas the second one indicates good calibration of time zero.

From Figure 4.23 it is evident that at time delays longer than 500 ps, the (integrated) signal can be approximated by the constant level. Therefore, for subtraction of the NGR contribution we average curves collected at long time delays ($\Delta t \geq 400$ ps) and than calculate the NGR contribution at each measured time point (Figure 4.24, NGR contribution contour plot). After subtraction of this component one obtains an experimental signal

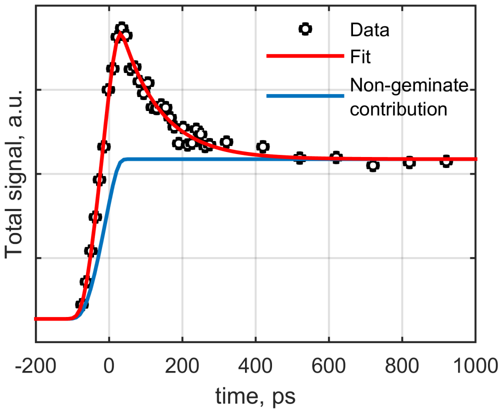

Figure 4.23. Illustration of the NGR subtraction from the total signal for I_3^-/MeCN.

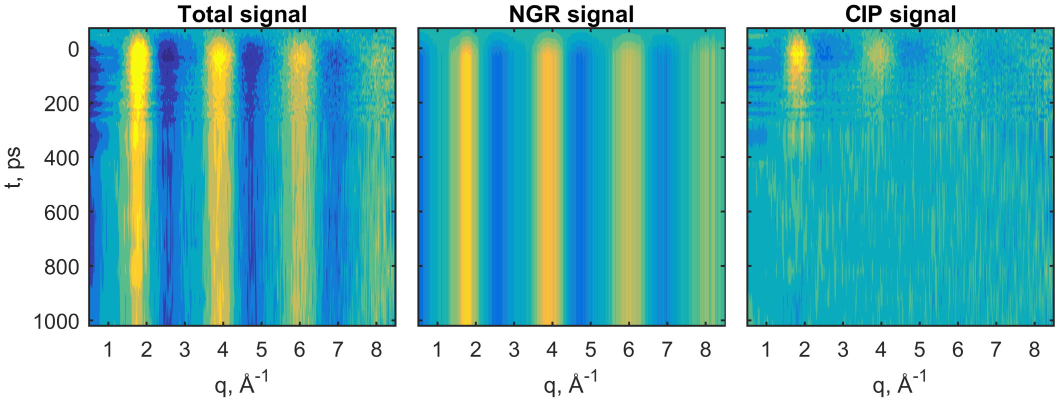

Figure 4.24. Decomposition of the total signal into NGR and CIP components for I_3^-/MeCN.

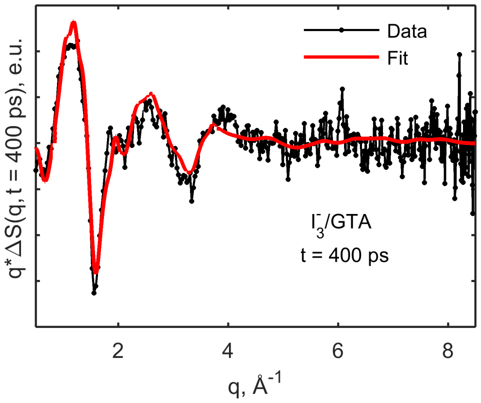

Figure 4.25. Comparison of the TR-WAXS signal for I_3^-/GTA collected at 400 ps with the heating signal for GTA collected independently.

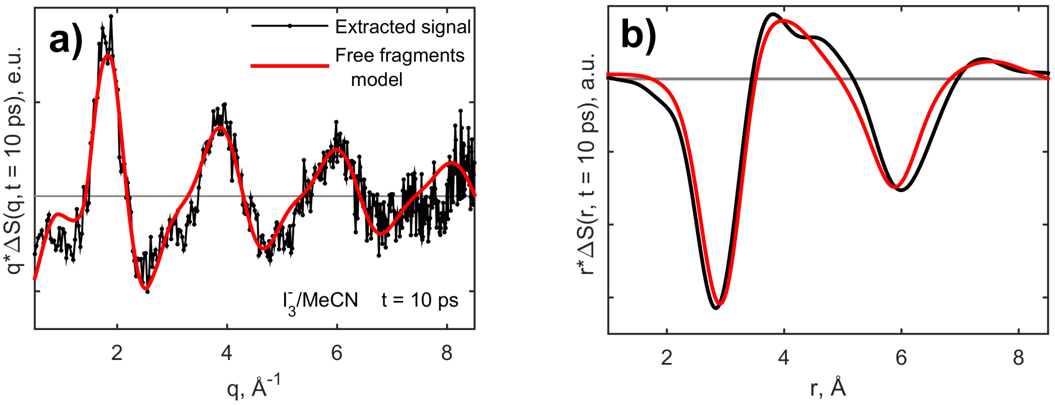

Figure 4.26. Comparison of the free photofragment model with the extracted CIP signal for I_3^-/MeCN at 10 ps in Q- (a) and R-space (b).

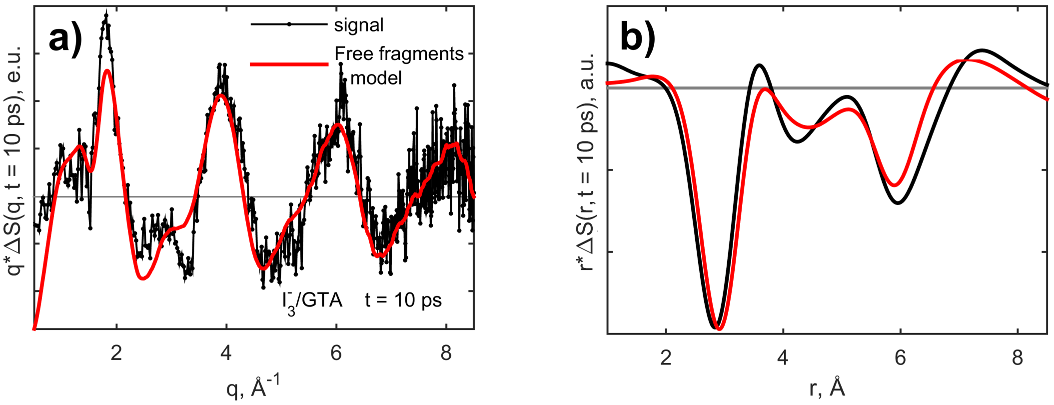

Figure 4.27. Comparison of the free photofragment model with the experimental signal for I_3^-/GTA at 10 ps time delay in Q- (a) and R-space (b).

which includes the contribution from the CIP and solvent contribution due to the temperature rise. From the CIP signal contour plot (Figure 4.24) it is clear that later time delays do not contain any signal, which indicates the success of the subtraction procedure. Note, that in this case the extracted signal contains a solvent contribution from a *negative* change in the temperature. Since the temperature is an additive value on short time scales and we subtract the NGR signal contribution obtained from the later time delays, the contribution from the solvent in the extracted signal is negative.

For I_3^-/GTA, the extraction of the CIP signal is not necessary, since the only observed recombination channel in this solvent is the formation of CIP. This is also confirmed by a direct comparison of the independently measured heat response of GTA and the experimental signal for I_3^-/GTA at 400 ps (Figure 4.25). Good agreement between the curves indicates the absence of the free photofragments which have left the parent cage.

The extracted signal for CIP in MeCN and the experimental data for CIP in GTA appear to be slightly different (Figures 4.26 and 4.27), which can be partially due to the different shape of the heat responses for the two solvents. Additionally, those differences can come from the different structures of CIP in the different solvents. By comparison of the data to the free photofragment model we observe a drastic structural differences between the two different reaction channels previously observed only spectroscopically (Figures 4.26 and 4.27). At the moment we do not have any structural description for the CIP reaction product. Some attempts have been made for predicting the CIP structure based on Reverse Monte Carlo methods. The efforts did not lead to reasonable results due to the absence of a good model for the cage term, which is why we do not report them here. Since the formation of CIP involves strong interactions with the solvent, the structural changes in the cage are also significant. For revealing the structure of such a system one needs to perform Molecular Dynamics simulations which will give a good prediction for the cage term. Therefore we will not speculate about possible structures and leave the simulations for future work.

Finally, based on the CIP signals in MeCN and GTA, the lifetimes can be obtained without the structural model in the following way. At any time point the experimental signal is a sum of CIP and heating contributions scaled by excited state fraction α and temperature rise ΔT: $\Delta S_{exp}(t) = \alpha(t) \cdot \Delta S_{CIP} + \Delta T(t) \cdot \delta S/\delta T$. Although we do not have model for ΔS_{CIP}, we can use the experimental signal itself for extracting the population dynamics. By doing so, we can represent data as a sum of scaled experimental signal measured at a certain time point t_0 and a heating signal: $\Delta S_{exp}(t) = a(t) \cdot \Delta S_{exp}(t_0) + b(t) \cdot \delta S/\delta T = a(t) \cdot [\alpha(t_0) \cdot \Delta S_{CIP} + \Delta T(t_0) \cdot \delta S/\delta T] + b(t) \cdot \delta S/\delta T$. The coefficients $a(t)$ and $b(t)$ do not provide direct information about absolute values of the CIP concentration and temperature values; however, the time evolution of the $a(t)$ follows the population dynamics of CIP. The lifetime can be then easily determined from single exponential fit of $a(t)$. Obviously, the $\Delta S_{exp}(t_0)$ can be defined as not only the experimental curve at a single time point, but an average from the range of time points (for improved statistics) given that the signal contains only one excited state specie. Therefore we average the experimental curves at early time delays (-50 ps $\leq t \leq$ 50 ps) for the extracted signal for I_3^-/MeCN and experimental signal for I_3^-/GTA. Then, these curves together with corresponding heating responses are used for fitting the each individual curve of the I_3^-/MeCN and I_3^-/GTA

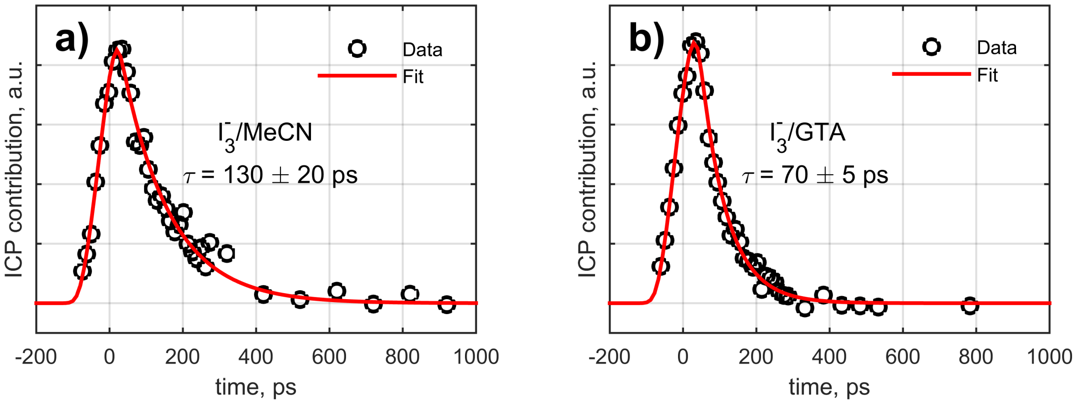

Figure 4.28. Extracted time dependent contributions from the CIP formation and corresponding fits for I_3^-/MeCN (a) and I_3^-/GTA (b).

data. Obtained amplitudes of the CIP contribution and corresponding exponential fits are shown in Figure 4.28. The agreement between the exponential decay model and the data is good and the obtained values of the lifetimes are as follows: $\tau_{\mathrm{CIP}} = 130 \pm 20$ ps and $\tau_{\mathrm{CIP}} = 70 \pm 5$ ps for MeCN and GTA respectively. The corresponding lifetimes are listed in Table 4.3.

The parameters from TR-WAXS for the CIP in MeCN are significantly longer than the ones obtained from optical spectroscopy. This might reflect some imperfections in the extraction procedure, for example, in the assumption about the constant NGR contribution in the investigated time range. In order to achieve a reliable estimate of the lifetime one needs to fit the raw data properly. In contrast, the CIP lifetime in GTA from TR-WAXS is in good agreement with the optical measurements. Here we have analyzed the raw data which is probably why the agreement is better. Again, this allows us to benchmark the reliability of the TR-WAXS measurements in the time-slicing scheme.

Now we will move towards structural analysis of another reaction channel, i.e. the formation of the free ions $[I_2^-]$+[I]. In the next section we will determine the structure of

Table 4.3. Lifetimes of ionic contact pair $[I_2^- + I]$ in MeCN and glycerol triacetate (GTA) obtained from different measurements.

Solvent	TR-WAXS	TA (800 nm)	TA (290 nm)
MeCN	130 ± 20 ps	72 ± 1 ps	65 ± 10 ps
GTA	70 ± 5 ps	–	75 ± 10 ps

ground state I_3^- and the photofragment I_2^-. The structures will be studied at later time delays for I_3^-/MeCN where the CIP contribution is negligible.

Structures of the I_3^- and I_2^- ions

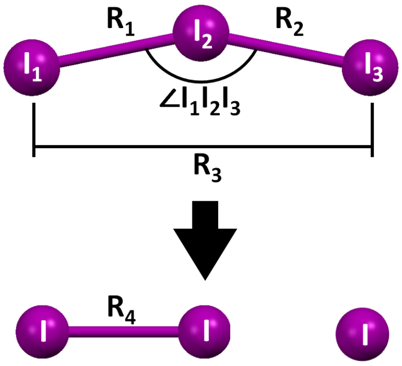

Figure 4.29. Structural model for I_3^- and I_2^-

Since the I_3^- molecule and its photodissociation products are structurally similar to that of HgX_2, the model for the structural optimization is also similar. Again, we use three parameters to describe the ground state structure: R_1 and R_2 for the bond lengths between closest I atoms ($I_1 \cdot\cdot I_2$ and $I_2 \cdot\cdot I_3$) and the angle $\angle I_1 I_2 I_3$ (Figure 4.29); the corresponding distance between $I_1 \cdot\cdot I_3$ (R_3) is derived from the other parameters. The final structural parameter describes the distance between I atoms (R_4) in the I_2^- photoproduct. In addition to that we have to include the scaling parameter for the model curve, i.e. the excited state fraction γ as well as the solvent contribution scaled by the temperature rise ΔT. The model containing these six parameters is fitted to the data collected at 400 ps after laser excitation with the 25.2 keV x-ray probe.

After fitting the data we arrive at the following values of the structural parameters. The distances R_1 and R_2 converge towards the same value 3.004 ± 0.006 Å; the triiodide ion appears to be bent with the angle $\angle I_1 I_2 I_3 = 157 \pm 2°$. As done previously with HgX_2, we investigated the significance of the bending by imposing a linearity constraint to the fit (Figure 4.30, a). In this case the corresponding χ^2 value increases significantly indicating the significance of bending. From the qualitative point of view the bent geometry gives a better fit of the shoulder-like feature at ~3 Å^{-1} and the dip at ~5 Å^{-1}. The calculated differential radial distribution functions also confirm that experimentally determined dip corresponding to the $I_1 \cdot\cdot I_3$ depletion is located at smaller distance than the one obtained from the linear model optimization (Figure 4.30, b). Finally, the obtained bond length of the I_2^- photofragment is $R_4 = 3.21 \pm 0.02$ Å. The obtained values except for the angle are in good agreement with the values published in the recent paper [32]. The parameters are summarized in the Table 4.4.

Similarly to HgX_2, the triiodide ion appears to be bent. Here, however, we used the

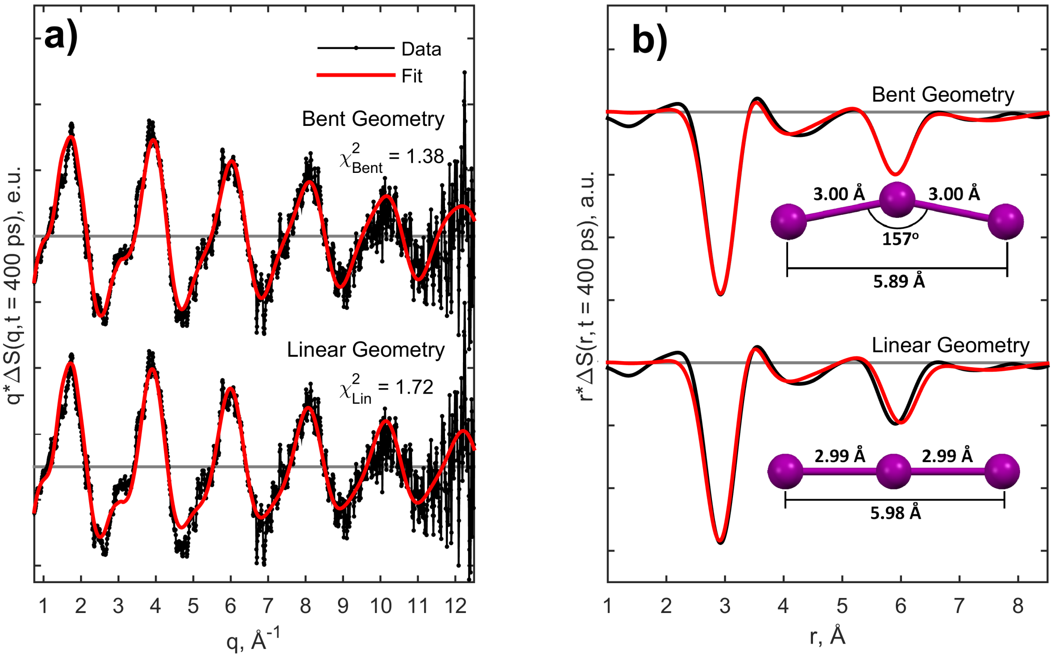

Figure 4.30. Comparison of the fit quality for bent and linear geometries of I_3^- solvated in MeCN. The a) and b) panels represent the comparisons in Q- and R-space respectively.

quasi-monochromatic x-ray beam rather than of the pink beam employed for HgX_2 studies, so we cannot attribute the bending to a systematic error in the experiment due to the poor definition of the pink spectrum. Moreover, our results contradict TR-WAXS work by Kim *et. al.* [32]. There, the authors also used a quasi-monochromatic beam, but with wider bandwidth (5 % versus 1.55 % in our case) and slightly lower x-ray energy (17.5 keV). The inconsistency requires further investigation. One of the first steps for understanding of the bending would be inclusion of the Bastiansen-Morino shrinkage effect, which was discussed for HgX_2. Another factor which has to be taken into account is the cage term contribution, which was neglected for both I_3^- and HgX_2. The inclusion of the latter is not expected to change the results drastically since the contribution only affects the low Q part of the signal, i.e. a small portion of the available data.

A striking result of the analysis is that the precision of the structural determination reaches the mÅ level. As shown below, this is due to the use of the quasi-monochromatic beam obtained with the multilayer monochromator and the extension of the available Q-range. Additionally, the precision reaches this level thanks to the high atomic numbers of I constituting the system (Z=53). This leads to the solute contribution to the measured signal to be the most significant, making the model sensitive to subtle structural features.

Precision analysis

As a final remark in this work it is important to consider a rather technical aspect of TR-WAXS experiments. Here we would like to quantify the precision of the structural optimization of I_3^-/MeCN performed on the data sets collected with different x-ray probes. Two effects are addressed. First, the effect of the extension of the available Q-range by using a higher x-ray energy. Second, we discuss the precision of the analysis based on the data sets collected with the polychromatic U17 spectrum and the quasi-monochromatic spectra produced with the (in-focus) multilayer monochromator. For a systematic study of the effects we used the two data sets described previously: photodissociation of I_3^-/MeCN measured with quasi-monochromatic 18 and 25.2 keV x-ray energies. In addition, two more data sets were measured with the same experimental conditions in regards to the concentration and laser beam properties (energy per pulse and laser spot size). One of the curves was measured with the 18 keV pink beam from the U17 undulator with a sample-to-detector distance of 42 mm, which mimics the standard conditions of TR-WAXS experiment on ID09. The second one was measured with a 15 keV quasi-monochromatic beam at a sample-to-detector distance of 100 mm in order to obtain a limited Q-range (Figure 4.31, a,d). Each of the curves were measured until sufficient statistics was obtained. Note that the noise in the curves has a different functional dependence of Q (see Chapter 2 for a discussion of noise sources). Therefore, for fair comparison, the number of the repeats of the measurement was chosen such that the standard error of the measurement is roughly the same as a function of the pixel number for each of the curves (Figure 4.31, c). In all cases the data was collected at 400 ps, so the contribution from the CIP is negligible. All the curves are fitted with the bent molecule geometry model discussed above (Figure 4.31, a,b) and the structural parameters with the uncertainties are calculated according to the procedure described in chapter 3. The experimental parameters, optimized values and corresponding uncertainties are summarized in Table 4.4.

The results from all the measurements agree with each other within the estimated uncertainties, which additionally confirms the results of the structural optimization. By looking at the errors, one observes a systematic improvement of the structural precision from extending the available Q-range. By nearly doubling of Q_{max} from 4.5 Å^{-1} up to 8.5 Å^{-1} one gains a 40 % increase in the precision of the bond distances and about 25 % for the angles. The extension of Q_{max} by an additional ~50 %, from 8.5 Å^{-1} up to 12.5 Å^{-1}, gives about 25-30 % gain in precision. The data collected with the pink beam (18 keV,

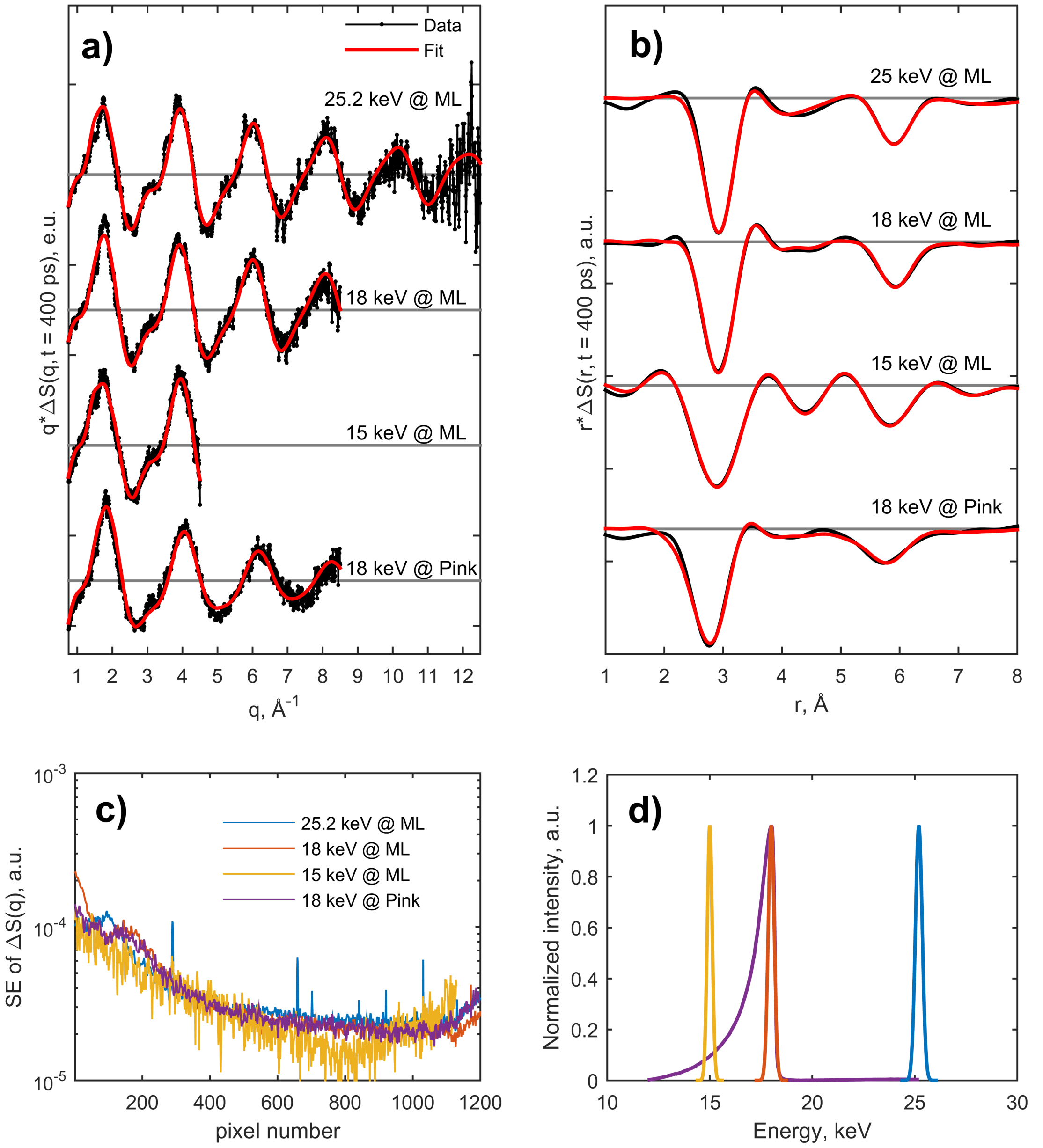

Figure 4.31. TR-WAXS precision analysis. a) Fits of different data sets with the bent geometry model in Q-space; b) the same as a), but in R-space; c) the standard error of $\Delta S(q)$ in the performed measurements as a function of pixel number; d) different spectra used for the study.

pink) appears to give uncertainties 25-30 % higher by comparison to the multilayer data (18 keV, ML). This agrees with previous work [37].

The trend of increasing the precision of the structural parameters by extending the Q-range can be explained in the following way. From chapter 2 we know that a successful

Table 4.4. Results of the structural optimization on different TR-WAXS data sets for I_3^-/MeCN.

Measurement	δE (%)[a]	D_x (mm)[b]	Q_{min} (Å^{-1})	Q_{max} (Å^{-1})	R_1 (Å)	R_2 (Å)	R_3 (Å)	$\angle I_1 I_2 I_3$ (°)	R_4 (Å)
Kim *et.al.* [32] 17.5 keV, ML[c]	5	40	1.0	8	3.01 ± 0.04	2.98 ± 0.04	5.99	180	3.24 ± 0.06
25.2 keV, ML[c]	1.55	42	0.75	12.5	3.004 ± 0.006[d]	3.004 ± 0.006	5.89 ± 0.02	157 ± 2	3.21 ± 0.02
18 keV, ML[c]	1.9	42	0.75	8.5	2.999 ± 0.008	2.999 ± 0.008	5.91 ± 0.03	160 ± 3	3.23 ± 0.03
15 keV, ML[c]	1.9	100	0.75	4.5	3.000 ± 0.016	3.000 ± 0.016	5.85 ± 0.04	154 ± 4	3.23 ± 0.06
18 keV, pink	3	42	0.75	8.5	3.000 ± 0.011	3.000 ± 0.011	5.93 ± 0.04	163 ± 5	3.21 ± 0.04

[a] Bandwidth of the x-ray spectrum;

[b] Distance between sample and detector;

[c] Data obtained with the multilayer (ML) optics;

[d] The values are not rounded for facilitating the comparisons.

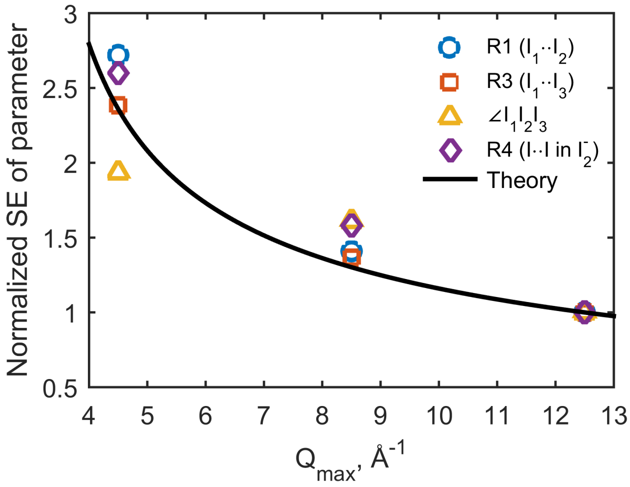

Figure 4.32. Uncertainties of different parameters derived from the structural optimization as functions of Q_{max}. The theoretical curve was calculated based on the equation 4.5.

fit gives a χ^2 value proportional to the number of degrees of freedom: $\chi^2 \sim (N_{\text{ind}} - p - 1)$. Here, N_{ind} is the number of independent points defined as $N_{\text{ind}} = \frac{2}{\pi}\Delta Q \Delta R$, where ΔQ and ΔR are the fitting ranges in Q- and R-space, and p is number of parameters. The variances of the parameters then can be estimated from the diagonal elements of the inverse Hessian matrix of χ^2. Hence, the errors are proportional to the inverse square root of $(N_{\text{ind}} - p - 1)$. This can be written as:

$$\sigma \sim \frac{1}{\sqrt{\frac{2}{\pi}(Q_{\text{max}} - Q_{\text{min}})(R_{\text{max}} - R_{\text{min}}) - p - 1}}, \tag{4.5}$$

where Q_{max}, Q_{min}, R_{max} and R_{min} are the fitting range limits in Q- and R-space. We can use this expression to check the consistency of the obtained results with an expected trend as a function of Q_{max}. Since the expression only gives the relative trend, we will use the uncertainties derived from the 25.2 keV data for normalization. The input values for eq. 4.5 were as follows: p = 6; R-range for fitting was spanning from 2 Åto 7.5 Å; $Q_{\text{min}} = 0.75$ Å^{-1} and Q_{max} was used as a variable.

The comparison of the calculated trend and the experimental result shows reasonable agreement (Figure 4.32). The result indicates that by using an x-ray beam with a well-defined energy spectrum, the structural precision is governed by the width of the available Q-range. Therefore, an experimentalist can use similar calculations for chosing appropriate experimental conditions for solving particular tasks, depending on the required precision.

4.2.3 Summary

In this section we have studied the recombination dynamics of the I_3^- ion in acetonitrile and glycerol triacetate solutions after laser excitation at 400 nm by transient absorption and TR-WAXS. It was proven that at longer time delays the photochemical behavior of I_3^- in MeCN is similar to MeOH. In contrast the early time delays show the presence of a short-lived excited species in the optical and x-ray experiments in both solvents. The shape of the TR-WAXS signals for these species was found to be significantly different from the signals corresponding to the free photofragment model ($[I_2^-] + [I]$), confirming the presence of an additional reaction channel tentatively assigned as a CIP ($[I_2^- + I]$) in previous studies. Although the structural characterization of this reaction product was not possible due to the absence of a structural model, the lifetimes of the CIP from all the measurements were found to be in good agreement. The only exception was the TR-WAXS value of the CIP lifetime in MeCN, which was attributed to the uncertainty of the extraction procedure of the CIP signal. The structures of the I_3^- ion's ground state and the free photofragment I_2^- ion were determined with the structural optimization procedure. Overall, structures were found to be in a good agreement with the published ones; however, by analogy to HgX_2, the bending angle of the ground state geometry was found to be significantly different from 180°. The Bastiansen-Morino shrinkage effect was proposed as a possible explanation for the bending effect. Further theoretical investigations are necessary to verify this effect. Finally, the effect of the probe energy spectrum on the precision of the structural analysis was addressed. The extension of the Q-range for the fitting procedure as well as the employment of a well defined Gaussian x-ray spectrum were shown to improve the structural resolution in TR-WAXS experiments.

Chapter 5

Electron transfer reactions

Electron transfer (ET) reactions play a key role in the functioning of many chemical and biological systems due to the ability to create charge separated states and control oxidation/reduction of catalytic centers. Interest in mechanisms standing behind the operation of solar cells, photosynthesis and molecular electronics makes the understanding of ET increasingly important from both technological and fundamental points of view. Some of the most interesting topics in ET research includes transition metal complexes and the associated metal-to-ligand charge transfer (MLCT) processes in them. In this chapter we are focused on two systems which employ MLCT transitions in for different purposes. The first one is an iron based complex which belongs to family of promising new systems for light harvesting applications. The second one is a bimetallic ruthenium-cobalt complex which serves as a model system for studying the ET process over large distances. Before examination of the systems and our experimental findings we will briefly introduce the theoretical background which is necessary for the discussion.

The electronic structure of a generic Fe(II) (or Co(III)) complex in octahedral environment can be described in the following way. Upon formation of the complex, six atoms (nitrogens or carbons) belonging to the ligands donate 12 electrons to the metal center and form so-called coordination bonds. The donation process appears due to mixing of the ligand orbitals with σ-symmetry and metal orbitals of appropriate symmetry. In an octahedral environment the latter includes the 4s (T_{1u} symmetry), 4p (A_{1g} symmetry) and $3d$ orbitals with E_g symmetry, i.e. $3d_{x^2-y^2}$ and $3d_{z^2}$ (Figure 5.1). In some complexes three other $3d$ orbitals (d_{xy}, d_{xz} and d_{yz}; T_{2g} symmetry) also participate (weakly) in the bonding via π-interactions with the ligand orbitals which is known as π-back-donation. The coor-

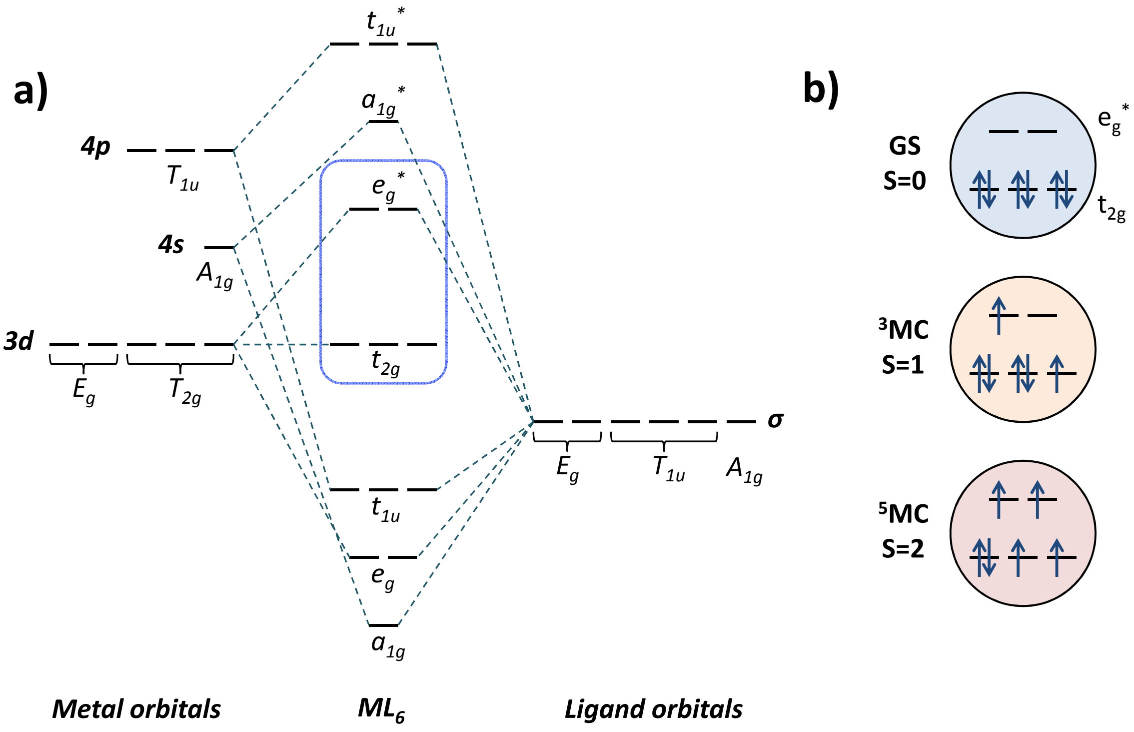

Figure 5.1. Electronic structure of a generic Fe(II) (or Co(III)) octahedral complex. a) Molecular orbitals involved in formation of the complex (adapted from [131]). Upon complex formation, only orbitals with appropriate symmetry and similar energy levels mix to form the coordination bonds. The π-interactions were omitted in the diagram for simplicity. b) Different occupation of the metal $3d$ orbitals results in different MC states: singlet (S=0 or low spin, LS), triplet (S=1) and quintet (S=2 or high spin, HS).

dination of the metal leads to splitting of the $3d$ orbitals: the antibonding e_g^* ($3d_{x^2-y^2}$ and $3d_{z^2}$) orbitals appear to be higher in energy than the t_{2g} orbitals by energy Δ. The splitting Δ between those orbitals is a parameter which controls the overall spin of the metal center in the ground state (GS). If Δ is smaller than the electron pairing energy, then the $3d$ electrons are distributed among the e_g^* and t_{2g} orbitals and the complex is in high spin state S=2 (HS, quintet); otherwise the electrons are placed in pairs on the t_{2g} orbitals and the complex is in the low spin state S=0 (LS, singlet) (Figure 5.1, b). The state with S=1 (triplet) can sometimes be involved in the deactivation of MLCT states (see next section) so it is also shown in Figure 5.1, b. In the present work we deal with strong ligand field complexes, for which the ground state is low spin. The dynamics of the systems considered in the chapter mostly concern the changes in occupation of the different $3d$ orbitals. In the following sections we will refer to the mentioned states as metal centered (MC) states.

This chapter is organized as follows. For the Fe-based chromophore, we study the structural dynamics of a MC state formed shortly after excitation to the MLCT. We determine the spin and the structure of the complex based on the TR-WAXS data. The population dynamics of the system is also addressed. In the second section we study a hetero-nuclear dyad consisting of a ruthenium based donor and a cobalt acceptor moiety, where the MLCT transition on the Ru site leads to ET to the Co, changing the oxidation and spin states of both metal centers. The structural and electronic dynamics of the system are tracked with both TR-WAXS and TR-XES giving complementary insights into the different aspects of the ET process. The excited state structure of the complex will be discussed in detail.

5.1 Structure and dynamics of quintet state in photoexcited Fe N-heterocyclic carbene complex

Metal polypyridine complexes have received wide attention due to a variety of practically attractive photophysical and photochemical properties. Particularly, Ru-based complexes have been shown to be efficient in light-harvesting applications due to the long lived MLCT states [132, 133]. Due to the high costs and potential environmental risk of ruthenium, it is highly desirable to develop Fe-based synthesizers with similar properties. Until recently this goal was impossible since most complexes of Fe have low lying MC states which efficiently deactivate the MLCT manifolds within less than 100 fs [134–136]. Lately, several strategies for the destabilization of MC states have been published. In polyimine complexes $[\mathrm{FeN_6}]^{2+}$, specific design of ligands allows the synthesis of push-pull Fe(II) compounds with nearly octahedral structure and degenerate triplet ^{3}MC and quintet ^{5}MC states [137–139]. Another approach relies on the employment of N-heterocyclic carbenes (NHC) as strongly σ-donating ligands, leading to destabilization of the MC states. For iron compounds this strategy leads to an increase of the MLCT lifetime by two orders of magnitude, to 9 ps and 16 ps in bis(tridentate) [140,141] and 13 ps in tris(bidentate) complexes [142]. Further computational studies also suggest that the substitution of nitrogen by carbon in the first coordination shell of the polyimine complexes can completely destabilize the MC states relatively to the MLCT [143].

The long MLCT lifetime is one of the steps on the route to successful design of Fe-based sensitized solar cells (DSCs) [144]. One of the key parameters controlling the performance of the dye sensitized solar cells (DSCs) is the electron injection efficiency from the dye molecule to the semiconductor conduction band [132, 145–147]. The injection efficiency is controlled by competition between the process of injection to semiconductor and relaxation of the dye to the ground state. In case of iron sensitizers the two processes have similar time scales ($\lesssim$100 fs) [148, 149] which obscures the injection process of electrons to the semiconductor conduction band. This explains the motivation of increasing the MLCT lifetime. In the present study we will examine the structure and dynamics of an iron based compound belonging to a recently introduced family of systems employing NHC ligands. Although the studied system cannot be used in real applications, establishing the link between its structure and photochemical behavior will improve the understanding of the compound family allowing the design of new and more efficient light harvesters in the

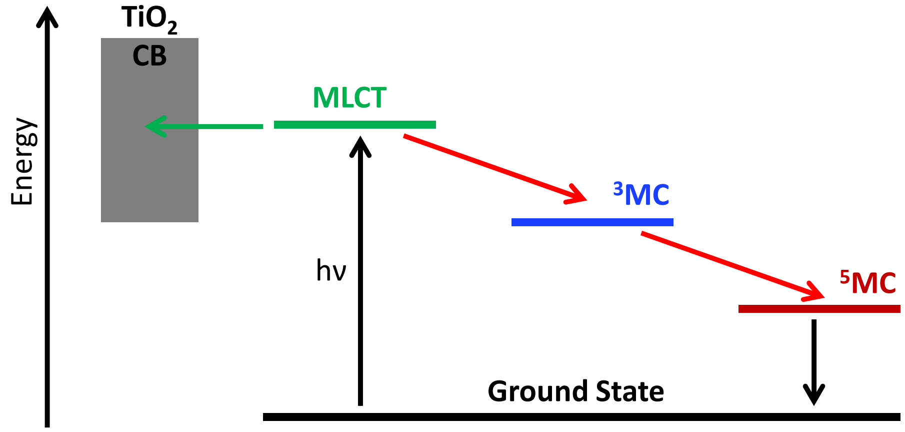

Figure 5.2. Possible channels of the MLCT state deactivation. One of the factors influencing the performance of Fe-based DSCs is the competition between the electron injection (green arrow) to semiconductor conduction band and MLCT relaxation through MC states (red arrows); adapted from [144].

future.

In this section we will characterize of the photochemical behavior of the iron N-heterocyclic carbene (NHC) complex, bis(2,6-bis(3-tert-butylimidazol-1-ylidene)pyridine) iron, denoted $[Fe(NHC)_2]^{2+}$. The system was previously characterized with TOAS and x-ray diffraction [140]. The known properties of the compound can be summarized as follows. The optical absorption spectrum of the complex in MeCN shows the presence of two MLCT bands corresponding to transitions from Fe to the carbenes and pyridine ring [141] (Figure 5.3, a). The band in the UV region (<350 nm) is due the strong ligand-centered $\pi - \pi^*$ absorption. The ground state (GS) atomic structure of the complex is characterized by a distorted octahedral configuration with two ligands perpendicular to each other (Figure 5.4). The distortion is manifested in compression of the axial bonds Fe-N_{ax} (1.935 Å) in comparison to the equatorial Fe-C_{eq} bonds (2.099 Å) in the first coordination shell (FCS) of the Fe center (Figure 5.5), which is due to a preferential π-back-donation from the d_{xz} and d_{yz} orbitals of the Fe center to the π^* orbitals of the pyridine rings[1]. The Jablonski diagram representing the photochemical behavior inferred from TOAS is shown in Figure 5.3, c. Excitation of the complex to the MLCT band leads to the formation of the short lived MLCT state which quickly decays (~300 fs) to the hot MC state. Vibrational cooling of the state takes 31 ps; the nature of the state was tentatively assigned to ^{5}MC. The relatively short lifetime of the ^{5}MC state (230 ps) indicates a moderate ligand field

---

[1] The distortions of the structure will be discussed in detail in the end of the chapter.

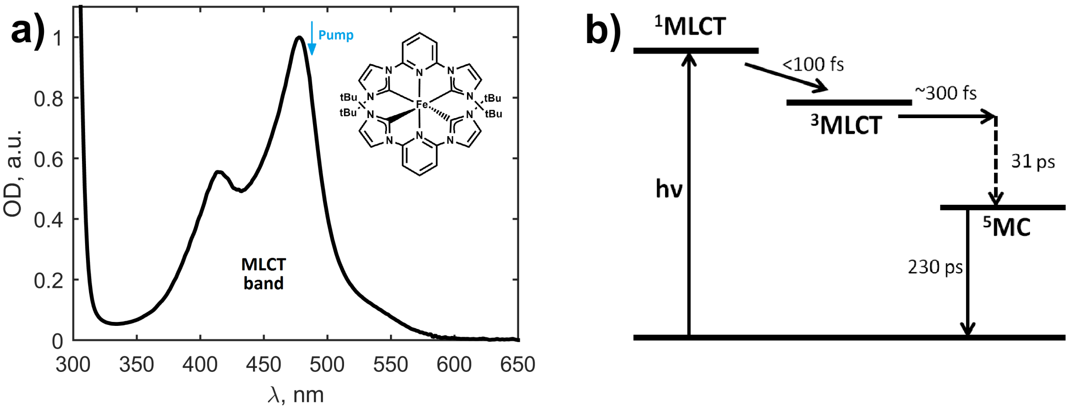

Figure 5.3. Electronic properties of $[Fe(NHC)_2]^{2+}$ in MeCN. a) Absorption spectrum of the $[Fe(NHC)_2]^{2+}$ in MeCN at room temperatire; b) Schematic Jablonski diagram of the complex.

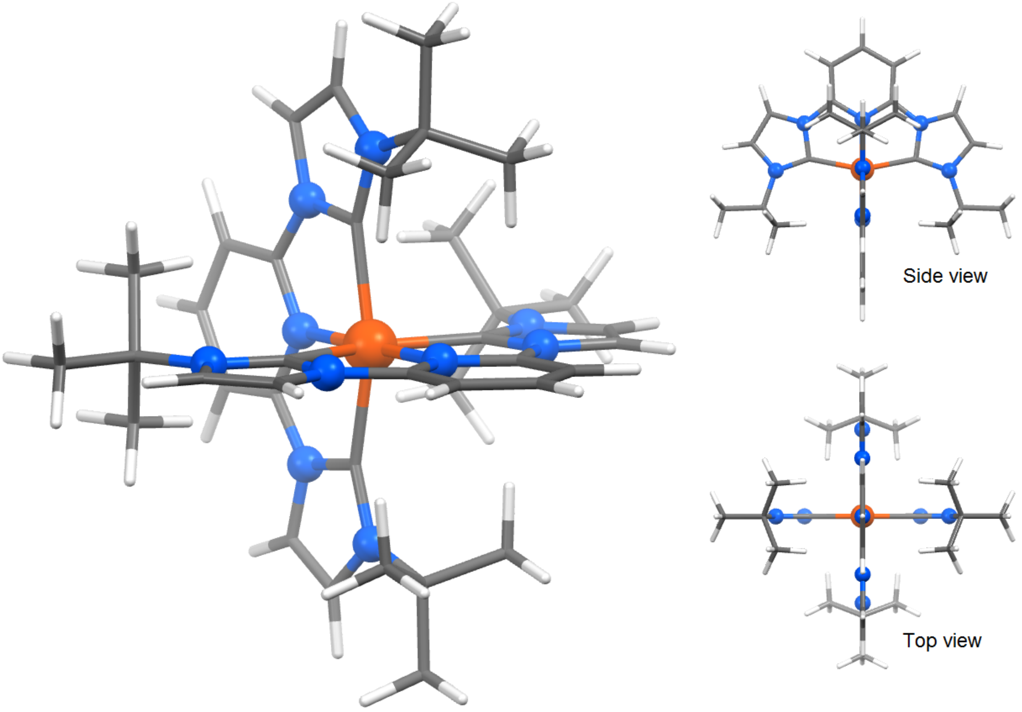

Figure 5.4. Structure of the $[Fe(NHC)_2]^{2+}$ complex in the ground state. The Fe center (orange) is exposed to the distorted octahedral environment formed by 2 axial nitrogens (blue) from pyridine rings and 4 equatorial carbons (gray) from carbenes. Hydrogens are depicted as white sticks.

strength of the $[Fe(NHC)_2]^{2+}$ ion in comparison to other NHC complexes which exhibit 10 ps MLCT lifetimes [140]. Based on this behavior and taking the 100 ps temporal resolution of the synchrotron experiment into account, we are focused on characterization of the excited MC state of the $[Fe(NHC)_2]^{2+}$ complex.

The results are reported in the following way. First, we will address the type of the MC state by comparing the signals from theoretically predicted structures to experimental TR-WAXS data. Then we will determine the structure of the complex with the optimization procedure developed in this work. The analysis of the kinetic and thermodynamic properties of the system will be followed by a discussion of the dynamic and structural properties of the complex with comparison to similar systems.

5.1.1 TR-WAXS results

The structure and dynamics of the $[Fe(NHC)_2]^{2+}$ complex were investigated by standard TR-WAXS measurements conducted in two steps. First, the kinetic properties of the compound were measured with the quasi-monochromatic 18 keV beam by collecting 25 time points between -100 ps and 1 ns. Then, the data for the structural analysis was collected with the high energy quasi-monochromatic 25.2 keV beam at one time point, 150 ps. The choice of this delay is based on spectroscopic work which revealed a 30 ps time constant of the vibrational cooling of the MC state; therefore for determining the equilibrium structure of the compound the 150 ps time delay was chosen. A 9 mM acetonirile solution of $[Fe(NHC)_2]^{2+}$ hexafluorophosphate salt was used as the sample. The synthesis of the compound was performed by Yizhu Liu from Lund University (Sweden) according to the procedure described in [140]. The flowing solution was excited to the MLCT state with a 1 ps pulse at 475 nm focused to 150 μm (FWHM) round spot with an energy of 40 μJ/pulse (fluence 0.16 J/cm^2).

Multiplicity of excited state

The optical assignment of the 230 ps state to ^{5}MC is based on the analogy with other typical Fe complexes, for example, $[Fe(bpy)_3]^{2+}$ (bpy = 2,2′-bypyridine), $[Fe(phen)_3]^{2+}$ (phen = 1,10-phenanthroline), $[Fe(tren(py)_3)]^{2+}$ ($tren(py)_3$ = tris(2-pyridin-2-ylmethanimino)ethyl amine) [5, 11, 150–159]. However, recent spectroscopic work on polyimine Fe complexes with strong ligand fields suggest that the observed MC states can have triplet character [137, 138], which was supported by calculations [139]. These works suggest that the MC state assignment for iron compounds with strong ligand fields has to be done with care.

Since TR-WAXS is a structural probe it does not probe the spin state of the iron ion. However, calculations for different iron complexes indicate that the structural differences between ^{3}MC and ^{5}MC are quite significant [139,142,160]. This is due to the difference in structural effects produced by different populations of the antibonding e_g^* orbitals. Therefore, one can address the type of the state by comparison of the corresponding signals from theoretical structures of the ^{3}MC and ^{5}MC states with experimental data.

Density Functional Theory (DFT) calculations of the structures in different states were performed by Lisa Fredin from Lund University. The ground state (GS), ^{3}MC and ^{5}MC geometries were freely optimized using PBE0 functional which is known to give good agreement to experimental structures [142, 160, 161], and the triple-ζ 6-311G(d,p) basis set with a complete acetonitrile polarizable continuum model (PCM) in Gaussian G09 [162]. The fully optimized excited state local minima were identified and can be clearly distinguished on the basis of the significant change in spin density on the Fe atom as MC like, consistent with the formal definition of MC states. Each minimum is characterized by its spin, energy and structure. The structures obtained from the DFT are used for for calculation of the associated TR-WAXS signals; the atomic XYZ coordinates of these DFT structures can be found in Appendix B.

The calculated GS structure is in good agreement with the one measured with x-ray diffraction [140]. For the other states, it is convenient to describe their structures by the changes of equatorial Fe-C$_{eq}$ and axial Fe-N$_{ax}$ bond lengths in the Fe FCS (Figure 5.5). The importance of these parameters will be discussed in detail below. The calculated ^{3}MC state of the complex is characterized by one of the ligands being repelled more than the other. The Fe-C$_{eq}$ and Fe-N$_{ax}$ bonds connecting one of the ligands, are elongated by ~0.2 Å, whereas the Fe-N$_{ax}$ bond to the other ligand is elongated by 0.1 Å. Therefore, this state is characterized by asymmetric expansion of the complex in comparison to the GS. The DFT structure of the quintet state has the same symmetry as the GS with elongated Fe-C$_{eq}$ and Fe-N$_{ax}$ bonds by 0.2 Å and 0.3 Å respectively. In contrast with ^{3}MC, the structural changes in ^{5}MC come from the symmetric expansion of the $[Fe(NHC)_2]^{2+}$ ion. The FCS parameters of the different states are summarized in Table 5.1 and the structural changes appearing upon transition from the GS to ^{3}MC and ^{5}MC are shown on Figure 5.6. The XYZ structures of the $[Fe(NHC)_2]^{2+}$ ion in all states can be found in Appendix X.

As we will see in the following discussion, the contribution from the solvation cage

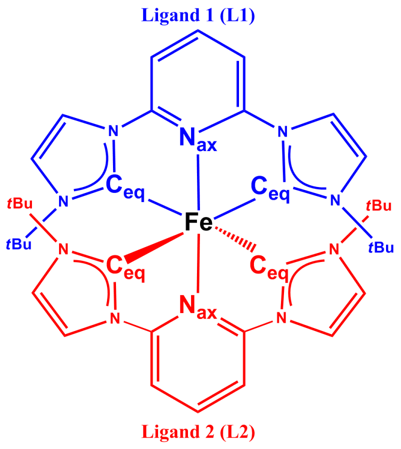

Figure 5.5. Atom and Ligand labeling

Table 5.1. Calculated parameters of the Fe FCS in different states.

		GS	^{3}MC	^{5}MC
L1	Fe-N$_{ax}$ (Å)	1.935	2.172	2.231
L2	Fe-N$_{ax}$ (Å)	1.936	2.035	2.231
L1	Fe-C$_{eq}$ (Å)	2.099	2.270	2.317
L2	Fe-C$_{eq}$ (Å)	2.099	2.110	2.316

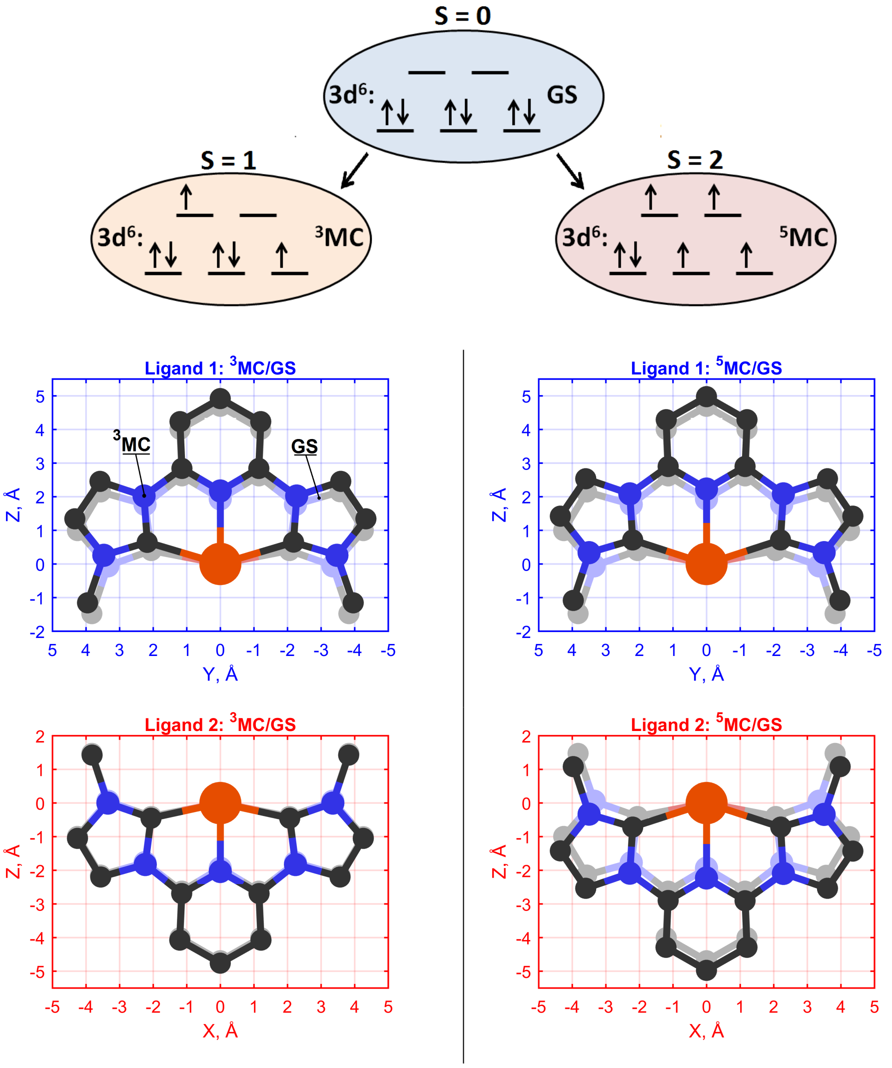

Figure 5.6. Electronic and structural changes appearing in the structure of the $[\mathrm{Fe(NHC)_2}]^{2+}$ ion in different MC states compared to the ground state (shown in pale colors). The *t*Bu groups are omitted for clarity. Color code: Fe is red, N is blue and C is black.

structural changes plays a more significant role here than in the previous projects. This is due to relatively low atomic number of the atoms constituting $[Fe(NHC)_2]^{2+}$ which in turn lowers the contrast with the signals arising due to the cage and solute alone. For this reason the cage term was included in the present analysis and simulated with Molecular Dynamics (MD). The simulations were performed by Elisa Basin from the Technical University of Denmark and the details are summarized as follows. The ground and excited state DFT structures of $[Fe(NHC)_2]^{2+}$ were solvated in a cubic box (50 Å size) of acetonitrile molecules using the three-site interaction potential derived by Guardia et al. [163]. The bond lengths of the solute molecule were constrained and MD trajectories were calculated with OPLS2005 force field parameters [164] and a Nose-Hoover thermostat at 300 K [165]. The system was equilibrated for 1 ns and, afterwards, the trajectories were recorded for a total time of 2 ns. The Radial Distribution Functions (RDFs) of the solute-solvent atom pairs were sampled in 0.01 Å radial bins with more than 2000 time steps. From the RDFs, the cage contribution to the difference scattering signal was calculated according to the procedure in [166].

The models including solute, cage and solvent contributions were fitted to the 25.2 keV data at 150 ps after laser excitation. Initially we tried to fit the data in the entire Q-range, which resulted in the ^{5}MC state being more likely than ^{3}MC (Figure 5.7, a). Although the ^{5}MC is closer to the experimental data than ^{3}MC, the difference between the χ^2 values is not large. A closer look at the fit reveals that the sharp features at 1.5 and 2 Å^{-1} cannot be described by neither of the fits. Since this region has the highest signal-to-noise ratio it has a significant impact on χ^2, which in turn reduces the contrast between the structures. We suggest that the discrepancy is due to an incapability of the classical MD method to take all the cage structural changes into account fully correctly. The performed simulations describe mainly excluded volume effects due to the overall expansion of the $[Fe(NHC)_2]^{2+}$ ion, which is most likely a simplified picture of the real process. Advanced molecular dynamics studies for $[Fe(bpy)_3]^{2+}$ indicate significant reorganization in the first few solvation shells upon spin changes [167–169], which is expected to appear for $[Fe(NHC)_2]^{2+}$ as well. On the other hand, the cage signal simulated in this work appears to be significant only in the low Q part up to 2-3 Å^{-1}, which agrees with the previous studies [76, 170–172] (Figure 5.8, a). Therefore, if we exclude the low Q part in the analysis, we will focus on the solute structure only. By performing the fit in the range 2.5-11.5 Å^{-1} we again find that the ^{5}MC state structure fits the data best (Figure 5.7, b). In this case however, we get much

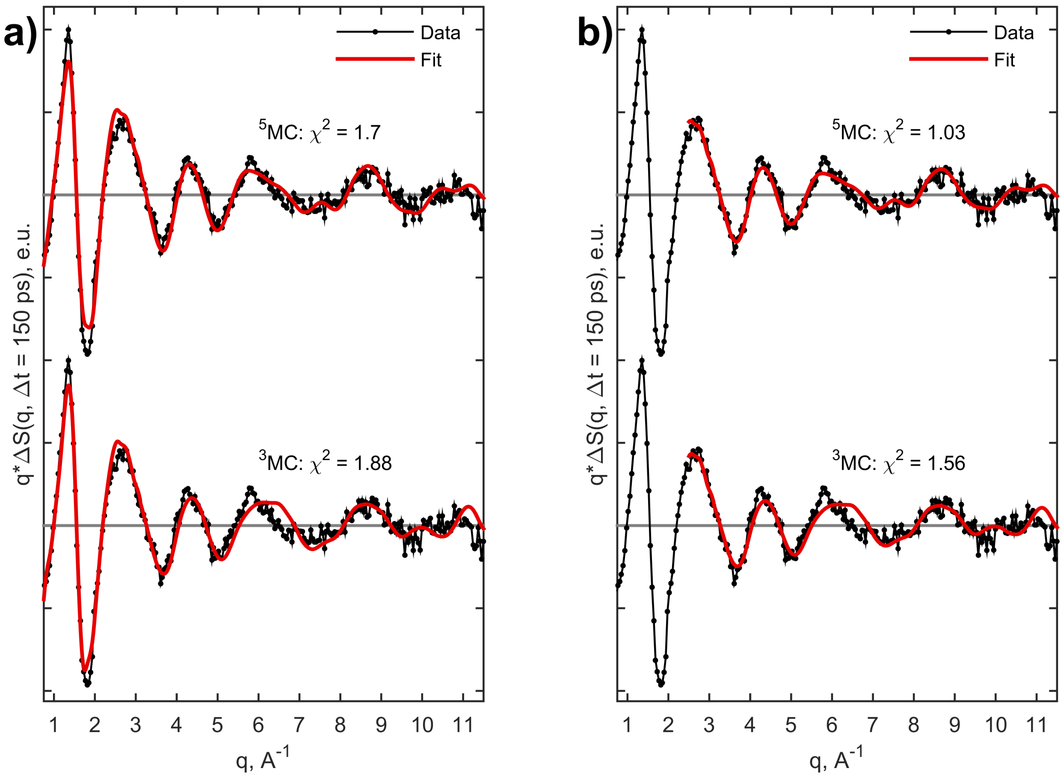

Figure 5.7. Fitting comparison for excited state of $[Fe(NHC)_2]^{2+}$ in q- (a) and r-space (b). The data is collected with 25.2 keV ML x-rays at 150 ps after laser excitation.

higher contrast between the structures from the χ^2-statistics point of view, which makes the conclusion more certain. Overall the analysis confirms the assignment made in the spectroscopic work. This result is not surprising based on the experience with the other Fe compounds mentioned above. It demonstrates the sensitivity of TR-WAXS to subtle differences in the structures of low-Z molecules. Moreover, our analysis implies that the structural analysis can be performed reliably without the inclusion of the cage term when the Q-range in sufficiently broad.

The decomposition of the theoretical signals is shown on Figure 5.8. First, we note that the solute signal spans the entire Q-range and dominates the experimental signal at high values of Q (Q≥6 Å). The corresponding differential RDF is rich in structure, which is due to the complex and multi-scale changes in the molecular structure upon transition from GS to ^{5}MC. The interpretation of certain dips and peaks is possible. For this purpose, the total and differential RDF for the two states were calculated and shown in Figure 5.10. The negative dips at 1.9 Å and 2.9 Å with corresponding positive features around 2.4 Å

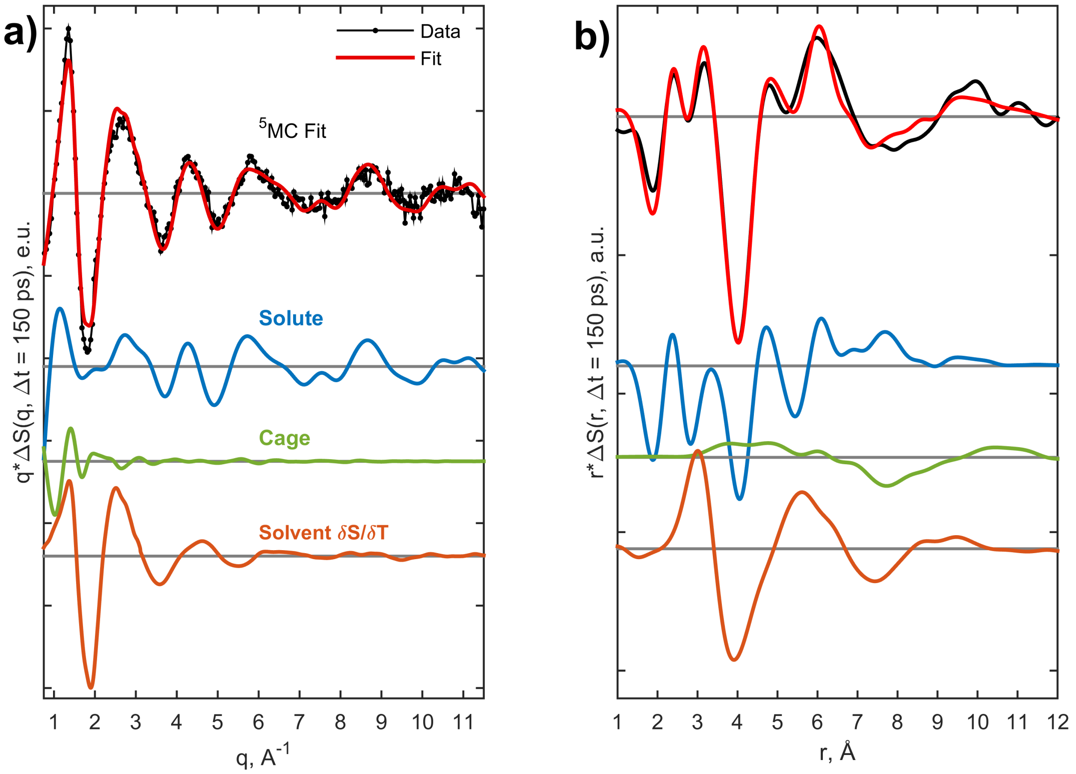

Figure 5.8. Decomposition of the contributions to the experimental signal in q- (a) and r-space (b). The data is collected with 25.2 keV ML x-rays at 150 ps after laser excitation.

and 3.5 Å are mainly due to the expansion of the first (Fe-C_1, N_1) and second (Fe-C_2, N_2) coordination shell of Fe (for the atom labeling see Figure 5.9). At higher $r \geq 3.5$ Å, the features involve more complex changes. Here the signal appears due to mixture of the elongation of the distances between Fe and the outer atoms of the pyridine rings and the carbenes (Fe-C_{4-5}) with a shortening in distances between Fe and the carbons in the *t*Bu (*tert*-Butyl) groups (Fe-C_{6-7}). These contributions only partially explain the signal. The mentioned correlations do not include the changes of the distances between carbon and nitrogen atoms, which are quite difficult to assign in compact and informative way. These complex changes are due to increase in distances between pyridine rings and carbenes. For example, the distance between the centers of the two pyridine rings increases from 6.63 by ∼0.6 Å, which results in a number of positive features from 7 to 10 Å. We will not discuss these changes in greater detail since they appear to be very complex and do not bring new insight into the dynamics of the system.

The second contribution to the signal is due to changes in the cage structure. Ex-

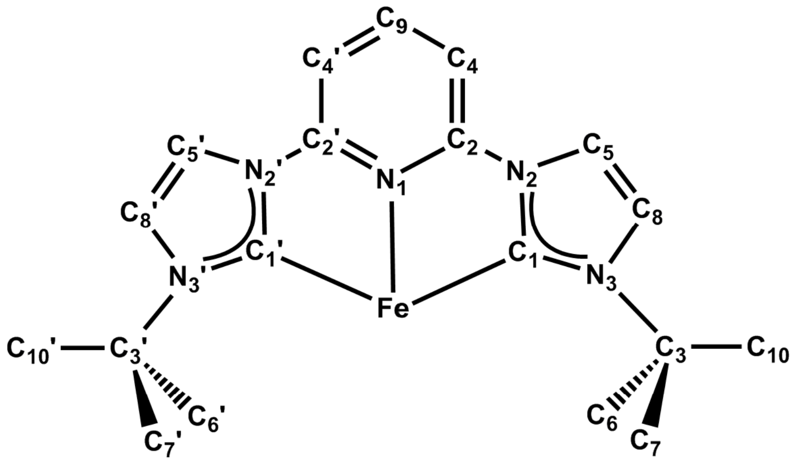

Figure 5.9. Atom labeling for $[Fe(NHC)_2]^{2+}$.

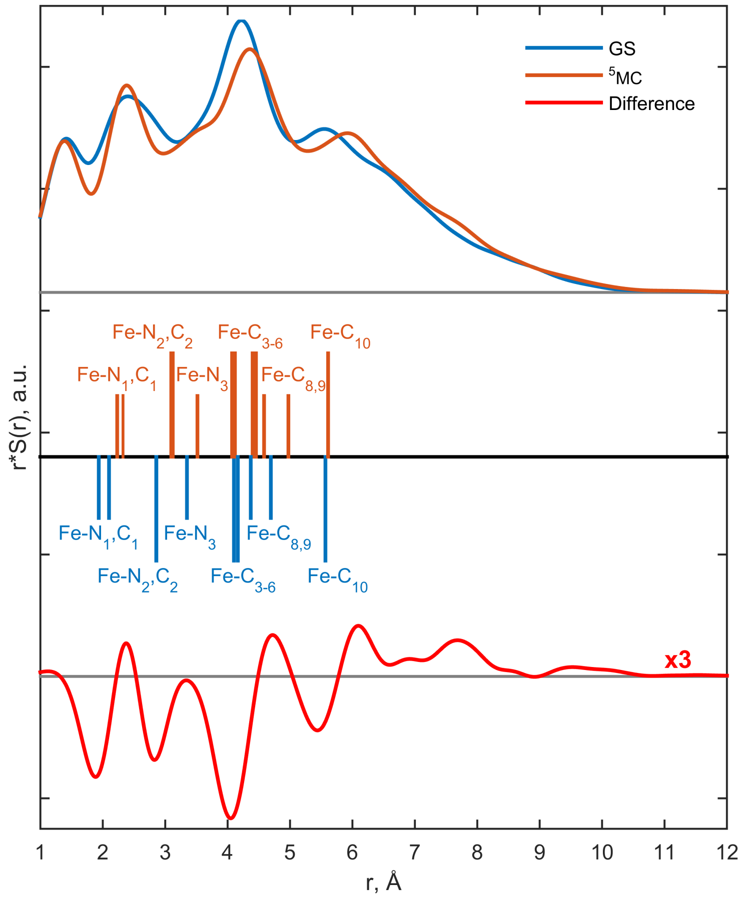

	GS	^{5}MC
Fe-N$_1$	1.935	2.231
Fe-C$_1$, C$'_1$	2.099	2.317
Fe-N$_2$, N$'_2$	2.856	3.097
Fe-C$_2$, C$'_2$	2.858	3.121
Fe-N$_3$, N$'_3$	3.348	3.516
Fe-C$_3$, C$'_3$	4.101	4.117
Fe-C$_4$, C$'_4$	4.180	4.454
Fe-C$_5$, C$'_5$	4.163	4.401
Fe-C$_6$, C$'_6$	4.165	4.072
Fe-C$_7$, C$'_7$	4.169	4.072
Fe-C$_8$, C$'_8$	4.371	4.584
Fe-C$_9$	4.692	4.973
Fe-C$_{10}$, C$'_{10}$	5.567	5.610

Figure 5.10. Total and differential radial distribution functions for GS and ^{5}MC states calculated from DFT structures. Fe-atom contributions to the differential signal are also shown.

planation of the appearing signals can be done by a close look into differential RDF. The positive broad peak between 3 and 6 Å indicates that the solvent atoms are located closer to $[Fe(NHC)_2]^{2+}$ in ^{5}MC than in the GS. This surprising result can be qualitatively explained as follows. Upon excitation to the ^{5}MC state, the ligands move away from the iron center and away from each other, which brings the bulky *t*Bu groups slightly closer to Fe (recall the Fe-C_{6-7} bonds). These groups serve as a main barrier between Fe and the cage. When they move closer to Fe, the cage molecules can also come closer to Fe. This leads to the appearance of the mentioned positive feature at small r values. The following negative and positive features between 7-12 Å represent the expansion of the cage due to expansion of the $[Fe(NHC)_2]^{2+}$ ion upon transition from ^{5}MC to GS.

The final contribution is the solvent heating, which is dominating the low-q region of the signal. In contrast to the previous contributions, the shape of the observed signal can be easily rationalized in Q-space. Upon heating the dispersion of interatomic distances between atoms of the liquid increase, resulting in the broadening of the liquid peak. In the differential signal it is manifested as the negative feature at 2 $Å^{-1}$ and positive peaks at 1 and 3 $Å^{-1}$. As mentioned in the previous chapter, the assignment of the actual changes in interatomic correlations and corresponding RDF signal require additional MD simulations which go beyond the scope of the present work.

Structure of $[Fe(NHC)_2]^{2+}$ in the ^{5}MC state

After having defined the type of excited state we now refine its structure. For $[Fe(NHC)_2]^{2+}$ it is not easy to parametrize the structure as we did for HgX_2 and I_3^-. According to the Debye formula, with 99 atoms in $[Fe(NHC)_2]^{2+}$, the number of degrees of freedom can by calculated as 99·(99-1)/2 = 4851. From the discussion in chapter 3, the maximum fitting parameters we can incorporate in the model is given by $N_{ind} \approx 2\Delta Q \Delta R/\pi$, where ΔQ and ΔR are the fitting ranges in Q- and R-space. In the present case we have $\Delta Q = 11.5 - 0.75 = 10.75$ $Å^{-1}$, and ΔR can be estimated to be roughly corresponding to the size of the molecule, which is about 12 Å. Therefore, the theoretical limit for the number of fitting parameters is ≈80, which is definitely smaller than the number of degrees of freedom of the $[Fe(NHC)_2]^{2+}$ ion. Therefore one needs to reduce the dimensionality of the problem. That can be done by selecting of the reaction coordinates driving the structural changes between the states. Note that since we have a reliable DFT calculation of the GS structure, which reproduces the x-ray diffraction results, it is only the ^{5}MC state which is going to be optimized.

Most of the hexa(monodentate) and tris(bidentate) Fe(II) compounds exhibit a simple expansion of the metal to ligand bonds by $\sim$0.2 Å upon the conversion from GS to ^{5}MC, which implies presence of only one reaction coordinate [5, 11, 150–159]. However, if the system undergoes more complex structural changes upon spin conversion [173, 174], additional reaction coordinates have to be introduced. Initially suggested by Hauser [175], and later confirmed with time-resolved x-ray absorption spectroscopy [6, 176, 177], the sister compound $[\mathrm{Fe(tpy)_2}]^{2+}$ (tpy = 2,2′:6′,2″-terpyridine) exhibits a distortion of the octahedral shape in the first coordination shell in both GS and ^{5}MC. In order to describe the transition between the two states, two reaction coordinates were proposed: the axial bond length R_{ax} and the ligand biting angle ϕ_{bite}. The choice of these reaction coordinates is directly related to the differences in electronic structure of the complex in the GS and ^{5}MC state. Indeed, the difference in occupation of the e_g^* and t_{2g} orbitals is responsible for the main structural changes in the complex. If the electrons occupy the former, the metal to ligand bonds are elongated due to the orbital's andibonding character. This in turn decreases the overlap between the t_{2g} and π^* orbitals of the ligands, reducing the π-back-bonding and therefore causing additional elongation of the bond lengths. The fact that charge redistribution between the $2p$ orbitals of N and $3d$ orbitals of Fe plays the key role in GS to ^{5}MC transition has recently been shown by direct probing of the 2p→3d transitions in iron [8, 178–180] and the 1s→2p transitions in nitrogen [181] in similar iron polyimine $[\mathrm{FeN_6}]^{2+}$ complexes. As evident from the previous discussion, DFT calculations for the $[\mathrm{Fe(NHC)_2}]^{2+}$ complex also indicate that the structural changes in the FCS can be parametrized with the proposed reaction coordinates. In this work however, we chose the axial Fe-N$_{ax}$ and the equatorial Fe-C$_{eq}$ bond lengths, R_{ax} and R_{eq} respectively, as the reaction coordinates (Figure 5.11, a). The alternative R_{ax} and ϕ_{bite} parameters are simple geometrical functions of our chosen bond lengths, so the results are independent of the choice of parameters.

The refinement procedure requires a functional dependence between the Cartesian coordinates (XYZ) of each atom and structural parameters R_{ax} and R_{eq}. In order to achieve it, the following procedure was implemented. First we take the values of the Fe-N$_{ax}$ and Fe-C$_{eq}$ bond lengths from the initial DFT structure of ^{5}MC (1.935, 2.099 Å) and varied them by 0.03 Å. By doing this we introduce the parameter grid consisting of 9 points

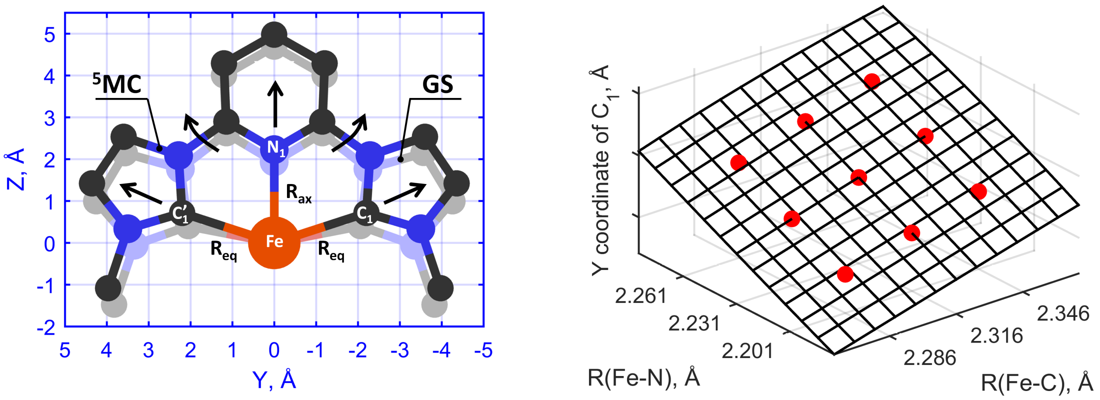

Figure 5.11. Structural optimization based on selection of reaction coordinates. Reaction coordinates of the system (left panel); illustration of the interpolation concept (right panel).

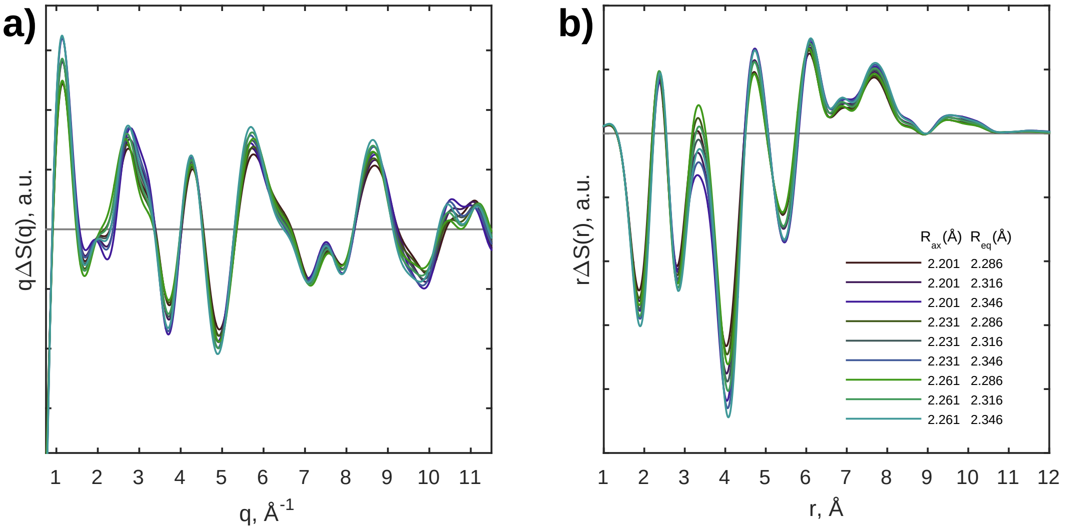

Figure 5.12. Calculated signals for different points on the grid of parameters (R_{ax}, R_{eq}) in q- (a) and r-space (b).

(Figure 5.11, b). Second, at each point of the grid we perform the DFT optimization[2] of the structure. Note, that during the optimization the Fe-N$_{ax}$ and Fe-C$_{eq}$ bond lengths are kept constant according to the values corresponding to each selected point. In order to obtain a continuous dependance we use two-dimensional interpolation for the bond length values located between the grid points. The interpolation procedure is based on a calculation of the second order surface which goes through all the nine points of the grid. After this procedure we have a functional dependence between each atom's XYZ coordinates and R_{ax} and R_{eq} (Figure 5.11, b). With this procedure we can optimize the excited state structure since the calculation of the associated TR-WAXS signals is straightforward. For

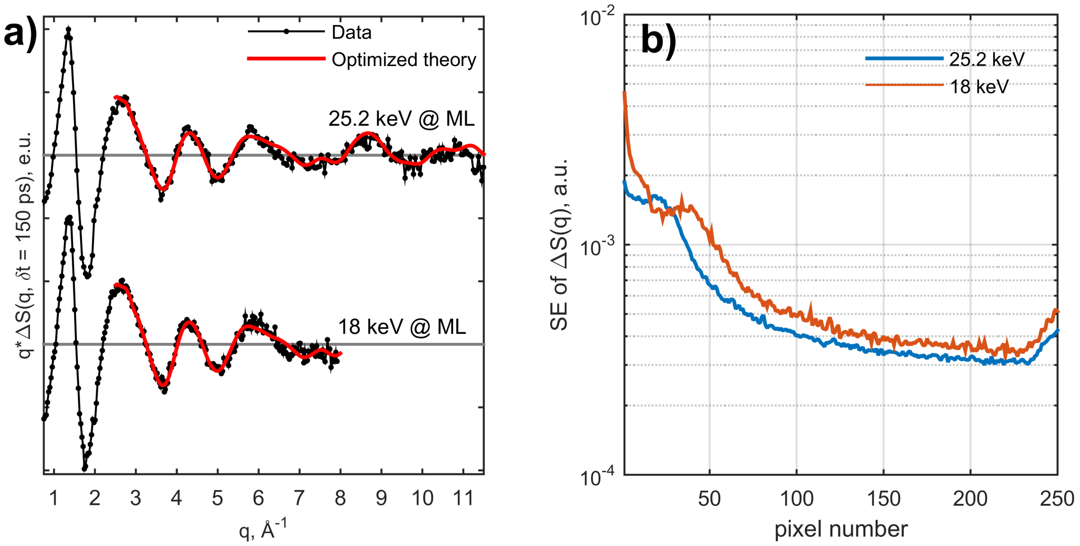

Figure 5.13. Structural optimization of the ^{5}MC state structure of $[Fe(NHC)_2]^{2+}$. (a) Comparison of results for 25.2 keV and 18 keV data sets; (b) Standard deviation of the curves as a function of the pixel number.

illustration of the signal variation upon changes in the parameters we calculated the solute signals for 9 grid points, as shown in Figure 5.12.

The refinement of the structure is done by fitting a four parameter model to the TR-WAXS data. The parameters include the two reaction coordinates discussed above, the excited state fraction and the temperature rise. Since the low Q part of the data cannot be described by the present model due to imperfections of the cage signal, it was decided to exclude this part of the data from the fitting. The data is fitted from 2.5 Å^{-1} up to 11.5 Å^{-1}. The optimized values of Fe-N$_{ax}$ and Fe-C$_{eq}$ bond lengths are 2.23 ± 0.03 Å and 2.31 ± 0.02 Å respectively, which is in good agreement with the theory. This result serves as a benchmark of the theoretical approach employed in this work.

For comparison, the data collected at 18 keV at 150 ps was also fitted with the same model. To investigate the effect of the extension of the Q-range, the number of individual scattering differential curves was chosen to have roughly the same noise level as the 25.2 keV curve (Figure 5.13, b). The obtained parameters are 2.24 ± 0.03 Å and 2.32 ± 0.03 Å for the Fe-N$_{ax}$ and Fe-C$_{eq}$ bond lengths respectively, which is similar to the 25.2 keV results. The uncertainty in the Fe-N$_{ax}$ bond length in the two experiments appears to be quite similar, which is probably due to the low small signal-to-noise ratio in the high-q region

---

2. using the same DFT approach as before.

Table 5.2. Results of structural optimization procedure performed on different TR-WAXS data sets for $[Fe(NHC)_2]^{2+}/MeCN$.

State	Method	R_{ax} (Å)	R_{eq} (Å)	ΔR_{ax} (Å)	ΔR_{eq} (Å)
GS	DFT	1.935	2.099	–	–
^{5}MC	DFT	2.231	2.317	0.296	0.218
^{5}MC	18 keV	2.24 ± 0.03	2.32 ± 0.03	0.30 ± 0.03	0.23 ± 0.03
^{5}MC	25.2 keV	2.23 ± 0.03	2.31 ± 0.02	0.30 ± 0.03	0.21 ± 0.02

of the 25.2 keV data. The latter effectively reduces the amount of available information, leading to similar uncertainty. The fits of both data sets are shown in Figure 5.13, and the results of the optimization are summarized in Table 5.2.

The refinement shows that the theoretical structure agrees with the experiment. Since TR-WAXS probes all interatomic distances in the sample and the optimization procedure addresses the structure of the whole molecule one can conclude that the DFT structure is fully consistent with the experimental data. However, considering the different contributions to the solute signal, intuitively it is clear that the strongest ones come from the interatomic correlations involving the iron center, which has the highest atomic number ($Z = 26$). This means that slight changes in the correlations between light atoms such as C, N and H would not significantly affect the fit quality. Therefore the present analysis is not sensitive to small errors of the ligand structure. In order to illustrate it, three signals from the solute were calculated. The first includes all the interatomic correlations in the molecule and is equal to the one shown before in the fitting discussion. The second includes only correlations of type Fe··C, Fe··N, Fe··H, i.e. involving only the Fe center (no N··N, N··C, C··C, etc.). Finally, the signal coming only from Fe··C and Fe··N correlations in the FCS were calculated for the third curve. The differential scattering signals and corresponding RDFs are shown in Figure 5.14. Obviously, the curve taking into account only the FCS appears to be oversimplified for description of the data. Opposed to that, the two other curves have quite a lot in common, particularly above 4 Å^{-1}. It means that the calculated signal is, by and large, determined by a small number of Fe··(N,C,H) correlations. The rest of correlations have a minor contribution to the signal. Of course, the similarity between the curves vanishes in the low-q region where correlations between C, N and H appear to contribute significantly to the signal. Since our structural analysis is performed mainly in

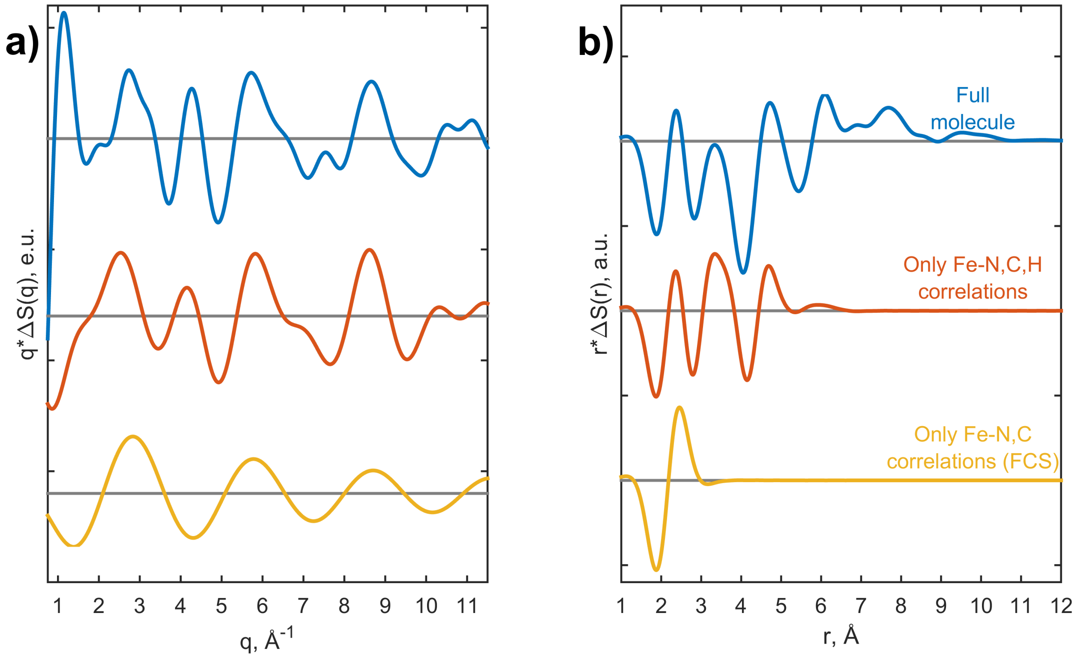

Figure 5.14. Contributions to the solute signal coming from the Fe center of $[\mathrm{Fe(NHC)_2}]^{2+}$ in q- (a) and r-spaces (b). From the comparison of red and blue curves it follows that the high-q part of the signal is dominated by contributions coming from Fe. On the other hand, the signal calculated based only on the FCS of Fe appears to be oversimplified compared to the full molecule signal.

the high-q range, the results are insensitive to small errors in the distances between the light atoms (N, C, H). The sensitivity to some of the details in the ligand structure can therefore be significantly improved by inclusion of the low-q region to the data analysis, which on the other hand requires a reliable cage term model. Deeper insight into the sensitivity of the technique to different interatomic correlations can be achieved by applying wavelet analysis, which is widely applied in x-ray absorption [182–184]. We leave this work for the future.

Population dynamics

Further details about the excited state can be retrieved from kinetic analysis of the 18 keV data. Now we use the optimized structural model for the ^{5}MC state to describe the solute contribution. Initially, a good estimate of the amplitude and timescale of the processes can be obtained with individual fits for each time point (Figure 5.15). At -90 ps, the signal is zero as expected for a correct time-zero calibration. The rise of the excited state population is broadened by the 100 ps time resolution of the experiment. At later time delays, one observes a rapid decay of the quintet state population, which is vanishing towards 1 ns. The temperature rise shows a somewhat similar behavior. Due to the fast relaxation from the MLCT to the ^{5}MC state and redistribution of most of the photon energy into the solvent, a sharp temperature rise appears around time zero. After 100 ps the temperature is growing slightly, however due to the wide distribution of the points it is difficult to define the rate of the process.

It is important to note, that careful analysis of the fit quality at early time delays did not reveal the presence of any significant deviations between the data and fits, which could appear due to the 31 ps vibrational cooling of the ^{5}MC state. It has also been confirmed with the analysis based on singular value decomposition (not shown), which indicates that only two components are contributing to the signal (the components obviously correspond to the ^{5}MC state decay and associated solvent heating). Although it has been shown that for I_2 in CCl_4 it is possible to measure the ultrafast process of the vibrational cooling with good resolution [25], in the present case we do not see any significant signals corresponding to such a process, which can explained as follows. First, as our precision analysis indicates, the structural sensitivity is limited to 0.02-0.03 Å, which is probably on the scale of the difference between the hot and relaxed structure. Second, based on the HgX_2 analysis the characterization of ultrafast processes appearing on the time scales of ∼50 ps with a synchrotron-based setup has limited precision and reliability. Here the process is even faster, which prevents it from being detected reliably with the present setup.

In order to retrieve the energy and kinetic parameters from the data we use the global fit approach described previously with one modification. Here, due to simplicity of the relaxation process, which involves only one species, we incorporated the energy difference between the GS and ^{5}MC into the fitting procedure. Otherwise, the model includes the standard set of parameters, the excited state fraction, lifetime of the ^{5}MC state, the temperature offset due to ultrafast dissipation of the energy to the solvent (this will be discussed below in detail), the width of the x-ray pulse and a time zero shift. The performed fitting procedure gives good agreement between the data and theory. The following parameters values were obtained. After laser excitation, the fraction of 0.33 ± 0.01 of the complexes quasi-instantly converts to the ^{5}MC state, which lifetime constitutes 270 ± 15 ps. The lifetime appears to be in reasonable agreement with optical spectroscopy, which gave the ^{5}MC lifetime 230 ps. The best fit value of the energy difference between GS and

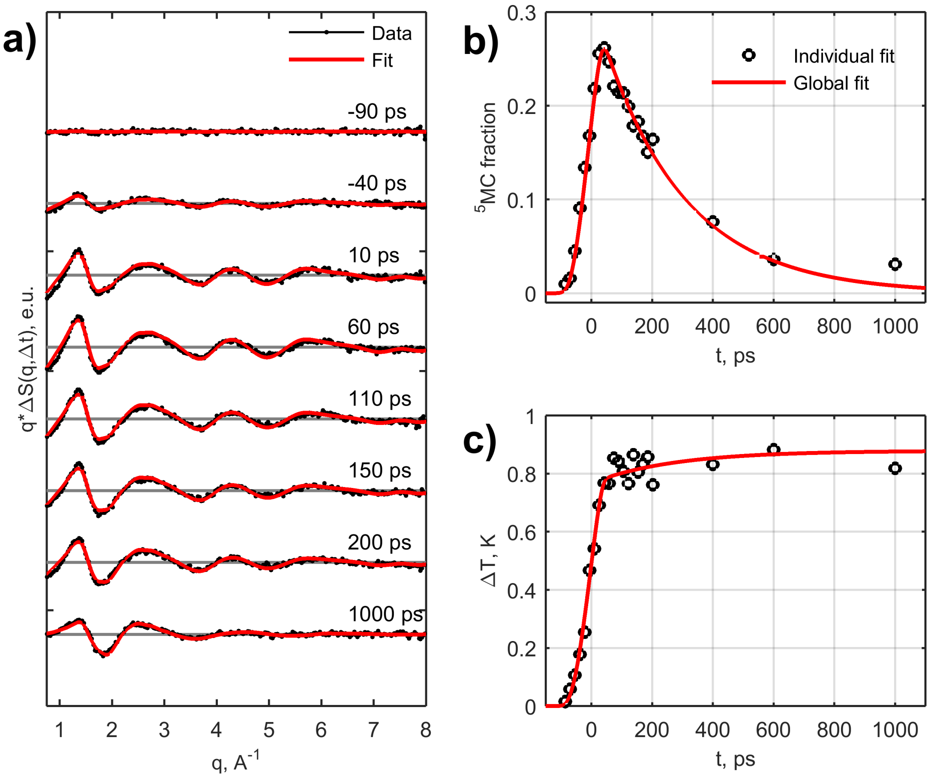

Figure 5.15. Global fitting result for 18 keV data on $[Fe(NHC)_2]^{2+}$. (a) Comparison of the data with the fit for representative set of curves; (b) Excited state fraction as a function of time; (c) Temperature dynamics as a function of time.

^{5}MC is 0.4 ± 0.2 eV. The large scatter of the individual temperature points explains the significant uncertainty of the energy determination. Despite the large error of the energy level it is still larger than the value of 0.135 eV coming from the DFT calculation, which requires further investigation.

After thermal equilibration and complete relaxation of the excited species we observe a total temperature rise of almost 0.9 K. Considering the initial excitation fraction and the amount of energy dissipated into the solvent from photon absorption process, we predict a 0.6 K temperature increase, whereas 0.3 K comes from an unknown heat source. The first concern for appearance of the temperature offset is the direct absorption of the light in the solvent. This was carefully checked by measuring the heating signal with the same experimental conditions on pure MeCN. This test gave no detectable signal (not shown), which allows us to conclude that the solute is the reason for the additional temperature rise. Taking into account the relatively low fluence of the experiment and quite long laser

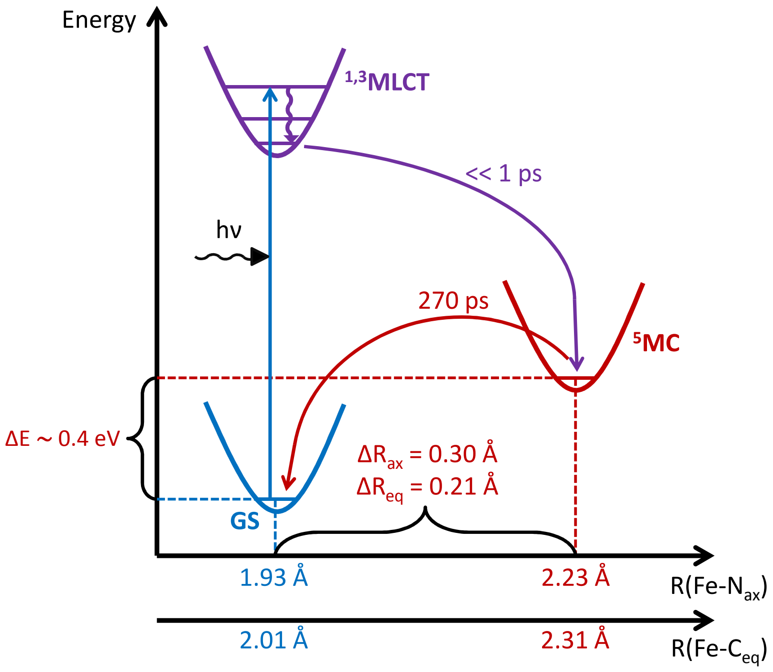

Figure 5.16. Energy diagram for the $[Fe(NHC)_2]^{2+}$ complex based on results of the present work.

pulse duration (∼1 ps), we can exclude multi-photon excitation of the solute as a heating source. Therefore, this temperature rise might point towards an ultra-fast deactivation of the MLCT state. It has been shown for the $[Fe(bpy)_3]^{2+}$ complex that the ultrafast transition between MLCT and ^{5}MC is mediated short-lived ^{3}MC state [135]. Based on that we can speculate that in the case of $[Fe(NHC)_2]^{2+}$, a fraction of the excited complexes decay directly to the GS while crossing the ^{3}MC state on the ultrafast time scale, which causes additional heating of the solution. We estimate that fraction of 0.16+0.01 of excited solutes relaxes this way. This hypothesis requires further confirmation with experiments performed with higher time resolution. The summary of all the experimental findings in this work is summarized on a diagram shown in Figure 5.16.

Comparison to other systems

In the following we will attempt explain structural properties of the $[Fe(NHC)_2]^{2+}$ complex by comparing its properties with other sister compounds. In the end we correlate these the observations about the structure with the overall photochemical behavior of the compound.

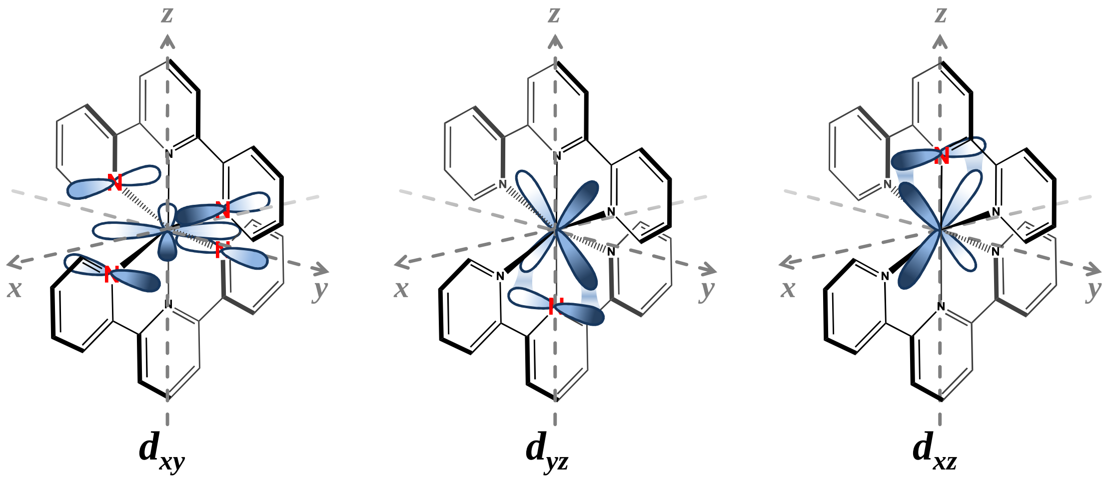

Figure 5.17. Schematic illustrating the preferential π-back-bonding in the $[Fe(tpy)_2]^{2+}$ complex adapted from [176]. From this illustration it is clear that the d_{xy} orbital efficiently overlaps with the equitorial nitrogens of $[Fe(tpy)_2]^{2+}$ complex. In the GS this overlap leads to a π-bonding effect between Fe d_{xy} orbitals and $2p$-like orbitals of equatorial nitrogens. The effect is small because two electrons are shared between four nitrogen atoms. In contrast, the d_{yz} orbital efficiently overlap only with one axial nitrogen, leading to stronger bonding effect in comparison to the equatorial nitrogens. The d_{xz} orbital shows the same effect. Overall, this preferential π-back-donation effect is partially responsible for the anisotropic changes in the Fe FCS in $[Fe(tpy)_2]^{2+}$ complex upon excitation from the GS to ^{5}MC state as explained in text. Due to geometrical similarity the $[Fe(NHC)_2]^{2+}$ complex shows similar behavior.

One of the striking results of this work is the pronounced anisotropy in the expansion of the Fe-N$_{ax}$ and Fe-C$_{eq}$ bonds, which is quite unusual in comparison to other spin crossover complexes such as $[Fe(bpy)_3]^{2+}$. Here we attempt to rationalize this anisotropy on the basis of the bonding considerations. In order to explain the effect it is convenient to first consider the sister compound $[Fe(tpy)_2]^{2+}$ which demonstrates similar properties. The systems have fairly similar structure: in $[Fe(tpy)_2]^{2+}$ the carbene units are replaced by pyridine rings, so that the metal is coordinated with six N atoms (Figure 5.19). The four links from Fe to N on the side pyridine rings correspond to the equatorial bonds, whereas the central pyridine rings hold the axial nitrogens as in $[Fe(NHC)_2]^{2+}$. Here, the anisotropy between the axial and equatorial bond lengths in the high and low spin state was measured in several experiments [6, 176, 177] and explained theoretically [185–187]. In the GS, the distortion of the octahedral symmetry in different states appears due to preferential π-back-donation from the d_{xz} and d_{yz} orbitals to the in-phase π^* orbitals of the central pyridines (Figure 5.17). This results in pronounced structural and energetic effects manifested in shortening

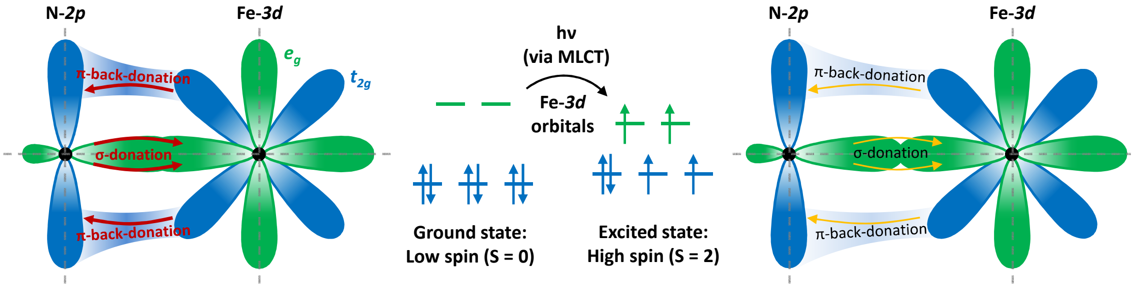

Figure 5.18. Illustration of the σ-bonding and π-back-bonding concepts for transition metal complexes adapted from [178]. In the GS the close proximity of the coordinating atoms from the ligand and Fe leads to the efficient overlap between the $2p$-like orbitals of N and the t_{2g} orbitals of Fe. This overlap results in π-back-donation effect which strengthen the bond between Fe and coordinating atom. Due to geometry of $[\mathrm{Fe(NHC)_2}]^{2+}$ this overlap results in shortening of the Fe-N$_{ax}$ bonds. Upon excitation to the ^{5}MC state the antibonding orbitals e_g^* become populated causing the expansion of the Fe FCS. This decreases the overlap between the $2p$-like orbitals of N and the t_{2g} orbitals of Fe and weakens the π-bonding effect. This results in the additional expansion of the Fe-N$_{ax}$ bonds compared to the equatorial Fe-C$_{eq}$ bonds.

of the axial bonds and stabilization of these two metal orbitals (d_{xz} and d_{yz}). Opposed to that, the d_{xy} orbital overlaps with the π^* orbitals of the side pyridine rings, which leads to sharing of the pair of electrons between four pyridine units. It reduces stabilization of the orbital and the shortening effect for each of the individual equatorial bonds explaining the anisotropy of the complex structure in the GS. If the complex is promoted to the ^{5}MC state, then the two antibonding e_g^* orbitals are populated, resulting in elongation of the axial and equatorial bonds. At the same time the t_{2g} orbitals become less populated (4 electrons instead of 6) and the overlap between t_{2g} and in-phase π^* orbitals of the central pyridine rings significantly reduces. This weakens the bonding character of the t_{2g} and additionally elongate the axial bond. The illustration of the orbit overlap in different spin states is shown in Figure 5.18. Overall, the mixing between t_{2g} orbitals and ligand orbitals is responsible for anisotropic bond elongation by changing the bonding character in the low spin state to the weakly-bonding in the ^{5}MC state.

For $[\mathrm{Fe(NHC)_2}]^{2+}$ the anisotropy is even more pronounced due to the nature of the carbene ligands. Here, the Fe center is coordinated by strongly σ-donating carbons, which results in significant destabilization of the e_g^* orbitals. Since the π-back-donation is synergetically enhanced by σ-donation (due to electrostatic repulsion between electrons on

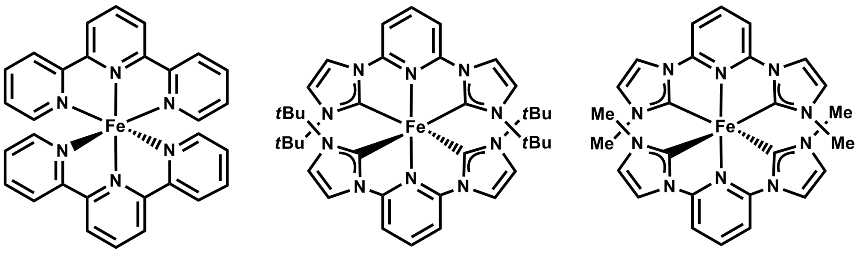

$[Fe(tpy)_2]^{2+}$

$[Fe(NHC)_2]^{2+}$ (*t*Bu)

$[Fe(NHC)_2]^{2+}$ (Me)

Figure 5.19. Compounds discussed in the text.

Table 5.3. Comparison of structural parameters and ^{5}MC state lifetimes of compounds discussed in text.

Compound	State	R_{ax}	R_{eq}	ΔR_{ax}	ΔR_{eq}	τ
$[Fe(tpy)_2]^{2+}$ [a]	GS	1.86 Å	1.97 Å	–	–	–
	^{5}MC	2.09 Å	2.18 Å	0.23 Å	0.21 Å	4 ns[b]
$[Fe(NHC)_2]^{2+}$ (*t*Bu)[c]	GS	1.935 Å	2.099 Å	–	–	–
	^{5}MC	2.23 Å	2.31 Å	0.30 Å	0.21 Å	270 ps
$[Fe(NHC)_2]^{2+}$ (Me)[d]	GS	1.93 Å	1.96 Å	–	–	–
	^{5}MC	2.27 Å	2.21 Å	0.34 Å	0.25 Å	n/a[e]

[a] structural parameters from [177];

[b] value from [140];

[c] this work;

[d] structural parameters from [160];

[e] optical spectroscopy detected only very short-lived MC state; in the later theoretical work [160] it was found that no ^{5}MC is populated during the MLCT relaxation.

different orbitals), the effect of electron withdraw to the central pyrindine rings is more pronounced giving a more significant bonding character to the d_{xz} and d_{yz} orbitals of iron. Again, in the ^{5}MC state the population of the e_g^* leads to a reduction of the t_{2g} bonding properties, leading to larger elongation of the axial bonds in comparison to $[Fe(tpy)_2]^{2+}$.

In the context of present discussion it is important to mention another NHC complex from [140]. The structure of that complex is similar to that of $[Fe(NHC)_2]^{2+}$, but the bulky *t*Bu groups are substituted with smaller methyl (Me) groups (see Figure 5.19, system

$[Fe(NHC)_2]^{2+}$ (Me)), resulting in shortening of the bonds between Fe and the ligands[3]. This in turn enhances the σ-donation from the carbenes and, as predicted by theory, the structural changes upon spin conversion appear to be very large: the axial and equatorial bonds are elongated by 0.34 and 0.25 Å respectively [160]. Based on the discussion above we propose that this dramatic step further in bond elongation is due to an even larger contrast between bonding character of the t_{2g} orbitals in the GS and ^{5}MC state due to enhanced π-back-donation. In this compound the ligand field is so strong that ^{3}MC appears to be lower in energy than ^{5}MC, so the latter is not populated at all during the MLCT relaxation process. The modification of this complex has recently been shown to be efficient for electron injection to the TiO_2 conduction band [188].

The present picture, based on bonding considerations, might not be the ultimate explanation of observed effects. An important factor omitted in the discussion was the strain in the ligands which restricts the range of the bite angles which the ligand can adopt. This effect is difficult to include precisely but it can also contribute to the anisotropic expansion of the equatorial and axial bonds upon conversion from GS to ^{5}MC. Thorough theoretical insights would help to disentangle the bonding (electronic) and geometrical contributions to the structure which will be provided in future works.

The observed structural and photochemical properties of the studied $[Fe(NHC)_2]^{2+}$ complex and the comparison with other compounds from its family (als studied in [140]) allow us to examine the results in a broader perspective. Due to the geometrical properties of the ligands, $[Fe(tpy)_2]^{2+}$ exhibits significant anisotropic expansion of the axial and equatorial bonds upon the conversion from the GS to ^{5}MC state. The ^{5}MC state lifetime of the complex in MeCN is 4 ns [140]. By introducing the strong σ-donating NHC ligands in place of the side pyridine rings in $[Fe(NHC)_2]^{2+}$, the lifetime of the ^{5}MC state shortens to 270 ps (this work), which indicates the destabilization of the ^{5}MC state according to the inverse energy gap law [150,151,189,190]. At the same time the amplitude and anisotropy of the structural changes in the complex upon spin conversion become larger. Further enhancement of the σ-donation of the carbenes is achieved by changing the side *t*Bu groups by Me, which increases the ligand field such that ^{5}MC is not populated in the relaxation cascade from the MLCT state. Here, theory predicts an even greater anisotropic elongation of the bonds upon transition from low to ^{5}MC state. The most important structural parameters of the systems are summarized in Table 5.3. Based on this analysis, we can

---

[3] for details refer to original publication [140]

conclude that for this family of systems the increase of the ligand field strength comes hand in hand with more pronounced structural differences between GS and ^{5}MC state.

5.1.2 Summary

In this chapter we have studied the structure and dynamics of the N-heterocyclic carbene iron complex $[\mathrm{Fe(NHC)_2}]^{2+}$ by TR-WAXS. It has been shown that upon laser excitation, the complex relaxes to the metal centered state within <1 ps. Based on comparisons of the experimental data with DFT structures, we conclude that the excited state is ^{5}MC, which confirms the tentative assignment from spectroscopic work. The developed structural optimization procedure based on careful choice of the reaction coordinates shows that the theoretically calculated structure of the ^{5}MC state is in good agreement with the data, which gives a good benchmark for the DFT methods employed in this work. The kinetic and thermodynamic analysis show that the lifetime of the ^{5}MC state is 270 ps and that it is located ~0.4 eV above the ground state energy level. The first value agrees with the optical spectroscopy result reasonably well, whereas the latter shows significant discrepancy from the energy derived from the DFT calculations (0.135 eV), which requires further investigation. The nature of the strong anisotropic expansion of the first coordination shell of iron is discussed on the basis of the interplay between σ-bonding and π-back-bonding in the course of transition from the GS to ^{5}MC. Finally, the results for the $[\mathrm{Fe(NHC)_2}]^{2+}$ complex are compared with sister compounds and the correlations between the structural changes appearing upon spin conversion with the degree of ^{5}MC state destabilization are discussed.

5.2 Charge transfer dynamics in a hetero-nuclear complex

Bimetallic complexes bound with a covalent bridge serve as model systems for studying ET processes in donor-acceptor systems [133, 191]. These complexes are supramolecular systems constituted of a light sensitizer, a linker and a catalytic center. A subclass of these compounds, where ruthenium and cobalt based complexes were chosen as chromophore and chemically active site respectively, have been investigated in detail with optical and x-ray spectroscopies as well as advanced DFT calculations [7, 192–198]. These systems appear to be promising prototypes for single photochemical molecular devices for water-splitting and photo-sensitization applications [199–201].

In this work we investigate the structural dynamics of the bimetallic complex $[(\mathrm{bpy})_2^1\mathrm{Ru}^{\mathrm{II}}$ (tpphz) $^1\mathrm{Co}^{\mathrm{III}}\,(\mathrm{bpy})_2]^{5+}$ (bpy = 2,2'- bipyridine, tpphz = tetrapyrido (3,2- a:2'3'-c:3",2"-h:2"',3"'-j) phenazine), denoted Ru=Co. The dyad consists of two metallic centers $^1\mathrm{Ru}^{\mathrm{II}}$ and $^1\mathrm{Co}^{\mathrm{III}}$, both in low spin states, separated by ~13 Å (Figure 5.21). The absorption spectrum of the Ru=Co complex is similar to the one of $[\mathrm{Ru(phen)}_3]^{2+}$ (phen = phenanthroline) [202–204] (Figure 5.20, a). The absorption features below 400 nm are due to ligand centered transitions in bpy and tpphz, whereas the broad band between 400 and 550 nm is due to MLCT transitions from Ru to bpy and tpphz. A schematic Jablonski diagram of the complex is shown in Figure 5.20(b). Excitation of Ru=Co to the MLCT band leads to a fast transfer of an electron from Ru to Co with a yield of ~0.8 [193]. The time scales of this process were thoroughly investigated with femtosecond optical and x-ray emission spectroscopies [7], which resolved different steps of the process. These steps can be summarized as follows:

$$[{}^1\mathrm{Ru}^{\mathrm{II}}{=}{}^1\mathrm{Co}^{\mathrm{III}}] + h\nu \xrightarrow{(1)} [({}^2\mathrm{Ru}^{\mathrm{III}\bullet}){=}{}^1\mathrm{Co}^{\mathrm{III}}] \xrightarrow{(2)} [{}^2\mathrm{Ru}^{\mathrm{III}}(=^{\bullet}){}^1\mathrm{Co}^{\mathrm{III}}] \xrightarrow{(3)}$$

$$\xrightarrow{(3)} [{}^2\mathrm{Ru}^{\mathrm{III}}{=}{}^2\mathrm{Co}^{\mathrm{II}}] \xrightarrow{(4)} [{}^2\mathrm{Ru}^{\mathrm{III}}{=}{}^4\mathrm{Co}^{\mathrm{II}}]$$

First, the excitation of the Ru MLCT band (1) leads to the injection of an electron to the tpphz bridge (2). Then the electron moves to the Co site (3), which forms a state with intermediate spin S=1/2 (for Co site). Since the arrived electron occupies the (antibonding) e_g^* orbitals, the Co-N distances in the FCS expand, resulting in a decrease in the ligand field strength and therefore a final transition to the HS state (4). All the steps in this process are completed in a few ps and therefore out of the scope of this work. After the

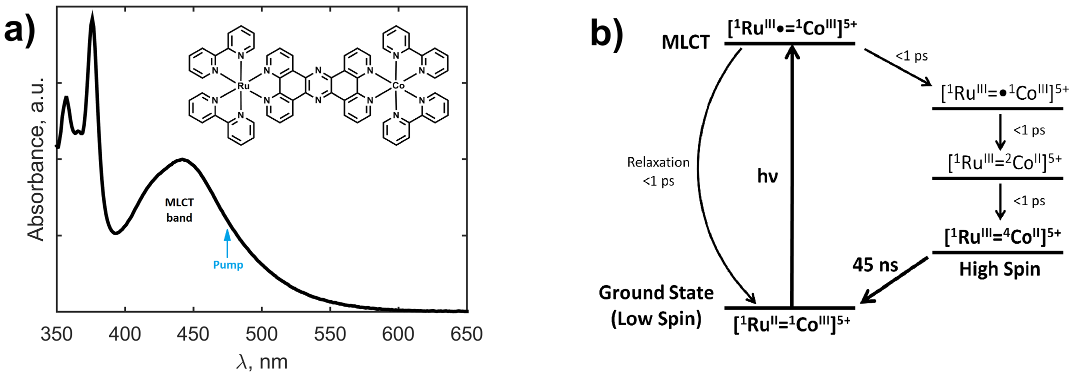

Figure 5.20. Properties of Ru=Co complex. a) Absorption spectrum of Ru=Co/MeCN. The broad band between 400 and 550 nm corresponds to a MLCT transition on the Ru site, which triggers dynamics in this study. b) Schematic Jablonski diagram. Upon excitation to MLCT, part of the molecules relaxes back to the ground state whereas others undergo the ET to the Co center via the tpphz bridge.

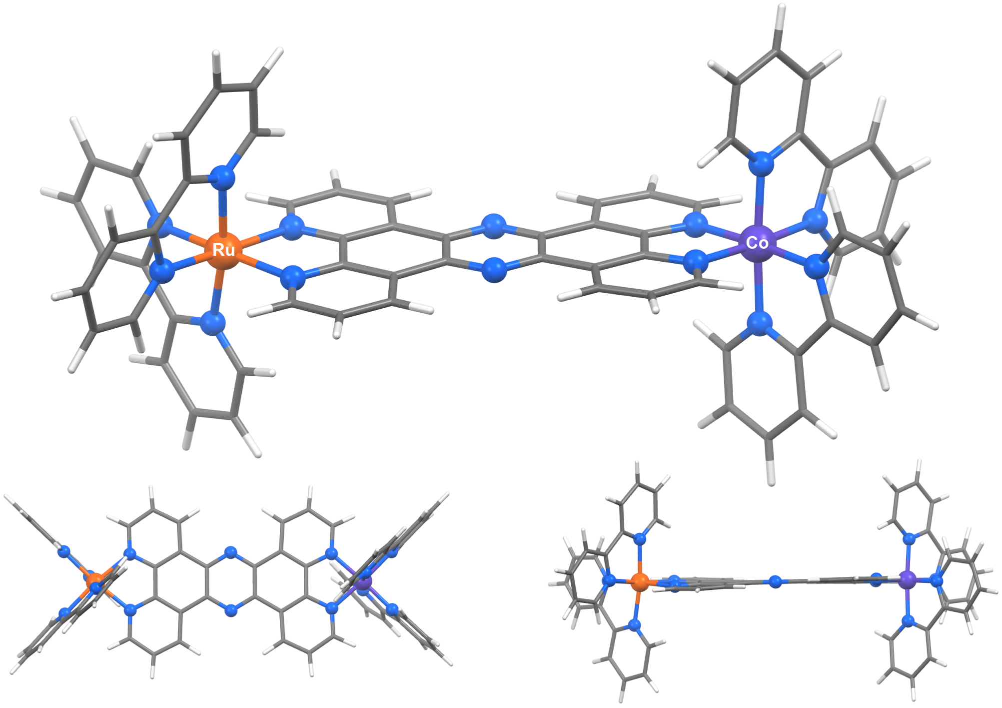

Top view

Side view

Figure 5.21. Ground state structure of Ru=Co complex. The complex consists of a light capturing Ru moiety (electron donor), a catalytic Co moiety (electron acceptor) and a linker (bridge). Both metal centers are surrounded by six nitrogens from the bpy ligands forming octahedral environments.

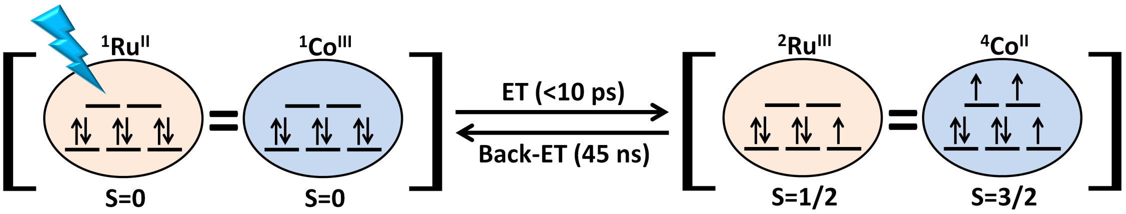

Figure 5.22. Electronic structure dynamics in Ru=Co upon light excitation. Upon excitation an electron from the Ru site is transferred to the Co site on very short time scales (<10 ps, see text for details). Upon formation of the HS state, the complex exhibits pronounced structural changes due to Co FCS expansion by ∼0.2 Å. The excited HS spin state then relaxes to the GS via thermal back-ET, which is in the scope of present work.

ET takes place, the system returns to the ground state via thermal back ET after tens of ns. Figure 5.22 shows a detailed representation of the $3d$ orbital occupation in the initial [^{1}Ru^{II}=^{1}Co^{III}] and final [^{2}Ru^{III}=^{4}Co^{II}] states. The structures in the LS and HS states were also investigated with time-resolved x-ray absorption spectroscopy (TR-XAS) [196]. Upon promotion to the HS state, two electrons occupy the (antibonding) e_g^* orbitals of Co center, leading to isotropic expansion of the Co-N bonds by $\sim$ 0.2 Å.

In this work we will focus on the structural and electronic dynamics of the back ET process in the Ru=Co complex. Although the Ru=Co behavior is relatively well understood, the detailed structural investigation is missing. Based on the previous experience with $[\mathrm{Fe(NHC)_2}]^{2+}$ which has shown that TR-WAXS is sensitive to multi-scale changes in the structure, we will show how the technique provides new insights into the structural dynamics of a complex system such as Ru=Co. The results are reported as follows. First we will investigate the nature of the excited state by probing of the Co center spin state with TR-XES. Then a detailed discussion of the DFT structural model and its fit to TR-WAXS data will be given based on quasi-monochromatic 25.2 keV measurements. This will be followed by the analysis of back ET dynamics obtained from simultaneous TR-WAXS and TR-XES measurements.

5.2.1 TR-WAXS and TR-XES results

The structural dynamics of Ru=Co were investigated by both TR-WAXS and TR-XES. The experimental procedure is described as follows. First, the XES spectrometer was aligned using one of the reference (crystalline) samples $[\mathrm{Co(bpy)_3}]^{3+}$. The alignment procedure was based on the fine tuning the position of the crystal analyzer such that scanned

Kα_1 line is as sharp as possible. This ensures that the Rowland condition is satisfied[4] and the resolution of the spectrometer is optimal. Then XES measurements on the reference compounds $[Co(bpy)_3]^{2+}$ and $[Co(bpy)_3]^{3+}$ were conducted for analysis of TR-XES signal (see below for details). After that, the liquid jet system was installed and time-resolved measurements were performed on the Ru=Co sample. We used a 4 mM MeCN solution of the Ru=Co complex which was excited by laser pulses with an energy of 100 μJ, focused to 210 μm (fluence of 0.20 J/cm^2) and wavelength of 475 nm (red side of the Ru moiety MLCT band). The compound was prepared by Jianxin Zhang from Tianjin Polytechnic University (China) according to the protocol presented in ref. [7]. First, the measurements of the Co Kα emission were done at 200 ps time delay with the pink beam ($E_f = 15$ keV) from by the U17 undulator at 6 mm gap. Then simultaneous TR-WAXS and TR-XES measurements were performed with the standard 18 keV pink beam from U17. During the course of these measurements we analyzed the kinetic traces of the differential XES signals at two energies (6930 and 6931.5 eV) which corresponded to the maxima in the differential spectrum. The time range included 20 time points between -100 ps and 1 μs. Finally, the precise structure of the complex was addressed by TR-WAXS measurements with 25.2 keV quasi-monochromatic x-ray pulses (BW = 1.5 %) at 200 ps delay.

Nature of the excited state

Direct information about the electronic structure of the Co center can be obtained from the Kα emission. The measured XES signals with and without laser are shown in Figure 5.24. Both Kα lines exhibit pronounced changes in width and position at 200 ps due to the change in spin and oxidation state of Co. As discussed in chapter 2, to quantify these changes one has to compare the TR-XES signals with the signals obtained from reference samples. In this work we chose $[Co(bpy)_3]^{2+}$ and $[Co(bpy)_3]^{3+}$ complexes as references since the chemical environment of the Co center is very similar to that in Ru=Co. The reference signals represent the expected changes in XES signals from the $^1Co^{III} \rightarrow {}^4Co^{II}$ transition (Figure 5.23). By constructing the differential time resolved and reference curves according to the procedure described in chapter 3, we can evaluate the TR-XES data. The curves are in good agreement (Figure 5.23, difference curves), which proves that the absorption of the photon by the Ru=Co complex leads to a spin and oxidation state change on the Co center. Based on previous optical studies it indicates that this spin change is due to the charge

---

[4] sample, crystal and detector are all on the Rowland circle.

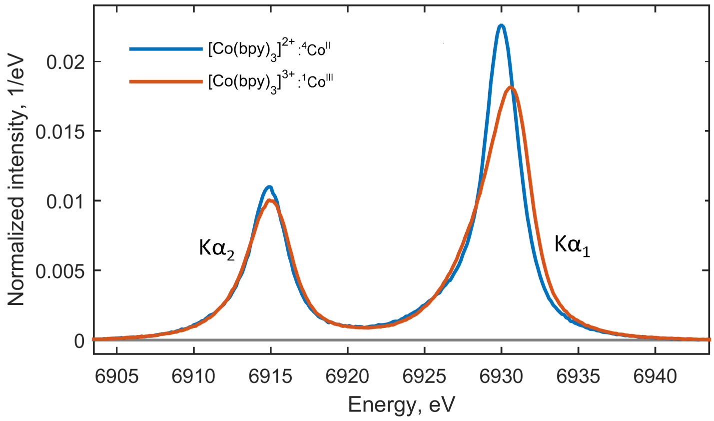

Figure 5.23. Reference XES results. Reference Co K$\alpha_{1,2}$ lines from $[\mathrm{Co(bpy)_3}]^{2+}$ and $[\mathrm{Co(bpy)_3}]^{3+}$ powders, which mimic the expected transition in the Ru=Co complex: $^1\mathrm{Co}^{\mathrm{III}} \rightarrow {}^4\mathrm{Co}^{\mathrm{II}}$.

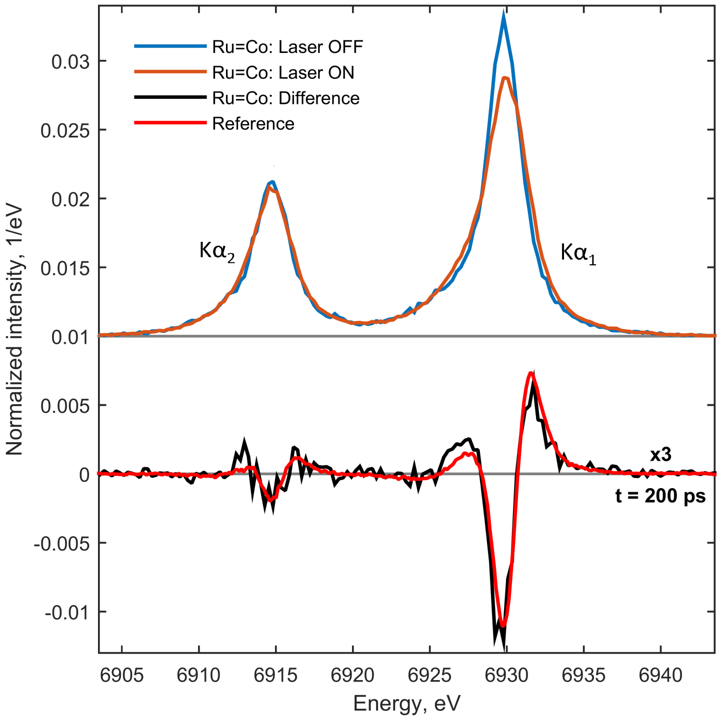

Figure 5.24. TR-XES results. Measured Co K$\alpha_{1,2}$ lines for Ru=Co/MeCN, with and without laser excitation, for a time delay $t = 200$ ps; difference spectrum and scaled reference. Analysis of the difference spectrum gives excitation fraction $\gamma = 0.54 \pm 0.03$.

transfer from the Ru moiety. Based on the integrated absolute difference analysis of the reference and time-resolved curves we estimate the excitation fraction as $\gamma = 0.54 \pm 0.03$. Note that the excitation fraction depends not only on the excitation efficiency of the Ru moiety in Ru=Co, but also on the electron transfer yield. It therefore reflects the overall efficiency of the light induced electron transfer in the present experimental conditions.

Structure of excited complex

In the following we will examine the structural changes associated with ET. The structural models for the low and high spin states were obtained from DFT calculations performed by Mátyás Pápai from the Technical University of Denmark. Calculations were carried out with the ORCA package [205]. The geometries of [^{1}Ru^{II}=^{1}Co^{III}] and [^{2}Ru^{III}=^{4}Co^{II}] were optimized with the B3LYP*/TZVP method which is known to provide satisfactory results for the structure and energetics of transition metal complexes [175, 186, 206–208]. The conducting-like screening solvation model (COSMO) [209] was used, by choosing the dielectric constant for acetonitrile ($\epsilon = 36.6$). The main changes appearing due to ET can be described with a single reaction coordinate, namely, the breathing mode of [Co(bpy)$_3$] moiety. In the ground state the distances between the Co center and the N atoms in the FCS are 1.972 Å. Upon conversion to the high spin state, it expands to 2.167 Å, which concurs with previous TR-XAS findings. Note, that donation of the electron from the Ru site depopulates the (non-bonging) t_{2g} orbitals of Ru, resulting in no significant changes in the Ru moiety. The XYZ coordinates used for the TR-WAXS signal calculation can be found in Appendix C.

The experimental data collected with 25.2 keV x-rays at 200 ps after excitation is fitted with the model consisting of two contributions: solute and solvent heating. The cage simulation was not available in the present study; however, as evident from the previous section on [Fe(NHC)$_2$]$^{2+}$, the cage term is only important at low $q \lesssim 2.0$ Å^{-1}. Therefore, only the data in the high q region above 2.0 Å^{-1} was analyzed. The fit shows reasonable agreement between experiment and theory (Figure 5.25, a). However, certain experimental features are not reproduced well: the amplitudes of the fine features at 3 and 5 Å^{-1} and the phase of the oscillations above 8 Å^{-1}. The discrepancies are manifested in an increased value of χ^2. Interestingly, the fit of 18 keV (pink) data at $t = 200$ ps does not show these discrepancies (Figure 5.25, a). Here the experimental features are smeared and damped due to the soft tail of the U17 spectrum, which makes the measurement insensitive to

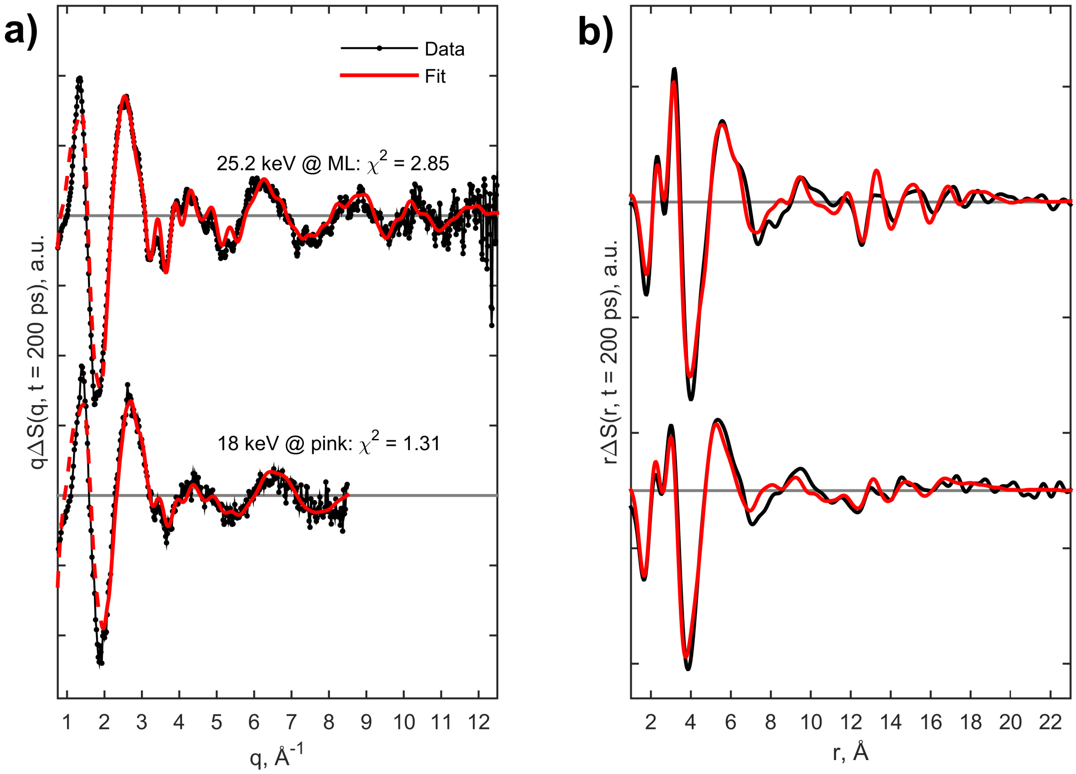

Figure 5.25. Fit of the 25.2 keV (ML) and 18 keV (pink) data at 200 ps with a structural model for the $^1Co^{III} \rightarrow {}^4Co^{II}$ transition in the Ru=Co dyad. The results are shown in q- (a) and r-space (b). The dashed part of the curves represents the extrapolation of the model to the low-q region which was not used for fit.

the finer structural details. The smearing is also pronounced in the calculated RDFs making the high frequencies above 12 Å almost indistinguishable from the high frequency experimental noise, therefore reducing the sensitivity of the analysis to the long range order of the molecule. This demonstrates again the strength of TR-WAXS using the multilayer monochromator in comparison to the classical pink experiment.

The decomposition of the model into components is shown in Figure 5.26. The experimental signal at low q is dominated by the solvent, the nature of which was discussed in the previous section. On the other hand, the solute dominates the data in the high q region and has a very rich structure. In order to unravel the structural changes, the full and differential RDFs for Ru=Co were calculated (Figure 5.28). According to the calculated differential RDF, the changes in solute structure appear on multiple scales, which can be roughly separated in three regions. The first region corresponds to the changes in

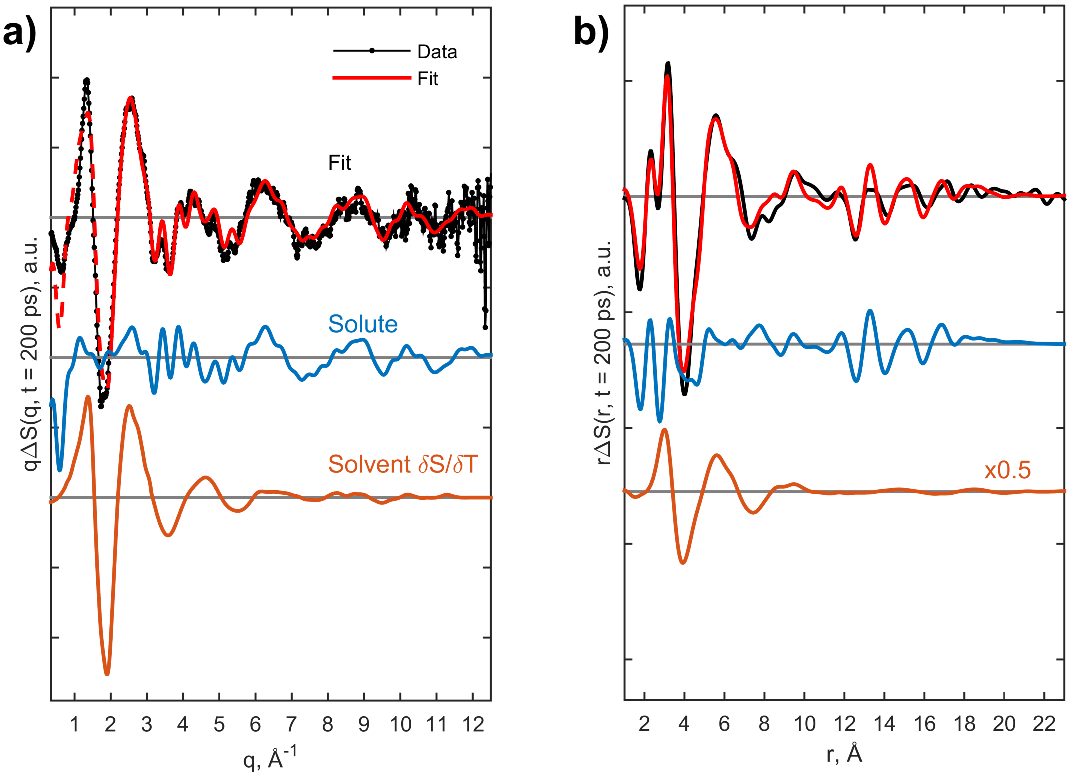

Figure 5.26. Decomposition of the model for 25.2 keV data ($t = 200$ ps) to solute and solvent components shown in q- (a) and r-space (b).

the Co local structure which shows up in the region $r \leq 6$Å. Here, the excitation leads to the expansion of the Co-N bonds in the FCS by ~0.2 Å (Co-$N_{1,2}$ bonds; for atom labeling see Figure 5.27), which is observed as negative and positive peaks located around 2 Å in the differential RDF. The following oscillations are due to an increase in distance between Co and the closest carbon atoms in the pyridine rings (C_{1-4}). The region between 4 and 6 Å involve a mixture of signals due to an increase in distances between Co and other atoms in pyridines and also between the pyridines themselves. The second region in r (6-11 Å) corresponds to the changes between the Co moiety and the tpphz bridge atoms, which are quite difficult to assign since a lot of interatomic correlations are involved. At longer distances above 12 Å we find the third region, which corresponds to the overall increase in the distance between the Co and Ru moieties. The change in the distance between the Co and Ru centers from ~12.8 to 13 Å appears as a well pronounced oscillation in this part of the RDF. Other features in this region are mainly due to changes in correlations between the metals and the N, C, H atoms in the bipiridines.

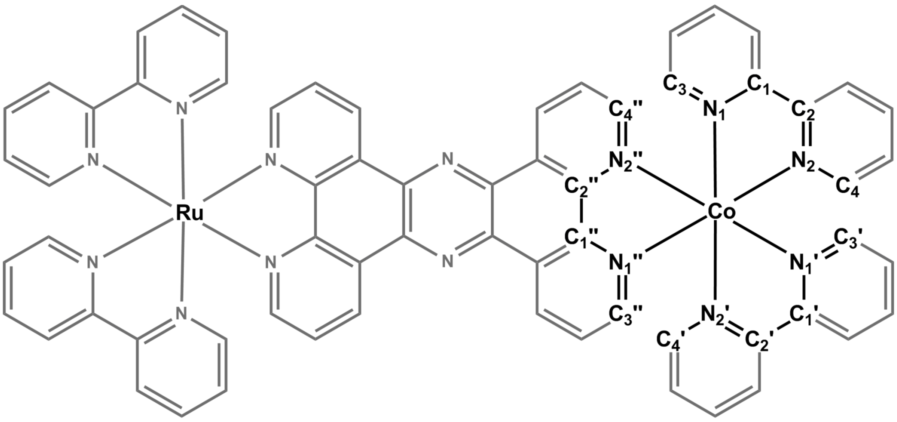

Figure 5.27. Atom labeling for Ru=Co used in Figure 5.28 .

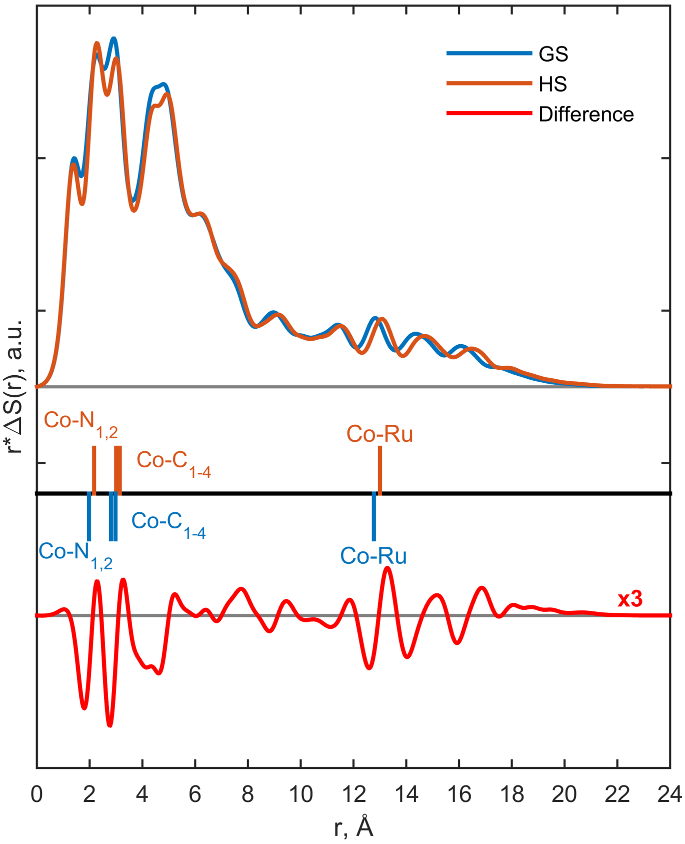

	GS	^{5}MC
Co-$N_{1,2}$ Co-$N'_{1,2}$ Co-$N''_{1,2}$	1.975	2.167
Co-$C_{1,2}$ Co-$C'_{1,2}$ Co-$C''_{1,2}$	2.805	3.005
Co-$C_{3,4}$ Co-$C'_{3,4}$ Co-$C''_{3,4}$	2.979	3.140
Co-Ru	12.773	13.006

Figure 5.28. Total radial distribution functions for the low and high spin states and the Co contributions from the differential signal. The signal at low r (0-6 Å) represents changes appearing mainly in the proxmity of Co due to the elongation of Co-N bonds. Due to the elongation of the Co-N''_1 and Co-N''_2 bonds, the Co moiety moves away from the bridge which shows up in middle range signal (6-11 Å). Similarly, the signal above 11 Å is due to changes in interatomic distances between Co and Ru moieties from the expansion.

Based on these insights one can now attempt to describe the main discrepancies between the model and the data. As evident from Figure 5.26 (b), the low-r region, $r < 7$ Å, is described fairly well with the theory, confirming the correctness of the DFT calculation for the Co moiety structure in the ground and HS state. At larger distances the fit deteriorates indicating some errors in the description of the bridge structure and the longer range order in the ground and/or excited state. A recent Quantum Mechanical/Molecular Mechanical (QM/MM) Dynamics [210] study has shown that the inclusion of solvent interactions significantly changes the structure of the Ru=Co complex compared to the DFT calculation. The new calculations predict a non-planar geometry of the ligands and changes in the orientation of the ligands around the metal centers in comparison to the DFT structure.

Population dynamics

Information about the dynamics of the back ET process can be obtained from the analysis of the 18 keV data. First, the individual fits of the DFT model (described above) to the TR-WAXS data at different time points were performed (Figure 5.29, a). The Co high spin state population dynamics shows a distinct decay from back ET from Co to Ru: $[{}^1\mathrm{Ru}^{\mathrm{II}}={}^1\mathrm{Co}^{\mathrm{III}}] \leftarrow [{}^2\mathrm{Ru}^{\mathrm{III}}={}^4\mathrm{Co}^{\mathrm{II}}]$. This observation is also confirmed by TR-XES. As mentioned in the experimental section the spectrometer was set to measure the kinetic traces at 6930 and 6931.5 eV, which correspond to the negative and positive peaks in the differential signal (Figure 5.29, b). The decays of the differential amplitude $dI_{\mathrm{XES}}(t)$ at both energies indicates that the population of the high spin state of Co is decreasing ($dI_{\mathrm{XES}}(t) = I_{\mathrm{XES}}(t) - I_{\mathrm{XES}}(-3\mathrm{ns})$).

We will now apply the global fit approach to the TR-WAXS data. The depopulation of the high spin state is modeled by a single exponential decay, whereas the rest of the procedure follows the standard protocol. A comparison of the global and individual fits for the excited state population is shown in Figure 5.29. The global fit agrees with the individual points, showing the success of the procedure; the best fit values of excited state fraction and lifetime of the high spin state are $\gamma = 0.17 \pm 0.02$ (0.68 ± 0.08 mM) and 40 ± 10 ns respectively. The TR-XES data was also fitted with a single exponential decay, giving the lifetime values of 50 ± 20 and 55 ± 25 ns for 6930 and 6931.5 eV energies respectively. The excited state fractions obtained from the two techniques disagree: $\gamma_{\mathrm{WAXS}} = 0.17 \pm 0.02$ and $\gamma_{\mathrm{XES}} = 0.54 \pm 0.03$. This might be due to laser and/or x-ray beam drifts during the course of the experiments. On the other hand, the lifetimes are consistent and also

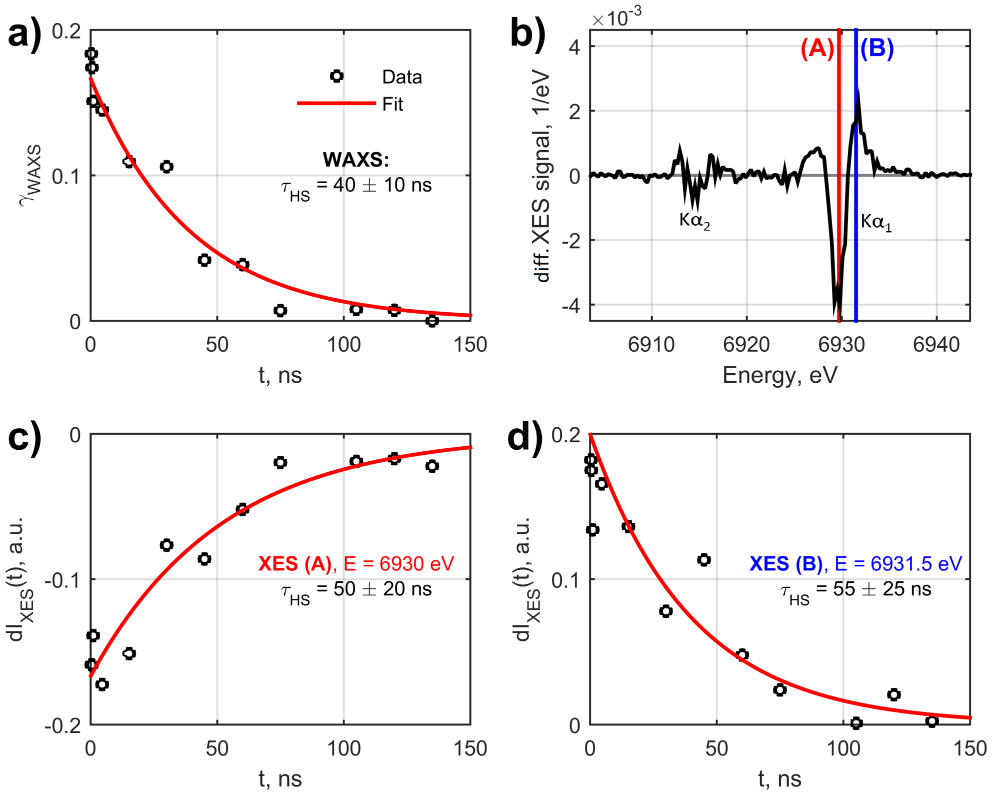

Figure 5.29. Determination of the Co HS state lifetime from TR-WAXS and TR-XES. a) Comparison of individual and global fit results for excited state fraction obtained from TR-WAXS. b) Differential XES spectrum collected at 200 ps with lines indicating position of crystal analyzer during simultaneous TR-WAXS and TR-XES measurements. c) The kinetic trace of A feature on the difference spectrum and its fit with single exponential decay model. d) The same as (c) but for feature B on the difference spectrum.

concurring with previous TR-XAS and optical spectroscopy work (see table on 5.29). The overall comparison of the fitted curves and the time-dependent changes in concentration, temperature and density are shown on Figure 5.30. The excitation state fraction and HS lifetime are shown in Table 5.4.

We also tried to optimize the energy difference between the ground and excited state as it was done for the $[\mathrm{Fe(NHC)_2}]^{2+}$ complex. However, in the present case the time scale of the high spin state relaxation is very close to the time scale of the liquid expansion due to laser heating (Figure 5.30 b,c). Therefore the temperature changes from the heating from the excited state relaxation and expansion coincide obscuring a reliable extraction of the energy difference ΔE. Moreover, the scales of temperature changes due to these processes appear to be very different. Recent theoretical work predicts ΔE to be 0.18 eV [197], from

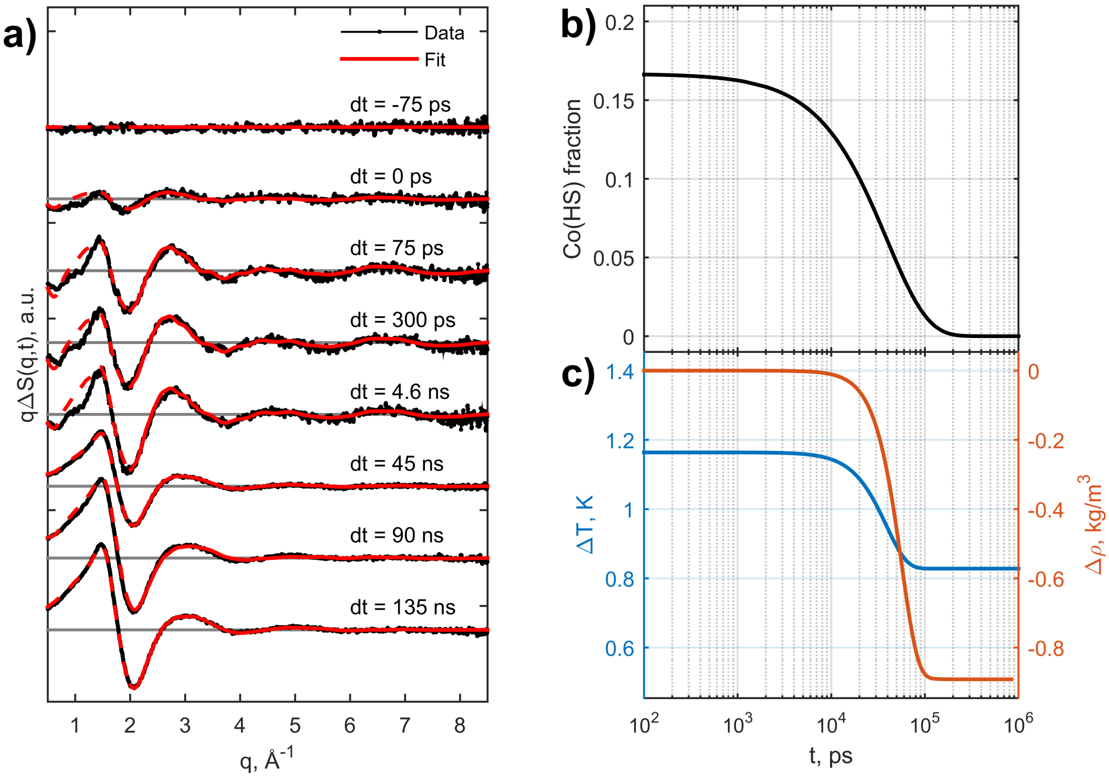

Figure 5.30. Results of global fitting results of TR-WAXS data. a) Comparison of global fit result and experimental data for representative set of curves. b) time-dependent changes in concentration of the Co center in the high spin state. The relaxation appears due to the back ET $[^1\mathrm{Ru}^{\mathrm{II}}={}^1\mathrm{Co}^{\mathrm{III}}]\leftarrow[^2\mathrm{Ru}^{\mathrm{III}}={}^4\mathrm{Co}^{\mathrm{II}}]$ with a time constant of 40 ± 10 ns. c) Temperature and density as a function of time. From panels (b) and (c) it is evident that main changes in excited state population and temperature/density changes appear between 10 and 100 ns, which obscures a reliable extraction of the energy difference between excited and ground state ΔE.

which we estimate a temperature change of only ∼0.006 K. The temperature change due to expansion can be derived from the hydrodynamics equations as described in literature [34]. Here we are interested in the difference between the temperatures at 100 ps and 1 μs, which can be calculated as $\Delta T(100\mathrm{ps}) - \Delta T(1\mu\mathrm{s}) = \Delta T(100\mathrm{ps}) \cdot (1 - C_V/C_P)$, where C_V and C_P are specific heat capacities at constant volume and pressure respectively. In the present experiment $\Delta T(100\mathrm{ps})$ is 1.17 K and the heat capacity values for acetonitrile are $C_V = 63.53$ J/(mol·K) and $C_P = 90.00$ J/(mol·K). Therefore the temperature difference is ∼0.34 K, which is much larger than the expected temperature change due to heating. For all of these reasons, the energy difference ΔE appears to be ill-defined in present

Table 5.4. Comparison of excited state fractions γ and lifetimes of high spin state τ obtained from different techniques.

Technique	Exc. state fraction γ	Lifetime τ (ns)
TR-WAXS	0.17 ± 0.02	40 ± 10
TR-XES	0.54 ± 0.03	50 ± 20 (E = 6930 eV) 55 ± 25 (E = 6931.5 eV)
TR-XAS[a]	–	45 ± 2
Optical spectroscopy[b]	–	48

[a] value from [196];

[b] value from [193];

measurements.

As in all previous experiments, at 1 μs we observe an additional temperature rise of 0.7 K which cannot be attributed to heat due to the relaxation of the Ru=Co complexes in the high spin state. For this system an additional temperature rise is expected, since the yield of electron transfer from Ru to Co center is not 1. Some part of the excited complexes relax either through fluorescence or non-radiative transition to the GS via Ru MC states. It is difficult to precisely estimate the fraction of complexes undergoing these types of relaxation due to lack of information about the energy levels which we leave for future work.

5.2.2 Summary

In this work we have studied the structural dynamics of the Ru=Co dinuclear complex with TR-WAXS and TR-XES. The changes in the spin state of the Co center due to the light induced charge transfer from the Ru donor were directly observed and quantified by TR-XES measurements. The DFT models for the high and low spin states were found to be in a reasonable agreement with the high resolution data collected with 25.2 keV x-rays. However, certain discrepancies between theory and experiment allow us to conclude that the DFT results do not accurately describe the long range structure of the complex upon transition from the ground to high spin state. This might point to the incapability of the DFT method for the description of such a complex system; future analysis based on QM/MM calculations is promising new insights into the structural dynamics of the complex. The population dynamics of the system was characterized with simultaneous TR-WAXS and TR-XES measurements. The values of the excited state fraction and lifetime of the high spin state from the two techniques are in agreement with each other and with the previous results from the literature. Overall, this work shows the complementarity of the two techniques in characterizing the local electronic and the global structural changes during the course of photochemical reactions.

Chapter 6

Conclusions

In this thesis we studied a number of systems spanning from simple triatomic molecules to transition metal complexes and obtained new insight into their photoinduced structural dynamics. Overall the results of the thesis demonstrate the superb sensitivity of TR-WAXS for probing multi-scale aspects of structural dynamics of molecular systems in solution. Being a global probe, TR-WAXS provides information about interatomic correlations spanning up to a few tens of Å (Ru=Co project), uncovering details inaccessible by other methods. The global sensitivity of the technique makes it possible to fully solve the excited state structure of molecules constituted of up to ∼100 atoms (HgX_2, I_3^-, $[Fe(NHC)_2]^{2+}$ projects). These structural investigations are possible thanks to the high quality hard x-ray beam with a well defined energy spectrum provided by multilayer monochromators on ID09 beamline. Additionally, for complex systems such as $[Fe(NHC)_2]^{2+}$, substantial theoretical support is necessary for producing structural models with a reduced number of degrees of freedom. Based on this combination of theory and experiment, the structural precision of TR-WAXS reaches a few hundredths of Å. The following paragraphs give a brief overview of the obtained scientific results and provide future perspectives for each of the project.

The study of the dissociation reaction of mercury halides HgX_2 ($X = I, Br$) have revealed that some of the initially formed photofragments (up to 30 %) undergo ultrafast recombination in les than 100 ps, which is attributed to so-called secondary (diffusion driven) geminate recombination. The observation of this behavior was confirmed by TR-WAXS and TOAS. Although this recombination channel was already observed by optical spectroscopy on organic molecules several decades ago [87–89], this study represents the first successful detection of this channel with x-rays. As suggested by our simulations, future experiments with better temporal resolution will capture the initial stages of photofragment separation and thus provide a understanding of the role of the solvent in chemical reactions.

TR-WAXS data on the dissociation reaction of triiodide (I_3^-) clearly demonstrates the presence of additional short-lived (∼70 ps) reaction product. Based on the literature, its appearance can be attributed to the formation of contact ion pairs ($[I_2^- + I]$) [112]. Although the structural model for this object is not available at the moment, we have found that the TR-WAXS signal from this species is significantly different from the signal calculated based on the free photofragment model ($[I_2^-] + [I]$). The main future goal in this project is to develop a theoretical model for the description of contact ion pairs based on MD simulations. As soon as this is accomplished, one can extend the work to other systems demonstrating various ion formations (contact or solvent-shared ion pairs).

Another striking result in regards to the studied triatomic molecules is the observation of the bend geometry of the ground state structures. This effect was found to be significant for HgX_2 and I_3^-; the bending of $HgBr_2$ was also detected but it was found to be statistically insignificant[1] due to low signal-to-noise ratio of the experiment. This observation contradicts the findings of optical and Raman spectroscopy on all the studied molecules [78, 126]. On the other hand, similar bending effect was also observed in early electron diffraction experiments on triatomic molecules such as CO_2 [95, 96]. This effect was explained theoretically: the bending appears due to perpendicular vibrations of the molecule, leading to efficient shortening of the distance between side atoms of a triatomic molecule. It is known as the Bastiansen-Morino shrinkage effect [93, 94]. Therefore, as a first step for the explanation of the observed data, we suggest to include this effect into the model. The extension of the study to other simple molecules would also help to understand the impact of this effect on the analysis of more complex systems.

Studies of the iron N-heterocyclic carbene complex ($[Fe(NHC)_2]^{2+}$) belonging to a new family of promising light-harvesting molecules, revealed characteristic structural changes upon the conversion from a low spin to a high spin state. The pronounced anisotropy in expansion of the axial and the equatorial bonds was found to correlate with the increased ligand field of the complex and therefore the high spin state lifetime. One of the main achievements of the study is the precise determination of the excited state structure based

---

[1] in comparison to the linear geometry model.

on a careful choice of reaction coordinates. The potential extension of this work includes experiments on similar systems, the application of other techniques (various x-ray spectroscopies) and measurements with increased temporal resolution. Such measurements will improve the understanding of photochemistry of iron complexes and will help to reach the long term goal of designing cheap and efficient solar cells.

The TR-XES study of the bimetallic complex Ru=Co have shown that optical photon absorption triggers an electron transfer from the Ru to Co site. The TR-WAXS data supports these observations; however, it is found that the structural model produced by DFT calculations do not precisely describe the experimental results. This discrepancy appears to be an important finding because it suggests that for such complex system, the solvent-solute interactions have to be taken into account in a more elaborate way. The future of this project is mainly focused on the detailed characterization of the complex structure using recent advanced theoretical results based on QM/MM calculations. Another conclusion of this work is that the simultaneous use of several techniques readily enriches the knowledge about transient dynamics and simplifies the physical interpretation of the results. Recently, the combined approach of using time-resoled x-ray scattering, emission and absorption as well as transient optical spectroscopy, became the standard for studies in the field of ultrafast solution phase chemistry [5–8, 211]. This study therefore gives another confirmation of the advantages of combined studies.

Conclusion

6.1 Conclusion (version française)

Dans cette thèse, nous avons étudié un certain nombre de systèmes couvrant à partir de molécules simples triatomiques de complexes de métaux de transition et nous avons obtenu de nouvelles informations sur leur dynamique structurelle photoinduite. Les résultats de la thèse montrent la sensibilité exceptionnelle du TR-WAXS pour sonder les aspects multi-échelles de la dynamique des structures des systèmes moléculaires en solution. Etant une sonde globale, TR-WAXS fournit des informations sur les corrélations interatomiques couvrant jusqu'à quelques dizaines de Å (projet Ru=Co), en découvrant les détails inaccessibles par d'autres méthodes. La sensibilité globale de la technique permet de résoudre complètement la structure des molécules constituées de jusqu'à ∼100 atomes à l'état excité (projets HgX_2, $I_3{}^-$, $[Fe(NHC)_2]^{2+}$). Ces enquêtes structurelles sont devenues possibles grâce à la haute qualité de faisceau à rayons X dur avec un spectre d'énergie bien définie fournie par monochromateurs multicouches sur ID09. En outre, pour les systèmes complexes tels que $[Fe(NHC)_2]^{2+}$, soutien théorique substantielle est nécessaire pour la production de modèles structurels avec un nombre réduit de degrés de liberté. Sur la base de cette combinaison de la théorie et de l'expérience, la précision structurelle de TR-WAXS atteint quelques centièmes de Å. La version anglaise des conclusions donne un bref aperçu des résultats scientifiques obtenus et des perspectives d'avenir pour chacun des projets.

Appendices

Appendix A

Energy resolution of x-ray emission spectrometer

The resolution of the XES spectrometer based on Rowland circle geometry is thoroughly discussed in the literature [212]. The contributions to the finite resolution of the instrument have various sources, such as Darwin width of the analyzer crystal, finite size of the source and intrinsic loss of resolution due to Johann geometry itself. The Darwin width of the crystal appears to be relatively small in comparison with the other contributions due to the employment of high order reflection in the crystal analyzer ($(\delta E/E)_{\mathrm{DW}}$ for Si (531) is 5.92×10^{-6}). The horizontal sample size is anticipated to be one of the dominating contributions to the resolution in the present geometry and expression for its calculation can be easily derived from the Bragg's law:

$$\left(\frac{\delta E}{E}\right)_{\mathrm{S}} = \frac{\delta y \cdot \cot\theta_B}{R},$$

where R is the crystal curvature radius ($\sim$ 1 m); δy is size of the source projection onto the crystal plane ($\sim$ 260 μm taking into account the thickness of the liquid jet, size of the x-ray beam and the takeoff angle); and θ_B is the Bragg angle (for Kα_1 at 6930 eV and Si(531) $\theta_B = 77°$). For the ID09 setup we estimate this contribution to be 6×10^{-5}.

The Johann geometry contribution comes from the following. The curvature of the crystal is equal to the diameter of the Rowland circle which results in a slight deviation of the outer part of the crystal surface from the Rowland condition (for point to point focusing). On the edge of the crystal this results in a slight energy shift expressed as [212]

$$\left(\frac{\delta E}{E}\right)_{\mathrm{J}} = \frac{1}{2}\left(\frac{r}{R}\right)^2 (\cot\theta_B)^2,$$

where r is the radius of the crystal analyzer (5 cm in our case). The corresponding value is estimated as 7×10^{-5}. The estimation of the overall resolution by combining all contributions $\delta E/E = \sqrt{(\delta E/E)^2_{\mathrm{DW}} + (\delta E/E)^2_{\mathrm{S}} + (\delta E/E)^2_{\mathrm{J}}}$ which gives the value of $\sim 1 \times 10^{-4}$. The experimentally measured width of Kα_1 line is 2.8 eV (Figure 2.10); taking into account the natural width of the Co Kα_1 line (2.33 eV, from [20]), one can estimate the experimental resolution to be 1.5×10^{-4}, which agrees with our estimation. The discrepancy between the experimental and calculated value might be due to the aberrations of the crystal.

Appendix B

Structure of [Fe(NHC)$_2$]$^{2+}$ complex

Table 2.1. Atomic XYZ coordinates (Å) of [Fe(NHC)$_2$]$^{2+}$.

Atom	GS			^{3}MC			^{5}MC		
	X	Y	Z	X	Y	Z	X	Y	Z
C	-0.9962	-3.0053	3.0129	-1.1510	-1.2361	4.0730	-3.4626	2.7784	-1.1573
C	-2.1460	-2.5172	2.5263	-2.3003	-1.0351	3.4120	-2.9271	2.3431	-2.3108
H	-0.8520	-3.7574	3.7652	-1.0055	-1.5452	5.0908	-4.2925	3.4438	-1.0027
C	-2.1464	2.5143	-2.5297	-2.3011	1.0349	-3.4111	2.6864	-2.1355	-2.7494
C	-0.9965	3.0015	-3.0172	-1.1520	1.2357	-4.0725	3.3296	-2.6522	-1.6881
H	-0.8518	3.7513	-3.7717	-1.0068	1.5444	-5.0904	4.1709	-3.3206	-1.6645
C	-4.0024	0.8523	-0.8503	-4.1781	0.3521	-1.1589	0.7285	-0.5898	-4.3528
C	-4.0021	-0.8499	0.8525	-4.1779	-0.3517	1.1605	-1.1565	0.9056	-4.2052
H	-4.5270	1.5210	-1.5180	-4.7127	0.6249	-2.0579	1.4356	-1.1549	-4.9425
H	-4.5266	-1.5178	1.5210	-4.7123	-0.6245	2.0595	-1.9197	1.5046	-4.6803
C	0.9951	3.0096	3.0113	1.2423	4.1497	1.2589	2.8413	3.3004	1.4222
C	2.1454	2.5217	2.5255	2.3564	3.4320	1.0410	2.4194	2.6654	2.5293
H	0.8497	3.7619	3.7632	1.1479	5.1740	1.5696	3.5223	4.1272	1.3327
C	2.1471	-2.5197	-2.5214	2.3551	-3.4326	-1.0414	-2.1689	-2.8765	2.5284
C	0.9970	-3.0076	-3.0077	1.2408	-4.1500	-1.2589	-2.6941	-3.4251	1.4193
H	0.8521	-3.7601	-3.7594	1.1460	-5.1743	-1.5697	-3.3735	-4.2531	1.3291
C	4.0037	-0.8461	-0.8527	4.1302	-1.1533	-0.3503	-0.5892	-1.0785	4.2815
C	4.0029	0.8495	0.8568	4.1306	1.1522	0.3496	0.9625	0.7663	4.2804
H	4.5285	-1.5110	-1.5238	4.6617	-2.0537	-0.6236	-1.1738	-1.8136	4.8150
H	4.5271	1.5144	1.5285	4.6623	2.0524	0.6228	1.5881	1.4682	4.8123
C	2.6191	0.8082	0.8125	2.7449	1.0932	0.3317	0.8658	0.7705	2.8972
C	2.6198	-0.8051	-0.8093	2.7446	-1.0939	-0.3321	-0.6051	-0.9899	2.8978

... Continued on the next page ...

Table 2.1. Atomic XYZ coordinates (Å) of [Fe(NHC)$_2$]$^{2+}$ (Continued).

Atom	GS			^{3}MC			^{5}MC		
	X	Y	Z	X	Y	Z	X	Y	Z
C	-2.6183	-0.8073	0.8099	-2.7938	-0.3336	1.1006	-1.0381	0.8251	-2.8259
C	-2.6186	0.8083	-0.8093	-2.7940	0.3339	-1.0994	0.7529	-0.6017	-2.9665
C	4.6926	0.0018	0.0022	4.8179	-0.0006	-0.0004	0.2144	-0.1790	4.9655
H	5.7758	0.0019	0.0025	5.9014	-0.0007	-0.0005	0.2577	-0.2149	6.0476
C	-4.6915	0.0014	0.0015	-4.8581	0.0002	0.0008	-0.2495	0.1807	-4.9632
H	-5.7748	0.0020	0.0023	-5.9417	0.0002	0.0009	-0.3061	0.2162	-6.0447
N	-1.9349	0.0005	0.0003	-2.1352	0.0000	0.0004	-0.1080	0.0890	-2.2261
N	1.9359	0.0017	0.0010	2.0714	-0.0002	-0.0001	0.1030	-0.0870	2.2270
C	0.3998	1.4583	1.4571	0.5467	2.0820	0.6320	1.4210	1.6811	0.7160
C	0.4008	-1.4557	-1.4544	0.5460	-2.0822	-0.6316	-1.3617	-1.7325	0.7137
C	-0.3992	-1.4549	1.4582	-0.5496	-0.5986	1.9732	-1.7498	1.4107	-0.5791
C	-0.3997	1.4560	-1.4577	-0.5500	0.5986	-1.9727	1.6760	-1.3485	-0.8487
H	-3.1679	-2.7533	2.7654	-3.3226	-1.1322	3.7325	-3.1995	2.5586	-3.3288
H	-3.1684	2.7486	-2.7701	-3.3235	1.1319	-3.7314	2.8626	-2.2695	-3.8019
H	3.1689	-2.7573	-2.7592	3.3907	-3.7108	-1.1259	-2.3038	-3.1374	3.5631
H	3.1671	2.7593	2.7637	3.3920	3.7100	1.1251	2.6627	2.8347	3.5633
N	-0.0548	2.3684	2.3676	0.1563	3.3237	1.0087	2.2285	2.6948	0.3358
N	1.7706	1.5836	1.5871	1.9193	2.1759	0.6602	1.5543	1.6803	2.0843
N	1.7718	-1.5813	-1.5835	1.9186	-2.1764	-0.6604	-1.3596	-1.8447	2.0838
N	-0.0533	-2.3658	-2.3653	0.1551	-3.3237	-1.0083	-2.1965	-2.7232	0.3319
N	0.0545	-2.3656	2.3689	-0.1020	-0.9723	3.2035	-2.7396	2.2073	-0.1212
N	-1.7702	-1.5813	1.5862	-1.9272	-0.6498	2.1424	-1.8838	1.5101	-1.9438
N	-1.7707	1.5811	-1.5869	-1.9276	0.6499	-2.1415	1.6807	-1.3428	-2.2233
N	0.0539	2.3649	-2.3701	-0.1027	0.9720	-3.2032	2.7064	-2.1683	-0.5478
Fe	0.0005	0.0011	0.0007	-0.1007	0.0000	0.0002	-0.0028	0.0007	0.0003
C	-1.4745	2.7086	2.7048	-1.2592	-3.7864	-1.1485	-2.5653	-3.0294	-1.0832
C	-2.1471	3.2659	1.4577	-1.9398	-3.6660	0.2096	-3.2971	-1.8188	-1.6533
C	-2.1554	1.4603	3.2498	-1.9397	-2.9319	-2.2111	-1.2857	-3.3367	-1.8511
C	-1.5255	3.7847	3.7888	-1.2958	-5.2461	-1.5913	-3.4847	-4.2449	-1.1359
H	-1.6581	4.1922	1.1450	-1.4527	-4.3156	0.9415	-4.2267	-1.6397	-1.1063
H	-2.0968	2.5615	0.6347	-1.8942	-2.6438	0.5770	-2.6815	-0.9235	-1.5797
H	-3.1973	3.4815	1.6670	-2.9884	-3.9612	0.1262	-3.5409	-1.9933	-2.7039
H	-1.6791	1.1452	4.1819	-1.4528	-3.0659	-3.1806	-0.8017	-4.2302	-1.4480
H	-3.2084	1.6696	3.4520	-2.9884	-3.2232	-2.3055	-1.5185	-3.5109	-2.9041
H	-2.0955	0.6394	2.5439	-1.8934	-1.8778	-1.9490	-0.5854	-2.5074	-1.7795
H	-2.5784	3.9887	3.9940	-2.3436	-5.5401	-1.6803	-3.7136	-4.4467	-2.1842

... Continued on the next page ...

Table 2.1. Atomic XYZ coordinates (Å) of $[Fe(NHC)_2]^{2+}$ (Continued).

Atom	GS			^{3}MC			^{5}MC		
	X	Y	Z	X	Y	Z	X	Y	Z
H	-1.0675	3.4563	4.7252	-0.8281	-5.3931	-2.5681	-3.0080	-5.1382	-0.7239
H	-1.0674	4.7232	3.4673	-0.8280	-5.9110	-0.8608	-4.4321	-4.0690	-0.6201
C	-1.4727	-2.7068	-2.7038	-1.2578	3.7869	1.1494	-3.0472	2.4405	1.3219
C	-2.1493	-3.2574	-1.4558	-1.9390	3.6667	-0.2084	-3.4723	1.1100	1.9345
C	-2.1511	-1.4611	-3.2573	-1.9383	2.9328	2.2124	-1.7970	3.0024	1.9869
C	-1.5221	-3.7883	-3.7826	-1.2936	5.2467	1.5921	-4.1845	3.4467	1.4625
H	-1.6630	-4.1837	-1.1383	-1.4520	4.3161	-0.9405	-4.3877	0.7451	1.4610
H	-2.0994	-2.5500	-0.6354	-1.8939	2.6445	-0.5757	-2.6967	0.3571	1.8015
H	-3.1993	-3.4716	-1.6669	-2.9874	3.9624	-0.1246	-3.6610	1.2361	3.0032
H	-1.6663	-1.1463	-4.1851	-1.4509	3.0667	3.1817	-1.5363	3.9725	1.5556
H	-3.2014	-1.6735	-3.4697	-2.9868	3.2246	2.3072	-1.9724	3.1323	3.0573
H	-2.1009	-0.6390	-2.5520	-1.8926	1.8787	1.9504	-0.9539	2.3293	1.8477
H	-2.5749	-3.9943	-3.9871	-2.3412	5.5411	1.6816	-4.3642	3.6017	2.5284
H	-1.0641	-3.4639	-4.7203	-0.8253	5.3936	2.5687	-3.9316	4.4163	1.0253
H	-1.0635	-4.7249	-3.4563	-0.8258	5.9114	0.8614	-5.1158	3.0824	1.0215
C	1.4735	-2.7094	2.7062	1.3207	-1.1099	3.6562	2.4517	3.1226	-1.0783
C	2.1503	-3.2535	1.4556	1.9922	-2.1786	2.8052	3.0881	1.9592	-1.8306
C	2.1530	-1.4671	3.2661	1.9925	0.2514	3.5433	1.1041	3.5163	-1.6716
C	1.5223	-3.7966	3.7792	1.3782	-1.5533	5.1164	3.3901	4.3237	-1.1227
H	1.6636	-4.1776	1.1328	1.5229	-3.1512	2.9755	4.0667	1.7179	-1.4069
H	2.1012	-2.5408	0.6399	1.9102	-1.9423	1.7500	2.4617	1.0711	-1.7697
H	3.2002	-3.4697	1.6659	3.0497	-2.2523	3.0691	3.2209	2.2252	-2.8819
H	1.6699	-1.1571	4.1965	1.5233	0.9650	4.2257	0.6897	4.3800	-1.1448
H	3.2036	-1.6810	3.4751	3.0499	0.1656	3.8036	1.2248	3.7762	-2.7258
H	2.1016	-0.6406	2.5660	1.9105	0.6418	2.5349	0.3940	2.6954	-1.5915
H	2.5748	-4.0056	3.9815	2.4325	-1.6357	5.3885	3.5162	4.6118	-2.1682
H	1.0667	-3.4767	4.7194	0.9218	-0.8255	5.7918	2.9805	5.1857	-0.5896
H	1.0609	-4.7304	3.4483	0.9222	-2.5341	5.2728	4.3804	4.0885	-0.7241
C	1.4730	2.7067	-2.7083	1.3198	1.1094	-3.6564	3.1498	-2.5064	0.8385
C	2.1486	3.2595	-1.4606	1.9918	2.1782	-2.8058	3.6262	-1.2218	1.5085
C	2.1522	1.4607	-3.2602	1.9915	-0.2519	-3.5437	1.9710	-3.1324	1.5736
C	1.5216	3.7874	-3.7879	1.3766	1.5528	-5.1167	4.2993	-3.5075	0.7944
H	1.6636	4.1876	-1.1469	1.5226	3.1508	-2.9760	4.4947	-0.8152	0.9834
H	2.0959	2.5544	-0.6386	1.9101	1.9419	-1.7506	2.8414	-0.4668	1.5019
H	3.1996	3.4713	-1.6705	3.0491	2.2517	-3.0701	3.9107	-1.4259	2.5434
H	1.6658	1.1423	-4.1860	1.5216	-0.9657	-4.2254	1.6774	-4.0715	1.0970

... Continued on the next page ...

Table 2.1. Atomic XYZ coordinates (Å) of [Fe(NHC)$_2$]$^{2+}$ (Continued).

Atom	GS			^{3}MC			^{5}MC		
	X	Y	Z	X	Y	Z	X	Y	Z
H	3.2017	1.6742	-3.4752	3.0487	-0.1663	-3.8050	2.2472	-3.3391	2.6102
H	2.1049	0.6405	-2.5524	1.9105	-0.6420	-2.5351	1.1136	-2.4631	1.5659
H	2.5741	3.9968	-3.9901	2.4309	1.6354	-5.3891	4.5790	-3.7411	1.8236
H	1.0675	3.4605	-4.7265	0.9202	0.8248	-5.7919	4.0101	-4.4435	0.3095
H	1.0583	4.7227	-3.4639	0.9204	2.5335	-5.2729	5.1841	-3.1008	0.2981

Appendix C

Structure of Ru=Co complex

Table 3.1. Atomic XYZ coordinates (Å) of Ru=Co.

Atom	GS			HS		
	X	Y	Z	X	Y	Z
Ru	2.2970	7.8077	0.6116	2.189241	7.792374	0.710492
Co	3.3456	10.3685	-11.8575	3.437996	10.383421	-11.973450
N	2.3835	9.4524	-0.7356	2.131394	9.421969	-0.657556
C	2.2417	10.7508	-0.4458	1.901470	10.706128	-0.364912
C	2.2117	11.7417	-1.4273	1.887566	11.693800	-1.349369
C	2.3367	11.3853	-2.7562	2.111519	11.345016	-2.667465
C	2.5031	10.0320	-3.0835	2.348116	10.000929	-2.994019
C	2.5150	9.0899	-2.0420	2.342035	9.059256	-1.954855
C	2.6609	9.5654	-4.4541	2.577248	9.539848	-4.357376
N	2.6408	6.8372	-1.2470	2.552851	6.817709	-1.147211
C	2.8238	5.5295	-1.4603	2.770029	5.512679	-1.338719
C	3.0504	5.0000	-2.7311	3.000607	4.984146	-2.608738
C	3.0829	5.8443	-3.8248	3.015830	5.825382	-3.704795
C	2.8968	7.2197	-3.6262	2.798036	7.199404	-3.521816
C	2.6882	7.6815	-2.3154	2.575135	7.662846	-2.216801
C	2.9052	8.1851	-4.7177	2.817112	8.163309	-4.614956
N	1.7887	8.9586	2.3112	1.700439	8.874768	2.449779
C	2.6602	9.4377	3.2165	2.598062	9.340936	3.335992
C	2.2651	10.2114	4.2978	2.215674	10.061181	4.455974
C	0.9149	10.5062	4.4524	0.862265	10.297377	4.670439
C	0.0086	10.0127	3.5239	-0.067321	9.804189	3.763884
C	0.4641	9.2380	2.4566	0.369367	9.090041	2.651808

... Continued on the next page ...

Table 3.1. Atomic XYZ coordinates (Å) of Ru=Co (Continued).

Atom	GS			HS		
	X	Y	Z	X	Y	Z
N	0.1872	7.9338	0.4606	0.077408	7.846013	0.622907
C	-0.5589	7.3800	-0.5111	-0.664097	7.298831	-0.356137
C	-1.9338	7.5432	-0.5826	-2.046939	7.385197	-0.363731
C	-2.5668	8.3111	0.3894	-2.680753	8.066744	0.669542
C	-1.8045	8.8803	1.4003	-1.916247	8.640531	1.677237
C	-0.4237	8.6804	1.4213	-0.529851	8.520103	1.639983
N	2.3595	6.0650	1.8040	2.401258	6.112339	1.963506
C	1.2908	5.3348	2.1686	1.377951	5.375516	2.430925
C	1.3948	4.2044	2.9646	1.581114	4.277980	3.251539
C	2.6533	3.8057	3.4014	2.882075	3.938738	3.606735
C	3.7617	4.5535	3.0283	3.939197	4.706199	3.134955
C	3.5953	5.6855	2.2302	3.681716	5.796530	2.309299
N	4.3661	7.6173	1.0316	4.284183	7.702189	0.985156
C	5.3339	8.4412	0.5915	5.167562	8.553838	0.436299
C	6.6756	8.2396	0.8781	6.531157	8.435777	0.651647
C	7.0371	7.1425	1.6543	6.994835	7.398785	1.453759
C	6.0442	6.2877	2.1119	6.084658	6.511592	2.013130
C	4.7110	6.5391	1.7879	4.724387	6.678070	1.768829
N	2.9215	11.3278	-10.1771	3.045133	11.347687	-10.053125
C	2.6546	12.6240	-10.0017	2.838881	12.647852	-9.844190
C	2.4181	13.1593	-8.7336	2.613494	13.181862	-8.573355
C	2.4609	12.3403	-7.6216	2.601865	12.334026	-7.483654
C	2.7467	10.9765	-7.7887	2.825302	10.962599	-7.680227
C	2.9576	10.5105	-9.0922	3.038501	10.507275	-8.993165
C	2.7986	10.0168	-6.6925	2.807677	10.000696	-6.586426
N	2.6100	10.4512	-5.4473	2.583248	10.432663	-5.346744
N	3.4864	8.8042	-10.6495	3.522606	8.739015	-10.539982
C	3.7621	7.5348	-10.9575	3.739192	7.453516	-10.818446
C	3.8247	6.5389	-9.9806	3.744616	6.459080	-9.837623
C	3.5984	6.8608	-8.6569	3.512979	6.814076	-8.523594
C	3.2993	8.1890	-8.3177	3.273229	8.160681	-8.209616
C	3.2618	9.1330	-9.3506	3.295746	9.099473	-9.255896
C	3.0710	8.6453	-6.9528	3.039840	8.617957	-6.846341
N	3.1085	7.7553	-5.9620	3.037335	7.728058	-5.855325
N	3.2734	11.9914	-12.9695	3.515115	12.186711	-13.157322
C	2.2020	12.4567	-13.6312	2.479857	12.712841	-13.826274

... Continued on the next page ...

Table 3.1. Atomic XYZ coordinates (Å) of Ru=Co (Continued).

Atom	GS			HS		
	X	Y	Z	X	Y	Z
C	2.2655	13.5899	-14.4292	2.591888	13.857067	-14.604231
C	3.4765	14.2579	-14.5552	3.834059	14.474901	-14.695234
C	4.5869	13.7766	-13.8726	4.912835	13.930058	-14.010416
C	4.4615	12.6432	-13.0762	4.726729	12.781646	-13.239251
N	5.2201	10.9275	-11.6143	5.503393	10.998827	-11.821748
C	6.1335	10.3261	-10.8364	6.445040	10.368949	-11.105755
C	7.4137	10.8354	-10.6801	7.746943	10.837771	-10.998517
C	7.7588	12.0018	-11.3508	8.081716	12.013148	-11.660856
C	6.8165	12.6218	-12.1612	7.109815	12.673210	-12.401712
C	5.5463	12.0683	-12.2775	5.820953	12.141799	-12.471212
N	1.4833	9.8580	-12.2375	1.397700	9.842218	-12.431532
C	0.4018	10.1957	-11.5176	0.325608	10.190323	-11.706806
C	-0.8744	9.7896	-11.8789	-0.963873	9.793928	-12.033752
C	-1.0366	9.0121	-13.0193	-1.144400	8.999227	-13.160313
C	0.0830	8.6578	-13.7616	-0.036883	8.630774	-13.913518
C	1.3383	9.0926	-13.3516	1.231275	9.069265	-13.528998
N	3.7037	9.2993	-13.4645	3.624221	9.183004	-13.754639
C	4.9100	9.0480	-13.9976	4.777802	8.915622	-14.382254
C	5.0588	8.2725	-15.1384	4.839676	8.180561	-15.558182
C	3.9269	7.7491	-15.7508	3.651923	7.708539	-16.105226
C	2.6783	8.0117	-15.2011	2.452227	7.986156	-15.461991
C	2.5892	8.7854	-14.0487	2.463866	8.727863	-14.279293
H	2.0880	12.7761	-1.1305	1.701210	12.721093	-1.062384
H	3.7028	9.1938	3.0583	3.641505	9.137157	3.133389
H	3.0096	10.5762	4.9949	2.972644	10.425745	5.138896
H	0.5689	11.1119	5.2823	0.529593	10.856843	5.537148
H	-1.0448	10.2363	3.6300	-1.123420	9.977020	3.924465
H	-2.2841	9.4780	2.1645	-2.398815	9.175539	2.484275
H	-3.6394	8.4678	0.3624	-3.761044	8.155881	0.691520
H	-2.4876	7.0741	-1.3868	-2.605342	6.923996	-1.168882
H	-0.0303	6.7862	-1.2463	-0.134100	6.774085	-1.140762
H	0.3297	5.6724	1.8038	0.381094	5.670988	2.130987
H	0.5006	3.6542	3.2315	0.728751	3.708286	3.599390
H	2.7731	2.9270	4.0248	3.075227	3.086870	4.248460
H	4.7479	4.2551	3.3582	4.954709	4.454492	3.409808
H	6.3085	5.4312	2.7180	6.434109	5.699412	2.636447

... Continued on the next page ...

Table 3.1. Atomic XYZ coordinates (Å) of Ru=Co (Continued).

Atom	GS			HS		
	X	Y	Z	X	Y	Z
H	8.0752	6.9518	1.9021	8.055374	7.277816	1.642546
H	7.4144	8.9336	0.4962	7.206263	9.149393	0.196043
H	5.0115	9.2842	-0.0068	4.767512	9.351044	-0.177056
H	2.3154	12.1304	-3.5415	2.106831	12.092292	-3.451260
H	2.1476	11.0089	0.6016	1.733335	10.956871	0.674831
H	3.2495	5.4615	-4.8240	3.193861	5.440242	-4.701076
H	3.1940	3.9319	-2.8413	3.165674	3.919142	-2.715037
H	2.7816	4.8845	-0.5919	2.751475	4.872457	-0.465608
H	2.2794	12.7359	-6.6298	2.426618	12.710447	-6.483470
H	2.1964	14.2155	-8.6454	2.447383	14.246329	-8.459972
H	2.6149	13.2528	-10.8803	2.848496	13.289362	-10.718288
H	3.9478	7.2959	-11.9955	3.919249	7.203569	-11.857862
H	4.0607	5.5261	-10.2822	3.931297	5.429847	-10.118861
H	3.6466	6.1052	-7.8824	3.509835	6.071811	-7.734913
H	0.5561	10.8128	-10.6438	0.509140	10.811477	-10.837468
H	-1.7178	10.0921	-11.2711	-1.798489	10.105901	-11.417888
H	-2.0203	8.6810	-13.3313	-2.134398	8.666511	-13.451295
H	-0.0224	8.0519	-14.6522	-0.166656	8.010924	-14.790854
H	1.7846	7.6103	-15.6603	1.522464	7.627618	-15.882843
H	4.0112	7.1425	-16.6448	3.655138	7.134796	-17.025184
H	6.0522	8.0862	-15.5269	5.797268	7.988763	-16.026736
H	5.7728	9.4642	-13.4985	5.679486	9.303712	-13.922938
H	5.8399	9.4158	-10.3341	6.142618	9.455988	-10.605579
H	8.1163	10.3161	-10.0406	8.472805	10.289824	-10.409947
H	8.7487	12.4296	-11.2429	9.086371	12.416520	-11.600090
H	7.0672	13.5314	-12.6907	7.359510	13.591332	-12.916332
H	5.5403	14.2810	-13.9601	5.884632	14.400632	-14.079272
H	3.5607	15.1419	-15.1764	3.965613	15.369739	-15.293148
H	1.3714	13.9304	-14.9365	1.723231	14.246835	-15.120766
H	1.2715	11.9207	-13.5161	1.530376	12.198779	-13.730654

Bibliography

[1] G. R. Fleming and M. Cho, "Chromophore-solvent dynamics," *Annual Review of Physical Chemistry*, vol. 47, no. 1, pp. 109–134, 1996.

[2] W. P. de Boei, M. S. Pshenichnikov, and D. A. Wiersma, "Ultrafast solvation dynamics explored by femtosecond photon echo spectroscopies," *Annual Review of Physical Chemistry*, vol. 49, no. 1, pp. 99–123, 1998.

[3] S. A. Kovalenko, N. Eilers-K onig, T. A. Senyushkina, and N. P. Ernsting, "Charge transfer and solvation of betaine-30 in polar solvents: A femtosecond broadband transient absorption study," *The Journal of Physical Chemistry A*, vol. 105, no. 20, pp. 4834–4843, 2001.

[4] M. Chergui and A. H. Zewail, "Electron and x-ray methods of ultrafast structural dynamics: Advances and applications," *ChemPhysChem*, vol. 10, no. 1, pp. 28–43, 2009.

[5] K. Haldrup, G. Vankó, W. Gawelda, a. Galler, G. Doumy, a. M. March, E. P. Kanter, a. Bordage, a. Dohn, T. B. Van Driel, K. S. Kjær, H. T. Lemke, S. E. Canton, J. Uhlig, V. Sundström, L. Young, S. H. Southworth, M. M. Nielsen, and C. Bressler, "Guest-host interactions investigated by time-resolved X-ray spectroscopies and scattering at MHz rates: Solvation dynamics and photoinduced spin transition in aqueous $[\mathrm{Fe(bipy)_3}]^{2+}$," *Journal of Physical Chemistry A*, vol. 116, pp. 9878–9887, 2012.

[6] G. Vankó, A. Bordage, M. Pápai, K. Haldrup, P. Glatzel, A. M. March, G. Doumy, A. Britz, A. Galler, T. A. Assefa, D. Cabaret, A. Juhin, T. B. van Driel, K. S. Kjær, A. O. Dohn, K. B. Moller, H. T. Lemke, E. Gallo, M. Rovezzi, Z. Németh, E. Rozsályi, T. Rozgonyi, J. Uhlig, V. Sundstrom, M. M. Nielsen, L. Young, S. H. Southworth, C. Bressler, and W. Gawelda, "Detailed Characterization of a Nanosecond-lived Excited State: X-Ray and Theoretical Investigation of the Quintet State in

Photoexcited [Fe(terpy)$_2$]$^{2+}$," *The Journal of Physical Chemistry C*, vol. 119, no. 11, pp. 5888–5902, 2015.

[7] S. E. Canton, K. S. Kjær, G. Vankó, T. B. van Driel, S.-i. Adachi, A. Bordage, C. Bressler, P. Chabera, M. Christensen, A. O. Dohn, A. Galler, W. Gawelda, D. Gosztola, K. Haldrup, T. Harlang, Y. Liu, K. B. Møller, Z. Németh, S. Nozawa, M. Pápai, T. Sato, T. Sato, K. Suarez-Alcantara, T. Togashi, K. Tono, J. Uhlig, D. A. Vithanage, K. Wärnmark, M. Yabashi, J. Zhang, V. Sundström, and M. M. Nielsen, "Visualizing the non-equilibrium dynamics of photoinduced intramolecular electron transfer with femtosecond x-ray pulses," *Nat Commun*, vol. 6, Mar 2015.

[8] J. Kim, K. H. Kim, K. Y. Oang, J. H. Lee, K. Hong, H. Cho, N. Huse, R. W. Schoenlein, T. K. Kim, and H. Ihee, "Tracking reaction dynamics in solution by pump-probe x-ray absorption spectroscopy and x-ray liquidography (solution scattering)," *Chem. Commun.*, vol. 52, pp. 3734–3749, 2016.

[9] R. Berera, R. Grondelle, and J. T. M. Kennis, "Ultrafast transient absorption spectroscopy: principles and application to photosynthetic systems," *Photosynthesis Research*, vol. 101, no. 2, pp. 105–118, 2009.

[10] A. M. March, A. Stickrath, G. Doumy, E. P. Kanter, B. Kr assig, S. H. Southworth, K. Attenkofer, C. A. Kurtz, L. X. Chen, and L. Young, "Development of high-repetition-rate laser pump/x-ray probe methodologies for synchrotron facilities," *Review of Scientific Instruments*, vol. 82, no. 7, p. 73110, 2011.

[11] F. A. Lima, C. J. Milne, D. C. V. Amarasinghe, M. H. Rittmann-Frank, R. M. V. D. Veen, M. Reinhard, V.-T. Pham, S. Karlsson, S. L. Johnson, D. Grolimund, C. Borca, T. Huthwelker, M. Janousch, F. van Mourik, R. Abela, and M. Chergui, "A high-repetition rate scheme for synchrotron-based picosecond laser pump?x-ray probe experiments on chemical and biological systems in solution," *Review of Scientific Instruments*, vol. 82, no. 6, p. 63111, 2011.

[12] M. Hart, C. Angelsen, S. Burge, J. Coughlan, R. Halsall, A. Koch, M. Kuster, T. Nicholls, M. Prydderch, P. Seller, S. Thomas, A. Blue, A. Joy, V. O'shea, and M. Wing, "Development of the LPD, a high dynamic range pixel detector for the european XFEL," in *Nuclear Science Symposium and Medical Imaging Conference (NSS/MIC), 2012 IEEE*, pp. 534–537, Oct 2012.

[13] I. Johnson, A. Bergamaschi, H. Billich, S. Cartier, R. Dinapoli, D. Greiffenberg, M. Guizar-Sicairos, B. Henrich, J. Jungmann, D. Mezza, A. Mozzanica, B. Schmitt, X. Shi, and G. Tinti, "Eiger: a single-photon counting x-ray detector," *Journal of Instrumentation*, vol. 9, no. 05, p. C05032, 2014.

[14] M. Wulff, Q. Kong, M. Cammarata, M. Lo Russo, P. Anfinrud, F. Schotte, M. Lorenc, H. Ihee, T. K. Kim, and A. Plech, "Picosecond diffraction at the ESRF: How far have we come and where are we going?," *AIP Conference Proceedings*, vol. 879, no. 1, pp. 1187–1194, 2007.

[15] M. Wulff, Q. Kong, J. H. Lee, T. K. Kim, M. Cammarata, D. Khakhulin, S. Bratos, J.-C. Leichnam, F. Schotte, and P. A. Anfinrud, *The Future of Dynamic Structural Science*, ch. Molecular Dynamics Probed by Short X-ray Pulses from a Synchrotron, pp. 261–284. Dordrecht: Springer Netherlands, 2014.

[16] L. Eybert, M. Wulff, W. Reichenbach, A. Plech, F. Schotte, E. Gagliardini, L. Zhang, O. Hignette, A. Rommeveaux, and A. K. Freund, "The toroidal mirror for single-pulse experiments on id09b," *Proc. SPIE*, vol. 4782, pp. 246–257, 2002.

[17] M. Wulff, A. Plech, L. Eybert, R. Randler, F. Schotte, and P. Anfinrud, "The realization of sub-nanosecond pump and probe experiments at the ESRF," *Faraday Discuss.*, vol. 122, pp. 13–26, 2003.

[18] P. Lechner, C. Fiorini, R. Hartmann, J. Kemmer, N. Krause, P. Leutenegger, A. Longoni, H. Soltau, D. St otter, R. St otter, L. Str uder, and U. Weber, "Silicon drift detectors for high count rate x-ray spectroscopy at room temperature," *Nuclear Instruments and Methods in Physics Research Section A: Accelerators, Spectrometers, Detectors and Associated Equipment*, vol. 458, no. 1-2, pp. 281–287, 2001. Proc. 11th Inbt. Workshop on Room Temperature Semiconductor X- and Gamma-Ray Detectors and Associated Electronics.

[19] C. Ponchut, J. M. Rigal, J. Clément, E. Papillon, A. Homs, and S. Petitdemange, "Maxipix, a fast readout photon-counting x-ray area detector for synchrotron applications," *Journal of Instrumentation*, vol. 6, no. 01, p. C01069, 2011.

[20] G. Hölzer, M. Fritsch, M. Deutsch, J. Härtwig, and E. Förster, "$K\alpha_{1,2}$ and $K\beta_{1,3}$ x-ray emission lines of the $3d$ transition metals," *Phys. Rev. A*, vol. 56, pp. 4554–4568, 1997.

[21] R. W. Schoenlein, S. Chattopadhyay, H. H. W. Chong, T. E. Glover, P. A. Heimann, C. V. Shank, A. A. Zholents, and M. S. Zolotorev, "Generation of femtosecond pulses of synchrotron radiation," *Science*, vol. 287, no. 5461, pp. 2237–2240, 2000.

[22] S. Khan, K. Holldack, T. Kachel, R. Mitzner, and T. Quast, "Femtosecond undulator radiation from sliced electron bunches," *Phys. Rev. Lett.*, vol. 97, p. 074801, 2006.

[23] P. Beaud, S. L. Johnson, A. Streun, R. Abela, D. Abramsohn, D. Grolimund, F. Krasniqi, T. Schmidt, V. Schlott, and G. Ingold, "Spatiotemporal stability of a femtosecond hard–x-ray undulator source studied by control of coherent optical phonons," *Phys. Rev. Lett.*, vol. 99, p. 174801, Oct 2007.

[24] S. L. Johnson, E. Vorobeva, P. Beaud, C. J. Milne, and G. Ingold, "Full reconstruction of a crystal unit cell structure during coherent femtosecond motion," *Phys. Rev. Lett.*, vol. 103, p. 205501, Nov 2009.

[25] J. H. Lee, M. Wulff, S. Bratos, J. Petersen, L. Guerin, J.-C. Leicknam, M. Cammarata, Q. Kong, J. Kim, K. B. Møller, and H. Ihee, "Filming the birth of molecules and accompanying solvent rearrangement," *Journal of the American Chemical Society*, vol. 135, no. 8, pp. 3255–3261, 2013.

[26] B. E. Warren, *X-ray Diffraction.* Dover, New York, 1990.

[27] J. Als-Nielsen and D. McMorrow, *Elements of Modern X-Ray Physics.* John Wiley & Sons, Hoboken, NJ, 2000.

[28] E. Prince, *International Tables for Crystallography, Mathematical, Physical and Chemical Tables*, vol. volume C of *IUCr Series. International Tables of Crystallography.* Wiley, 3rd ed., 2004.

[29] G. Pálinkás, "Analytic approximations for the incoherent X-ray intensities of the atoms from Ca to Am," *Acta Crystallographica Section A*, vol. 29, pp. 10–12, Jan 1973.

[30] Q. Kong, J. Kim, M. Lorenc, T. K. Kim, H. Ihee, and M. Wulff, "Photodissociation reaction of 1,2-diiodoethane in solution: A theoretical and x-ray diffraction study," *The Journal of Physical Chemistry A*, vol. 109, no. 45, pp. 10451–10458, 2005.

[31] M. Christensen, K. Haldrup, K. Bechgaard, R. Feidenhans, Q. Kong, M. Cammarata, M. L. Russo, M. Wulff, N. Harrit, and M. M. Nielsen, "Time-resolved x-ray scattering of an electronically excited state in solution. structure of the ${}^3\mathrm{A}_u^2$ state of tetrakis-μ-

pyrophosphitodiplatinate(II)," *Journal of the American Chemical Society*, vol. 131, no. 2, pp. 502–508, 2009.

[32] K. H. Kim, J. H. Lee, J. Kim, S. Nozawa, T. Sato, A. Tomita, K. Ichiyanagi, H. Ki, J. Kim, S.-i. Adachi, and H. Ihee, "Solvent-dependent molecular structure of ionic species directly measured by ultrafast X-ray solution scattering," *Phys. Rev. Lett.*, vol. 110, p. 165505, Apr 2013.

[33] K. Haldrup, T. Harlang, M. Christensen, A. Dohn, T. B. van Driel, K. S. Kjær, N. Harrit, J. Vibenholt, L. Guerin, M. Wulff, and M. M. Nielsen, "Bond shortening (1.4 å) in the singlet and triplet excited states of $[Ir_2(dimen)_4]^{2+}$ in solution determined by time-resolved x-ray scattering," *Inorganic Chemistry*, vol. 50, no. 19, pp. 9329–9336, 2011.

[34] H. Ihee, M. Lorenc, T. K. Kim, Q. Y. Kong, M. Cammarata, J. H. Lee, S. Bratos, and M. Wulff, "Ultrafast x-ray diffraction of transient molecular structures in solution," *Science*, vol. 309, no. 5738, pp. 1223–1227, 2005.

[35] M. Cammarata, M. Lorenc, T. K. Kim, J. H. Lee, Q. Y. Kong, E. Pontecorvo, M. Lo Russo, G. Schiró, A. Cupane, M. Wulff, and H. Ihee, "Impulsive solvent heating probed by picosecond x-ray diffraction," *The Journal of Chemical Physics*, vol. 124, no. 12, p. 124504, 2006.

[36] K. S. Kjaer, T. B. van Driel, J. Kehres, K. Haldrup, D. Khakhulin, K. Bechgaard, M. Cammarata, M. Wulff, T. J. Sorensen, and M. M. Nielsen, "Introducing a standard method for experimental determination of the solvent response in laser pump, x-ray probe time-resolved wide-angle x-ray scattering experiments on systems in solution," *Phys. Chem. Chem. Phys.*, vol. 15, pp. 15003–15016, 2013.

[37] K. Haldrup, M. Christensen, and M. Meedom Nielsen, "Analysis of time-resolved X-ray scattering data from solution-state systems," *Acta Crystallographica Section A: Foundations of Crystallography*, vol. 66, pp. 261–269, 2010.

[38] T. Brandt van Driel and M. Nielsen, *Time Resolved X-Ray Scattering of molecules in Solution: Approaching the Molecular Movie.* PhD thesis, Technical University of Denmark, 2014.

[39] G. Hura, J. M. Sorenson, R. M. Glaeser, and T. Head-Gordon, "A high-quality x-ray scattering experiment on liquid water at ambient conditions," *The Journal of Chemical Physics*, vol. 113, no. 20, pp. 9140–9148, 2000.

[40] E. Curis and S. Bénazeth, "Propagation of statistical errors across EXAFS extraction and Fourier filtering," *Journal of Synchrotron Radiation*, vol. 7, no. 4, pp. 262–266, 2000.

[41] C. H. Booth and Y.-J. Hu, "Confirmation of standard error analysis techniques applied to exafs using simulations," *Journal of Physics: Conference Series*, vol. 190, no. 1, p. 012028, 2009.

[42] B. Ravel and M. Newville, "*ATHENA*, *ARTEMIS*, *HEPHAESTUS*: data analysis for X-ray absorption spectroscopy using *IFEFFIT*," *Journal of Synchrotron Radiation*, vol. 12, no. 4, pp. 537–541, 2005.

[43] K. V. Klementev, "Package VIPER (visual processing in EXAFS researches) for Windows," *Nuclear Instruments and Methods in Physics Research Section A: Accelerators, Spectrometers, Detectors and Associated Equipment*, vol. 448, no. 1-2, pp. 299–301, 2000.

[44] E. A. Stern, "Number of relevant independent points in x-ray-absorption fine-structure spectra," *Phys. Rev. B*, vol. 48, pp. 9825–9827, Oct 1993.

[45] G. G. Pavlov and J. A. Nousek, "Charge diffusion in CCD X-ray detectors," *Nuclear Instruments and Methods in Physics Research Section A: Accelerators, Spectrometers, Detectors and Associated Equipment*, vol. 428, no. 2-3, pp. 348–366, 1999.

[46] X. Yang, P. Juhás, and S. J. L. Billinge, "On the estimation of statistical uncertainties on powder diffraction and small-angle scattering data from two-dimensional X-ray detectors," *Journal of Applied Crystallography*, vol. 47, pp. 1273–1283, Aug 2014.

[47] G. Peng, F. M. F. de Groot, K. Haemaelaeinen, J. A. Moore, X. Wang, M. M. Grush, J. B. Hastings, D. P. Siddons, and W. H. Armstrong, "High-resolution manganese x-ray fluorescence spectroscopy. Oxidation-state and spin-state sensitivity," *Journal of the American Chemical Society*, vol. 116, no. 7, pp. 2914–2920, 1994.

[48] P. Glatzel and U. Bergmann, "High resolution 1s core hole X-ray spectroscopy in 3d transition metal complexes-electronic and structural information," *Coordination Chemistry Reviews*, vol. 249, no. 1-2, pp. 65–95, 2005.

[49] G. Vankó, T. Neisius, G. Molnár, F. Renz, S. Kárpáti, A. Shukla, and F. M. F. de Groot, "Probing the 3d spin momentum with x-ray emission spectroscopy: The case of molecular-spin transitions," *The Journal of Physical Chemistry B*, vol. 110, no. 24, pp. 11647–11653, 2006.

[50] G. Vankó, P. Glatzel, V.-T. Pham, R. Abela, D. Grolimund, C. Borca, S. Johnson, C. Milne, and C. Bressler, "Picosecond time-resolved x-ray emission spectroscopy: Ultrafast spin-state determination in an iron complex," *Angewandte Chemie International Edition*, vol. 49, no. 34, pp. 5910–5912, 2010.

[51] G. Vankó, A. Bordage, P. Glatzel, E. Gallo, M. Rovezzi, W. Gawelda, A. Galler, C. Bressler, G. Doumy, A. M. March, E. P. Kanter, L. Young, S. H. Southworth, S. E. Canton, J. Uhlig, G. Smolentsev, V. Sundstr om, K. Haldrup, T. B. van Driel, M. M. Nielsen, K. S. Kjaer, and H. T. Lemke, "Spin-state studies with XES and RIXS: From static to ultrafast," *Journal of Electron Spectroscopy and Related Phenomena*, vol. 188, pp. 166–171, 2013.

[52] M. J. Rosker, M. Dantus, and A. H. Zewail, "Femtosecond clocking of the chemical bond," *Science*, vol. 241, no. 4870, pp. 1200–1202, 1988.

[53] B. J. Schwartz, J. C. King, J. Z. Zhang, and C. B. Harris, "Direct femtosecond measurements of single collision dominated geminate recombination times of small molecules in liquids," *Chemical Physics Letters*, vol. 203, no. 5-6, pp. 503–508, 1993.

[54] C. T. C.H. Bamford and R. C. (Eds.), *Diffusion-Limited Reactions.* Comprehensive Chemical Kinetics 25, Elsevier, 1985.

[55] A. L. Harris, J. K. Brown, and C. B. Harris, "The nature of simple photodissociation reactions in liquids on ultrafast time scales," *Annual Review Of Physical Chemistry, Vol 61*, vol. 39, pp. 341–366, 1988.

[56] I. V. Khudyakov, "Transient free radicals in viscous solvents," *Research on Chemical Intermediates*, vol. 39, no. 3, pp. 781–804, 2012.

[57] A. B. Stickrath, E. C. Carroll, X. Dai, D. A. Harris, A. Rury, B. Smith, K.-C. Tang, J. Wert, and R. J. Sension, "Solvent-dependent cage dynamics of small nonpolar radicals: lessons from the photodissociation and geminate recombination of alkylcobalamins.," *The journal of physical chemistry. A*, vol. 113, no. 30, pp. 8513–22, 2009.

[58] M. Hyde and G. Beddard, "Picosecond photodissociation and geminate radical recombination in alkane solutions of tetraphenylhydrazine," *Chemical Physics*, vol. 151, no. 2, pp. 239–248, 1991.

[59] G. S. Beddard and A. J. Masters, "Rotationally controlled geminate recombination," *Chemical Physics Letters*, vol. 188, no. 5-6, pp. 513–519, 1992.

[60] R. A. Marcus, “Relation between charge transfer absorption and fluorescence spectra and the inverted region,” *The Journal of Physical Chemistry*, vol. 93, no. 8, pp. 3078–3086, 1989.

[61] T. Yabe and J. K. Kochi, “Contact ion pairs. Picosecond dynamics of solvent separation, internal return, and special salt effect,” *Journal of the American Chemical Society*, vol. 114, no. 12, pp. 4491–4500, 1992.

[62] B. R. Arnold, D. Noukakis, S. Farid, J. L. Goodman, and I. R. Gould, “Dynamics of interconversion of contact and solvent-separated radical-ion pairs,” *Journal of the American Chemical Society*, vol. 117, no. 15, pp. 4399–4400, 1995.

[63] J. Zhou, B. R. Findley, A. Teslja, C. L. Braun, and N. Sutin, “Ion pairs from photoexcited, random electron donors and acceptors:alkylbenzenes and tetracyanoethylene,” *The Journal of Physical Chemistry A*, vol. 104, no. 49, pp. 11512–11521, 2000.

[64] O. F. Mohammed and E. Vauthey, “Simultaneous generation of different types of ion pairs upon charge-transfer excitation of a donor-acceptor complex revealed by ultrafast transient absorption spectroscopy,” *The Journal of Physical Chemistry A*, vol. 112, no. 26, pp. 5804–5809, 2008.

[65] J. Maya, “Ultraviolet absorption cross sections of HgI_2, $HgBr_2$, and tin (II) halide vapors,” *The Journal of Chemical Physics*, vol. 67, no. 11, p. 4976, 1977.

[66] D. P. Greene, K. P. Killeen, and J. G. Eden, “Excitation of the HgBr $B^2\Sigma^+_{1/2} \leftarrow X^2\Sigma^+_{1/2}$ band in the ultraviolet,” *J. Opt. Soc. Am. B*, vol. 3, pp. 1282–1287, Oct 1986.

[67] J. H. Parks, “Laser action on the HgBr $B^2\Sigma^+_{1/2} \leftarrow X^2\Sigma^+_{1/2}$ band of HgCl at 5576 å,” *Applied Physics Letters*, vol. 31, no. 3, pp. 192–194, 1977.

[68] W. R. Wadt, “The electronic structure of HgCl and HgBr,” *Applied Physics Letters*, vol. 34, no. 10, pp. 658–660, 1979.

[69] M. J. Rosker, M. Dantus, and A. H. Zewail, “Femtosecond realtime probing of reactions. V. The reaction of IHgI,” *The Journal of Chemical Physics*, vol. 89, p. 6113, 1988.

[70] T. Baumert, S. Pedersen, and A. H. Zewail, “Femtosecond real-time probing of reactions. 12. vectorial dynamics of transition states,” *The Journal of Physical Chemistry*, vol. 97, no. 48, pp. 12447–12459, 1993.

[71] D. Zhong, , and A. H. Zewail, “Femtosecond real-time probing of reactions. 23. studies of temporal, velocity, angular, and state dynamics from transition states to final products by femtosecond-resolved mass spectrometry,” *The Journal of Physical Chemistry A*, vol. 102, no. 23, pp. 4031–4058, 1998.

[72] N. Pugliano, A. Z. Szarka, and R. M. Hochstrasser, “Relaxation of the product state coherence generated through the photolysis of HgI_2 in solution,” *The Journal of Chemical Physics*, vol. 104, no. 13, pp. 5062–5079, 1996.

[73] M. Lim, M. F. Wolford, P. Hamm, and R. M. Hochstrasser, “Chirped wavepacket dynamics of HgBr from the photolysis of $HgBr_2$ in solution,” *Chemical Physics Letters*, vol. 290, pp. 355 – 362, 1998.

[74] M. Volk, S. Gnanakaran, E. Gooding, Y. Kholodenko, N. Pugliano, and R. M. Hochstrasser, “Anisotropy measurements of solvated HgI_2 dissociation: Transition state and fragment rotational dynamics,” *The Journal of Physical Chemistry A*, vol. 101, no. 4, pp. 638–643, 1997.

[75] A. Geis, M. Bouriau, A. Plech, F. Schotte, S. Techert, H. P. Trommsdroff, M. Wulff, and D. Block, “Direct time-resolved studies of photochemical reactions in liquids by X-ray scattering,” *Journal of Luminescence*, vol. 94, pp. 493–498, 2001.

[76] T. K. Kim, M. Lorenc, J. H. Lee, M. Lo Russo, J. Kim, M. Cammarata, Q. Kong, S. Noel, A. Plech, M. Wulff, and H. Ihee, “Spatiotemporal reaction kinetics of an ultrafast photoreaction pathway visualized by time-resolved liquid X-ray diffraction,” *Proceedings of the National Academy of Sciences*, vol. 103, no. 25, pp. 9410–9415, 2006.

[77] S. Jun, J. H. Lee, J. Kim, J. Kim, K. H. Kim, Q. Kong, T. K. Kim, M. Lo Russo, M. Wulff, and H. Ihee, “Photochemistry of $HgBr_2$ in methanol investigated using time-resolved x-ray liquidography,” *Phys. Chem. Chem. Phys.*, vol. 12, pp. 11536–11547, 2010.

[78] T. R. Griffiths and R. A. Anderson, “Structure of mercury(II) halides in solution and assignment of their resolved electronic spectra,” *Journal of the Chemical Society, Faraday Transactions 2*, vol. 75, p. 957, jan 1979.

[79] M. M. Savas and W. R. Mason, “Vapor-phase electronic absorption spectra and solution magnetic circular dichroism and absorption spectra for dihalo- and halomethylmercury(II),” *Inorganic Chemistry*, vol. 27, no. 4, pp. 658–665, 1988.

[80] N. Pugliano, D. K. Palit, a. Z. Szarka, and R. M. Hochstrasser, "Wave-packet dynamics of the HgI_2 photodissociation reaction in solution," *Journal of Chemical Physics*, vol. 99, pp. 7273–7276, 1993.

[81] N. Pugliano, a. Z. Szarka, S. Gnanakaran, M. Triechel, and R. M. Hochstrasser, "Vibrational population dynamics of the HgI photofragment in ethanol solution," *Journal of Chemical Physics*, vol. 103, pp. 6498–6511, 1995.

[82] H. Hofmann and S. R. Leone, "Tunable laser photodissociation of HgI_2: Quantum yield for formation of excited i(5 $^2P_{1/2}$) atoms," *The Journal of Chemical Physics*, vol. 69, no. 8, pp. 3819–3825, 1978.

[83] A. Sanov, T. Sanford, S. Nandi, and W. C. Lineberger, "Spin-orbit relaxation and recombination dynamics in $I_2^-(CO_2)_n$ and $I_2^-(OCS)_n$ cluster ions: A new type of photofragment caging reaction," *The Journal of Chemical Physics*, vol. 111, no. 2, pp. 664–675, 1999.

[84] A. C. Moskun, , S. E. Bradforth, J. Thøgersen, , and S. Keiding, "Absence of a signature of aqueous $I(^2P_{1/2})$ after 200-nm photodetachment of I^-(aq)," *The Journal of Physical Chemistry A*, vol. 110, no. 38, pp. 10947–10955, 2006.

[85] P. F. de Violet, "Polyhalide radical anions as intermediates in chemistry," *Reviews of Chemical Intermediates*, vol. 4, pp. 121–169, 1981.

[86] J. C. Owrutsky, D. Raftery, and R. M. Hochstrasser, "Vibrational relaxation dynamics in solutions," *Annual review of physical chemistry*, vol. 45, pp. 519–55, 1994.

[87] K. J. Shin and R. Kapral, "Kinetic theory of reactive pair dynamics in liquids," *The Journal of Chemical Physics*, vol. 69, no. 8, p. 3685, 1978.

[88] M. Hyde and G. Beddard, "Picosecond photodissociation and geminate radical recombination in alkane solutions of tetraphenylhydrazine," *Chemical Physics*, vol. 151, no. 2, pp. 239 – 248, 1991.

[89] T. W. Scott and C. D. Jr., "Picosecond photolysis of azo compounds in liquid alkanes: germinate recombination kinetics for polyatomic free radical pairs," *Chemical Physics Letters*, vol. 178, no. 1, pp. 9 – 18, 1991.

[90] H. Kim, S. Shin, S. Lee, and K. J. Shin, "Monte Carlo simulation study of recombination dynamics in solution," *The Journal of Chemical Physics*, vol. 105, pp. 7705–7711, 1996.

[91] K. H. Kim, H. Ki, J. H. Lee, S. Park, Q. Kong, J. Kim, J. Kim, M. Wulff, and H. Ihee, "Solvent-dependent structure of molecular iodine probed by picosecond X-ray solution scattering," *Phys. Chem. Chem. Phys.*, vol. 17, pp. 8633–8637, 2015.

[92] M. Sandstr om, "An x-ray diffraction and Raman study of chloride, bromide and iodide complexes of mercury (II) in dimethyl sulfoxide solution and of mercury(ii) chloride solution," *Acta Chemica Scandinavica A*, vol. 32, pp. 627 – 641, 1978.

[93] S. J. Cyvin, "Molecular Vibrations and Mean Square Amplitudes. Supplement III Mean Amplitudes of Vibration for Inorganic Six-Atomic Molecules," *Zeitschrift f ur anorganische und allgemeine Chemie*, vol. 378, no. 1, pp. 117–127, 1970.

[94] Y. Morino, "The effect of thermal vibration of gaseous molecules in electron diffraction studies," *Acta Crystallographica*, vol. 13, no. 12, p. 1107, 1960.

[95] A. Almenningen, O. Bastiansen, and T. Munthe-Kaas, "The structure parameters of Dimethyldiacetylene," *Acta Chemica Scandinavica*, vol. 10, pp. 261–264, 1956.

[96] O. Bastiansen and M. Trætteberg, "The influence of thermal motion on structure determination of linear molecules using the electron-diffraction method," *Acta Crystallographica*, vol. 13, p. 1108, Dec 1960.

[97] G. Nagarajan, "Mean amplitudes of vibration and Bastiansen-Morino shrinkage effect in some linear symmetrical metal dihalides," *Journal of Molecular Spectroscopy*, vol. 13, pp. 361–392, 1964.

[98] I. Persson, M. Sandstrom, P. L. Goggin, and A. Mosset, "Structure and solvation of mercury(II) iodide, bromide, and chloride in pyridine solution; refinement of the crystal structure of di-iodobis(pyridine)mercury(II), $[HgI_2(py)_2]$," *J. Chem. Soc., Dalton Trans.*, pp. 1597–1604, 1985.

[99] U. Banin and S. Ruhman, "Ultrafast photodissociation of I3. Coherent photochemistry in solution," *The Journal of Chemical Physics*, vol. 98, p. 4391, 1993.

[100] U. Banin and S. Ruhman, "Ultrafast vibrational dynamics of nascent diiodide fragments studied by femtosecond transient resonance impulsive stimulated raman scattering," *The Journal of Chemical Physics*, vol. 99, no. 11, pp. 9318–9321, 1993.

[101] U. Banin, R. Kosloff, and S. Ruhman, "Vibrational relaxation of nascent diiodide ions studied by femtosecond transient resonance impulsive stimulated raman scattering (TRISRS); experiment and simulation," *Chemical Physics*, vol. 183, no. 2, pp. 289 – 307, 1994.

[102] T. Kühne and P. Vöhringer, "Vibrational relaxation and geminate recombination in the femtosecond-photodissociation of triiodide in solution," *Journal of Chemical Physics*, vol. 105, pp. 10788–10802, 1996.

[103] Y. Nishiyama, M. Terazima, and Y. Kimura, "Ultrafast relaxation and reaction of diiodide anion after photodissociation of triiodide in room-temperature ionic liquids," *Journal of Physical Chemistry B*, vol. 116, pp. 9023–9032, 2012.

[104] E. Gershgoren, U. Banin, and S. Ruhman, "Caging and geminate recombination following photolysis of triiodide in solution," *Journal of Physical Chemistry A*, vol. 102, no. 97, pp. 9–16, 1998.

[105] Y. Nishiyama, M. Terazima, and Y. Kimura, "Photo-dissociation and recombination of triiodide in room temperature ionic liquids," *Chemical Physics Letters*, vol. 491, no. 4-6, pp. 164–168, 2010.

[106] G. Boschloo and A. Hagfeldt, "Characteristics of the iodide/triiodide redox mediator in dye-sensitized solar cells," *Accounts of Chemical Research*, vol. 42, no. 11, pp. 1819–1826, 2009.

[107] R. Kawano and M. Watanabe, "Equilibrium potentials and charge transport of an I^-/I^{3-} redox couple in an ionic liquid," *Chem. Commun.*, pp. 330–331, 2003.

[108] R. Kawano and M. Watanabe, "Anomaly of charge transport of an iodide/tri-iodide redox couple in an ionic liquid and its importance in dye-sensitized solar cells," *Chem. Commun.*, pp. 2107–2109, 2005.

[109] M. Zistler, P. Wachter, P. Wasserscheid, D. Gerhard, A. Hinsch, R. Sastrawan, and H. Gores, "Comparison of electrochemical methods for triiodide diffusion coefficient measurements and observation of non-stokesian diffusion behaviour in binary mixtures of two ionic liquids," *Electrochimica Acta*, vol. 52, no. 1, pp. 161 – 169, 2006.

[110] F. C. Küpper, M. C. Feiters, B. Olofsson, T. Kaiho, S. Yanagida, M. B. Zimmermann, L. J. Carpenter, G. W. Luther, Z. Lu, M. Jonsson, and L. Kloo, "Commemorating two centuries of iodine research: An interdisciplinary overview of current research," *Angewandte Chemie International Edition*, vol. 50, no. 49, pp. 11598–11620, 2011.

[111] Z. Wang, T. Wasserman, E. Gershgoren, J. Vala, R. Kosloff, and S. Ruhman, "Geminate recombination of I^{3-} in cooled liquid and glassy ethanol," *Chemical Physics Letters*, vol. 313, no. November, pp. 155–161, 1999.

[112] A. Baratz and S. Ruhman, "UV photolysis of I3 - in solution - Multiple product channels detected by transient hyperspectral probing," *Chemical Physics Letters*, vol. 461, pp. 211–217, 2008.

[113] G. Boche, "Penetrated ion pairs: a new form of ion pair," *Angewandte Chemie International Edition in English*, vol. 31, no. 6, pp. 731–732, 1992.

[114] Y. Marcus and G. Hefter, "Ion pairing," *Chemical Reviews*, vol. 106, no. 11, pp. 4585–4621, 2006.

[115] J. Barthel, R. Buestrich, E. Carl, and H. J. Gores, "A new class of electrochemically and thermally stable lithium salts for lithium battery electrolytes: II. conductivity of lithium organoborates in dimethoxyethane and propylene carbonate," *Journal of The Electrochemical Society*, vol. 143, no. 11, pp. 3565–3571, 1996.

[116] H. S. Lee, X. Q. Yang, C. L. Xiang, J. McBreen, and L. S. Choi, "The synthesis of a new family of boron-based anion receptors and the study of their effect on ion pair dissociation and conductivity of lithium salts in nonaqueous solutions," *Journal of The Electrochemical Society*, vol. 145, no. 8, pp. 2813–2818, 1998.

[117] R. Aroca, M. Nazri, G. A. Nazri, A. J. Camargo, and M. Trsic, "Vibrational spectra and ion-pair properties of lithium hexafluorophosphate in ethylene carbonate based mixed-solvent systems for lithium batteries," *Journal of Solution Chemistry*, vol. 29, no. 10, pp. 1047–1060, 2000.

[118] R. B. Ross, C. M. Cardona, D. M. Guldi, S. G. Sankaranarayanan, M. O. Reese, N. Kopidakis, J. Peet, B. Walker, G. C. Bazan, E. Van Keuren, B. C. Holloway, and M. Drees, "Endohedral fullerenes for organic photovoltaic devices," *Nature Materials*, vol. 8, pp. 208–212, Mar 2009.

[119] E. Vauthey, "Investigations of bimolecular photoinduced electron transfer reactions in polar solvents using ultrafast spectroscopy," *Journal of Photochemistry and Photobiology* A: *Chemistry*, vol. 179, no. 13, pp. 1 – 12, 2006.

[120] K. K. Mentel, R. M. D. Nunes, C. Serpa, and L. G. Arnaut, "Dynamics of radical ion pairs following photoinduced electron transfer in solvents with low and intermediate polarities," *The Journal of Physical Chemistry B*, vol. 119, no. 24, pp. 7571–7578, 2015. PMID: 25588979.

[121] J.-M. Lü, S. V. Rosokha, S. V. Lindeman, I. S. Neretin, and J. K. Kochi, ""Separated" versus "Contact" ion-pair structures in solution from their crystalline states:

Dynamic effects on dinitrobenzenide as a mixed-valence anion," *Journal of the American Chemical Society*, vol. 127, no. 6, pp. 1797–1809, 2005. PMID: 15701015.

[122] T. Kühne, R. Küster, and P. Vöhringer, "Femtosecond photodissociation of triiodide in solution: Excitation energy dependence and transition state dynamics," *Chemical Physics*, vol. 233, pp. 161–178, 1998.

[123] K. H. Kim, H. Ki, K. Y. Oang, S. Nozawa, T. Sato, J. Kim, T. K. Kim, J. Kim, S.-i. Adachi, and H. Ihee, "Global reaction pathways in the photodissociation of I_3^- ions in solution at 267 and 400 nm studied by picosecond x-ray liquidography," *ChemPhysChem*, vol. 14, no. 16, pp. 3687–3697, 2013.

[124] K. Hwan Kim, J. Kim, J. Hyuk Lee, and H. Ihee, "Topical review: Molecular reaction and solvation visualized by time-resolved x-ray solution scattering: Structure, dynamics, and their solvent dependence," *Structural Dynamics*, vol. 1, no. 1, 2014.

[125] H. Sakane, T. Mitsui, H. Tanida, and I. Watanabe, "XAFS analysis of triiodide ion in solutions," *Journal of Synchrotron Radiation*, vol. 8, pp. 674–676, Mar 2001.

[126] A. E. Johnson, , and A. B. Myers, "Solvent effects in the raman spectra of the triiodide ion: Observation of dynamic symmetry breaking and solvent degrees of freedom," *The Journal of Physical Chemistry*, vol. 100, no. 19, pp. 7778–7788, 1996.

[127] F. S. Zhang and R. M. Lynden-Bell, "Solvent-induced symmetry breaking," *Phys. Rev. Lett.*, vol. 90, p. 185505, 2003.

[128] E. Gershgoren, *Ultrafast Time Resolved Photodissociation of Trihalide Ions in Solution.* PhD thesis, Hebrew University (Jerusalem), 2002.

[129] A. A. Hoops, J. R. Gascooke, A. E. Faulhaber, K. E. Kautzman, and D. M. Neumark, "Two- and three-body photodissociation of gas phase I_3^-," *The Journal of Chemical Physics*, vol. 120, no. 17, pp. 7901–7909, 2004.

[130] R. Nakanishi, N. Saitou, T. Ohno, S. Kowashi, S. Yabushita, and T. Nagata, "Photodissociation of gas-phase I_3^-: Comprehensive understanding of nonadiabatic dissociation dynamics," *The Journal of Chemical Physics*, vol. 126, no. 20, p. 204311, 2007.

[131] G. L. Miessler, P. J. Fischer, and D. A. Tarr, *Inorganic Chemistry (5th Edition)*, ch. Coordination Chemistry II: Bonding, pp. 366–367. Prentice Hall, 2013.

[132] M. Grätzel, “Conversion of sunlight to electric power by nanocrystalline dye-sensitized solar cells,” *Journal of Photochemistry and Photobiology A: Chemistry*, vol. 164, pp. 3–14, jun 2004.

[133] S. Campagna, F. Puntoriero, F. Nastasi, G. Bergamini, and V. Balzani, *Photochemistry and Photophysics of Coordination Compounds. An extended view.*, vol. 280 of *Topics in Current Chemistry*. Berlin, Heidelberg: Springer Berlin Heidelberg, 2007.

[134] C. Creutz, M. Chou, T. L. Netzel, M. Okumura, and N. Sutin, “Lifetimes, spectra, and quenching of the excited states of polypyridine complexes of iron(II), ruthenium(II), and osmium(II),” *Journal of the American Chemical Society*, vol. 102, pp. 1309–1319, feb 1980.

[135] C. Bressler, C. Milne, V.-T. Pham, A. Elnahhas, R. M. van der Veen, W. Gawelda, S. Johnson, P. Beaud, D. Grolimund, M. Kaiser, C. N. Borca, G. Ingold, R. Abela, and M. Chergui, “Femtosecond XANES study of the light-induced spin crossover dynamics in an iron(II) complex.,” *Science*, vol. 323, no. 5913, pp. 489–92, 2009.

[136] G. Auböck and M. Chergui, “Sub-50-fs photoinduced spin crossover in $[Fe(bpy)_3]^{2+}$,” *Nature Chemistry*, vol. 7, pp. 629–633, Aug 2015.

[137] J. K. M. Lindsey L. Jamula, Allison M. Brown, Dong Guo, “Synthesis and Characterization of a High-Symmetry Ferrous Polypyridyl Complex: Approaching the $^5T_2/^3T_1$ Crossing Point for Fe^{II},” *Inorganic Chemistry*, vol. 53, pp. 15–17, 2014.

[138] A. K. C. Mengel, C. Förster, A. Breivogel, K. Mack, J. R. Ochsmann, F. Laquai, V. Ksenofontov, and K. Heinze, “A Heteroleptic Push-Pull Substituted Iron(II) Bis(tridentate) Complex with Low-Energy Charge-Transfer States,” *Chemistry - A European Journal*, vol. 21, no. 2, pp. 704–714, 2015.

[139] D. N. Bowman, A. Bondarev, S. Mukherjee, and E. Jakubikova, “Tuning the Electronic Structure of Fe(II) Polypyridines via Donor Atom and Ligand Scaffold Modifications: A Computational Study,” *Inorganic Chemistry*, vol. 54, no. 17, pp. 8786–8793, 2015.

[140] Y. Liu, T. Harlang, S. E. Canton, P. Chábera, K. Suárez-Alcántara, A. Fleckhaus, D. a. Vithanage, E. Göransson, A. Corani, R. Lomoth, V. Sundström, and K. Wärnmark, “Towards longer-lived metal-to-ligand charge transfer states of iron(II) complexes: an N-heterocyclic carbene approach.,” *Chemical communications*, vol. 49, pp. 6412–6414, 2013.

[141] T. Duchanois, T. Etienne, C. Cebrián, L. Liu, A. Monari, M. Beley, X. Assfeld, S. Haacke, and P. C. Gros, "An Iron-Based Photosensitizer with Extended Excited-State Lifetime: Photophysical and Photovoltaic Properties," *European Journal of Inorganic Chemistry*, vol. 2015, no. 14, pp. 2469–2477, 2015.

[142] Y. Liu, K. S. Kjær, L. a. Fredin, P. Chábera, T. Harlang, S. E. Canton, S. Lidin, J. Zhang, R. Lomoth, K.-E. Bergquist, P. Persson, K. Wärnmark, and V. Sundström, "A heteroleptic ferrous complex with mesoionic bis(1,2,3-triazol-5-ylidene) ligands: Taming the MLCT excited state of iron(II).," *Chemistry (Weinheim an der Bergstrasse, Germany)*, vol. 21, no. 9, pp. 3628–3639, 2014.

[143] I. M. Dixon, F. Alary, M. Boggio-Pasqua, and J.-L. Heully, "Reversing the relative ^{3}MLCT-^{3}MC order in Fe(II) complexes using cyclometallating ligands: a computational study aiming at luminescent Fe(II) complexes," *Dalton Trans.*, vol. 44, no. 30, pp. 13498–13503, 2015.

[144] E. Galoppini, "Light harvesting: Strike while the iron is cold," *Nat Chem*, vol. 7, no. 11, pp. 861–862, 2015.

[145] M. K. Nazeeruddin, A. Kay, I. Rodicio, R. Humphry-Baker, E. Mueller, P. Liska, N. Vlachopoulos, and M. Graetzel, "Conversion of light to electricity by cis-X2bis(2,2'-bipyridyl-4,4'-dicarboxylate)ruthenium(ii) charge-transfer sensitizers (X = Cl^-, Br^-, I^-, CN^-, and SCN^-) on nanocrystalline titanium dioxide electrodes," *Journal of the American Chemical Society*, vol. 115, no. 14, pp. 6382–6390, 1993.

[146] A. Hagfeldt, G. Boschloo, L. Sun, L. Kloo, and H. Pettersson, "Dye-sensitized solar cells," *Chem. Rev.*, vol. 110, pp. 6595–6663, 2010.

[147] M. K. Nazeeruddin, E. Baranoff, and M. Gr atzel, "Dye-sensitized solar cells: A brief overview," *Solar Energy*, vol. 85, no. 6, pp. 1172–1178, 2011.

[148] J. Schnadt, P. A. Bruhwiler, L. Patthey, J. N. O'Shea, S. Sodergren, M. Odelius, R. Ahuja, O. Karis, M. Bassler, P. Persson, H. Siegbahn, S. Lunell, and N. Martensson, "Experimental evidence for sub-3-fs charge transfer from an aromatic adsorbate to a semiconductor," *Nature*, vol. 418, no. 6898, pp. 620–623, 2002.

[149] N. A. Anderson and T. Lian, "Ultrafast Electron Transfer At the Molecule-Semiconductor Nanoparticle Interface," *Annual Review of Physical Chemistry*, vol. 56, no. 1, pp. 491–519, 2005.

[150] a. Hauser, “Intersystem crossing in the $[Fe(ptz)_6](BF_4)_2$ spin crossover system (ptz=1-propyltetrazole),” *J. Chem. Phys.*, vol. 94, no. 4, p. 2741, 1991.

[151] A. Hauser, A. Vef, and P. Adler, “Intersystem crossing dynamics in Fe(II) coordination compounds,” *The Journal of Chemical Physics*, vol. 95, no. 12, p. 8710, 1991.

[152] L. Wiehl, “Structures of hexakis(1-propyltetrazole)iron(II) bis(tetrafluoroborate), [Fe(CHN4C3H7)6](BF4)2, hexakis(1-methyltetrazole)iron(II) bis(tetrafluoroborate), [Fe(CHN4CH3)6](BF4)2, and the analogous perchlorates. Their relation to spin crossover behaviour and,” *Acta Crystallographica Section B Structural Science*, vol. 49, no. 1988, pp. 289–303, 1993.

[153] J. Jeftic, R. Hinek, S. C. Capelli, and A. Hauser, “Cooperativity in the iron(II) spin-crossover compound [Fe(ptz)(6)](PF(6))(2) under the influence of external pressure (ptz = 1-n-propyltetrazole).,” *Inorganic chemistry*, vol. 36, no. 14, pp. 3080–3087, 1997.

[154] E. Dova, A. F. Stassen, R. A. Driessen, E. Sonneveld, K. Goubitz, R. Peschar, J. G. Haasnoot, J. Reedijk, and H. Schenk, “Structure determination of the [Fe(teec)(6)](BF(4))(2) metal complex from laboratory and synchrotron X-ray powder diffraction data with grid-search techniques,” *Acta Crystallographica B*, vol. 57, pp. 531–538, 2001.

[155] J. Kusz, H. Spiering, and P. Gütlich, “X-ray structure study of the light-induced metastable states of the spin-crossover compound [Fe(mtz)6](BF4) 2,” *Journal of Applied Crystallography*, vol. 34, no. 3, pp. 229–238, 2001.

[156] W. Gawelda, V.-T. Pham, M. Benfatto, Y. Zaushitsyn, M. Kaiser, D. Grolimund, S. L. Johnson, R. Abela, A. Hauser, C. Bressler, and M. Chergui, “Structural Determination of a Short-Lived Excited Iron(II) Complex by Picosecond X-Ray Absorption Spectroscopy,” *Physical Review Letters*, vol. 98, no. 5, p. 057401, 2007.

[157] S. Nozawa, T. Sato, M. Chollet, K. Ichiyanagi, A. Tomita, H. Fujii, S.-i. Adachi, and S.-y. Koshihara, “Direct probing of spin state dynamics coupled with electronic and structural modifications by picosecond time-resolved XAFS.,” *Journal of the American Chemical Society*, vol. 132, pp. 61–3, jan 2010.

[158] A. Cannizzo, C. Milne, C. Consani, W. Gawelda, C. Bressler, F. van Mourik, and M. Chergui, “Light-induced spin crossover in Fe(II)-based complexes: The full photo-

cycle unraveled by ultrafast optical and X-ray spectroscopies," *Coordination Chemistry Reviews*, vol. 254, pp. 2677–2686, nov 2010.

[159] H. T. Lemke, C. Bressler, L. X. Chen, D. M. Fritz, K. J. Gaffney, A. Galler, W. Gawelda, K. Haldrup, R. W. Hartsock, H. Ihee, J. Kim, K. H. Kim, J. H. Lee, M. M. Nielsen, A. B. Stickrath, W. Zhang, D. Zhu, and M. Cammarata, "Femtosecond X-ray absorption spectroscopy at a hard X-ray free electron laser: application to spin crossover dynamics.," *The journal of physical chemistry. A*, vol. 117, no. 4, pp. 735–40, 2013.

[160] L. a. Fredin, M. Pápai, E. Rozsályi, G. Vankó, K. Wärnmark, V. Sundström, and P. Persson, "Exceptional excited-state lifetime of an iron(II)-N-heterocyclic carbene complex explained," *Journal of Physical Chemistry Letters*, vol. 5, no. 12, pp. 2066–2071, 2014.

[161] G. A. Parada, L. A. Fredin, M.-P. Santoni, M. Jäger, R. Lomoth, L. Hammarström, O. Johansson, P. Persson, and S. Ott, "Tuning the electronics of bis(tridentate)ruthenium(II) complexes with long-lived excited states: modifications to the ligand skeleton beyond classical electron donor or electron withdrawing group decorations.," *Inorganic chemistry*, vol. 52, no. 9, pp. 5128–5137, 2013.

[162] M. J. Frisch, G. W. Trucks, H. B. Schlegel, G. E. Scuseria, M. A. Robb, J. R. Cheeseman, G. Scalmani, V. Barone, B. Mennucci, G. A. Petersson, H. Nakatsuji, M. Caricato, X. Li, H. P. Hratchian, A. F. Izmaylov, J. Bloino, G. Zheng, J. L. Sonnenberg, M. Hada, M. Ehara, K. Toyota, R. Fukuda, J. Hasegawa, M. Ishida, T. Nakajima, Y. Honda, O. Kitao, H. Nakai, T. Vreven, J. A. Montgomery Jr., J. E. Peralta, F. Ogliaro, M. Bearpark, J. J. Heyd, E. Brothers, K. N. Kudin, V. N. Staroverov, R. Kobayashi, J. Normand, K. Raghavachari, A. Rendell, J. C. Burant, S. S. Iyengar, J. Tomasi, M. Cossi, N. Rega, J. M. Millam, M. Klene, J. E. Knox, J. B. Cross, V. Bakken, C. Adamo, J. Jaramillo, R. Gomperts, R. E. Stratmann, O. Yazyev, A. J. Austin, R. Cammi, C. Pomelli, J. W. Ochterski, R. L. Martin, K. Morokuma, V. G. Zakrzewski, G. A. Voth, P. Salvador, J. J. Dannenberg, S. Dapprich, A. D. Daniels, . Farkas, J. B. Foresman, J. V. Ortiz, J. Cioslowski, and D. J. Fox, "Gaussian 09 Revision D.01."

[163] E. Guàrdia, R. Pinzón, J. Casulleras, M. Orozco, and F. J. Luque, "Comparison of different three-site interaction potentials for liquid acetonitrile," *Molecular Simulation*, vol. 26, no. 4, pp. 287–306, 2001.

[164] W. L. Jorgensen et al., "Development and testing of the opls all-atom force field on conformational energetics and properties of organic liquids," *Journal of the American Chemical Society*, vol. 118, pp. 11225–11236, 1996.

[165] G. J. Martyna, M. L. Klein, and M. Tuckerman, "Nosé-hoover chains: The canonical ensemble via continuous dynamics," *The Journal of Chemical Physics*, vol. 97, no. 4, pp. 2635–2643, 1992.

[166] A. Dohn, E. Biasin, K. Haldrup, M. Nielsen, N. Henriksen, and K. Møller, "On the calculation of x-ray scattering signals from pairwise radial distribution functions," *ournal of Physics B: Atomic, Molecular and Optical Physics*, vol. 48, p. 244010, 2015.

[167] L. M. L. Daku and A. Hauser, "Ab initio molecular dynamics study of an aqueous solution of $[\mathrm{Fe(bpy)_3}](\mathrm{Cl})_2$ in the low-spin and in the high-spin states," *The Journal of Physical Chemistry Letters*, vol. 1, no. 12, pp. 1830–1835, 2010.

[168] M. Swart, M. Guell, and M. Sola, "A multi-scale approach to spin crossover in fe(ii) compounds," *Phys. Chem. Chem. Phys.*, vol. 13, pp. 10449–10456, 2011.

[169] S. Iuchi, "A model electronic hamiltonian to study low-lying electronic states of $[\mathrm{Fe(bpy)_3}]^{2+}$ in aqueous solution," *The Journal of Chemical Physics*, vol. 136, no. 6, 2012.

[170] J. Lee, J. Kim, M. Cammarata, Q. Kong, K. Kim, J. Choi, T. Kim, M. Wulff, and H. Ihee, "Transient x-ray diffraction reveals global and major reaction pathways for the photolysis of iodoform in solution," *Angewandte Chemie International Edition*, vol. 47, no. 6, pp. 1047–1050, 2008.

[171] Q. Kong, J. H. Lee, M. Lo Russo, T. K. Kim, M. Lorenc, M. Cammarata, S. Bratos, T. Buslaps, V. Honkimaki, H. Ihee, and M. Wulff, "Photolysis of Br_2 in CCl_4 studied by time-resolved X-ray scattering," *Acta Crystallographica Section A*, vol. 66, pp. 252–260, Mar 2010.

[172] H. Ihee, M. Wulff, J. Kim, and S. ichi Adachi, "Ultrafast x-ray scattering: structural dynamics from diatomic to protein molecules," *International Reviews in Physical Chemistry*, vol. 29, no. 3, pp. 453–520, 2010.

[173] M. Marchivie, P. Guionneau, J.-F. Létard, and D. Chasseau, "Towards direct correlations between spin-crossover and structural features in iron(II) complexes," *Acta Crystallographica Section B Structural Science*, vol. 59, no. 4, pp. 479–486, 2003.

[174] S. Alvarez, "Relationships between temperature, magnetic moment, and continuous symmetry measures in spin crossover complexes.," *Journal of the American Chemical Society*, vol. 125, pp. 6795–802, jun 2003.

[175] A. Hauser, C. Enachescu, M. L. Daku, A. Vargas, and N. Amstutz, "Low-temperature lifetimes of metastable high-spin states in spin-crossover and in low-spin iron(II) compounds: The rule and exceptions to the rule," *Coordination Chemistry Reviews*, vol. 250, no. 13-14, pp. 1642–1652, 2006.

[176] S. E. Canton, X. Zhang, L. M. Lawson Daku, A. L. Smeigh, J. Zhang, Y. Liu, C. J. Wallentin, K. Attenkofer, G. Jennings, C. a. Kurtz, D. Gosztola, K. Wärnmark, A. Hauser, and V. Sundström, "Probing the anisotropic distortion of photoexcited spin crossover complexes with picosecond X-ray absorption spectroscopy," *Journal of Physical Chemistry C*, vol. 118, no. 8, pp. 4536–4545, 2014.

[177] X. Zhang, M. L. Lawson Daku, J. Zhang, K. Suarez-Alcantara, G. Jennings, C. a. Kurtz, and S. E. Canton, "Dynamic Jahn-Teller Effect in the Metastable High-Spin State of Solvated [Fe(terpy)2]2+," *The Journal of Physical Chemistry C*, vol. 119, no. 6, pp. 3312–3321, 2015.

[178] N. Huse, T. K. Kim, L. Jamula, J. K. McCusker, F. M. F. de Groot, and R. W. Schoenlein, "Photo-induced spin-state conversion in solvated transition metal complexes probed via time-resolved soft x-ray spectroscopy," *Journal of the American Chemical Society*, vol. 132, no. 19, pp. 6809–6816, 2010.

[179] N. Huse, H. Cho, K. Hong, L. Jamula, F. M. F. de Groot, T. K. Kim, J. K. McCusker, and R. W. Schoenlein, "Femtosecond soft x-ray spectroscopy of solvated transition-metal complexes: Deciphering the interplay of electronic and structural dynamics," *The Journal of Physical Chemistry Letters*, vol. 2, no. 8, pp. 880–884, 2011.

[180] H. Cho, M. L. Strader, K. Hong, L. Jamula, E. M. Gullikson, T. K. Kim, F. M. F. de Groot, J. K. McCusker, R. W. Schoenlein, and N. Huse, "Ligand-field symmetry effects in Fe(II) polypyridyl compounds probed by transient x-ray absorption spectroscopy," *Faraday Discuss.*, vol. 157, pp. 463–474, 2012.

[181] B. E. V. Kuiken, H. Cho, K. Hong, M. Khalil, R. W. Schoenlein, T. K. Kim, and N. Huse, "Time-resolved x-ray spectroscopy in the water window: Elucidating transient valence charge distributions in an aqueous Fe(II) complex," *The Journal of Physical Chemistry Letters*, vol. 7, no. 3, pp. 465–470, 2016.

[182] H. Funke, A. C. Scheinost, and M. Chukalina, “Wavelet analysis of extended x-ray absorption fine structure data,” *Phys. Rev. B*, vol. 71, p. 094110, Mar 2005.

[183] H. Funke, M. Chukalina, and A. C. Scheinost, “A new *FEFF*-based wavelet for EXAFS data analysis,” *Journal of Synchrotron Radiation*, vol. 14, pp. 426–432, Sep 2007.

[184] J. Timoshenko and A. Kuzmin, “Wavelet data analysis of {EXAFS} spectra,” *Computer Physics Communications*, vol. 180, no. 6, pp. 920 – 925, 2009.

[185] D. N. Bowman and E. Jakubikova, “Low-spin versus high-spin ground state in pseudo-octahedral iron complexes,” *Inorganic Chemistry*, vol. 51, no. 11, pp. 6011–6019, 2012.

[186] M. Pápai, G. Vankó, C. de Graaf, and T. Rozgonyi, “Theoretical investigation of the electronic structure of Fe(II) complexes at spin-state transitions,” *Journal of Chemical Theory and Computation*, vol. 9, no. 1, pp. 509–519, 2013.

[187] J. Nance, D. N. Bowman, S. Mukherjee, C. T. Kelley, and E. Jakubikova, “Insights into the spin-state transitions in $[Fe(tpy)_2]^2$+: Importance of the terpyridine rocking motion,” *Inorganic Chemistry*, vol. 54, no. 23, pp. 11259–11268, 2015.

[188] T. C. B. Harlang, Y. Liu, O. Gordivska, L. A. Fredin, C. S. Ponseca Jr, P. Huang, P. Chábera, K. S. Kjær, H. Mateos, J. Uhlig, R. Lomoth, R. Wallenberg, S. Styring, P. Persson, V. Sundström, and K. Wärnmark, “Iron sensitizer converts light to electrons with 92% yield,” *Nature Chemistry*, vol. 7, pp. 883–889, Nov 2015.

[189] A. Hauser, P. G utlich, R. Hinek, H. Spiering, and D. Schollmeyer, “The $[Fe(etz)_6](BF_4)_2$ spin-crossover system-part one: High-spin - low-spin transition in two lattice sites,” *Chemistry - A European Journal*, vol. 2, no. 11, pp. 1427–1434, 1996.

[190] A. Hauser, *Spin Crossover in Transition Metal Compounds II*, ch. Light-Induced Spin Crossover and the High-Spin→Low-Spin Relaxation, pp. 155–198. Berlin, Heidelberg: Springer Berlin Heidelberg, 2004.

[191] J. P. Sauvage, J. P. Collin, J. C. Chambron, S. Guillerez, C. Coudret, V. Balzani, F. Barigelletti, L. D. Cola, and L. Flamigni, “Ruthenium(II) and Osmium(II) bis(terpyridine) complexes in covalently-linked multicomponent systems: Synthesis, electrochemical behavior, absorption spectra, and photochemical and photophysical properties,” *Chemical Reviews*, vol. 94, no. 4, pp. 993–1019, 1994.

[192] X. Song, Y. Lei, S. V. Wallendal, M. W. Perkovic, D. C. Jackman, J. F. Endicott, and D. P. Rillema, "Photoinduced electron-transfer processes involving covalently linked ruthenium and cobalt polypyridyl complexes: comparison of electronic coupling in bridged and nonbridged ruthenium and cobalt complexes," *The Journal of Physical Chemistry*, vol. 97, no. 13, pp. 3225–3236, 1993.

[193] H. Torieda, K. Nozaki, A. Yoshimura, and T. Ohno, "Low quantum yields of relaxed electron transfer products of moderately coupled Ruthenium(II)-Cobalt(III) compounds on the subpicosecond laser excitation," *The Journal of Physical Chemistry A*, vol. 108, no. 22, pp. 4819–4829, 2004.

[194] C. Creutz, "Nonadiabatic, short-range, intramolecular electron transfer from ruthenium(ii) to cobalt(iii) complexes," *The Journal of Physical Chemistry B*, vol. 111, no. 24, pp. 6713–6717, 2007.

[195] G. Smolentsev, S. Canton, J. Lockard, V. Sundstrom, and L. Chen, "Local structure of photoexcited bimetallic complexes refined by quantitative XANES analysis," *Journal of Electron Spectroscopy and Related Phenomena*, vol. 184, no. 3-6, pp. 125–128, 2011. Advances in Vacuum Ultraviolet and X-ray Physics The 37th International Conference on Vacuum Ultraviolet and X-ray Physics (VUVX2010).

[196] S. E. Canton, X. Zhang, J. Zhang, T. B. van Driel, K. S. Kjær, K. Haldrup, P. Chabera, T. Harlang, K. Suarez-Alcantara, Y. Liu, J. Pérez, A. Bordage, M. Pápai, G. Vankó, G. Jennings, C. A. Kurtz, M. Rovezzi, P. Glatzel, G. Smolentsev, J. Uhlig, A. O. Dohn, M. Christensen, A. Galler, W. Gawelda, C. Bressler, H. T. Lemke, K. B. Møller, M. M. Nielsen, R. Lomoth, K. W arnmark, and V. Sundstr om, "Toward highlighting the ultrafast electron transfer dynamics at the optically dark sites of photocatalysts," *The Journal of Physical Chemistry Letters*, vol. 4, no. 11, pp. 1972–1976, 2013.

[197] K. Kuhar, L. A. Fredin, and P. Persson, "Exploring photoinduced excited state evolution in heterobimetallic Ru(II)-Co(III) complexes," *The Journal of Physical Chemistry B*, vol. 119, no. 24, pp. 7378–7392, 2015.

[198] S. E. Canton, X. Zhang, Y. Liu, J. Zhang, M. Papai, A. Corani, A. L. Smeigh, G. Smolentsev, K. Attenkofer, G. Jennings, C. A. Kurtz, F. Li, T. Harlang, D. Vithanage, P. Chabera, A. Bordage, L. Sun, S. Ott, K. Warnmark, and V. Sund-

strom, “Watching the dynamics of electrons and atoms at work in solar energy conversion,” *Faraday Discuss.*, vol. 185, pp. 51–68, 2015.

[199] P. Connolly and J. H. Espenson, “Cobalt-catalyzed evolution of molecular hydrogen,” *Inorganic Chemistry*, vol. 25, no. 16, pp. 2684–2688, 1986.

[200] V. Artero, M. Chavarot-Kerlidou, and M. Fontecave, “Splitting water with cobalt,” *Angewandte Chemie International Edition*, vol. 50, no. 32, pp. 7238–7266, 2011.

[201] E. Mosconi, J.-H. Yum, F. Kessler, C. J. G. García, C. Zuccaccia, A. Cinti, M. K. Nazeeruddin, M. Gr atzel, and F. D. Angelis, “Cobalt electrolyte/dye interactions in dye-sensitized solar cells: A combined computational and experimental study,” *Journal of the American Chemical Society*, vol. 134, no. 47, pp. 19438–19453, 2012.

[202] J. Bolger, A. Gourdon, E. Ishow, and J.-P. Launay, “Mononuclear and binuclear tetrapyrido[3,2-a:2’,3”-c:3”,2”-h:2”’,3”’-j]phenazine (tpphz) ruthenium and osmium complexes,” *Inorganic Chemistry*, vol. 35, no. 10, pp. 2937–2944, 1996.

[203] L. Flamigni, S. Encinas, F. Barigelletti, F. M. MacDonnell, K.-J. Kim, F. Puntoriero, and S. Campagna, “Excited-state interconversion between emissive mlct levels in a dinuclear Ru(II) complex containing a bridging ligand with an extended π system,” *Chem. Commun.*, pp. 1185–1186, 2000.

[204] C. Chiorboli, M. A. J. Rodgers, and F. Scandola, “Ultrafast processes in bimetallic dyads with extended aromatic bridges. energy and electron transfer pathways in tetrapyridophenazine-bridged complexes,” *Journal of the American Chemical Society*, vol. 125, no. 2, pp. 483–491, 2003.

[205] F. Neese, “Orca, an ab initio, density functional and semiempirical electronic structure program package, version 2.8,” *Universitat Bonn: Bonn, Germany*, 2010.

[206] H. Paulsen and A. X. Trautwein, *Spin Crossover in Transition Metal Compounds III*, ch. Density Functional Theory Calculations for Spin Crossover Complexes, pp. 197–219. Berlin, Heidelberg: Springer Berlin Heidelberg, 2004.

[207] A. Vargas, M. Zerara, E. Krausz, A. Hauser, and L. M. L. Daku, “Density-functional theory investigation of the geometric, energetic, and optical properties of the cobalt(ii) tris(2,2’-bipyridine) complex in the high-spin and the jahn-teller active low-spin states,” *Journal of Chemical Theory and Computation*, vol. 2, no. 5, pp. 1342–1359, 2006.

[208] Y. Shiota, D. Sato, G. Juhász, and K. Yoshizawa, "Theoretical study of thermal spin transition between the singlet state and the quintet state in the [Fe(2-picolylamine)$_3$]$^{2+}$ spin crossover system," *The Journal of Physical Chemistry A*, vol. 114, no. 18, pp. 5862–5869, 2010.

[209] A. Klamt and G. Schuurmann, "COSMO: a new approach to dielectric screening in solvents with explicit expressions for the screening energy and its gradient," *J. Chem. Soc., Perkin Trans. 2*, pp. 799–805, 1993.

[210] A. Dohn, K. Møller, and N. Henriksen, *Transient Changes in Molecular Geometries and How to Model Them.* PhD thesis, Technical University of Denmark, 2014.

[211] K. Kjær, *Filming Femtosecond Molecular Movies with X-ray Pulses.* PhD thesis, The Niels Bohr Institute, Faculty of Science, University of Copenhagen, 2013.

[212] U. Bergmann and S. P. Cramer, "High-resolution large-acceptance analyzer for x-ray fluorescence and raman spectroscopy," *Proc. SPIE*, vol. 3448, pp. 198–209, 1998.